Atomically defined tips in scanning probe microscopy

William Paul
Physics Department, McGill University,
Montreal, Québec, Canada.
March 2013

A thesis submitted to McGill University in partial fulfillment
of the requirements of the degree of Doctor of Philosophy

To Sara, secret enthusiast of materials science,
and baby Juliet

Table of contents

Abstract

Scanning probe microscopy (SPM) studies are carried out with atomically defined tips, characterized by field ion microscopy (FIM). This combination of microscopies allows for the characterization of the SPM probe apex which is usually of unknown atomic geometry – in principle, an atomically defined tip would predetermine SPM resolution and the tip's electronic structure for spectroscopy. In a set of exploratory experiments to investigate the use of atomically defined tips in SPM, we investigate issues of tip integrity, material transfer and tip modifications, and implement the tips in the study of mechanical properties of nanoscale contacts by indentation.

In order to perform SPM studies with the characterized tips, a protocol is introduced to preserve the atomic structure of the tip apex from etching due to gas impurities during the transfer period from FIM to SPM. Estimations are made regarding the time limitations of such an atomically-defined experiment due to contamination by ultra-high vacuum (UHV) rest gases. We conclude from tunneling experiments with several types of surfaces that transferred atoms from the sample limit the choice of surfaces for which the tip integrity is preserved in tunneling experiments at room temperature. The atomic structure of FIM tip apices is unchanged only after tunneling to the highly reactive Si(111) surface.

Atoms transferred to W(111) and W(110) tip apices from the Au(111) surface during tunneling and approach to contact experiments are characterized in FIM at room temperature and at 158 K. The different activation energies for diffusion on the (111) and (110) tip planes and the experiment temperature are shown to be important considerations in observing changes to the atomic structure of the tip in FIM. Resolution of atomically defined tips in scanning tunneling microscopy (STM) and scanning tunneling spectroscopy (STS) is investigated on the Si(111)-2×1 surface, but tip integrity remains a challenge even for this substrate at room temperature.

In spite of changes to the atomic structure of tip apices, FIM-characterized SPM tips are very well suited to the study of nanoscale plasticity in atomic-scale nanoindentation. Accurate characterization of the probe tip is required for estimating contact stresses and is also used as input for atomistic simulations on the same size scale. We investigate unique phenomena in mechanical contacts between dissimilar metals with clean FIM tips, then the formation of the smallest permanent indentation on the Au(111) surface is studied at the transition of elastic to plastic loading. Nanoindentation and characterization of the plastic damage to the surface are accomplished by simultaneous STM and atomic force microscopy

(AFM) with a 9.5 nm radius W(111) tip. Elastic and plastic indentations are identified both in the residual impression image and by features in their force-displacement curves such as the sink-in depth, pop-ins and hysteresis energy. Plasticity is best identified quantitatively in the force-displacement curves by the sink-in depth. The minimum 'quantum' of plastic damage to the substrate is associated with an energy budget of ~70 eV.

In summary, we have introduced a protocol for implementing atomically defined tips in SPM experiments and explored the limitations in preserving the integrity of the tip. We conclude that within the constraints of room temperature experiments on metal surfaces, their use in atomic-scale nanoindentation experiments is still extremely valuable.

Résumé

Des études de microscopie à sonde locale (scanning probe microscopy, SPM) sont effectuées à l'aide de pointes définies à l'échelle atomique caractérisées par microscopie à champ ionique (field ion microscopy, FIM). La combinaison de ces microscopies permet de caractériser la géométrie, généralement inconnue, des atomes situés à la pointe d'une sonde SPM. En principe, cette information détermine la résolution de la SPM ainsi que la structure électronique de la pointe en spectroscopie. Une séquence d'expériences exploratoires en SPM utilisant ces pointes, permet d'étudier les problèmes reliés au maintient de leur intégrité, au transfert de matériel et à leur modification. Ces pointes sont ensuite utilisées lors d'expériences d'indentation afin d'étudier les propriétés mécaniques des contacts à l'échelle nanométrique.

Afin de réaliser des études de SPM avec des pointes définies, un protocole est développé pour protéger la structure atomique des pointes contre les attaques chimiques par des impuretés gazeuses, lors de leur transfert du FIM au SPM. Une fois dans un ultra haut vide (UHV), ces expériences sont soumises à des contraintes de temps dû à l'éventuelle contamination des pointes par des gaz résiduels. Une estimation de ces contraintes est présentée. À partir d'expériences de jonction tunnel effectuées sur différents types de surface, nous observons que pour plusieurs d'entre elles, le transfert d'atome de l'échantillon à la pointe ruine l'intégrité de la sonde à température ambiante. Cela limite grandement le choix des matériaux pour ce type d'expérience. Dans nos expériences, la structure atomique des pointes imagées par FIM reste inchangée seulement dans le cas de la surface très réactive Si(111).

Les atomes transférés de la surface d'or Au(111) vers une pointe de W(111) et W(110) lors du maintient d'une jonction tunnel et pendant l'approche à contact mécanique sont caractérisés par FIM à température ambiante, ainsi qu'à 158 K. Les différentes énergies d'activation associées à la diffusion sur les plans (111) et (110) de la pointe, ainsi que la température influencent considérablement le changement de structure atomique de la pointe en FIM. La résolution obtenue avec ces pointes en microscopie à effet tunnel (MET) et en spectroscopie par effet tunnel (scanning tunneling spectroscopy, STS) est étudiée sur une surface Si(111)-2×1. Même pour ce substrat, la préservation de l'intégrité de la pointe à température ambiante demeure un défi.

En dépit des changements qui modifient la structure atomique des pointes lors d'une expérience, ces sondes caractérisées par FIM sont intéressantes pour l'étude de la plasticité

à l'échelle nanométrique par nano-indentation. Une caractérisation exacte de la pointe de la sonde est nécessaire pour estimer le tenseur des contraintes associé à un contact mécanique et permet de déterminer les paramètres d'entrées pour des simulations atomistiques. L'observation d'un nouveau phénomène lors d'un contact mécanique entre différents métaux et des pointes propres caractérisées par FIM est présentée. La formation de la plus petite indentation permanente sur une surface d'or Au(111) est étudiée à la transition entre les régimes de déformation élastique et plastique. La nano-indentation et la caractérisation de la déformation plastique sur la surface sont réalisées par une mesure simultanée de microscopie à effet tunnel (MET) et de microscopie à force atomique (MFA) avec une pointe de W(111) de 9.5 nm de rayon. Les indentations plastiques et élastiques sont identifiées à l'aide des images des impressions résiduelles ainsi que par les caractéristiques des courbes de force-déplacement, telles que la profondeur de *sink-in*, les *pop-ins* et l'énergie d'hystérésis. La plasticité s'identifie mieux par une analyse quantitative de la profondeur de *sink-in* dans les courbes de force-déplacement. Le "quanta" de la plus petite déformation plastique sur un substrat est associé à une énergie d'environ 70 eV.

En résumé, nous avons développé un protocole pour implémenter des pointes définis à l'échelle atomique pour des expériences de SPM et nous avons exploré les limitations associées à la préservation de leur intégrité. Nous concluons que malgré les contraintes reliées à leur usage à température ambiante, ces pointes demeurent néanmoins très intéressantes pour des expériences de nano-indentations.

Acknowledgments

I would like to thank my supervisor, Peter Grütter, for the opportunity to work on a very unique project, and giving me the freedom and support to pursue great science. It's inspiring to learn from and discuss things with someone who is directly involved with many recent great achievements in science and technology.

Work on the "FIM System" is not easy, so I would like to express my deepest appreciation to Mehdi El Ouali and Till Hagedorn for having taught me the operation of the UHV system, bungee cord adjustment, sample transfer, STM and FIM operation, tip etching, gold evaporation, etc. during my first year in the lab. Thanks for the excellent introduction to the instrument. Yoichi Miyahara has been an indispensable resource for working on the system. Thanks for help with the many repairs over the years, and your expertise in optics, Linux, electronics, and SPM techniques is most appreciated.

John Smeros and Robert Gagnon have contributed a lot of help behind the scenes helping to spec out new bungee cords, keep rotary vane pumps spinning, teach me how to use various saws and things – thanks! Your knowledge and support is crucial to the success of experimental physics at McGill.

Thank you to two excellent students whom I had the pleasure to supervise for undergraduate research projects – you guys were inspiring individuals to work with: Jean-Benoît Lalanne, NSERC USRA student in Summer 2010 and 2011 worked on iridium tip etching and C_{60} sample preparation and STM characterization. Félix Dumont, undergraduate research project student in Fall 2012 worked on single crystal cantilever beams for the system, and succeeded in making a Cu(100) beam. I am grateful to Prof. Moh'd Rezeq for sharing his insight on tip sharpening and FIM with us for several weeks in Summer 2010.

I am truly fortunate to have had excellent comments on my manuscripts from David Oliver – thank you for reading them with fresh eyes and giving great scientific advice. Thanks also for lots of discussions on nanoindentation and cool ideas for experiments.

Thanks to all the members, present and past, of the SPM group for making this a fun place to work. Thanks in particular to Antoine for having translated this abstract (and a few others) for me over the years – I really appreciate your diligence and scientific insight. Thank you to Jeff and James for help with GXSM operation. Thanks to Antoni for help with the vacuum system, SEM imaging, and listening to me rant about things like my Pompeii'd sample holders when I needed someone to listen to me.

Thanks to Roland Bennewitz, in whose group I first learned UHV AFM as a summer student, and to Phil, Tobin, and Aleks for lots of fun times, many involving beer. Thanks especially to Aleks for a significant contribution to the way I understand AFM instrumentation and noise, for help with lots of little machining projects over the years, for inviting me to work on cool projects with you, and for lots of placemat/napkin physics at McGill Pizza. Thanks also to Aleks for the excellent Microsoft Word thesis template which brings scientific typesetting into the 21st century.

I want to thank Alastair McLean and his group at Queen's for having given me a rigorous introduction to science. I feel like I learned a lot about how to work like a scientist that year. Thanks to Andrew, Jay, Ben, Jason for making it a memorable time. Thanks to Ben for many good discussions on SPM over the years.

I am grateful for the work of Dr. Percy Zahl at Brookhaven National Labs for his development of the GXSM open-source scanning probe microscopy controller. Dr. Zahl has been very helpful in quickly implementing some new features in the controller at my request – many thanks.

Thanks to the inspiration and creativity of Dieu Du Ciel, Bruichladdich, and Mackmyra – one day I hope to join you.

Thanks to friends and family for support and good times – James, Ben, Paul, Massimo, Carissa, Chris (good thing you graduated or we'd still be having coffee), Karen, Nick, Damla, Mary, Andrew, Isaac, Mélisande.

NSERC has provided me with significant support over my graduate career, first as a Canada Graduate Scholarship holder at the Masters' level, and then as a Vanier Scholar – thank you, these programs help a lot with one's motivation to pursue hard work. I also thank the McGill Faculty of Science for supporting me with a Schulich Graduate Fellowship.

Thanks to my grandmother for love and encouragement that I so deeply miss, and for keeping grandpa's oscilloscope down in the basement for me to later find.

Thanks to mom and dad for your love and support for the many years spent at school and not thinking I was too crazy for doing it.

Thanks to my wife Sara and baby Juliet for your love, motivation, inspiration, patience, and understanding.

Statement of originality

- Numerous original techniques and instrumentation developed for these experiments. Notable examples that are most relevant to the experimental results in this thesis are: new sample mounting procedure and holder (section 2.5.3), mica cleavage technique (section 2.7.1), interferometer calibration tools (section 2.6.3), simple cleavage method and sample holder for Si(111)-2×1 [1], insights and new solutions regarding noise sources in scanning probe microscopy (sections 3.2-3.4), high voltage coaxial wiring for field ion microscopy and scanning tunneling microscopy (section 3.5.1), high voltage data acquisition for field ion microscopy (section 3.5.3), automatic relay timing circuits for tip and sample piezo motor connections (Appendix C), versatile antialiasing filters for data acquisition (Appendix D), 4-axis stick-slip motor controller based on a PC audio card, parallel port and Wiimote (Appendix E).

- Novel protocol for implementing atomically defined tips from field ion microscopy (FIM) in scanning probe microscopy (SPM) experiments [2]. This method was developed to maintain atomic integrity of the tip apex against modification by impurity gases. This ensures that it can be transferred to a tip-sample junction with statistical confidence that the apex is unmodified. The work was identified by a referee to be "of particular interest" due to its broad importance to the increasing number of researchers investigating SPM with FIM tips.

- First detailed investigations of material transfer during tunneling experiments with FIM tips. This was carried out with W(110) and W(111) FIM tips and Au(111) surfaces at 150 K and room temperature. This work yields new insight into the choice of tip crystallographic orientation and operation temperature for atomically-defined SPM studies. The exponential distribution of peak heights in tunneling current spikes was characterized and an adatom diffusion model was proposed.

- First study of the initial tip changes that occur with FIM tips while imaging in STM and performing scanning tunneling spectroscopy (STS). Results reported also relate

the geometry of tip convolution artifacts in STM images to real-space coordinates on FIM tip images.

- Study of tip wetting during initial indentation of clean tungsten tips into Au(111) surfaces, manifested as a drop in adhesion force and in maximum junction conductance. The novel investigation of mechanics between clean tungsten tips and gold samples is made possible by our understanding of tip integrity and much improved experimental reliability.

- Studies of the transition from elastic to plastic loading during indentation of fresh tungsten tips reveal new insight into initial plastic indentation between dissimilar metals. The following unique phenomena are simultaneously observed at the onset of plastic deformation with clean FIM tips: pop-ins during the loading of the contact, giant junction conductance increase, linear unloading force profile, large adhesive force, and an anomalous negative hysteresis loop indicating a transfer of some mechanical energy from the indentation volume to the force transducer.

- Newly improved STM resolution and stability allowing for detailed images of surface structures after indentation which help to elucidate the nature of sub-surface damage.

- Studies of the transition from elastic to plastic loading using tungsten tips fully wetted with substrate material (gold) reflect incipient plasticity in the sample rather than effects associated with the wetting of clean tips. A measurable minimum 'quantum' of plastic damage was shown to govern incipient plasticity in Au(111) just above the threshold of elastic loading [3].

Contributions of co-authors

The text from the following sections are based on manuscripts prepared with co-authors. Their contributions are summarized below:

Section 2.7.7 is based on Paul, W., Miyahara, Y. & Grütter, P. Simple Si (111) surface preparation by thin wafer cleavage. *J. Vac. Sci. Technol. A* **31**, 023201 (2013). W.P. designed the experimental method and sample holder apparatus, collected and analyzed the data, and wrote the paper. Y.M. provided technical support on the experimental apparatus and offered suggestions for the sample preparation methods. Y.M. and P.G. edited the manuscript. P.G. supervised the project.

Sections 4.2.2, 4.2.3, 4.3, 4.3.2, 4.3.3, 4.3.4, and 4.4 are based on Paul, W., Miyahara, Y. & Grütter, P. H. Implementation of atomically defined field ion microscopy tips in scanning probe microscopy. *Nanotechnology* **23**, 335702 (2012). W.P. prepared the samples, designed the experimental protocol, collected and analyzed the data, and wrote the paper. Y.M. provided technical support on the experimental apparatus. Y.M. and P.G. helped with the outline of the paper and edited the manuscript. P.G. supervised the project.

Section 6.5 is based on Paul, W., Oliver, D., Miyahara, Y. & Grütter, P. Minimum threshold for incipient plasticity in the atomic-scale nanoindentation of Au(111). *Phys. Rev. Lett.* **110**, 135506 (2013). W.P. prepared the samples, designed the experimental protocol, performed the experiment, analyzed the data, and wrote the paper. D.O. consulted on the experimental protocol, made valuable contributions to the interpretation and analysis of the data, and contributed to the writing of the paper. Y.M. provided technical support on the experimental apparatus. D.O., Y.M. and P.G. edited the manuscript. P.G. supervised the project.

1. Introduction

1.1 Atomically defined contacts

As transistor gate lengths approach the limits set by the discretized building blocks of matter, many challenges and exciting research questions arise. In order to keep us on track with Moore's law, the International Technology Roadmap for Semiconductors has scheduled the implementation of 6 nm technology by 2026, using a "manufacturable solution not known" [4]. If we are to shrink silicon-based CMOS technology, we will first hit a length scale at which the stochastic placement of individual dopant atoms in a device will determine its performance [5, 6]. To fabricate even smaller devices, one might consider using single atoms and molecules as transistor elements, and indeed many scientists have worked toward this [7, 8].

The idea of using a single molecule as a circuit element is often credited to Aviram and Ratner for their proposal of the 'molecular rectifier' in 1974 [9]. Molecular nanoelectronics then became a significant goal of the field of nanotechnology, for which the invention of the scanning tunneling microscope (STM) [10] and the discovery of the buckminsterfullerene [11] were catalysts in the 1980s. The popularization of nanotechnology in the early 2000s forecasted that molecular devices were on the horizon; so where are our single molecule devices?

Only recently have we begun to see the results that were anticipated for about a decade due to the necessary developments in experimental and theoretical techniques. On the experimental side, the dream of the molecular transistor pushed rapid technique development in STM and atomic force microscopy (AFM) [12] – these microscopes needed to operate in ultra-high vacuum, at low temperature [13] for spectroscopic resolution and to maintain the stability of atomic structures. Atomic resolution had to be routinely achievable, and to fully characterize mechanical and electronic properties of nanoscale contacts to molecules, these microscopes would ideally measure force and current simultaneously [14]. Fantastic achievements in understanding resolution [15], contrast mechanisms [16, 17], atomic manipulation [13, 18], chemical identification [19], and electronic spectroscopy [20] now make it possible to attain a rigorous understanding of the physics happening in the tip-sample junction.

Also necessary for the development of a molecular device is a detailed understanding of surface science – how do these molecules bind to the surfaces onto which they are placed?

How can their placement be controlled [21, 22]? What kind of charge transfer occurs, and at what energies are the molecular orbitals with respect to the surface [23]? How can we study intrinsic properties of these molecules and control their coupling to substrates [15]? These are not only valid questions of technological relevance to a molecular transistor, but are of fundamental interest in understanding electron transport in nanoscale physical systems, chemical reactions at surfaces, and catalysis.

On the theoretical side, *ab initio* density functional theory calculations of electronic transport through nanoscale structures have aided the understanding of experimental results – from single-atom contacts [24], to the stretching of nanowires [25], to reaction pathways [26], and STM/AFM resolution and contrast [27, 28]. Motivated to investigate larger atomic configurations and study their evolution during simulated experiments, computational efficiency has been productively increased in recent years [29]. The holy grail of computation in the field of molecular nanoelectronics is the prediction of new types of structures (say, assemblies of molecules) that would make useful devices, but computational efficiency and the rigorous testing of the mean field description of electron correlation [30] are still limiting factors.

In 2012, Fuechsle *et al.* from Michelle Simmons' group at the University of New South Wales 'finally' fabricated a single-atom transistor [31] by employing a STM to lithographically create conductive electrodes and position a single phosphorous atom at a desired location on a silicon surface. This experiment stands upon the shoulders of years of technique development and a mature understanding of surface science. Transistors built from single molecules were also recently realized in 2009 by Song *et al*. [32]. This was an extreme achievement in understanding how to experimentally realize a single molecule bonded to source and drain electrodes with a gate electrode close enough to be able to modulate the electrostatic potential at the molecule.

In a single molecule device, the exact atomic arrangement of the metallic contacts affects metal-molecule coupling, energy-level lineup, and the electrostatic potential profile across the junction resulting in considerable changes to I-V curves [33, 34]. Therefore, to rigorously test and contribute to the refinement of theoretical modeling of nanoscale structures, one still needs data from experiments in which the atomic-scale contact geometry is known and controllable.

The fabrication of atomically defined nanoscale contacts has been a major driving force in this thesis. We have set out to implement atomically defined tips from field ion

microscopy (FIM) in scanning probe microscopy (SPM) experiments toward the fabrication and characterization (mechanical and electronic) of atomically defined junctions. A sketch of such a junction with a C_{60} molecule is shown in Figure 1.1 – the top electrode is an atomically defined tungsten tip, characterized by FIM. The atomically flat crystal surface to which the C_{60} is bonded serves as a second electrode. By combining AFM and STM, we can simultaneously measure force and current through this type of junction. An atomically defined tip-molecule-surface sandwich could provide high quality experimental data for testing *ab initio* electronic transport calculations.

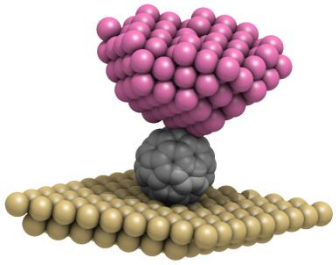

Figure 1.1: Illustration of an atomically defined metal-molecule-metal junction comprising an atomically defined tungsten tip (top), C_{60} molecule (middle), and flat gold surface (bottom).

A cartoon is nice, but back in the lab, things aren't always so simple: From an experimental standpoint, relatively little has been determined about the implementation of atomically defined tips in SPM, even though the advantages of performing STM with an atomically defined FIM tip have been discussed since 1986 [35]. It turns out that protecting the atomic integrity of the tip from corrosion by rest gases (even in ultra-high vacuum) is nontrivial, and ultimately imposes short experiment durations if one desires statistical confidence that the apex remains unaltered. We have also determined that atoms from gold surfaces are uncontrollably transferred to the tip, disqualifying it as being 'atomically defined' [2]. This began a search for alternative substrates for molecular junction experiments which were investigated by STM to determine their suitability with regard to tip changes. Tip changes are, unfortunately, unsuitably common at room temperature[1].

Even though the loss of the tip apex structure from transferred atoms seems somewhat unavoidable, the combination of FIM and SPM still give us a unique opportunity to study electrical and mechanical properties of contacts between dissimilar metals by indentation of

[1] For the substrates which can be prepared in our current apparatus. Not to worry, recommendations for future experiments will be given in these areas based on our exploratory research.

a tungsten tip into a gold surface. At the atomic scale, the roughness of indenters plays a large role in modifying contact pressure distributions [36], and ultimately affects how materials yield [37, 38] and succumb to frictional wear [39]. By its preparation in FIM, the cleanliness of the indenter surface is guaranteed, so we may study phenomena unique to clean nanoscale mechanical contacts such as metallic adhesion [40] in experiments which exactly match the length scales accessible to molecular dynamics atomistic simulations [41, 42]. The combination of STM spatial resolution, force resolution during indentation, knowledge of the indenter's geometry and surface chemistry, and the simultaneous measurement of junction conductance yield unique insights into atomic-scale plasticity.

Bringing this story back to Moore's law, by forming mechanical nanocontacts between dissimilar metals, our precise knowledge of tip geometry (and thus contact area) has allowed us to deduce that the conductance across junctions between tungsten and gold is much lower than expected at the nanometer length scale [43]. In collaboration with Hong Guo's group at McGill, we have found that the decreased conductance is attributable to backscattering at the interface due to the mismatch of electron orbitals of tungsten and gold, as well as at disordered regions and vacancies within the indented volume. At the length scales being pushed by the microelectronics industry, electron scattering at interfaces between dissimilar metals, grain boundaries, and other material defects threatens continued device miniaturization – characterizing these effects is the first step toward understanding how to better control electron conduction.

In summary, our investigations of atomically defined contacts using FIM and SPM are motivated by the sensitivity of contact geometry in single molecule nanoelectronics, the effects of single-crystalline atomic roughness on plastic deformation, and the formation of well-characterized nanoscale electrical contacts between dissimilar metals.

1.2 Outline

A thesis serves several purposes – it relays original contributions to knowledge in the form of new results, discussions and conclusions. But it must also contain a significantly detailed description of the experimental work to provide others with a basis from which to continue research in the discipline. This is especially true when the techniques used are unique and complete references do not exist on the subjects. This thesis is heavily involved with custom instrumentation and techniques, as well as their implementation in original

experiments – we provide an outline below to help readers with different interests decide how to navigate its contents.

Chapter 2 "Gear, Ways, Samples, and Tips" is about experimental methods. We cover the basic design and history of the STM/AFM/FIM apparatus used in our experiments and present the physical operating principles of these forms of microscopy. The way in which forces are transduced in our microscope is non-standard, and it is described in a dedicated section 2.5. The measurement of forces also relies on interferometric detection of the force transducer. We have added new insight to the derivation of the interferometer's operation and improved its ease of calibration – this is described in section 2.6, along with a discussion on the systematic measurement uncertainties inherent in our force transduction technique. The experiments that are described in subsequent chapters require several types of clean surface-science quality samples to be prepared. Sections 2.7 and 2.8 describe the preparation of samples and tips in the context of our experiments; in later chapters we refer back to exact figure and page numbers when necessary. These sections are intended to provide complete descriptions for researchers interested in the methods we have employed (in some cases they are novel and in some cases they are adapted from a number of cited sources).

Chapter 3 "Focus on Low Noise and Systematic Reliability" describes key milestones in our efforts to make combined FIM/SPM experiments possible on a routine basis. Thanks to the developments described in Chapter 3, we are able to report on the results of numerous experiments with a logical progression that gives detailed insight to the implementation of FIM tips in SPM. In order to sort through noise issues, we start with a noise map for detection (force and current) and mechanical noise sources. Then, dealing with these sources individually, we discuss the fundamental physical limits and practical limits to noise in our experiments. Although this chapter is anecdotal at times, we hope that the physical insights it provides about noise sources and the ideas regarding their classification, measurement, and correction are useful for researchers attempting to improve the quality of their experiments. The understanding of high voltage breakdown mechanisms was essential in solving several issues with FIM reliability, so a section is devoted to this effect.

The results described in Chapters 4 to 6 could comprise a thesis on their own. But due to their reliance on somewhat uncommon techniques (Chapter 2), and on recent major improvements to experimental noise and reliability (Chapter 3), we feel that Chapters 2 and 3 belong in the core of the thesis, and not in an appendix.

Chapter 4 “Atomically Defined Tips: From FIM to SPM” starts with a review of the relatively few previous studies which combined FIM with STM, and mentions a few new experiments under development elsewhere which will combine FIM with STM or AFM. We then introduce a protocol developed to prevent tip changes due to impurities in the FIM imaging gas or rest gases in vacuum. The time limitations for transferring an atomically-defined FIM tip to a STM experiment are also estimated based on rest gas pressure and composition. We then study the formation of tunneling gaps with various substrates at room temperature – Au(111), graphite (HOPG), Si(111), InSb(001) and GaAs(110) – with regard to the inadvertent transferal of atoms from the sample to the tip.

Chapter 5 “SPM with Atomically Defined Tips” explores the use of atomically defined FIM tips in SPM experiments in the context of STM and STS. Through experiments conducted at room temperature and 150 K, we show that the diffusion of transferred atoms makes (111) oriented tungsten tips preferable to (110) tips in atomically-defined SPM experiments. The statistical distribution of spikes measured in the tunneling current on Au(111) is then analyzed and interpreted using a model of an adatom momentarily residing under the STM tip and escaping to another surface sites, or to the tip. We then investigate STM and scanning tunneling spectroscopy (STS) on Si(111), the most stable surface accessible to us at room temperature with regard to atom transfer from sample to tip. Tips remain atomically defined only on the order of minutes on well-ordered 2×1 reconstructed regions. STM is shown to be much more stable in regions where the cleavage process was less successful resulting in a high density of steps.

Chapter 6 “Atomic-Scale Nanoindentation” reports on the use of FIM tips in nanoindentation studies. Using our expertise in maintaining tip integrity between FIM and SPM, we present novel experimental results on atomic-scale mechanical contacts formed between clean tungsten and gold single crystals. With the clean tungsten tips, we investigate tip wetting behaviour, adhesion, and the transition from elastic contact loading to plastic indentation of the substrate. Owing to the considerable improvements in mechanical and detection noise of the apparatus, we present STM images of residual impressions created in the substrate during indentation with much better resolution and stability than previously reported on Au(111). The high resolution imaging enables some new conclusions to be drawn regarding the defect configuration left in the surface after indentation. Finally, we show that after saturating the wetting behaviour of the tungsten tips, the features of the force-displacement curves are more indicative of plasticity in the

substrate rather than initial tip wetting effects. Indentation of Au(111) at the threshold of plasticity was investigated with wetted tips, and we observe a correlation between features in the force-displacement curves and the STM images of residual impressions. A clear albeit stochastic transition from elastic loading to plastic indentation of the contact is measured. The transition to plastic indentation is associated with a minimum obtainable 'quantum' of plastic damage, for which we estimate an energetic budget and discuss nucleation mechanisms.

2. Gear, ways, samples, and tips

The instrument fundamental to the studies presented in this thesis is a combined scanning tunneling microscope (STM) and atomic force microscope (AFM) with a uniquely integrated field ion microscope (FIM). The integration of FIM in the same unit allows for the atomic characterization of the tips used in the scanning probe measurements – a feature which is unique worldwide for AFM, and exceedingly rare for STM. The microscope hails from Zurich, Switzerland, where it was originally designed by Alain Stalder, during his PhD work under Urs Dürig at IBM Rüschlikon [44]. The microscope was commissioned at McGill University by Graham Cross [45] and André Schirmeisen [46] in the late 1990's. In the early 2000's, Yan Sun [47] designed and built a new sample preparation chamber to extend the system's capabilities to study more elaborate systems such as molecules on metal surfaces, and wrote his PhD thesis on force and current interactions between tungsten tips and gold surfaces. Ann-Sophie Lucier [48] contributed very valuable work on this system in a MSc thesis devoted to preparation of tips suitable for scanning probe studies. The microscope was transferred to students Mehdi El Ouali [49] and Till Hagedorn [50], contributing PhD theses on nanoindentation and tunneling regime interactions respectively in 2010.

My work on the system began in September 2008 (MSc which was converted to PhD), and as El Ouali and Hagedorn finished experiments, I gained familiarity with experimental procedures and designed new electronics (photodiode amplifiers, antialiasing filters, etc.) to improve detection noise issues and increase system reliability. The overwhelming instrumentation complexity necessary to run such experiments made successful experiments few and far between. With the goal in mind of studying systems requiring even more complex sample preparation than had been previously employed, it was imperative that the instrument would work dependably.

In this chapter, experimental methods are summarized in order to provide a necessary overview of the basic instrumentation, techniques and their underlying physics. The reader will be referred to other resources when appropriate, whereas complete discussions will be given when important details are needed.

First, the ultra-high vacuum (UHV) system is introduced, followed by a review of the operating principles of FIM, STM, and AFM force detection using cantilever beams. The interferometric detection method will be covered in some detail; substantial improvements to calibration and data acquisition in this area will be discussed. Sample preparation of numerous well-defined surfaces, whether they play a major or minor role in subsequent

chapters, is covered for completeness – they will prove very useful for future work. Finally, the preparation of tips for FIM and SPM is described.

2.1 Ultra-high vacuum system

The ultra-high vacuum (UHV) system consists of three vacuum chambers connected by gate valves, such that repairs and bakeout can be carried out independently on each of them. The chambers are individually described below:

1. **Airlock Chamber:** A small ConFlat (CF) 2.75" 6-way cross is the main body of this chamber and opens on the top to load samples. It is pumped by a Pfeiffer/Balzers TMU 062 turbo pump (56 l/s N_2 pumping speed), backed by a rotary vane pump. Pressure is measured by a Pfeiffer/Balzers IKR 020 cold cathode gauge. It achieves a pressure of $\sim 3.5\times 10^{-6}$ mbar in around 30-45 min, appropriate for introducing samples into the preparation chamber. The pressure reaches $\sim 1.5 \times 10^{-7}$ mbar after 12 hours of pumping. The chamber is typically not baked, and is sealed with a reusable CF flange Viton gasket (rather than a typical disposable copper UHV gasket) to facilitate frequent opening.
2. **Preparation Chamber:** This chamber houses facilities for preparation of samples and tips in vacuum before they are introduced to the measurement chamber. It contains a resistively heated sample preparation stage (specified to 950 °C), a Varian ion bombardment gun and leak valve for sputter gases, an Omicron EFM-3T triple pocket electron beam evaporator, a SRS RGA-200 residual gas analyzer, and a Varian Auger Electron Spectrometer. Tips are prepared on a heating stage with two separate electrodes for passing current through the tip base wire, and a copper anode plate used as a counter electrode in field emission preparation of tip apices. The chamber is pumped with a Pfeiffer TMU 261 turbo pump (210 l/s N_2 pumping speed), and a 500l/s Varian Vacion Starcell 500 ion pump with an integrated titanium sublimation pump. The ion pump can be separated from the chamber with a gate valve as to avoid pumping large quantities of gas during sample transfer to the airlock or sputtering. The pressure is measured with a Kurt Lesker hot cathode gauge, and is typically $\sim 5 \times 10^{-10}$ Torr.
3. **Measurement Chamber:** The combined STM/AFM/FIM microscope is located in this chamber, separated from the preparation chamber in order to keep tips and samples clean while sample degassing and preparation procedures are carried out in the

preparation chamber. The chamber is pumped by a Leybold Turbovac 340M magnetically levitated turbo pump (270 l/s N_2 pumping speed) and a Leybold titanium sublimation pump surrounded by a cryogenic shield. Typical UHV pressure is in the range of 4×10^{-11} mbar (winter) to 2×10^{-10} mbar (summer) (seasonal variation is not well understood, perhaps humidity and a small forevacuum leak?).

The measurement and preparation chambers of the UHV system are interlocked such that in the event of a power interruption, valves close between the turbo pumps and the chambers and between the turbo pumps and their roughing pumps. This is an important safety feature designed to prevent oil mist from the roughing pumps diffusing through the non-rotating turbo pumps and coating the insides of the UHV chambers (thereby rendering them scrap). The preparation chamber was not properly interlocked at the time of the system's transfer to me (it was more complicated to interlock it due to the mix of 115 V American and 230 V Swiss power equipment). New transformers were installed, allowing it to be interlocked as the measurement chamber was.

The measurement chamber's Leybold Turbovac 340M turbo pump caused a several-month delay in 2011 after some Darlington transistors caught fire in its controller upon starting the pump after an interlock-prompted shutdown. The magnetically levitated pump acts as a generator when it loses power: power generated from its rotation is fed back to keep the magnetic bearing engaged. Eventually, the electromagnet current can no longer be sustained and the rotor falls onto emergency touch-down bearings. These bearings can seize upon start-up and cause failure of the drive electronics. Additionally, they are 'disposable' and require $5000 of repair every 'several' uses[1]. In order to exclude future use of the touch-down bearings, a ~$200 uninterrupted power supply (UPS) was added to the interlock system to keep the magnetic bearing levitated during the entire spin-down process. Upon triggering of the interlock, the pump receives a 'stop' command and continues to be powered during the rotor's spin-down.

An interlock was also designed and implemented to monitor the forevacuum line pressure and shut off the sensitive Turbovac if its forevacuum should be above normal operating pressure. This is described elsewhere in detail [51], and would have saved $30000 for a replacement pump when a rotary vane roughing pump overheated and failed

[1] This fact is not well described in manuals, but well known to the manufacturer.

in the late 1990s. It saved the pump in June 2012 when a vacuum flange clamp broke unexpectedly overnight [51], exposing the exit port of the turbo to atmospheric pressure! The interlock shut it down quickly before any damage occurred – time and money extremely well invested in the implementation of interlock systems.

2.2 Combined STM/AFM/FIM

The combined STM/AFM/FIM is operated in two modes illustrated in Figure 2.1. In FIM mode, the apex of a sharp tip is imaged with atomic resolution. As per the illustration in Figure 2.1 (a), the measurement chamber is back-filled with He gas to $\sim 10^{-5}$ mbar and a high positive voltage of $\sim$ 10 kV is applied to the tip. The ionized He gas atoms, reporting on the atomic arrangement of the tip apex, are detected by a microchannel plate (MCP) and phosphorous screen.

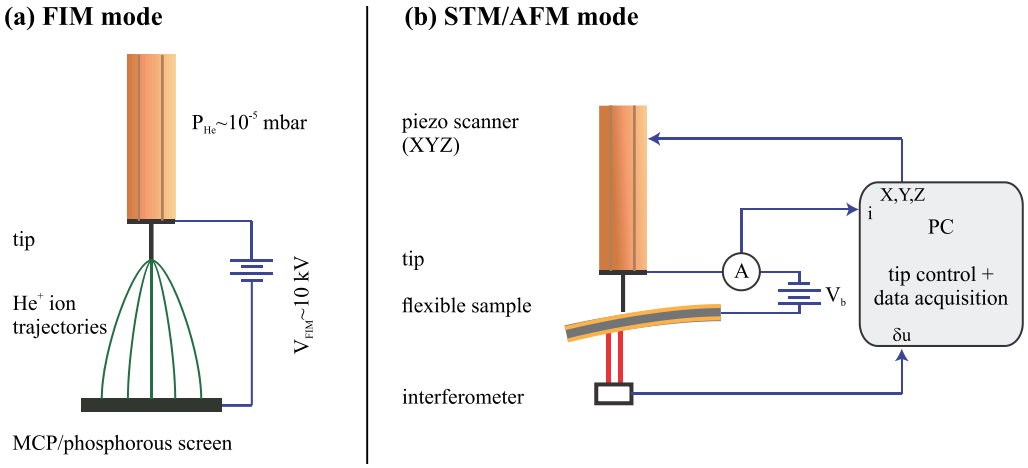

Figure 2.1: Schematic of the microscope's two principle modes of operation: (a) FIM mode; (b) STM/AFM mode.

In the STM/AFM mode shown schematically in Figure 2.1 (b), a cantilevered sample is placed under the tip. The tip is approached to tunneling interaction under applied bias V_B while current I is measured by an ammeter. A computer monitors the current and regulates the tip height with the piezo tube scanner to maintain a constant current. Meanwhile, a dual-beam interferometer is used to record the deflection of the cantilevered samples, which allows for the determination of forces in the tip-sample junction.

2.3 Field ion microscopy (FIM)

The field ion microscope was invented in 1951 by Erwin W. Müller [52], and by 1956 had achieved the first real-space images of matter with atomic resolution. The first FIM images were of the atomic arrangement of the apex of very sharp tungsten needles. By 1957, the surfaces of other refractory metals had been imaged as well [53]. Although the atomic resolution of FIM is no longer unique among microscopes (TEM, SEM, STM, and AFM have all demonstrated sub-Angstrom spatial resolution), there are still unique experimental applications of FIM. Particularly well suited to FIM is the study of diffusion of single atoms or clusters on crystal surfaces, and this technique has produced most of the existing experimental data about the diffusion of atoms and clusters on surfaces [54].

Another unique feature of the FIM (which we do not exploit) is the possibility of integrating a Time of Flight (ToF) mass spectrometer to enable chemical analysis with single atom sensitivity and a spatial resolution of several angstroms. The combined technique is known as atom probe field ion microscopy (AP-FIM), or more simply as the atom probe [55-58]. In AP-FIM, a pulsed field is applied to the FIM specimen to field evaporate a small amount of material from its surface which is chemically analyzed in the ToF unit; it is a destructive technique, consuming the sample as data is collected. Tien T. Tsong, a colleague of Müller's from the beginning of FIM, wrote in his book on AP-FIM [53] that the technique provides the "ultimate sensitivity in chemical analysis" because of its exquisite single atom sensitivity. Since 1990, single atom chemical sensitivity has been demonstrated to some extent in STM[1] and AFM[2]. Unlike scanning probe methods, AP-FIM can access the chemical composition in the bulk of samples, and technique development remains very active today in the computational reconstruction of the data into 3D element-specific atomic maps. Applications of AP-FIM include the chemical segregation of materials at crystalline defects (steels and semiconductors), local studies of grain boundaries in nanocrystalline materials (with grains too small for techniques like electron backscatter diffraction (EBSD) [59]), and short range ordering in materials (in high temperature superconductors, for example).

---

[1] Inelastic electron tunneling spectroscopy in STM allows for measurement of the vibrational energies of individual chemical bonds, which is a form of chemical sensitivity – for example one can distinguish between hydrogen and deuterium bonds [291, 292].

[2] In the case of AFM, however, it is more of a *relative* chemical sensitivity obtained by comparing force-distance interaction curves from different atomic species with the same tip. Absolute chemical identification relies on the specifics of the tip apex which is generally unknown, mostly uncontrolled, and often altered unintentionally during experiments [19].

2.3.1 Operating principle

FIM is a particularly simple microscopy technique in comparison to the complexities of electron optics in SEM and TEM, or the control systems and vibration isolation required for scanning probe microscopies. In its most basic implementation, FIM requires a sample in the shape of a sharp tip, a phosphorous screen at a distance of ~10 cm from the tip, a vacuum system backfilled with $\sim 10^{-5}$ mbar of He, and a high voltage supply.

In FIM, a high positive voltage is applied to the tip, and when the electric field approaches ~4 V/Å at the tip, He gas atoms will be ionized and accelerated toward the screen. The ionization of He atoms occurs with the highest rate near surface sites on the tip where the electric field is largest: the field is locally enhanced in positions of reduced radius of curvature such as at atoms located at the edges of atomic planes, individual atoms adsorbed in the middle of atomic planes, and over protruding atoms of highly corrugated planes (such as the W(111) plane). The image which forms on the phosphorous screen reflects these sites of high He ionization rate and gives atomically resolved information regarding the tip shape.

It is important to point out that the specimen must be shaped like a needle with a very sharp apex in order to achieve a sufficient geometric enhancement of the electric field at its apex[1]. Another important consideration in dealing with such high electric fields is that not all materials can withstand such fields. To some extent, this can be dealt with by cooling the tip to low temperatures in order to inhibit thermally activated field desorption. Another strategy is to use a different imaging gas such as Ar or Ne which ionize at lower electric fields, 2.2 V/Å and 3.75 V/Å respectively compared to 4.4 V/Å for He [10]. Tungsten is the only metal which can withstand room temperature FIM with He without field evaporating during imaging: using Ne gas, we were also able to image an iridium tip at room temperature (Figure 2.37 and Ref. [60]).

The process of field ionization is illustrated in Figure 2.2. The dipole attraction of gas atoms occurs near the apex in the presence of the strong electric field. If the tip is cooled, the gas atoms will thermalize to the tip as they hop over the its surface – this contributes to a lower initial random thermal velocity when the gas atom ionizes and helps improve lateral

[1] These fields are the highest achievable by laboratory techniques and are comparable in magnitude to those inside ionic crystals [10].

spatial resolution. The He gas atom has the highest probability of being ionized over a protruding atom where the field is locally enhanced, such as those indicated in orange. Once ionized, the He^+ ions are accelerated by the field toward a microchannel plate and phosphorous screen for detection.

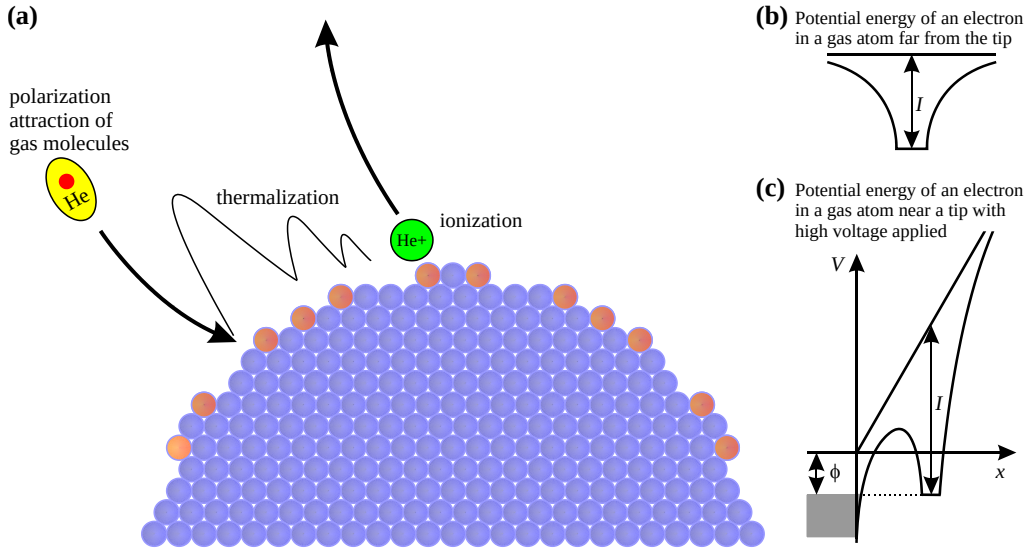

Figure 2.2: (a) Side view of a tip apex showing schematically the dipole attraction of imaging gas atoms, thermal accommodation to the tip, and ionization over an atomic site of locally enhanced field (orange). (b) Potential energy diagram of a valence electron in a gas atom. (b) Potential energy diagram when the atom is within tunneling distance of the metal tip and in a large electric field.

The loss of an electron from the gas atom to the tip happens by quantum mechanical tunneling. The potential energy landscape of a valence electron in a gas atom with ionization energy I is shown in Figure 2.2 (b). In an applied field, the potential becomes sloped. When brought sufficiently close to a metal tip, as illustrated by Figure 2.2 (c), the barrier between the electron state in the gas atom and an available electron state in the tip becomes small enough to tunnel through. Applying the WKB method to an equilateral triangle potential, it is possible to calculate the barrier penetration probability analytically as [53]

$$D(x_c, F) = \exp\left\{-\left(\frac{8m}{\hbar^2}\right)^{\frac{1}{2}}\frac{2}{3}\left(I - 2\sqrt{e^3F}\right)^{\frac{1}{2}}\frac{I-\phi}{F}\right\}, \qquad (1)$$

where m is the free electron mass, $\hbar$ is the reduced Planck's constant, e is the elementary charge, I is the ionization energy of the gas atom, F is the magnitude of the applied electric field, and ϕ is the work function of the tip. It is clear from the illustration of the barrier in Figure 2.2 (c) and by the result of Eq. (1) that the tunneling rate is strongly dependent on the

ionization energy of the gas itself (increases with decreasing ionization energy), as well as the magnitude of the applied field (increases with increasing applied field).

2.3.2 Resolution in FIM

The excellent spatial resolution of FIM allows us to resolve individual atoms on the W(111) plane, where the tip is corrugated enough to allow substantial variations in the electric field over the surface. I am often asked how we obtain atomic resolution images of tips at room temperature since most implementations of FIM are cryogenic – at least at liquid nitrogen temperatures, if not below. The answer has two components: first, our tips are extraordinarily sharp compared to most used in traditional FIM experiments, and secondly, the cryogenic component of traditional FIM design is essential for studying diffusion of adsorbed atoms (used to 'freeze' their position on the surface during high field FIM imaging), but not required for characterizing a stable tungsten tip.

We will now discuss the origins of the spatial resolution, and show that for tips with sufficiently small radii, that the expected spatial resolution is adequate for atomic resolution imaging. In the imaging process, helium atoms are ionized over specific sites on the tip – we consider what effects will broaden the projection of these ionization sites when the helium ions are visualized on the screen. Three factors affect this resolution [53]: the ionization disk size, Heisenberg's uncertainty principle, and thermal broadening. Since they are statistically uncorrelated, they are added in quadrature to give the total resolution broadening as a quadrature sum of the components listed above (in order):

$$\delta = \sqrt{\delta_0^2 + \delta_u^2 + \delta_T^2}\,. \tag{2}$$

The ionization disk size reflects the diameter of the imaging disk above each surface atom and is approximated to be a constant on the order of $\delta_0 = 2.5$ Å [61] (the lateral spatial extent of the ionization process). The subsequent terms in Eq. (2) contribute to a broadening beyond this limit. The second term considers the Heisenberg uncertainty contribution on the tangential velocity component of the gas atom when it is ionized:

$$\delta_u = 2\left(\frac{\beta^2 r_t \hbar^2}{2kem_{gas}F_0}\right)^{\frac{1}{4}}. \tag{3}$$

In the above equation, β is a geometric factor taking into account image compression due to the fact that the tip is not a perfect hemisphere but has a shank. β is on the order of 1.5-1.8 [53] and is taken to be 1.65 in the following calculation. r_t is the tip radius, k is a geometric

field reduction factor of ~ 6 (depends on tip shape, usually $3 < k < 8$ [62]), m_{gas} is the mass of the imaging gas atom, and F_0 is the magnitude of the ionizing electric field.

The last term represents the broadening due to the initial thermal velocity of the gas atoms

$$\delta_T = 4\left(\frac{\beta^2 k_B T r_t}{keF_0}\right)^{\frac{1}{2}}, \tag{4}$$

where k_B is the Boltzmann constant and T is the temperature of the gas atom; the other variables have been described previously.

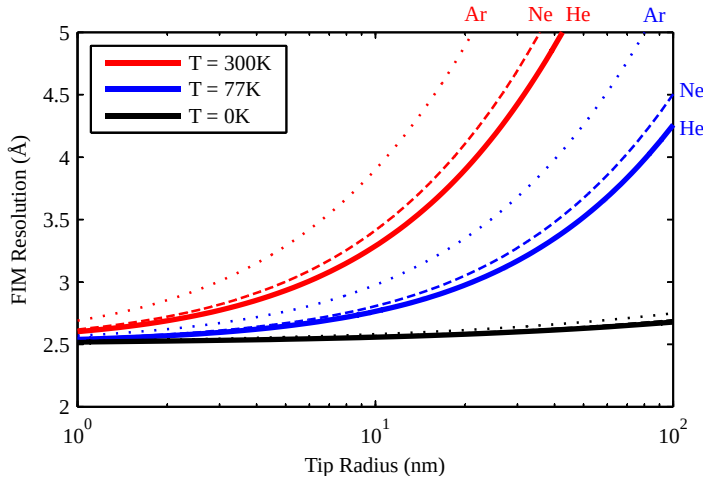

Figure 2.3: Resolution of FIM as a function of tip radius at room temperature, liquid nitrogen temperature, and absolute zero. Curves for ionization fields corresponding to He, Ne, and Ar imaging gases are shown as solid, dashed, and dotted lines.

Practically, the experimental parameters we can modify are temperature, tip radius, and species of imaging gas. The choice of imaging gas affects the mass term in Eq. (3) but this is generally outweighed by the modification of best imaging field which enters more strongly into Eq. (4), and is 4.4, 3.7, 2.2 V/Å for He, Ne, and Ar respectively. The combined resolution of FIM, given by Eqs. (2), (3), and (4), is plotted in Figure 2.3 as a function of tip radius. Temperatures of 300 K, 77 K, and 0 K are shown in red, blue and black respectively. For each temperature, the effect of imaging gas species is shown for He, Ne and Ar as indicated by solid, dashed and dotted lines. Our FIM tip radii mostly fall in the range of 3 – 12 nm, where for room temperature (and those below), the resolution is sufficient to image atoms on the W(111) plane spaced by ~4.5 Å. Larger tips in the range of tens to hundreds of nanometers require low temperatures to achieve atomic resolution.

A last comment on resolution is that the preceding discussion applies to the smallest distance between surface atoms that can be resolved in an image. However, when an

adatom is deposited on a surface for diffusion studies in FIM, one can fit the image intensity distribution and locate its centroid to ~0.3 Å [53]. Another important effect that doesn't enter into the resolution equation is the selective imaging of atoms where the electric field is enhanced by local corrugation and the suppression of imaging on large flat planes of atoms. On smooth, densely packed planes such as the W(110), FIM resolution can be effectively non-existent as surface atoms cannot be imaged.

The use of FIM for determining tip geometry will be addressed in greater detail in section 2.8. In case the reader is yearning to see some images, examples of FIM images of W(110) and W(111) tips are shown in Figure 2.31 on page 64.

2.4 Scanning probe microscopy (SPM)

Scanning probe microscopy uses a physical probe to image surfaces by raster scanning the surface and monitoring some type of interaction between the probe's apex and the sample. In STM, a small current tunneling between the tip and the sample on the order of pA to nA is used as an imaging mechanism. Due to the current's exponential dependence on the tip-sample distance, with one decade of variation per Ångström, excellent spatial resolution is possible. In AFM, the force or force gradient between the tip and sample is responsible for image contrast. Electrostatic, van der Waals, and chemical bonding forces all contribute to the force-distance profile, so AFM resolution depends on which particular force interaction is dominant. Both STM and AFM theory will be covered in more detail in subsequent sections.

STM and AFM are often operated under feedback to maintain either constant current or force (or force gradient); feedback is used to track the 'topography' of the sample under constant tip-sample interaction. In particularly stable instruments, often at cryogenic temperatures, a constant height scan over the sample can be performed while the variations of current or force are recorded as a function of tip position, forming an image. SPM can also be used to perform spectroscopy, in which one parameter is modified and the response of another is measured, such as force vs. distance, current vs. voltage etc.

In all SPM experiments, the tip structure has a crucial role in contrast formation and data interpretation. Surface science has progressed to the point where the SPM community is able to study exquisitely well-defined surfaces, but the tip of the SPM remains mostly uncharacterized – often one turns to atomistic modeling to guess at possible structures [24, 63]. Exceedingly few SPMs exist with tip characterization facilities – in our experiments,

FIM is the characterization tool for the sharp tips. A review of the literature of SPM with characterized tips is given in Chapter 4.

The microscope used in this thesis has a tip and sample configuration as shown in Figure 2.4. The tungsten wire tip is mounted via a 0.25 mm stainless steel support wire to a tip holder with electrically isolated contacts for resistive heating (section 2.8). The sample consists of a thin ~50 μm beam clamped at one end to form a cantilever[1], which serves as a transducer to measure forces between the tip and sample (section 2.5). The horizontal and vertical holes through the sample holder enable it to be transferred between UHV chambers for preparation, storage, and measurements.

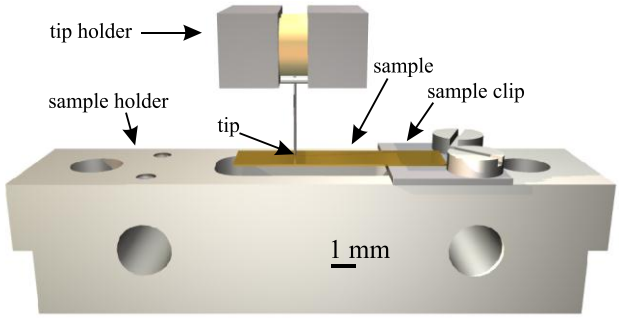

Figure 2.4: CAD rendering of tip and sample holder illustrating the size scale and geometry of the scanning probe system.

Our microscope is operated primarily under constant current feedback: although it is designed to measure forces, it is not practical to image under force feedback because of drift of the interferometer signal with time – force is acquired as an extra channel simultaneously with the tunneling current.

2.4.1 Scanning tunneling microscopy (STM)

The STM was developed at IBM Research in Zürich by Gerd Binnig and Herinrich Rohrer along with their personal technicians Christoph Gerber and Edi Weibel. Their first patent application was submitted in 1979, and the first scientific paper on tunneling through a controllable vacuum gap appeared in 1982 [64]. The invention earned Binnig and Rohrer the Nobel Prize in Physics in 1986, shared with Ernst Ruska, the inventor of the electron microscope (dating from 1933). The first STM, shown in Figure 2.5, was housed in a primitive desiccator vacuum chamber and a low-vibration environment was achieved by

[1] Adhesive not shown in this rendering.

brute force using a magnetic stage suspended above a superconducting lead bowl consuming 20 L of liquid helium per hour, according to Binnig and Rohrer's Nobel Lecture [10]. The STM achieved substantial scientific credibility once it contributed evidence supporting the dimer adatom stacking-fault (DAS) model for the 7×7 reconstruction of the Si(111) surface [65]. Quick progress in vibration isolation techniques simplified the design considerably in the following years. The elegantly simple technology of the STM demonstrated that it was possible to investigate atomic-scale phenomena occurring at the junction between two macroscopically controlled bodies – a feat that "should not have worked in principle" according to many [10].

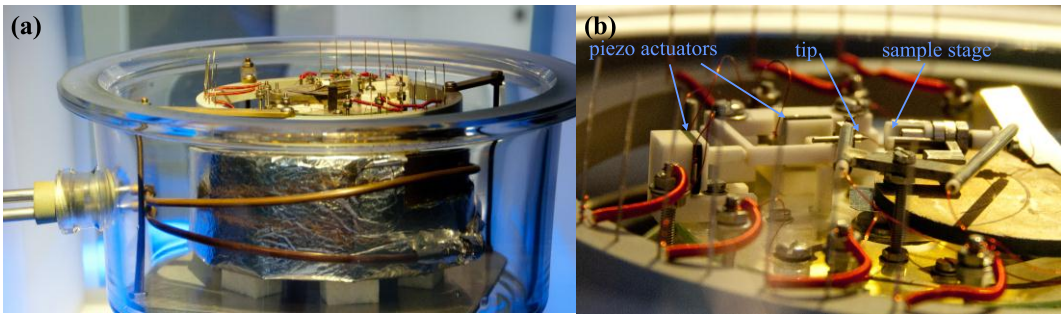

Figure 2.5: Photographs of the first STM on display at the Deutsches Museum in Munich, Germany (photos: William Paul). (a) The vacuum desiccator jar with cryogenic feedthroughs for cooling the superconducting lead bowl. (b) Detail, from the opposite side as in (a), of the microscope construction with several recognizable parts.

STM relies on the quantum mechanical tunneling of electrons across the tip-sample vacuum gap. As many reviewers of the technique have done [66-69], we present here the 1-D solution for an electron tunneling through a rectangular barrier – it serves as a simple model through which one may appreciate the sensitivity of the tunneling current to gap distance. Within the rectangular barrier, electron wavefunctions decay exponentially; the solution of the Schrödinger equation has the form

$$\psi = e^{\pm \kappa z}\,, \tag{5}$$

where the parameter κ is given by

$$\kappa = \frac{\sqrt{2m(V-E)}}{\hbar} = \frac{\sqrt{2m\phi}}{\hbar}\,. \tag{6}$$

The tunneling current is proportional to the probability density of the decaying wavefunction, which is the square of the decaying solution of Eq. (5):

$$I \propto e^{-2\kappa z} \approx e^{-1.025\sqrt{\phi(\mathrm{eV})}\,z(\text{Å})}\,. \tag{7}$$

Using units of eV's and Å's, and assuming a work function of ~5 eV for clean metals, it is apparent that the tunneling current decays by a factor of ten per Ångstrom displacement in

z. This provides the STM with its high sensitivity in the direction perpendicular to the surface, but also requires that the tip-sample gap be isolated from external vibrations which would make stable tunneling currents unmeasurable. The tip and sample must be kept stable to well below one Ångstrom of vibration amplitude. Another consequence of the fast decay of the tunneling current is that most of the current will arise from the 'last atom' on the tip – atoms one atomic layer away (~2 Å) will contribute only ~1% of the current provided by the apex atom. Even with a relatively blunt tip, it is possible to achieve high lateral resolution as long as the apex has a small protrusion.

The tunneling current is usually measured with a transimpedance amplifier having a gain of ~1 V/nA (i.e. 10^9 Ω). For systems employing a ±10 V data acquisition card, the maximal measurable current is 10 nA. To measure currents from the tunneling regime to those arising in nanoscale mechanical contacts consisting of hundreds of atoms, even at a low bias of 50 mV, one must be able to measure from pA to mA[1]. To accommodate currents from the pA to mA range, we use a current preamplifier [70] which, in addition to the standard 1 GΩ transimpedance resistor, also contains diodes in parallel with the resistor. These diodes make the output voltage of the current preamplifier equal to approximately the logarithm of the input current for currents > 2.5 nA. A recent calibration curve for the linear-log transition can be found in Ref. [49].

In this introduction to STM using the simple 1D rectangular barrier model, we have not discussed the contribution of the local density of states of the surface or tip to the tunneling current. The STM can be used as a spectroscopic tool to investigate the local density of states of the sample, which is introduced later on in Chapter 5

2.4.2 Atomic force microscopy (AFM)

The atomic force microscope was introduced by Binnig in 1986 [12]. In the AFM, the rigid tip of the STM has been replaced by a force sensor so that the surface structures of insulators can be investigated by measuring force interactions. Several excellent reference works review the design and operating principles of the AFM [66, 68, 71-73].

Electrostatic, van der Waals and chemical bonding interactions (and magnetism if applicable) contribute to a potential energy landscape between the tip and sample as a

[1] 1 mA/50 mV ≈ 260 G_0, where $G_0 = 2e^2/h$ is the quantum of conductance [241].

function of their relative position. This potential energy landscape, $V(x, y, z)$, gives rise to tip-sample forces in the direction normal to the surface[1], $F_{ts} = -\partial V_{ts}/\partial z$, as well as force gradients, $k_{ts} = -\partial F_{ts}/\partial z$. Depending on the imaging mode, AFM will record F_{ts} or k_{ts} or some closely related quantity.

For a conductive tip and sample at a potential difference ΔV, an electrostatic force arises from the tip-sample capacitance gradient:

$$F_{el}(z) = \frac{1}{2}\frac{\partial C}{\partial z}\,\Delta V^2\,. \tag{8}$$

In the case of a spherical tip of radius R above a flat surface where the proximity to the surface, z, is much smaller than the radius, the electrostatic force is given by

$$F_{el}(z) = -\frac{\pi\epsilon_0 R(\Delta V)^2}{z}. \tag{9}$$

Inserting a tip radius of 5 nm for our sharp FIM-characterized tungsten tips (typical range is 3-10 nm) and a distance of 0.5 nm gives 0.28 nN force for a 1 V potential difference. The electrostatic force is always attractive.

In the absence of an external bias voltage, the contact potential difference between the tip and sample materials (given by the difference of their work functions) contributes to a potential difference on the order of several hundred millivolts. The contact potential difference between W(111) and Au(111) is 0.86 eV ($\phi_{W(111)} = 4.45$ eV and $\phi_{Au(111)} = 5.31$ eV), and given that externally applied bias voltage is often less than 0.1 V for force spectroscopy, the estimate of the electrostatic force using 1 V above is of the correct order. The electrostatic force provides a rather small background at the size of our tip radii and our detection noise does not allow it to be easily resolved. In systems with larger tips and those operating on frequency modulation detection, it is often desirable to minimize the contact potential difference by seeking the minimum of the $k_{ts}(\Delta V)$ parabola (k_{ts}, the tip sample stiffness, is defined as the $\partial/\partial z$ derivative of Eq. (9))[2].

Although the electrostatic force can always be nulled by applying an external bias, the van der Waals force, also electric in origin, is always present in the tip-sample interaction potential. The van der Waals attraction arises from the fluctuations in the electric dipoles of atoms in the tip and sample. The van der Waals attraction between two atoms has a z^{-6} dependence, but the functional form in AFM will depend on the tip-sample geometry. The

[1] Lateral forces and force gradients of course also occur, which we will not address here.

[2] Tracking local variations in the contact potential as a function of tip position forms the basis of Kelvin Probe Force Microscopy (KPFM) [293-295].

Hamaker approach can be used to calculate the van der Waals interaction between macroscopic bodies, however this is only valid for distances up to a few hundred angstroms as it does not take into account retardation effects due to the finite speed of light. Solutions for various model geometries are discussed in Ref. [73]. For a sphere-plane tip-sample geometry, the van der Waals force is given by

$$F_{vdW}(z) = -\frac{A_H R}{6z^2}, \tag{10}$$

where A_H is the Hamaker constant ($\sim 4 \cdot 10^{-19}$ J), R is the tip radius, and z is the tip-sample separation. The van der Waals force is also always attractive and provides a rather sizable background force for large tip radii, however for our geometry this amounts to ~0.33 nN for a 5 nm radius tip at 0.5 nm separation. A more exact solution [74, 75] for the van der Waals force for a sphere-cone tip geometry is in very good agreement with the simple spherical tip model of Eq. (10), as shown in Ref. [50].

Atomic resolution contrast in AFM is due to the detection of chemical bonding forces, F_{chem}, between the tip and sample. These are due to the formation of chemical bonds in the attractive region, $F_{chem} < 0$, and to Pauli repulsion in the repulsive region, $F_{chem} > 0$. Chemical bonding forces are often modeled by the Morse potential, a potential that describes well the quantum mechanical bonding of a diatomic molecule, of the form

$$F_{chem-Morse}(z) = \frac{2U_0}{\lambda}\left[\exp\left(-2\frac{z-z_0}{\lambda}\right) - \exp\left(-\frac{z-z_0}{\lambda}\right)\right], \tag{11}$$

where U_0 is the bond energy, λ is a decay constant, and z_0 sets the equilibrium position where $F_{chem-Morse}(z) = 0$. The Morse potential does not describe the directionality of chemical bonding, however. Generally, the exponential behaviour of the force profile matches well with experimental observations [24], and an active area of research is understanding of the relationship between the exponential decay constants of force and current [76, 77].

In the repulsive regime, the AFM measures forces arising from Pauli exclusion. Since this has to do with the overlap of the total electron density of the tip and sample atoms, the AFM should be able to achieve higher spatial resolution than the STM, where tunneling currents arise from the overlap of the valence electron density. The resolution enhancement is expected due to the smaller spatial extent (greater inverse decay length) of the total electron density versus the lower inverse decay length of the valence electron density.

The total tip-sample force profile obtained by summation of the electrostatic, van der Waals, and chemical contributions, $F_{total} = F_{el} + F_{vdW} + F_{chem}$, is shown in Figure 2.6 for a

tip of 5 nm radius at a 1 V potential difference. Atomically resolved information in the force-distance behaviour lies within the spatial variation of F_{chem} over the sample surface, which is buried within the van der Waals and electrostatic backgrounds. Not only do these background signals obstruct the signal of interest, but the chemical bonding force is a non-monotonic signal, which makes feedback operation much more difficult than in STM – once the force minimum is crossed, the feedback gains must somehow be changed in sign or else the tip will crash! In STM, one may linearize the relationship of the control signal (current) to the tip-sample distance by taking its logarithm in the digital feedback loop; the linearization of the control signal to the tip-sample distance is not possible in AFM, making the setting of feedback gains much more challenging.

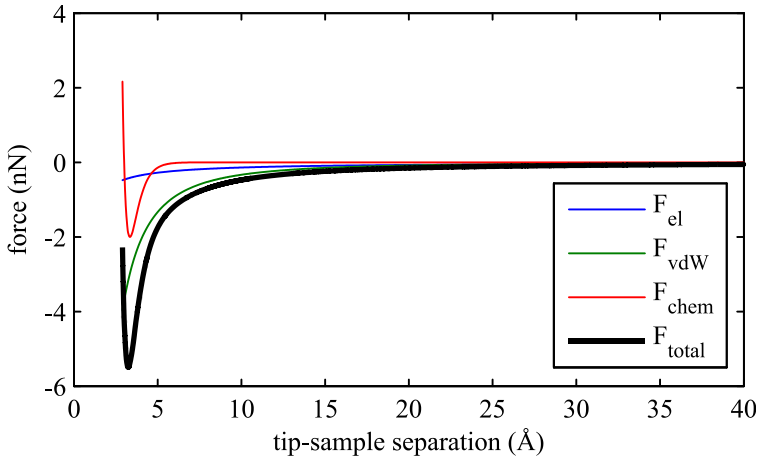

Figure 2.6: Tip-sample force profile as a function of tip-sample separation distance for a tip of 5 nm radius at 1 V potential difference. The total measured force (black curve) is the sum of electrostatic (blue), van der Waals (green), and chemical (red) forces. Parameters for the Morse potential plotted as F_{chem} are $U_0 = 0.2 \times 10^{-18}$ J, $\lambda = 0.05$ nm, $z_0 = 0.3$ nm.

As we have seen, the features of the force-distance curve are much more complex than those of the current-distance curve. Some additional effects that we have not discussed include atomic-scale relaxations of the tip, where the rigid body separation deviates from the actual tip-sample separation [27], as well as the collapse of the tunneling barrier in the transition from tunneling to point contact[1] [78].

[1] This is the transition from the situation where the bias voltage drops off across the vacuum gap to across a larger region of the metallic contact, once contact has been established.

2.4.3 Microscope control, data acquisition & signal paths

The STM/AFM is controlled by the open source GXSM software [79, 80] running on Ubuntu Linux. The migration to this controller was carried out in August 2011 after identifying our old microscope controller as a severely limiting factor in experiment control and quality of acquired data. Due to the delicate nature of the tip-sample junction, controllers must be robust – tolerance for software bugs is very limited. GXSM has been proven in many research labs worldwide, and the introduction of the second generation of Signal Ranger data acquisition hardware from Soft dB (coincidentally Québec-based), marked the release of a full-featured SPM control package, comparable to hardware/software packages retailing for 20× the cost. The GXSM project is maintained on Sourceforge and supported primarily by Percy Zahl of Brookhaven National Labs. A web-based archive of our notes on GXSM implementation and operation is maintained on our group website [81].

The SPM control software is not enough to run the microscope alone. It is imperative to monitor signals 'live' for debugging, and for this there is no better way than to use an oscilloscope. A second computer runs Matlab and a National Instruments USB-6259 BNC data acquisition card for various purposes (Auger Electron Spectroscopy data acquisition, UHV bakeout monitoring, interferometer calibration, field emission data acquisition, FIM data acquisition). Several Matlab routines were written to facilitate the acquisition, analysis, and plotting of Power Spectral Densities from the microscope in the context of SPM experiments. We monitor the tunneling current and interferometer noise spectra regularly since abnormalities often signal problems before they lead to destroyed tips or samples.

A set of computer speakers is used to acoustically monitor the tunneling current and interferometer signals – the trained ear can quickly perceive issues such as a bad connection from abnormally 'loud' line noise, a poorly aligned magnetic damping stage coupling the first harmonic of a turbomolecular pump at 1720Hz, a sample which has a driven resonance by acoustic coupling to the outside world. I cannot stress enough the effectiveness of the auditory monitoring of these signals (which are conveniently in the bandwidth of human hearing) for performing successful routine experiments.

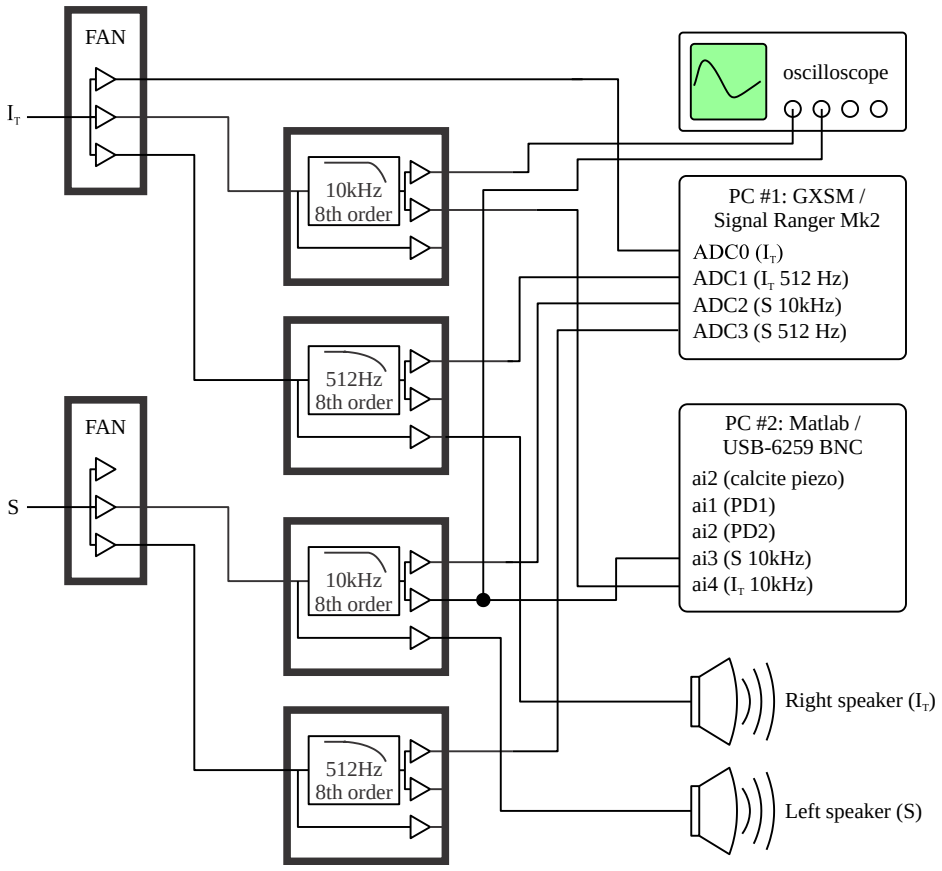

Figure 2.7: Block diagram of tunneling current (I_T) and interferometer signal (S) acquisition system. The FAN units provide independently buffered outputs for robust signal routing. Custom antialiasing filters provide appropriate signal conditioning prior to data acquisition. An oscilloscope, two PCs and a pair of computer speakers provide adequate means to monitor the signal integrity of the experiment.

A block diagram starting with the tunneling current and interferometer signals (labeled I_T[1] and S, respectively) and ending with the oscilloscope, two PCs, and audio speakers is shown in Figure 2.7. Some pieces of analog electronics are needed to minimize cross-talk and ground loops between the devices into which the signals are plugged. The FAN units are buffer amplifiers which simply provide a buffered copy of the input signal to various data acquisition devices and filters (built by the University of Basel for our previous SPM controller). The signals also pass through custom designed and built antialiasing filters: an 8th order filter (custom frequency response, see LTC1564 data sheet for specs) with a 10 kHz cutoff implemented with a Linear Technology LTC1564 chip, and an 8th order Bessel

[1] Although we refer to the signal as I_T, we mean the voltage corresponding to the tunneling current – not the tunneling current itself.

filter with a 512 Hz cutoff implemented with a pair of Linear Technology LTC1563-3 in series. Each of the filter modules contains two independently buffered outputs, as well as one buffered unfiltered copy of the input signal. The design of the input stage that can be configured as DC/AC coupled or differential/single ended and is also protected against input overvoltage. These filters have proven to be extremely versatile and configurable pieces of signal conditioning equipment – their design is detailed in Appendix D (page 273).

2.5 Cantilever beam force transduction

The key element of instrumentation which distinguishes the AFM from STM is the spring which is used to detect forces in the tip-sample junction. It is typical to measure forces using either microfabricated silicon cantilever beams (with a silicon tip) detected by optical beam deflection [82, 83] or interferometry [84, 85]. Another common approach is to use a quartz tuning fork from a standard Swiss watch (typically with an etched metal tip attached) with one tine clamped (qPlus sensor) [86]. Cantilever beams most often fulfill the task of force transduction in AFM, but other strategies, such as the length extension resonator [87, 88] also exist. In all of the force sensing implementations discussed above, the sample is rigid, and the AFM tip is mounted on a compliant force transducer.

Force transduction happens in a rather unique way in the microscope we use. Here, the tip is made from a rigid wire (like a standard STM), and the sample is cantilevered and simultaneously acts as a surface-science quality substrate and as a force transducer. The choice to cantilever the sample is appropriate for a microscope designed with FIM-compatible tips: silicon tips cannot survive the high electric fields required for FIM, and qPlus sensors do not allow for the implementation of FIM tips that can be well-prepared by heat treatment in UHV and present significant challenges in controlling the axis of the tip. Another advantage of the cantilevered sample is that it allows for the direct detection of forces, rather than force gradients. The calibration of static force from voltage data is rather straightforward and not subject to deconvolution procedures [89, 90] (and inherent non-linear error propagation) required to interpret dynamic force spectroscopy measurements with an oscillating tip.

In the following sections, we describe the cantilever beam mechanics relevant to data interpretation and experimental implementation.

2.5.1 Response to point loading

The mechanical response of a cantilever beam to a point load can be calculated using the Euler-Bernoulli equation [71]. Here, we summarize the results relevant to the experiments in this thesis. A beam with rectangular cross-section of dimensions $L \times w \times \tau$ (length, width, thickness respectively) loaded by a force F at position $z_{tip} = t$ along its length will bend by a vertical distance

$$u_t = u(z = t) = -\frac{4t^3}{Ew\tau^3}F \tag{12}$$

at the location of the point load, t. E is the Young's modulus of the cantilever material. The geometry of this setup is shown in Figure 2.8, where the point load is supplied at the location of the tip, and the cantilever bends by amount u_t at a distance t from its clamped end. Other features illustrated in Figure 2.8 pertaining to interferometric detection will be discussed in section 2.6.4.

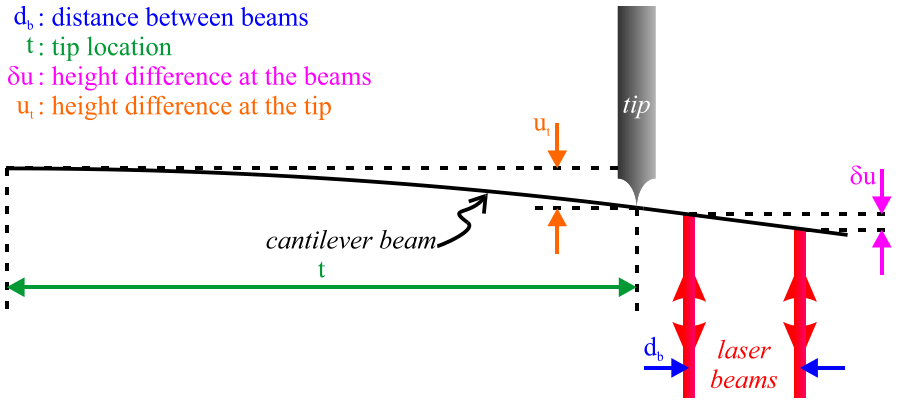

Figure 2.8: Cantilever beam, tip and laser geometry illustrating important measurement variables.

At z locations closer to the clamped end than the location of the tip, $z \leq t$, the deflection profile, $u(z)$, is given by

$$u(z \leq t) = u_t\left[\frac{3}{2}\frac{z^2}{t^2} - \frac{1}{2}\frac{z^3}{t^3}\right], \tag{13}$$

where u_t is given by Eq. (12). At z locations farther than the location of the tip from the clamped end, $z \geq t$, the slope of the cantilever is constant, hence the profile of the beam follows a first order polynomial in z:

$$u(z \geq t) = u_t\left[\frac{3}{2}\frac{z}{t} - \frac{1}{2}\right]. \tag{14}$$

From Eq. (12) we can extract the spring constant profile of the rectangular cantilever beam, that is, its stiffness as a function of the position, t, of the point load:

$$k = \frac{Ew\tau^3}{4t^3} \tag{15}$$

For convenience, we define the spring constant at the free end of the cantilever, where $t = L$ to be

$$k_0 = \frac{Ew\tau^3}{4L^3}, \tag{16}$$

which allows us to write the spring constant profile of the cantilever as

$$k = k_0 \left(\frac{L}{t}\right)^3. \tag{17}$$

We determine k_0 from a fit to several stiffness measurements along the length of the beam using a digital balance. This method is described in Mehdi El Ouali's PhD thesis [49]. The spring constant at the tip location is then determined for the tip position measured using a photograph calibrated in ImageJ [91, 92] to the known 21.5 mm length of our sample holder. Factors contributing to the force measurement uncertainty are discussed in section 2.6.5.

2.5.2 Cantilever beam dynamics

The resonant frequency of the nth mode of a rectangular cantilever beam of thickness τ and length L is given by [71]

$$f_n = \frac{(k_n L)^2}{4\pi\sqrt{3}} \sqrt{\frac{E}{\rho}} \frac{\tau}{L^2}, \tag{18}$$

where the stiffness-length product $k_n L$ is a constant for each mode (for the first mode $k_1 L = 1.875$), E is the Young's modulus, and ρ is the density of the cantilever material. For a mica beam ($E = 110$ GPa, $\rho = 2.7$ g/cm^3), the first mode simplifies to

$$f_1 \approx 0.16 \sqrt{\frac{E}{\rho}} \frac{\tau}{L^2} = 1030 \text{ Hz} \frac{\tau(\mu\text{m})}{L^2(\text{mm})}, \tag{19}$$

allowing for a quick estimation based on the cantilever length and thickness. For our cantilever beams of thickness ~ 45 μm and length 5 mm, this corresponds to ~ 1850 Hz. It is worth noting that the resonance frequency is independent of the width, w, of the beam. This can be easily understood by observing that the resonance frequency scales as $f \propto \sqrt{k/m}$ (any harmonic oscillator obeys this relation with some effective mass). Since the stiffness k (see Eq. (15)) and mass m both scale linearly with the beam width, the frequency is width independent.

2.5.3 *Clamping of cantilever beams*

The experimental realization of clamping the cantilever beams is very important to the interpretation of cantilever deflection signals since it literally sets the boundary condition for the Euler-Bernoulli equation at the clamped end. Mehdi El Ouali investigated this in detail [49], and concluded that mechanical clamping of a mica cantilever beam between metal clips damaged the clamped end. The clamped end became the weakest point and the cantilever beam simply rotated around the damaged clamping point. Clamping by embedding the end in an adhesive was shown to produce samples with the expected deflection and spring constant profiles (a thin application of SPI Silver Paint for electrical conductivity followed by encapsulation with Aron Ceramic type E Heat Resistant Inorganic Adhesive or just Pelco High Performance Silver Paste work well for beam clamping). The anchoring of the clamped end of a cantilever beam in adhesive is illustrated in Figure 2.9 (a).

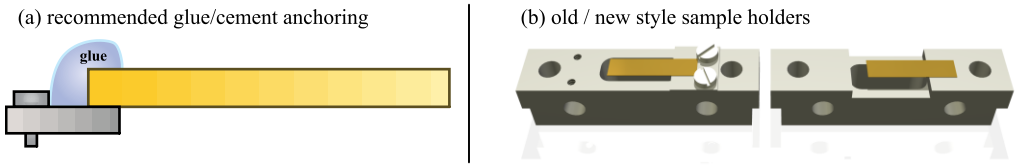

Figure 2.9: (a) recommended anchoring of a cantilever beam to a sample clip. Figure courtesy of M. El Ouali; (b) old style sample holder employing clips, new style sample holder for direct mounting of cantilever beams.

Cantilever beams were previously anchored to clips which provided a straight-edge boundary condition. The clips were then mounted to sample holders using small M1 screws, shown on the left in Figure 2.9 (b). A new sample holder, on the right in Figure 2.9 (b), integrates a straight-edge for direct cantilever beam mounting and eliminates risky sample transfer and mounting procedures associated with the sample clip design. This sample holder, in combination with a gluing jig which secures the holder magnetically and supports the cantilever beam during gluing, contributed to a several-fold yield increase in the rate of successful sample mounting.

2.6 Interferometric deflection measurement

The deflection of the cantilevered sample is measured by a dual-beam differential interferometer. The two beams are positioned at a distance of $d_b = 1$ mm apart, as shown in Figure 2.8. By measuring the phase offset due to the path difference between the two reflected beams, the height difference at the position of the two beams, δu, can be inferred.

Using the known bending profile of the cantilever beam (discussed in Eqs. (12), (13), and (14)), we can recover the cantilever's deflection, u_t, at the position of the tip, $z = t$. The operating principle, relevant equations, experimental considerations, and measurement uncertainty will be described below.

2.6.1 Operating principle

The interferometer is based on a design by Schönenberger and Alvarado [93], and the current implementation is described by Stalder [44]. A diagram of the interferometer and a photograph of the corresponding components are presented in Figure 2.10.

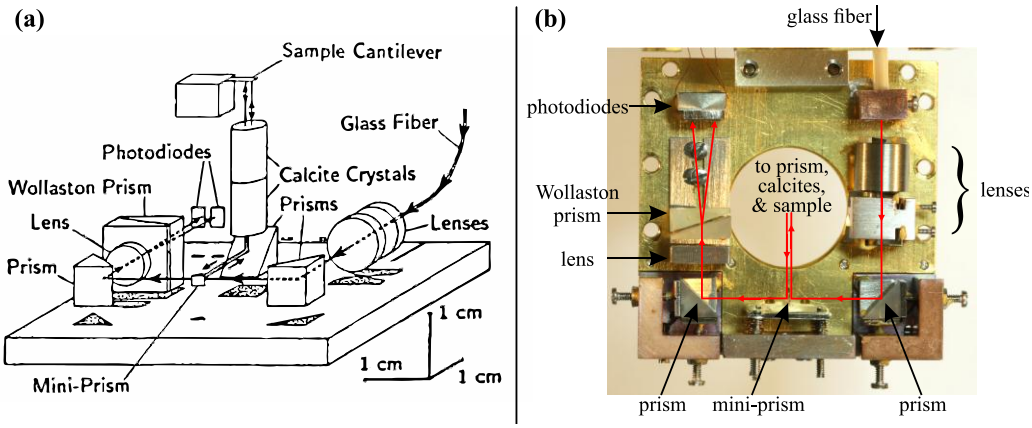

Figure 2.10: (a) Drawing of the differential interferometer from Ref. [44]. (b) Photograph of the interferometer with labeled components corresponding to those in (a).

The optical axis is shown unfolded in Figure 2.11. A more complete derivation of the fields is presented here in order to understand the differential mode of operation in better detail. This expanded derivation also considers the case of arbitrary angles between the calcite and Wollaston prism axes.

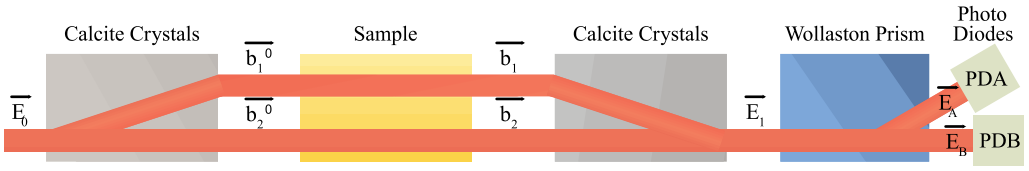

Figure 2.11: Optical design of the dual-beam differential interferometer. Figure adapted from [6] and courtesy of M. El Ouali.

An incident beam is collimated by the lenses after the exit of the optical fiber, as shown in Figure 2.10. The incident beam has a field given by $\overrightarrow{E_0} = E_0 e^{i(\boldsymbol{k}\cdot\boldsymbol{r}-\omega t)}\hat{\boldsymbol{n}}$. $\overrightarrow{E_0}$ is split into two

beams with electric fields $\vec{b}_1^0$ and $\vec{b}_2^0$, shown in Figure 2.11, of orthogonal polarization by projecting $\vec{E}_0$ along the axes of a calcite crystal $\hat{\boldsymbol{c}}_1$ and $\hat{\boldsymbol{c}}_2$:

$$\begin{aligned}\vec{b}_1^0 &= E_0 e^{i(\boldsymbol{k}\cdot\boldsymbol{r}-\omega t)}\hat{\boldsymbol{n}}\cdot\hat{\boldsymbol{c}}_1\,\hat{\boldsymbol{c}}_1\\ \vec{b}_2^0 &= E_0 e^{i(\boldsymbol{k}\cdot\boldsymbol{r}-\omega t)}\hat{\boldsymbol{n}}\cdot\hat{\boldsymbol{c}}_2\,\hat{\boldsymbol{c}}_2\,.\end{aligned} \tag{20}$$

The beams are then reflected from the bottom surface of the sample and pick up phase shifts ϕ_1 and ϕ_2 due to the path length. We can re-express these phase differences as having a common mode and differential mode component, that is, $\phi_1 = \phi_{cm} + \phi_{dm}$, and $\phi_2 = \phi_{cm}$:

$$\begin{aligned}\overrightarrow{b_1} &= \overrightarrow{b_1^0}e^{i\phi_1} = \overrightarrow{b_1^0}e^{i(\phi_{cm}+\phi_{dm})}\\ \overrightarrow{b_2} &= \overrightarrow{b_2^0}e^{i\phi_2} = \overrightarrow{b_2^0}e^{i\phi_{cm}}\,.\end{aligned} \tag{21}$$

The beams are then recombined upon a second pass through the calcite crystal, such that $\overrightarrow{E_1} = \overrightarrow{b_1} + \overrightarrow{b_2}$. $\overrightarrow{E_1}$ is then projected along the orthogonal axes $\hat{\boldsymbol{w}}_{\boldsymbol{A}}$ and $\hat{\boldsymbol{w}}_{\boldsymbol{B}}$ of a Wollaston prism, which is at an angle β relative to the calcite axes, as per Figure 2.12.

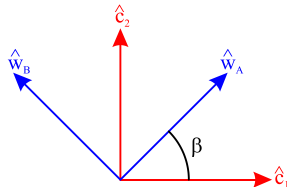

Figure 2.12: Orthogonal axes of the calcite relative to the orthogonal axes of the Wollaston prism. The axes are rotated by angle β. In the optimal case, $\beta = 45°$.

The resulting fields, $\overrightarrow{E_A}$ and $\overrightarrow{E_B}$, are given by

$$\begin{aligned}\overrightarrow{E_A} &= \overrightarrow{E_1}\cdot\hat{\boldsymbol{w}}_{\boldsymbol{A}}\hat{\boldsymbol{w}}_{\boldsymbol{A}}\\ &= E_0 e^{i(\boldsymbol{k}\cdot\boldsymbol{r}-\omega t)}\left\{\begin{matrix}e^{i(\phi_{cm}+\phi_{dm})}\hat{\boldsymbol{n}}\cdot\hat{\boldsymbol{c}}_1\hat{\boldsymbol{c}}_1\cdot\hat{\boldsymbol{w}}_{\boldsymbol{A}}\\ +e^{i(\phi_{cm})}\hat{\boldsymbol{n}}\cdot\hat{\boldsymbol{c}}_2\hat{\boldsymbol{c}}_2\cdot\hat{\boldsymbol{w}}_{\boldsymbol{A}}\end{matrix}\right\}\hat{\boldsymbol{w}}_{\boldsymbol{A}}\\ &= E_0 e^{i(\boldsymbol{k}\cdot\boldsymbol{r}-\omega t)}\left\{\begin{matrix}e^{i(\phi_{cm}+\phi_{dm})}n_1\cos\beta\\ +e^{i(\phi_{cm})}n_2\sin\beta\end{matrix}\right\}\hat{\boldsymbol{w}}_{\boldsymbol{A}}\\ \overrightarrow{E_B} &= \overrightarrow{E_1}\cdot\hat{\boldsymbol{w}}_{\boldsymbol{B}}\hat{\boldsymbol{w}}_{\boldsymbol{B}}\\ &= E_0 e^{i(\boldsymbol{k}\cdot\boldsymbol{r}-\omega t)}\left\{\begin{matrix}e^{i(\phi_{cm}+\phi_{dm})}\hat{\boldsymbol{n}}\cdot\hat{\boldsymbol{c}}_1\hat{\boldsymbol{c}}_1\cdot\hat{\boldsymbol{w}}_{\boldsymbol{B}}\\ +e^{i(\phi_{cm})}\hat{\boldsymbol{n}}\cdot\hat{\boldsymbol{c}}_2\hat{\boldsymbol{c}}_2\cdot\hat{\boldsymbol{w}}_{\boldsymbol{B}}\end{matrix}\right\}\hat{\boldsymbol{w}}_{\boldsymbol{B}}\\ &= E_0 e^{i(\boldsymbol{k}\cdot\boldsymbol{r}-\omega t)}\left\{\begin{matrix}e^{i(\phi_{cm}+\phi_{dm})}n_1(-\sin\beta)\\ +e^{i(\phi_{cm})}n_2\cos\beta\end{matrix}\right\}\hat{\boldsymbol{w}}_{\boldsymbol{B}}\,,\end{aligned} \tag{22}$$

where we have replaced $\hat{\boldsymbol{n}} \cdot \hat{\boldsymbol{c}}_{\boldsymbol{i}}$'s by scalar constants n_i (these reflect the magnitude of the projection of the incident beam $\overrightarrow{E_0}$'s polarization on each of the calcite axes) and replaced dot products between $\hat{\boldsymbol{c}}_{\boldsymbol{i}}$'s and $\hat{\boldsymbol{w}}_{\boldsymbol{i}}$'s by trigonometric functions of the angle β.

These fields then impinge on photodiodes PD_A and PD_B. The measured photocurrent is proportional to the intensity of the light beams, obtained by squaring the fields in Eq. (22). The intensity on PD_A is given by

$$\begin{aligned} I_A &\propto |\boldsymbol{E_A}|^2 \\ &\propto E_0^2\big\{|n_1|^2\cos^2\beta + |n_2|^2\sin^2\beta \\ &\qquad + e^{i(\phi_{dm}+\phi_{cm}-\phi_{cm})}n_1^* n_2 \sin\beta\cos\beta \\ &\qquad + e^{i(\phi_{cm}-\phi_{cm}-\phi_{dm})}n_1 n_2^* \sin\beta\cos\beta\big\} \\ &\propto E_0^2\big\{|n_1|^2\cos^2\beta + |n_2|^2\sin^2\beta + e^{i(\phi_{dm})}n_1^* n_2 \sin\beta\cos\beta \\ &\qquad + e^{i(-\phi_{dm})}n_1 n_2^* \sin\beta\cos\beta\big\}, \end{aligned} \tag{23}$$

which can be simplified to

$$I_A \propto E_0^2\{|n_1|^2\cos^2\beta + |n_2|^2\sin^2\beta + 2n_1 n_2 \sin\beta\cos\beta\cos\phi_{dm}\}. \tag{24}$$

Similarly, for PD_B, the measured intensity is given by

$$\begin{aligned} I_B &\propto |\boldsymbol{E_B}|^2 \\ &\propto E_0^2\{n_1^2\sin^2\beta + n_2^2\cos^2\beta - 2n_1 n_2 \sin\beta\cos\beta\cos\phi_{dm}\}. \end{aligned} \tag{25}$$

From Eqs. (24) and (25), it is apparent that there is no dependence of the resulting beam intensities on the common mode phase shift, ϕ_{cm}, picked up by each beam. This reflects the differential nature of this interferometer design, which is not sensitive to common phase shifts, but only differences in phase shifts (note that there is another very important differential characteristic of this interferometer which will be discussed in Chapter 3).

It is also apparent that the first two terms reflect a DC component to the intensity which is not a function of the differential mode phase shift ϕ_{cm}: they depend only on the magnitude of the projection of the incident polarization on the calcite axes, n_i's, and the angle between the calcite and Wollaston axes, β. The last terms of Eqs. (24) and (25) contain the interferometric signal, proportional to the cosine of the differential mode phase shift ϕ_{dm}. The amplitude of the interferometric signal is dependent on the n_i's and angle β.

We also see that the amplitude of the interferometer signal is maximized by setting $n_1 = n_2$, and $\beta = 45°$. Experimentally, the latter condition is effectively true, and we try to attain the former condition by adjusting the input polarization, discussed in section 2.6.2. In the case of an optimized alignment, at $\phi_{dm} = 0$, when I_A is maximized, $I_B = 0$. When $n_1 \neq n_2$, a nulled intensity on either of PD_A or PD_B cannot be reached for any value of ϕ_{dm}.

2.6.2 Input beam polarization control

In practice, the n_i's discussed in 2.6.1 represent the brightness of the incident beams exiting the calcite splitter and impinging on the sample. If the one of the beams has no intensity, there is obviously no hope of operating the interferometer. In order to balance the intensity of the two beams exiting the calcite (such that $n_1 = n_2$), we must start with either linearly polarized light on an axis with equal projection on $\hat{\boldsymbol{c}}_1$ and $\hat{\boldsymbol{c}}_2$ (i.e. at 45°), elliptically polarized light with equal projection on $\hat{\boldsymbol{c}}_1$ and $\hat{\boldsymbol{c}}_2$, or circularly polarized light.

A method of adjusting the input beam polarization should therefore exist. Adjustments had been previously achieved by moving around a length of optical fiber outside of the UHV system until it was in a lucky position where the stresses on the fiber and its birefringence happened to result in an appropriate incident beam polarization. This method was particularly inconvenient and resulted in major trial-and-error sessions any time the laser diode assembly was un-mounted/remounted to the UHV system (necessary for bakeout). A fiber holder was built which bolts onto the top UHV flange and guides the fiber through a Thorlabs FPC020 miniature polarization controller, as illustrated in Figure 2.13. By adjusting the angle of the paddles of the polarization controller, one modifies the axis along which the fiber's birefringence adds a phase delay. This is analogous to rotating waveplates in free optics. While monitoring the laser alignment signals (Figure 2.14), one can modify the paddle angles to maximize the peak-to-peak voltage of the interference fringes.

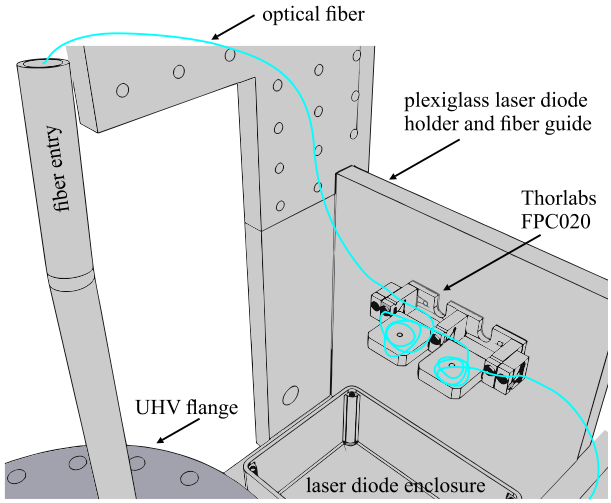

Figure 2.13: A Thorlabs FPC020 Miniature Polarization controller is used to adjust the polarization of the interferometer's incident beam. It is mounted to a Plexiglas holder which guides the optical fiber from the laser diode, through the FPC020, and then to the UHV feedthrough.

2.6.3 Calibration of path difference

The photocurrent signals (converted to volts) from the two photodiodes are subtracted to yield an interferometer output signal with the form

$$V_{int} = \frac{V_{PP}}{2}\cos(\phi_0 + \phi_{dm}) \tag{26}$$

where ϕ_0 is an arbitrary phase offset set so that $\phi_0 + \phi_{dm} = \pi/2$ for maximal sensitivity. This is experimentally realized by adjusting the angle of the sample on piezo motors which correspondingly changes the initial path difference between the beams. A path difference can also be set with a DC voltage applied to a piezo tube inside which the calcite optics are mounted.

By sweeping the path difference over the interference fringe, one can measure the peak-to-peak voltage V_{PP} output and determine the sensitivity of the interferometer. The differential mode phase difference relates to the path difference, d, and the height difference of the cantilever at the beam positions, $\delta u = d/2$ (Figure 2.8), by

$$\phi_{dm} = \frac{2\pi}{\lambda}d = \frac{4\pi}{\lambda}\delta u. \tag{27}$$

The sensitivity of the interferometer is found by taking the derivative of the output voltage in Eq. (26) with respect to the height difference δu. We take the reciprocal of the maximum slope to convert from V to nm,

$$S_{\delta u} = \left(\max\frac{\mathrm{d}V_{int}}{\mathrm{d}\delta u}\right)^{-1} = \frac{\lambda}{2\pi V_{pp}}, \tag{28}$$

such that $\delta u = S_{\delta u}V_{out}$.

The interferometer calibration signals are illustrated in Figure 2.14 from a screenshot of the output of Matlab function `getLaserAlignment`, which was written to drive the phase offset (green signal) of the interferometer (electrically via the piezo tube mounted calcite) and record the interferometer output signal (black), as well as the signals coming from each photodiode (red and blue). A continuously repeating version of this function, `getLaserAlignmentContinous`, can be used to monitor the peak-to-peak response of the fringe, as well as its phase offset while adjusting sample and optics alignment. The peak-to-peak voltage of 15.91 V in Figure 2.14 corresponds to a sensitivity of $S_{du} = 780\ \mathrm{nm}/(2\pi \cdot 15.91\ V)$ = 7.8 nm/V.

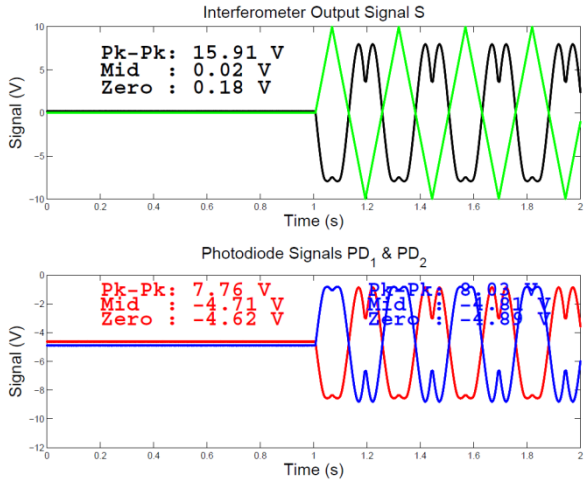

Figure 2.14: Laser alignment curve output by `getLaserAlignment`. The displayed signals are the phase offset in green, interferometer output in black, individual photodiode signals in red and blue.

It is not always practical to monitor the peak-to-peak value of the interference signals: A new photodiode preamplifier was constructed having remotely settable gains so that the signal could be amplified at the preamplifier (located at the top of the UHV chamber). The amplification ensures that the voltage level of the signals being recorded is well above the 16-bit quantization level of the analog-to-digital conversion, and ensures that excess noise picked up over the long signal path is minimized. When a gain of 10× is applied, the white noise power coming from the laser phase noise (discussed in section 3.3) is fully resolved and exceeds the noise of the analog-to-digital converter. At this high gain, however, one cannot measure the peak-to-peak voltage, which would greatly exceed the ± 15 V rails of our detection electronics and the ± 10 V range of the analog-to-digital converter.

To allow calibration to be carried out while high gain is enabled, the piezotube used to actuate path differences inside the interferometer was calibrated relative to the peak-to-peak voltage. Using this calibration, one may sweep the path difference of the interferometer over a small distance, 1 nm for example, and record the high-gain output signal. This function `getInterferometerSensitivity` directly returns $S_{\delta u}$ (nm/V) by modulating the path difference by a known distance. Its output is shown in Figure 2.15.

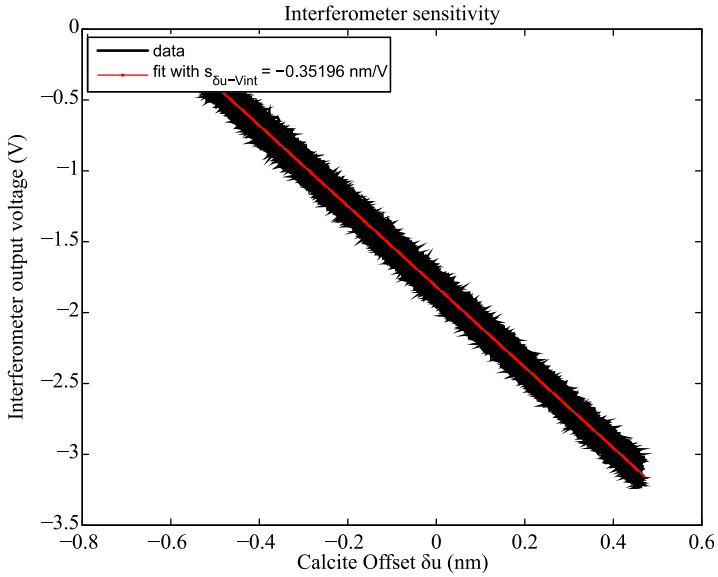

Figure 2.15: Interferometer sensitivity calibration based on piezo modulated path difference. The output of Matlab function `getInterferometerSensitivity` returns a direct measurement of $S_{\delta u}$.

A major advantage of the calibrated piezo approach to measuring the interferometer sensitivity is that it is impervious to sloppy record keeping of what gains may or may not have been turned on for a particular measurement. This measurement can also be done periodically during a scanning probe experiment to verify interferometer alignment without changing gains or laser power (which would be necessary to acquire the full peak-to-peak waveform).

2.6.4 Calibration of deflection and force at the tip location

Now that we have calibrated volts to nm of height difference at the beams, δu, all that remains is the determination of deflection at the tip u_t, and then the force at the tip follows easily as $F = ku_t$ (we again refer the reader to Figure 2.8 on page 28 as a reminder of the cantilever beam geometry and associated measurement variables). In the experimental setup, the tip and sample can be arranged so that both of the interferometer beams reflect from the free end where the slope is constant, as shown in Figure 2.8. The following discussion assumes that the interferometer reflects from the free end of the cantilever, which maximizes sensitivity.

From Eq. (14) which describes the cantilever beam profile on the free end with respect to the tip position ($z > t$), one can derive the deflection of the cantilever beam at the position of the tip, u_t, to be

$$u_t = \frac{2t}{3d_b}\delta u = S_{u_t} V_{int} = \frac{\lambda}{3\pi V_{pp}} \frac{t}{d_b} V_{int}, \tag{29}$$

where t is the tip position and $d_b = 1$ mm is the distance between the two interferometer beams.

Finally, combining Eqs. (29), (17), and $F = ku_t$, the force at the tip position is found to be:

$$F = S_F V_{int} = \frac{\lambda}{3\pi V_{pp}} \frac{k_0 L^3}{d_b t^2} V_{int}. \tag{30}$$

The sensitivities S_{u_t} and $S_F = kS_{u_t}$ required to convert interferometer signals to deflections and forces at the tip are easily computed using Matlab functions `getNMAtTip` and `getKfromK0`.

2.6.5 Measurement uncertainty

We now consider the measurement uncertainty on the determination of forces using this method. Starting from Eq. (30), we compute partial derivatives and estimate the uncertainty on F:

$$\begin{aligned}\left(\frac{\Delta F}{F}\right)^2 = &\left(\frac{\Delta\lambda}{\lambda}\right)^2 + \left(\frac{\Delta V_{int}}{V_{int}}\right)^2 + \left(\frac{\Delta V_{pp}}{V_{pp}}\right)^2 + \left(\frac{\Delta k_0}{k_0}\right)^2 + \left(\frac{\Delta d_b}{d_b}\right)^2 \\ &+ \left(3\frac{\Delta L_0}{L_0}\right)^2 + \left(2\frac{\Delta t}{t}\right)^2.\end{aligned} \tag{31}$$

Among the largest sources of error in the above terms are the determination of the tip position t, and the free cantilever beam length L. Each of these is determined to ~ 0.1 mm. The relative uncertainty in the interferometer beam separation is estimated to have an upper bound of $\Delta d_b/d_b < 4\%$ [49]. The spring constant of the free end, k_0, is typically determined to $\sim$3%. Inserting typical values of $t = 3$ mm and $L = 5$ mm gives relative uncertainties of (in order of appearance in Eq. (31)) $\ll$1%, $\ll$1%, $\sim$1%, $\sim$3%, 4%, 2%, and 3%. Multiplying by the pre-factors associated with partial derivatives and adding in quadrature suggests that there is a $\sim$10% uncertainty in forces determined in this experiment.

The parameters $\lambda, V_{pp}, k_0, d_b, L$, and t are static throughout the duration of an experiment, therefore the 10% uncertainty we estimated above is a systematic uncertainty

in the determination of forces. This systematic uncertainty must be taken into account when comparing data from different experiments. Forces measured during one experiment, however, can be compared with an error bar of much less than 10%: in this case, detection noise on the order of ~1 nN is the limiting factor, and is discussed in Section 3.3.

2.7 Sample preparation

In order to carry out the experiments presented in subsequent sections, several types of well-defined surfaces had to be prepared. We review preparation procedures for these samples, and highlight particularly those that are new to our lab or where significant improvements have been made to quality, reliability or yield.

2.7.1 Mica for cantilever beams

The first step in the preparation of our standard gold-on-mica cantilever beams is a high-quality mica substrate. These are made from premium grade V-1 muscovite mica supplied by Axim as 3" x 1" sheets with a thickness of 50 μm. The sheets are cut into strips of ½" × 1-2 mm using a wire saw with a boron carbide slurry. This is a very slow and tedious process, each cut taking several minutes, but the edge quality is excellent and very little of the mica substrate is damaged by the cutting procedure. A comparison of edges cut by various suppliers is given in Ref. [49].

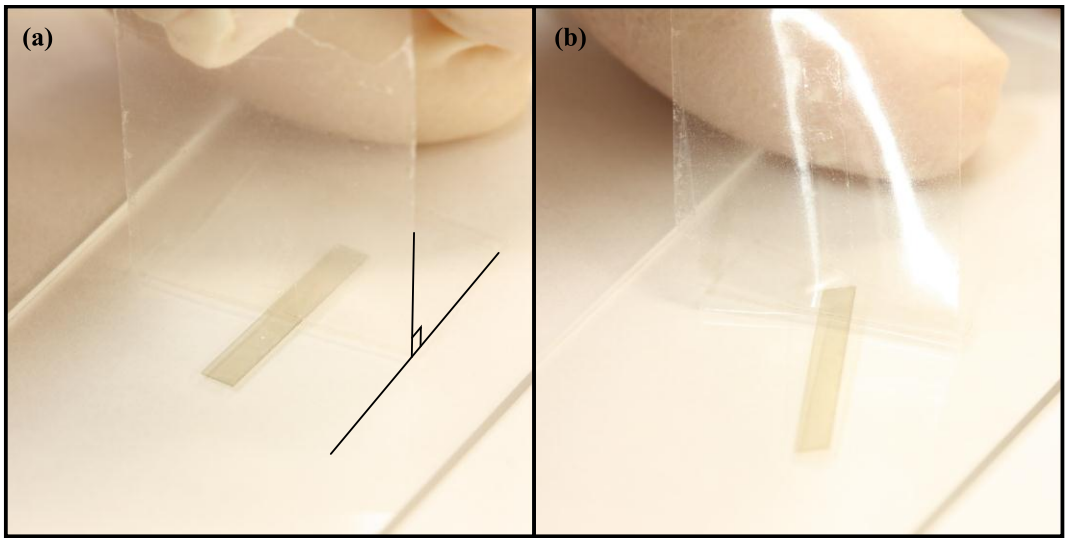

Figure 2.16: Cleavage of mica beams prior to gold evaporation. (a) The mica beam is cleaved by pulling an adhered piece of scotch tape at a 90° angle. (b) The mica film adhering to the tape should be checked for completeness of the cleave.

A major improvement in sample yield was obtained by refining the mica cleaving procedure. In order to obtain a clean surface for the epitaxial growth of Au(111) by thermal evaporation, it is necessary to freshly cleave the mica beam. This had a yield of ~20% with the previous precarious technique involving loops of scotch tape and careful tweezer work. The yield has been improved to nearly 100% by the procedure presented in Figure 2.16. We also point out that an improved yield is particularly desirable since the cleavage must be done twice in order to prepare top *and* bottom surfaces for each cantilever beam.

The mica cleavage procedure begins by placing the mica beam on a glass slide. The beam is then covered with a piece of scotch tape (clear type works best) which is pressed thoroughly with a finger to ensure good adhesion to the top layer of the mica beam and to the glass slide. The tape is then peeled up at a 90° angle. Typically, 1 μm or less of mica is removed from the beam during this cleavage procedure. Most of the beam (~98% of its thickness) remains rigidly held to the glass slide by the tape, meanwhile a very thin piece is removed, adhering to the tape as it is peeled up. A major advantage of this technique is that it does not harm the mechanical integrity of the remaining beam – previous techniques involving grabbing the beam with tweezers would often produce cracks in the mica, rendering them useless as cantilevered samples.

Finally, the completeness of the cleave should be checked by examining the mica film adhering to the tape. If a complete layer has not been removed, the cleavage procedure should be repeated until it is. An easy way to check this is by touching a latex gloved finger to the sticky side of the tape and peeling it off – this will change the texture of the adhesive and make the mica film attached to the tape visibly obvious.

2.7.2 Au(111)

The study of epitaxial growth of Au on mica substrates dates back to the work of R. Hines in the 1960s [94], who reported that the growth mode of Au films is highly sensitive to gas contamination and suggested the importance of freshly cleaved and degassed mica. The general consensus in literature from the last two decades is that high quality Au(111) films with large grain sizes (>1 μm) can be easily prepared on freshly cleaved mica substrates in high vacuum as long as the mica is sufficiently degassed and maintained at elevated temperature during deposition [95-98]. We prepare the films by inserting freshly cleaved mica substrates (as described in section 2.7.1) into high vacuum (10^{-8} Torr), and degassing them at 450 °C for at least 12 hours. The substrate temperature is then lowered to 400 °C

and a 100 nm film of Au is evaporated at a rate of ~1 Å/s, as measured on a quartz crystal monitor. A temperature of 400 °C is maintained for 60 min following the evaporation, and then the sample is cooled at a rate of ~100 °C/hour to room temperature. Cantilever beam substrates must be flipped, re-cleaved and evaporated on the opposite side to aid in thermal compensation during sample annealing and to ensure a highly uniform reflective surface for interferometer beam reflection.

The cantilever beams have an excellent shelf-life and can be stored in air in a petri dish for great lengths of time (up to years) before being used as substrates. After they are mounted using the gluing procedure described in section 2.5.3, they are cleaned by a thorough rinsing of ethanol over the sample surface and dried gently using nitrogen just prior to insertion into vacuum. Samples are prepared by Ne^+ ion sputtering[1] and thermal annealing cycles in the UHV sample prep chamber. These cycles are typically carried out with a sputter duration of ~5 min (1 keV, 20 mA emission current, $P_{Ne} = 1 \times 10^{-5}$ Torr, beam current density not known), and an annealing duration of ~20 min at ~400 °C (controlled by a constant heating stage current of ~1.7 A). New samples can be cleaned in about seven to ten sputter-anneal cycles. Two or three cycles are required to prepare a surface from contamination after weeks in vacuum.

The cleanliness of the Au(111) samples is verified by Auger Electron Spectroscopy (AES) [99]. Briefly, AES functions by first ejecting core electrons from sample atoms using a ~2 keV incident electron beam. Inner-shell transitions occur to fill the lower-lying levels, for example a 2*s* electron could fill a 1s hole. The extra kinetic energy is transferred to a valence electron, 2p for example, which is ejected. The kinetic energy of the ejected valence electron, or Auger electron, is analyzed and reports on the unique lower-lying electron transition spectrum of the element. As there is a rather large continuous background to the number of electrons returned as a function of energy, $N(E)$, we acquire and analyze its derivative, $dN(E)/dE$, obtained by lock-in detection. We point out that the energy axis calibration of AES is affected by the position of the sample in the vertical direction since this determines the angle of electrons collected by the circular mirror analyzer. The miscalibration can be remedied by adjusting the sample height so that the elastic peak (calibrated to a 2 keV incident beam) is measured at the correct energy. We don't normally

[1] Ion bombardment is a common surface preparation technique for metal surfaces as well as those of some semiconductors. The high-energy ions remove the topmost layers of surface material and contaminants. The resulting 'rough' surface is healed by annealing. See Ref. [296]

bother with this procedure as there are height variations between samples we commonly investigate, and Auger signatures are quite easily discernible to the experienced user.

In typical use, we seek the presence of four strong gold peaks, identified by small circles in Figure 2.17, without the signature of a carbon peak at 271 eV, identified by the large circle. The ~11 eV offset on the energy axis is due to the vertical alignment of the sample. The sample should be sputtered and annealed to a few cycles beyond the disappearance of the C peak, since the detection limit of AES is only on the order of ~1%.

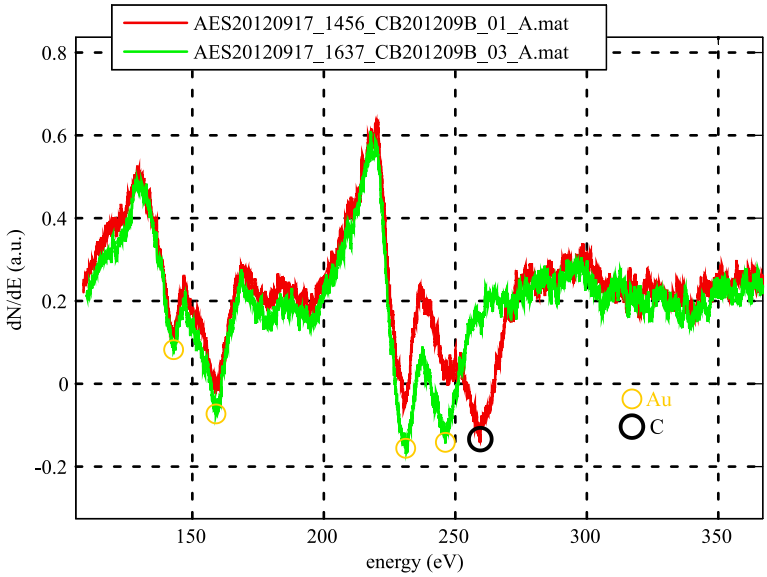

Figure 2.17: AES spectrum of a new gold cantilever beam after one 6 minute sputtering cycle (red), and after three sputter-anneal cycles (green). Small gold-coloured circles indicate some of the signature peaks of gold, and the larger black circle indicates the carbon peak which we seek to eliminate.

The close-packed Au(111) surface reconstructs[1] into a $22 \times \sqrt{3}$ surface unit cell, and has been investigated by many techniques such as low-energy electron diffraction (LEED), reflection high-energy electron diffraction (RHEED), transmission electron microscopy (TEM), helium atom scattering (HAS), and STM [100-102]. The reconstructed surface unit cell accommodates 23 atoms in 22 surface atom sites along the $(1\bar{1}0)$ direction of the surface. The lateral dimension of the reconstruction is $22 \cdot a/\sqrt{2}$ = 6.3 nm, where $a = 0.408$ nm is the lattice constant of gold [103]. To accommodate the extra atoms, the surface

[1] Surface reconstruction is a common theme in surface science whereby atoms at (or near) the surface layer have lower symmetry than their bulk counterparts. The atomic rearrangements happen for varying reasons in metals and semiconductors. See Refs. [296, 297].

contains hcp stacking fault regions, separated from the bulk-terminated fcc regions by atoms on bridge sites. The atoms stacked on bridge sites are elevated with respect to those in the fcc or hcp atoms, and show up as two bright stripes in topography, known as discommensuration lines. The unit cell extends by $\sqrt{3}$ atomic spacings in the $(11\bar{2})$ direction to accommodate the shift in the $(11\bar{2})$ direction necessary to transition from fcc to hcp stacking.

Furthermore, to reduce elastic strain in an isotropic manner, a longer range reconstruction with periodicity ~25 nm is also present on the Au(111) surface, known as the 'herringbone' reconstruction. A regular 120° 'zigzag' alternation of the direction along which the $22 \times \sqrt{3}$ is oriented is typical of this surface. Several 'elbows' of the reconstruction can be seen on the lower terrace in Figure 2.18 (a), and are numerous in Figure 2.18 (b).

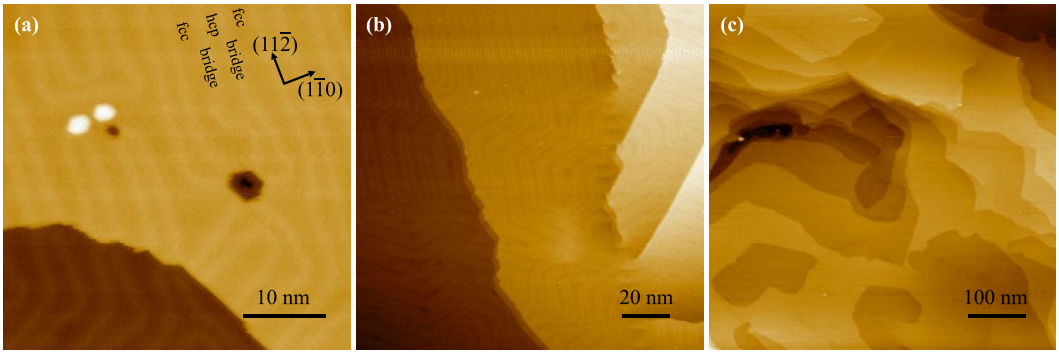

20120918A#039 -0.9V 8pA | 20120918A#185 -0.95V 8pA | 20120217#299 -0.05V 20pA

Figure 2.18: Constant current topographic STM images of the Au(111) surface (false colour map to topographic height). (a) One atomic step down of height $a/\sqrt{3}$ = 0.236 nm occurs in the bottom-left part of the image. Two indentations with the STM tip have been carried out and have left hexagonally shaped holes which reflect the symmetry of the surface. The top-left hole shows two islands of single atomic layer high Au pileup which resulted from the indentation. Regions of fcc, hcp, and bridge site stacking are labeled on the discommensuration lines. (b) One atomic terrace step runs from top to bottom of the image. Four screw dislocations are visible in the right part of the image, from which single atomic steps propagate. (c) Large scale topographic image of Au(111) surface.

We briefly comment that we have obtained atomically flat Au(111) surfaces by evaporation on gold on Schott D263T glass (70 μm thickness). There are a small number of reports in the literature that suggest it is possible to produce Au(111) surfaces on glass slides [104, 105]. Although the surfaces show smaller grains with a lateral size of a few hundred nanometers separated by many atomic steps, Figure 2.19 (a), they are often capped by large atomically flat terraces which exhibit the $22 \times \sqrt{3}$ reconstruction, Figure 2.19 (b). We have not investigated these samples in as much detail as gold on mica, but they may

serve to produce more well-defined mechanical force transducers than mica sheets (D263T glass can be obtained in 30, 50 and 70 μm thicknesses).

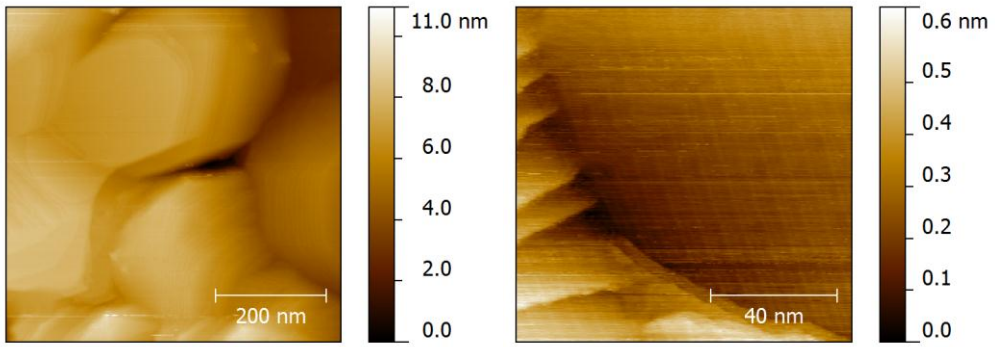

20120312#043: +0.1V 130pA 20120312#023: +0.1V 80pA

Figure 2.19: (a) Au(111) prepared on D263T glass. Atomically flat terraces are separated by many steps between grains with lateral sizes of several hundred nm. The height scale extends 11nm, as shown by the false colour ruler. (b) Small angle grain boundary between a flat terrace on one grain and steps on another. The intersection of ~7 atomic steps with a flat terrace over a distance of ~100 nm indicates an angle of ~1° between the (111) surface normals.

2.7.3 Au(111)-C_{60}

A procedure for the evaporation of C_{60} molecules on Au(111) surfaces was established using the Omicron EFM-3T electron beam (e-beam) evaporator in our preparation chamber. Many of the initial experiments with the evaporation of C_{60} were carried out with the help of summer student Jean-Benoît Lalanne in May 2011. Several issues such as the un-documented workings of the e-beam power supply, evaporator spot location, flux rates, etc. were worked out and are summarized here.

One might say that an electron beam evaporator is 'overkill' for depositing organic molecules that need to be heated to a far lower temperature than sources such as refractory metals or carbon (section 2.7.4) – in some sense a Knudsen cell might be easier to control. At any rate, the C_{60} powder was loaded into a Mo crucible and packed slightly with the end of an Allen key wrapped in clean Al foil. Packing the evaporant helps it stay inside the crucible, shown in Figure 2.20 (a), while the crucible is being inserted into the evaporator.

The e-beam evaporator works in a manner illustrated in Figure 2.20 (b). A tungsten filament, built of the same 0.1 mm diameter tungsten wire as our polycrystalline STM tips (Alfa Aesar), is heated with a current I_{FIL}, illustrated by the orange loop. I_{FIL} should be limited to ~2 A to avoid filament failure which typically occurs around 2.3-2.5 A. When the e-beam controller is powered on, the crucible is biased to 180 V and this voltage cannot be reduced – this is not documented in the manual and gives the impression that the controller

may be broken. In fact, it seems that this is a feature to ensure that once thermionic emission starts from the filament, electrons will be collected by the crucible or rod of evaporant at positive bias. The minimum settable voltage remains 180 V until an emission current is detected in the low mA range, at which point the voltage can be reduced to a minimum of ~148 V. Once an e-beam emission current of I_{EM} = 3 mA is detected on the crucible, the controller can be operated in emission current feedback, where a desired emission current is set and the controller adjusts the filament current to achieve the desired emission current. Since such a low heating power is required for C_{60}, we can keep the emission and filament currents relatively low throughout evaporation, I_{EM} = 3 mA. The power of the e-beam is adjusted by changing the crucible voltage.

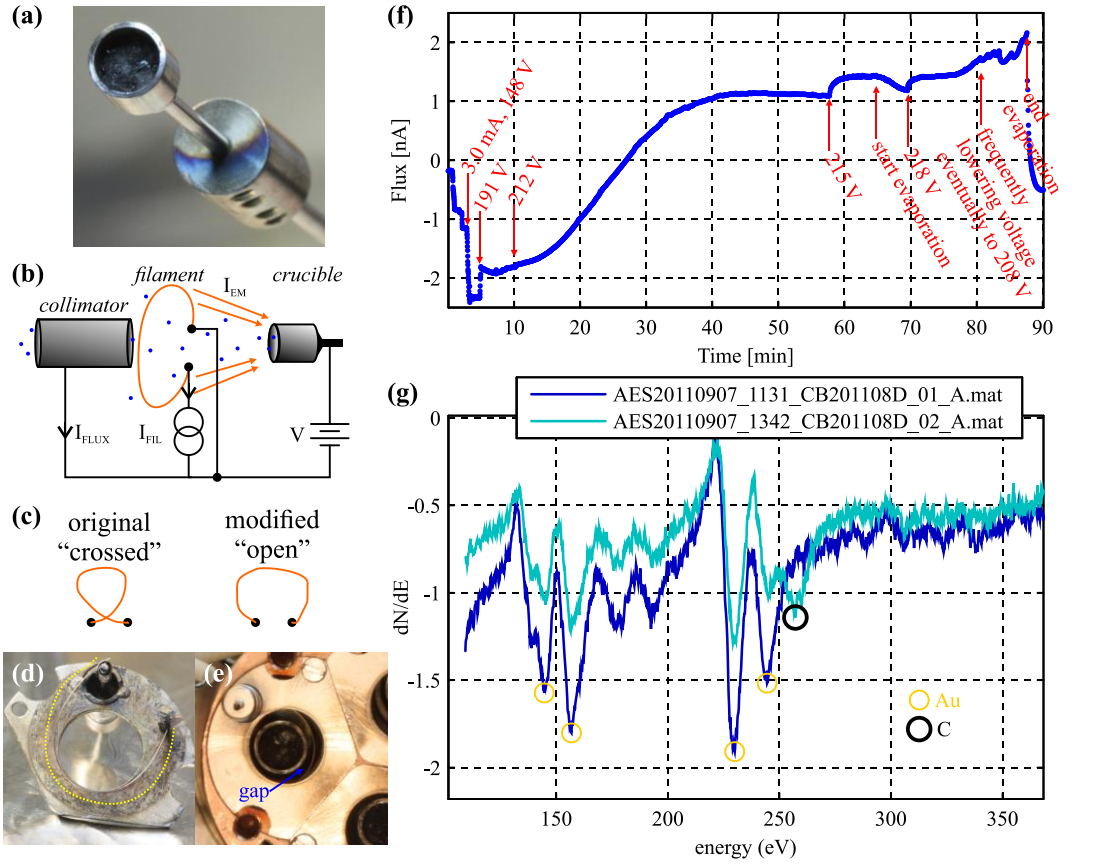

Figure 2.20: (a) 5 mm diameter molybdenum crucible filled with C_{60} and lightly packed; (b) Diagram of the e-beam evaporator showing the principal components and electrical operation parameters; (c) Filament design showing original "crossed" filament and modified "open" filament which is better suited to evaporation from crucibles; (d) Photograph of "open" filament design, filament path highlighted by the dotted yellow line; (e) Photograph of the safety gap between the "open" filament and crucible; (f) Flux monitor reading during evaporation; (d) Auger spectrum of clean gold (dark blue), and after a flux dose of 2.0×10^3 nA·s of C_{60} was deposited on the sample.

A flux monitor is built into the evaporator, consisting of a conductive tube which acts both as a collimator and an electrode to collect a flux monitor current. Some fraction of the evaporant, shown as blue dots in Figure 2.20 (b), is ionized from its passage through the electron beam, and when it impinges on the flux monitor, registers a current, I_{FLUX}, typically in the nA regime. The flux monitor current is not a quantitative measure of deposition thickness – for this, a quartz microbalance is ideal, but in our system we must rely on estimation by the evolution of the Auger signal and surface investigation by STM. The flux monitor does give a relative measure for a given setup, and can be used to repeat deposition parameters with acceptable accuracy.

We mention here an important modification to the filament design which makes evaporation from crucibles less precarious. The filament design suggested by the evaporator manual is a "crossed" filament design shown in Figure 2.20 (c) which has the advantages of increased filament wire length, and decreased distance to the evaporant source (good for high power). The crossed filament has a drawback in that the crucible may collide with the filament when its position is adjusted – a collision nearly always damages the fragile filament requiring a full evaporator disassembly[1]. Since very little heating power is needed for C_{60}, the filament design is modified to be "open", also shown in Figure 2.20 (c) along with a photograph in Figure 2.20 (d). The safety gap between the open filament and the crucible is highlighted in Figure 2.20 (e).

Figure 2.20 (f) shows the flux monitor current, I_{FLUX}, recorded during the evaporation. The evaporator is water cooled during evaporation to minimize degassing from other components. At the beginning, the voltage on the crucible is kept at the 180 V minimum and the filament current is increased until 3 mA of emission current is measured (at a filament current of ~1.5 A). The flux monitor shows an increasingly negative reading as the filament becomes hotter and some of the emitted electrons are collected by the flux monitor. The heating power is adjusted by increasing the voltage while the 3 mA emission current is kept constant. At a voltage of 212 V, corresponding to a heating power of 212 V × 3 mA = 0.64 W, the flux begins to rise and takes a few tens of minutes for the temperature and rate to stabilize. Evaporation on the sample starts at ~65 minutes and ends at ~87 minutes. The

[1] Full disassembly of the evaporator is not necessary for inserting new evaporant. Evaporant can be loaded through separate 1.33" CF flanges with the evaporator still mounted to the preparation chamber, but it takes some practice and familiarity with the design to help with blind insertion of the rod and crucible (it's a good idea to get some experience with inserting evaporant when the evaporator is out for repair, and eventually trying it while blindfolded).

voltage was manually adjusted several times during the evaporation to keep the flux stable. An Auger spectrum is presented in Figure 2.20 (g) showing an increased carbon signal arising from the deposited C_{60}.

The evaporant spot is a circle of ~ 10 mm diameter at the position of the sample stage. The spot position can be estimated by looking at the filament glow emanating from the evaporator. However, the filament glow is not *exactly* identical to the spot location and deviations of several millimeters can occur. The spot position may have to be found by Auger or by STM scanning at several locations on the sample. In the case of a rod evaporant, such as carbon used in section 2.7.4, the evaporant glows brighter than the filament and the exact spot of the bright glow corresponds to the deposition location. This would be an ideal way of obtaining sample stage coordinates for all three evaporator pockets, which are in principle designed to overlap at one point if the correct distance is used. For Cell #3, the sample stage was positioned at $(x, y, z, \theta) = (15.3\ \text{mm}, 11.6\ \text{mm}, 173\ \text{mm}, 140°)$ during evaporation.

STM investigations of Au(111)-C_{60} samples are shown in Figure 2.21. A large scale composite topographic image of C_{60} on a solid (non-cantilevered) Au(111) sample is shown in Figure 2.21 (d). Three principal adsorption structures are observed on the surface and indicated in the image: molecules individually adsorbed in regular arrays at elbows of the Au(111) herringbone surface reconstruction, very similar to structures recently reported by Tang *et al.* [106]; C_{60} molecules attaching to step edges; and large islands of C_{60} molecules. An island of molecules is also shown in detail in Figure 2.21 (f) across a step edge of the substrate running from top to bottom of the image. Molecules within the island also have variable contrast (bright/dark) likely due to differing bonding geometry and resulting charge transfer to the substrate. In terms of creating a well-defined metal-molecule-metal junction for force and current spectroscopy, the individually adsorbed C_{60}'s are an excellent structure.

C_{60} deposited on a cantilevered Au(111) sample is shown in Figure 2.21 (a), (b), and (c): topography, current, and force images were acquired simultaneously. The islands formed on the surface show several orientations – at least three, and the orientation of the Au(111) surface could not be resolved through the scanning noise. The current error signal shows a typical corrugation of ~ 1 pA from the desired 10 pA setpoint while scanning over the C_{60} due to feedback lag. The force signal shows a larger repulsive force on the order of ~0.1 nN

over the C_{60} islands compared to the bare Au(111) for the same average tunneling current (boxed regions with corresponding line profiles in Figure 2.21 (e)).

Tunneling conditions (bias voltage and current setpoint) were difficult to optimize over both the C_{60} and Au(111) regions simultaneously. This observation of the molecular film instability at room temperature is consistent with the experience of Eric Altman, a pioneer of C_{60} investigations by STM [107-109], in a discussion on this data at the 2011 non-contact Atomic Force Microscopy (nc-AFM) conference. The mobility of the C_{60} molecules on the surface and their diffusion through the tip-sample junction results in a very noisy current signal when the tip is over Au(111) regions, but still allows rather stable imaging over islands of the molecules.

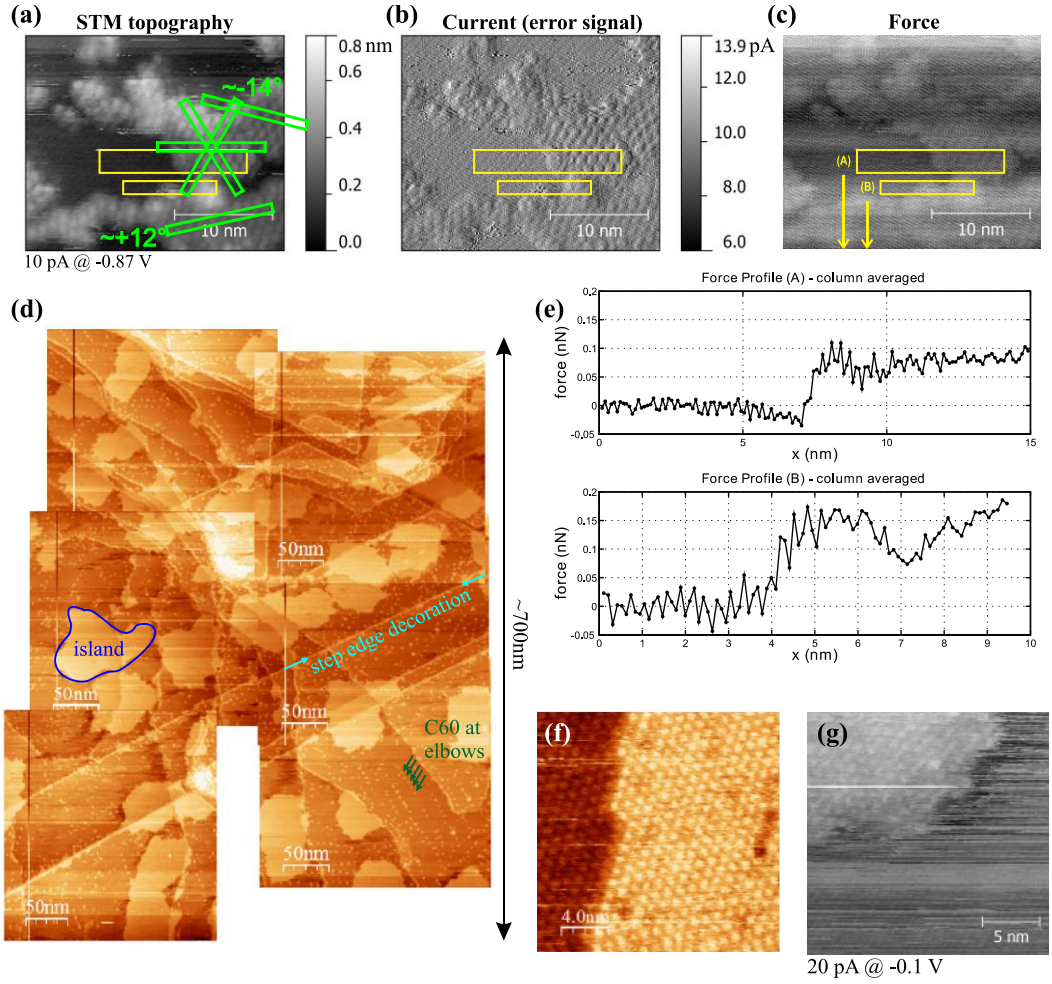

Figure 2.21: (a), (b), (c) Simultaneously acquired STM topography, current error signal, and force data for C_{60} molecules on a Au(111)/mica cantilever beam; (d) Large scale composite image showing typical features of Au(111)-C_{60} surface structures; (e) Column averaged force profiles across the yellow rectangles shown in (a), (b), (c); (f) Detailed view of C_{60} molecules adsorbed over a step edge of the Au(111) substrate; (g) STM topography of a C_{60} island and bare Au(111) – the ill-defined edge of the island points to diffusing molecules, as does the unstable tunneling on the Au(111) substrate.

Distance spectroscopy was performed on the C_{60} island and the bare Au(111) regions shown in Figure 2.21 (g). Five force- and current-displacement curves are shown in Figure 2.22 for each of these areas. For each curve, the tip was retracted by 2 nm from the tunneling setpoint, and then extended to +0.5 nm beyond the tunneling setpoint. The most notable feature of this data is the relative instability in the mechanics of the tip-sample junction on the Au(111) region compared to the C_{60} island. The force curves shown in Figure 2.22 (a) show small steps of discontinuities as the tip-sample junction rearranges, likely due to mobile molecules diffusing and rearranging. When the tip is pressed into the C_{60} island, Figure 2.22 (b), the force evolves much more continuously without the frequent jumps. The minimum of the force curve is reached for all of the C_{60} indentations, and it begins to become repulsive for approximately the same magnitude of current. The relative stability of the force profile on C_{60} compared to Au(111) is in support of the observation during imaging that the tip-sample junction rearranges much more readily over the Au(111) region.

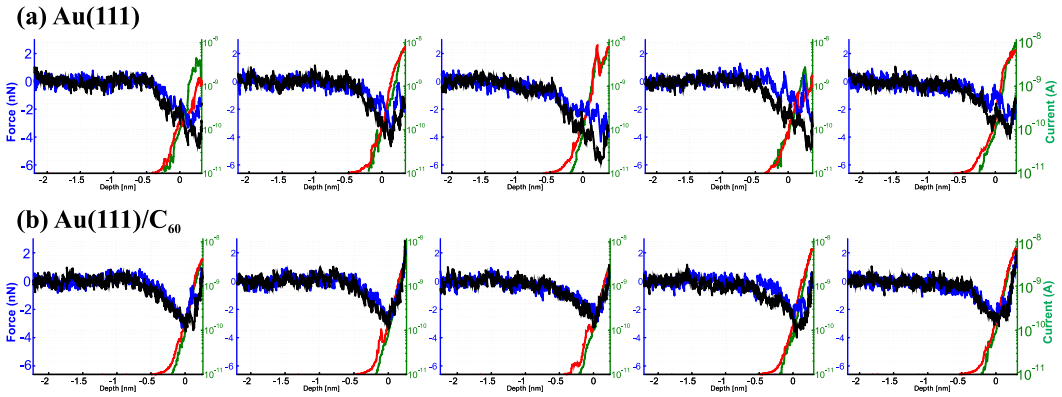

Figure 2.22: Five force- and current-displacement curves for (a) Au(111) and (b) C_{60} island regions shown in Figure 2.21 (g). Legend: Blue = force IN, Black = force OUT, Green = current IN, Red = current OUT.

The Au(111)-C_{60} system was left aside after work was steered toward nanomechanics with FIM tips after showing that the cryogenic performance of the microscope was inadequate for any reasonable measurements at 150 K to be performed, and that atomically defined tungsten FIM tips were not experimentally achievable with Au(111) substrates (Chapter 4). Simultaneous AFM/STM investigations of transport through a metal-C_{60}-metal junction may perhaps may be better achieved on another crystal surface at room temperature such as Cu(100) due to its larger atomic corrugation and correspondingly larger diffusion barriers.

2.7.4 Au(111)-graphene

The epitaxial growth of graphene layers on the Au(111) surface by physical vapour deposition (PVD) was recently reported: the first article introduced the new surface system and characterized it with low energy electron microscopy (LEEM), low energy electron diffraction (LEED), angle-resolved photoemission spectroscopy (ARPES), and STM [110], and a follow-up paper by the same authors addressed more in-depth STM characterization [111]. The sample preparation technique can be carried out in UHV, and over 95% of the graphene islands are shown to grow epitaxially with the Au(111) substrate. The graphene interacts relatively weakly with the Au(111) substrate, and the $22 \times \sqrt{3}$ reconstruction is still visible in STM with an additionally resolved graphene lattice and Moiré pattern from the mismatch between the graphene and Au(111) substrate lattices.

To date, the most popular means of obtaining graphene are mechanical exfoliation, thermal decomposition of SiC, and chemical vapour deposition (CVD) on polycrystalline copper [112]. PVD is virtually unheard of, and at the time of writing, the aforementioned Au(111)-graphene results are the only reports of graphene grown by PVD on a metal surface. Other UHV compatible techniques for preparation of graphene layers include the segregation of carbon from Ru(0001) [113] and the decomposition of hydrocarbons at elevated temperature on metal surfaces [114, 115] – it is notable that the latter technique predates the discovery of graphene itself.

As a possibly interesting new system to study in atomic-scale nanoindentation experiments, and having extensive experience with the Au(111) surface, we investigated the preparation of graphene on Au(111) on our cantilever beam samples. 1.5 mm diameter 99.997% purity graphite carbon rods (Goodfellow Inc.) were installed in our Omicron EFM-3T electron beam evaporator to be used as a vapor source of carbon. They were installed in all three pockets of the evaporator, as shown in Figure 2.23 (a). The first trial with existing filaments, built with the modified "open" design for crucible evaporation of C_{60}, required currents large enough to break the filaments (>2.3 A) before sufficient e-beam power was obtained for evaporation. In our experience, limiting the filament current to 2 A eliminates problems of filament failure (this safety limit can be set on the evaporator controller). Re-building the filaments as "crossed" spiral loops that are close to the carbon rod, ~3 mm judging by the 1.5 mm diameter of the rods in Figure 2.23 (a) allowed for sufficient e-beam power required to sublimate the carbon.

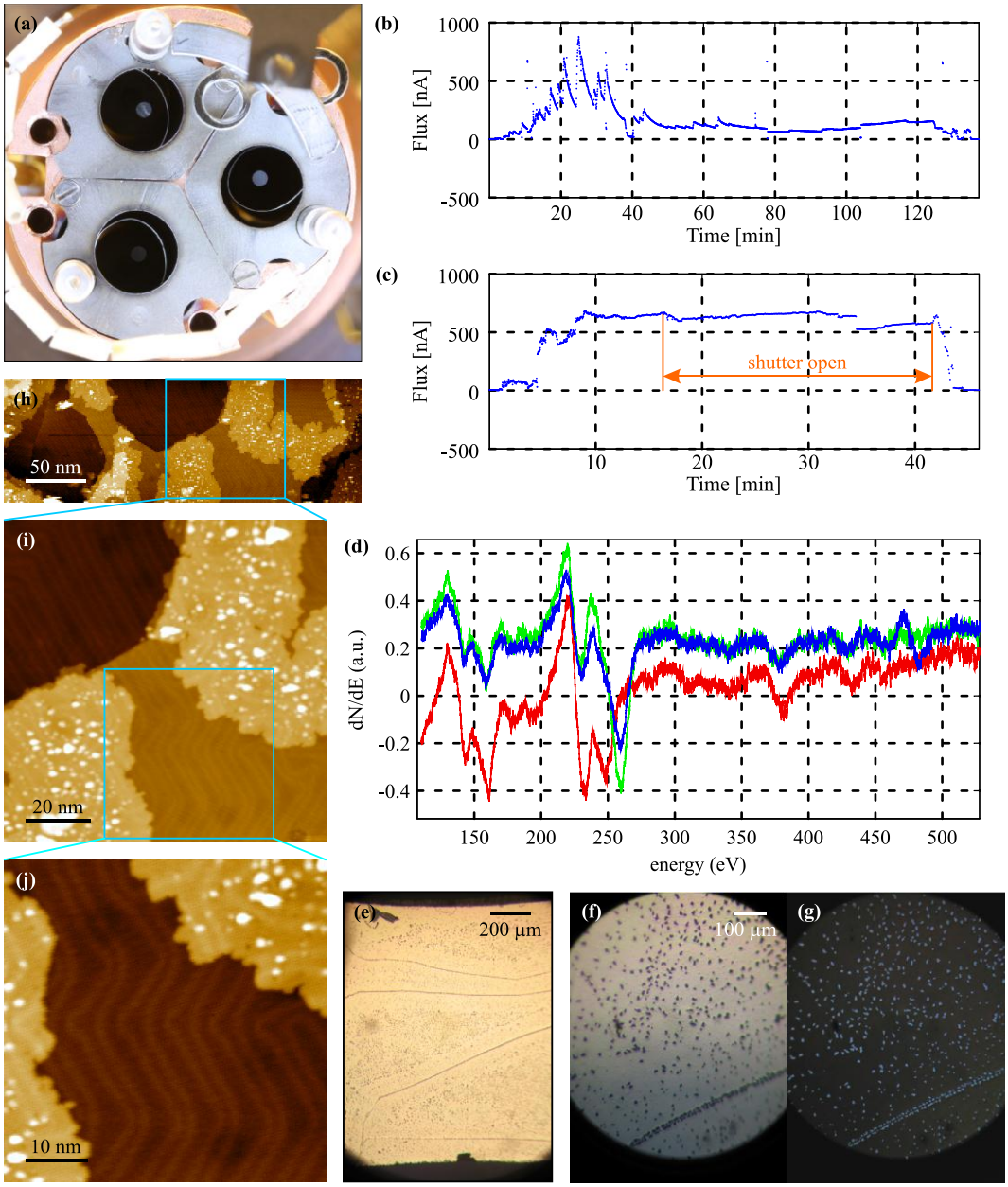

Figure 2.23: (a) Three pockets of the electron beam evaporator loaded with 1.5 mm graphite rods and "crossed" tungsten wire filaments positioned within 3mm of the rods. (b) Flux monitor reading during the initial degassing cycle of the carbon rod until a stable flux was obtained (deposition_20120625-161503). (c) Flux monitor reading during an evaporation with a total flux of 1e6 nA·s (deposition_20120724-121905). (d) AES showing clean gold (red), and large carbon peak after evaporation (green). An oxygen peak is revealed after excessive heating of the mica/gold cantilever beam (blue). (e), (f), (g) Optical microscope images of a damaged mica beam after excessive heating showing many ~5 µm pits in the Au film, especially visible in (g) which is backlit. (h), (i), (j) STM characterization of the carbon films. Imaging parameters: -0.7V, 12 pA (20120724, #076 #077, #078).

The initial e-beam heating of the carbon rods is shown in Figure 2.23 (b). As the rod heats up, a large ion flux is registered by the flux monitor which quickly decays

exponentially. The exponential decay is indicative of the degassing of the evaporant – one seeks to degas the material until a stable, non-decaying flux can be obtained. Here, the carbon rod is set to the maximum possible potential of 1000 V in order to minimize the filament current required for a given e-beam power. A stable, non-decaying flux is finally registered after around 80 min when the filament current is 1.69 A and the emission current is ~55 mA (for an e-beam power of 55 mA × 1000 V = 55 W).

Figure 2.23 (c) shows the flux monitor trace during a deposition to a total flux dose of 1×10^6 nA·s. The procedure described by Wofford *et al.* [110] requires heating of the substrate from 700 to 900 °C. We carried out the evaporation with the sample stage thermocouple reading 510 °C (a heater current of 1.98 A), however one expects the temperature of the cantilever beam to be greater than this because of its freestanding geometry over the heating element. AES is plotted in Figure 2.23 (d), indicating a clean gold surface before the evaporation (red) and a significant carbon signal after (green).

STM imaging indicates that ~25% of the Au(111) surface is covered with adsorbed material, shown in Figure 2.23 (h), (i), (j). The carbon islands contain disordered second layers, however in the well-ordered regions of the films, it is clear that the Au(111) herringbone reconstruction continues under the overlayer, as expected for a graphene film. This is best observed in Figure 2.23 (j). The islands have a height of 2.0 Å, compared to the 2.4 Å step height of Au(111). Resolution of a Moiré pattern between the island lattice and the Au(111) lattice was not observed suggesting that they are perhaps not well ordered at larger length scales. Resolution of the atomic structure within the islands could not be achieved. An ideal tool for characterization of these films would be low-energy electron diffraction (LEED), which would allow much quicker characterization of surface lattices in reciprocal space – unfortunately this doesn't exist in our sample preparation facilities.

We suspected that an increased sample temperature during evaporation would yield higher quality films, as suggested in Ref. [110]. Excessive heating of the sample led to visible damage of the mica beam resulting in a dull gold surface and a blistered and curled mica substrate. The decomposition of mica was systematically investigated by annealing the sample for ~30 min at progressively higher temperatures and AES was carried out at regular intervals. Annealing to 614 °C as measured on the sample stage (2.4 A heater current) seemed to be the highest safe annealing temperature, leading to no visible change in AES. Increasing to 636 °C (2.5 A) revealed an oxygen peak shown in the blue curve of

Figure 2.23 (d) appearing at ~480 eV[1]. Optical microscope images of the damaged samples are shown in Figure 2.23 (e), (f), (g). Small pits of ~5 μm lateral dimension have opened up in the Au film, likely due to the decomposition of the mica substrate. The bare areas are illuminated when the sample is backlit in Figure 2.23 (g). A quick image analysis in Matlab reveals that gold has been removed from ~ 7% of the sample's surface area.

Additional evaporations were carried out on Au(111) substrates heated to 614°C, but the surface qualities were very poor upon STM investigation, suggesting that perhaps some damage occurs even before direct observation in AES. Graphene on a metal surface is a promising sample for future atomic-scale nanoindentation experiments if a heat-resistant cantilever beam can be designed. A pure single crystal cantilever beam may fulfill this purpose. Another option is to mount the substrate of interest, such as a small Au or Cu single crystal, to a cantilever beam made out of a material able to withstand high temperature annealing (a refractory metal such as tungsten or molybdenum might suffice). Cantilever beams could possibly be produced in a manner similar to the mica beams but using sapphire (likely too stiff) or quartz as a substrate for evaporation of Au(111).

2.7.5 Cu(100)

The transfer of adatoms from the Au(111) substrate during STM with atomically defined tips, addressed in Chapter 4, stimulated the investigation of substrates with higher diffusion barriers so as to decrease the surface adatom population. Although adatom motion is not frozen out at room temperature, the copper adatoms on the Cu(100) surface are immobile below ~ 145 K, as determined by low-energy ion scattering (LEIS) [54, 116]. This temperature is perhaps accessible to our instrument if necessary. In addition, C_{60} molecules adsorbed to the Cu(100) surface are stationary at room temperature, allowing for submolecular resolution and well-defined contacts to the molecules [117].

A Cu(100) single crystal was purchased from SPL (Surface Preparation Laboratory, Zaandam, The Netherlands) to our specifications. Studies with bulk single crystals were new to the FIM/STM/AFM system, so a new sample holder was designed as a modification of our standard holders, shown in Figure 2.24 (a). The single crystal is clipped by one molybdenum clip to allow for low-stress thermal cycling. The sample surface is raised 1mm

[1] The actual oxygen peak energy is 503 eV, but the energy axis calibration depends on sample geometry as discussed in 2.7.2.

in height above the clip; this is done to minimize the effect of stresses produced by clamping at the clip on the sample's surface strictire. The raised surface also helps to reduce material transferred from other parts of the sample holder during the sputter cleaning process. The Cu(100) plane normal was oriented to within 0.1° of the polished top surface. The geometry of this sample is shown in Figure 2.24 (b) and (c).

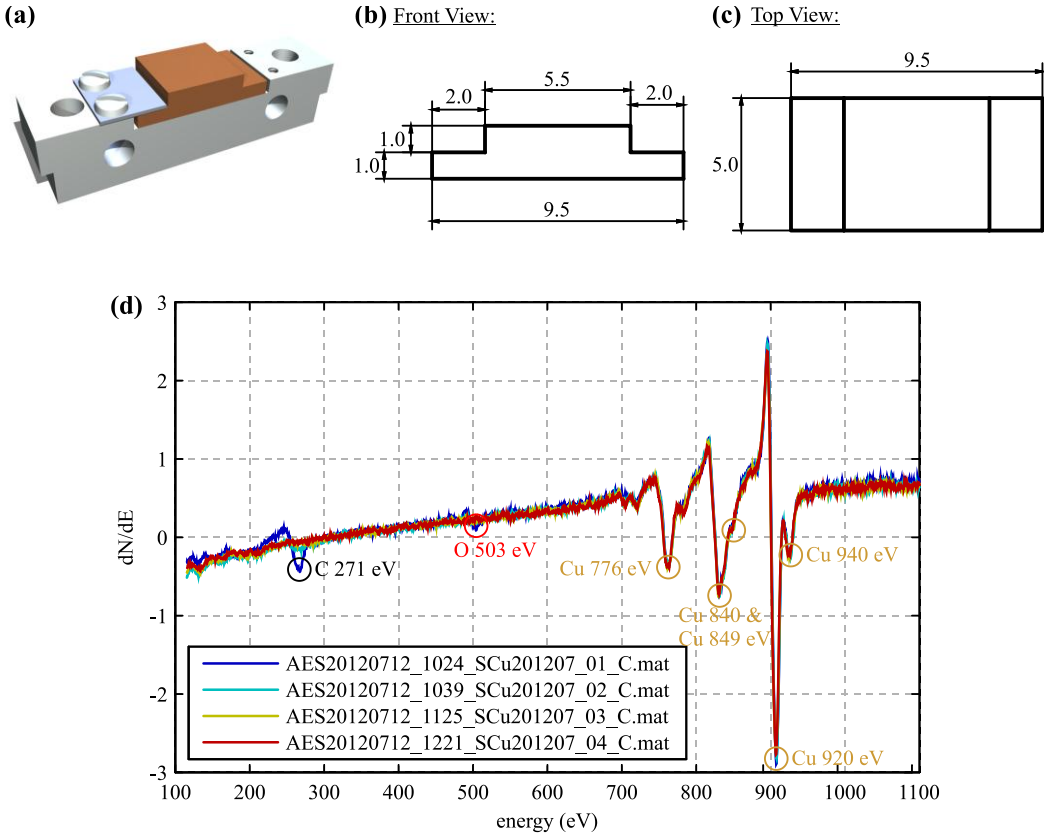

Figure 2.24: (a) Sample holder design for single crystals. (b) Front view of single crystal design, dimensions in mm. (c) Top view of single crystal. (d) AES on Cu(100) single crystal sample showing disappearance of the carbon and oxygen peaks after three sputtering cycles.

The surface is prepared by repeated cycles of Argon ion sputtering at 1 keV for several minutes (typically 5 min at 20 mA emission current) followed by annealing at ~375 °C for some tens of minutes (typically ~ 20 min). The Auger spectra shown in Figure 2.24 (d) correspond to the initial state of the sample after degassing overnight in UHV (dark blue), and after the first three sputtering cycles. Annealing the sample for an extended period of time (~1 hr) resulted in more C segregating to the surface (not shown). Many cycles of sputtering and annealing are necessary to remove the supply of contaminants stored in the bulk. Annealing in the presence of hydrogen or oxygen gas can help to expedite the removal of carbon and sulfur as they diffuse to the surface, however this was not performed.

After ~30 cycles of sputtering and annealing, the surface shows large atomic terraces, as shown in Figure 2.25. The step edges show some signs of residual contamination in Figure 2.25 (b) on the order of some two dozen atoms in the 150 × 150 nm field of view, corresponding to ~0.007% of the surface atoms. An indentation has been performed at the top of Figure 2.25 (b); the same indentation and two 5 × 5 indentation arrays below it are seen toward the right side of Figure 2.25 (a).

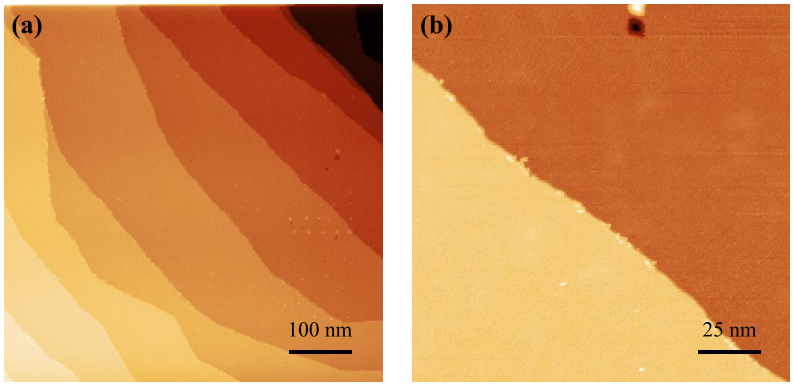

Figure 2.25: Constant current STM topography images of Cu(100) after > 25 sputter/anneal cycles. Imaging parameters: (a) -0.75 V, 6 pA 20121010#093 (b) -0.82 V, 9 pA 20121010#015

2.7.6 InSb(001)

InSb(001) surfaces were investigated as part of the search for substrates with different surface chemistry from Au(111) which might be appropriate for STM with atomically defined FIM tips at room temperature (the subject of Chapter 4). InSb(001) is the most well-suited surface of the III-V semiconductors to preparation by ion sputtering and annealing cycles [118]. One concern when preparing III-V surfaces is the loss of balanced surface stoichiometry due to the preferential depletion of the group V species yielding areas of different surface reconstructions driven by surface stoichiometry [119] – this can make surface preparation much more sensitive to the details of the sputtering and annealing procedures compared to pure metals [120].

A 10 × 10 × 0.45 mm piece of undoped InSb(001), polished on one side, was obtained from MTI Corp. The crystal was easily scribed and cleaved into smaller ~2 x 5 mm pieces which were mechanically clamped to sample holders, thoroughly rinsed in ethanol, dried with nitrogen, introduced into UHV, and degassed at 350 °C overnight (constant current control at 1.35 A). The sputtering and annealing procedure was based on the extensive work of the Szymonski group on this crystal surface [118, 120-125] as well as others [119, 126-129]. The sample temperature is increased to 400 °C (1.50 A current) and maintained

at this temperature throughout the sputtering and annealing cycles. Ar^+ ion sputtering at $P_{Ar} = 1 \times 10^{-5}$ Torr was carried out at 700 eV for a total of 30 minutes divided into 15 minutes at +60° from the sample normal, and 15 minutes at -60°. Annealing cycles lasted 60 minutes at the same temperature of 400 °C (in the absence of sputter gas). Carbon disappeared from AES after the first sputter-anneal cycle, and oxygen disappeared after three cycles.

A large scale STM image after four sputter-anneal cycles is shown in Figure 2.26 (a). Large regions of the well-known c(8 × 2) surface reconstruction cover most of the surface, and atomically flat terraces extend up to several hundred nanometers. The same sample after two days in UHV and another sputter-anneal cycle is shown in Figure 2.26 (b). These large scale STM images show a Moiré pattern due to spatial aliasing of the surface reconstruction periodicity with the pixels of the STM images. A minority of the surface, in regions marked by orange x's on these images, has a disordered surface reconstruction – perhaps an indium rich surface due to a loss of surface stoichiometry. Occasionally large, ~8 nm tall piles of unknown surface contamination are seen, as in the lower left of Figure 2.26 (b) – other than these, the surface is very well ordered.

STM images of the InSb(001) c(8 × 2) reconstruction are shown in Figure 2.26 (c) for positive and negative biases (+2.09 V, -2.09 V). The rows of the reconstruction run along the (110) direction, as indicated. The (8 × 2) surface unit cell is highlighted by the yellow rectangle (which is slightly skewed due to thermal drift). The contrast at positive and negative bias is markedly different, and is similar to STM contrasts seen in the literature referenced above. The topographic contrast change is due to imaging different local density of states derived from the In and Sb sites which may lie above or below the Fermi level. Due to the dependence on the tip electronic states, tip changes have a large effect on measured STM contrast, which adds to difficulty in image interpretation.

In Figure 2.26 (d), the (8 × 2) reconstruction covers most of the upper and lower terraces. On the lower terrace, two bright stripes extend diagonally across the image. These stripes correspond to domain boundaries between adjacent (8 × 2) reconstructed domains. An enlarged image of one of the domain boundaries is seen in Figure 2.26 (e), and further detailed in (f). It is apparent that the boundary between the (8 × 2) areas has a unique surface structure extending over 7 lattice sites in the $(1\bar{1}0)$ direction, and shows regular stripes with a 2× periodicity in the (110) direction, indicated in Figure 2.26 (f).

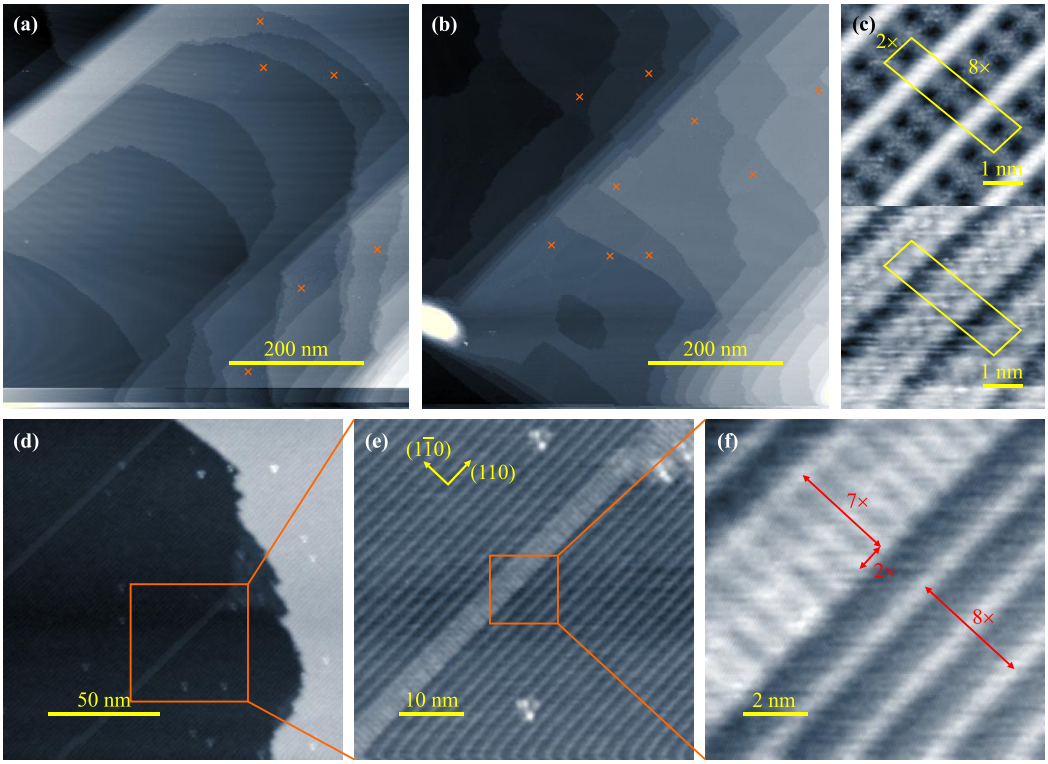

Figure 2.26: Constant current STM topography of the InSb(001) surface. Crosses in (a) and (b) indicate some of the regions which do *not* show the (8 × 2) reconstruction. The surface unit cell is shown in (c) for positive and negative bias. (d), (e), and (f) show the reconstruction, domain boundaries, and mobile point defect protrusions (see text for details). Imaging parameters: (a) 20120605#032 +2V 100pA, (b) 20120607#061 +2V 20pA, (c) top: 20120605#082 +2.09 V 1.2nA bottom: 20120605#087 -2.09 V 1.0nA (d) 20120607#037 +2V 24pA (e) 20120607#039 +2V 24pA (f) 20120607#043 +2V 120pA

Point defect protrusions are seen in the STM images of Figure 2.26 (d) and (e). The defects all have a similar structure repeated at each location, suggesting that this is a reverse image of the tip apex due to tip convolution. The location of the defects also changes on the surface between these two scan frames (4 minutes), however they are immobile enough to be imaged for several scan lines (a few seconds). The diffusion of these defects was identified after acquiring this data, so the mechanism or directionality of their motion has not been investigated, however it seems to happen on an experimentally observable timescale for STM.

2.7.7 Si(111)-2×1

In the search for alternative surface chemistries which would have an exceedingly low mobile adatom population (to investigate FIM tip integrity in STM experiments, the subject of Chapter 4), a reactive silicon surface seemed to be an ideal choice. However, its reliable preparation requires careful mounting to a sample holder, delicate control over flash annealing parameters, challenging thermometry, and extreme care in specimen handling in order to avoid contamination [130]. These are areas with which we had little practical experience, and the semiconductor surface preparation tools are not present on the preparation chamber geared toward ion sputtering and annealing of metal surfaces.

We therefore turned toward cleaved silicon samples and developed a reliable procedure for obtaining high quality Si(111)-2 × 1 surfaces. The technique is suitable for straightforward implementation in ultra-high vacuum surface science systems that are not explicitly designed to prepare semiconductor samples by either flash annealing or cleaving methods. The ease of sample preparation also makes these samples ideal starting points for the studies with the Si(111)-5 × 5 and 7 × 7 surfaces by subsequent annealing [131].

Due to the simplicity and reproducibility of preparing the cleaved Si(111)-2 × 1 samples, we also consider them very appropriate for testing STM functionality, a procedure often reserved for highly oriented pyrolytic graphite (HOPG). Two notable advantages for using Si(111)-2 × 1 samples over HOPG suggest themselves. Firstly, true atomic resolution can be verified, as opposed to lattice resolution obtained on HOPG by scanning commensurate carbon flakes over each other [132, 133]. Secondly, the tunneling gap is exceptionally stable and free of spikes resulting from the transfer of physisorbed species or carbon flakes.

Since the UHV system lacked a formal sample cleaving assembly, we began experimenting with different methods of mounting silicon wafer samples so that they could be cleaved using regular UHV manipulator arms. This required a sample that could be cleaved with a relatively low force to ensure that the manipulators were not damaged. In addition, the surface had to be homogeneously flat so that a STM tip could be coarse approached by monitoring its reflection in the sample. These requirements influenced our

choice of wafer orientation, sample size and method of scribing to initiate cleavage. The result of our successively refined sample preparation procedure is described below.

We start with a 0.26 mm thick, 2" diameter Si(111) wafer (Boron doped, 10-15 Ωcm), polished on the top side. Si(111) is chosen over Si(100) because the (111) cleavage plane is closer to perpendicular to the wafer's surface ($\theta_{(111)-(11\bar{1})} \simeq 70.5°$ whereas $\theta_{(100)-(111)} \simeq 54.7°$). We use a thin 0.26 mm wafer to reduce the force necessary to cleave the sample. The use of a Si(110) wafer would allow for a cleaved surface perpendicular to the wafer, however this crystal orientation is very difficult to obtain in thin wafers.

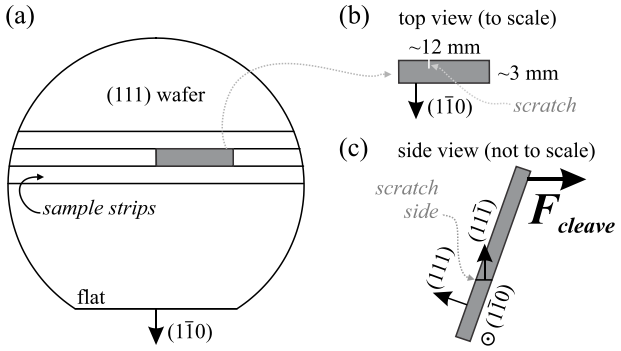

Figure 2.27: (a) The 2" diameter Si(111) wafer is sectioned into sample strips. The sample strips are further sectioned smaller pieces, shown in (b). (b) Top view of the ~12 x 3 mm sample pieces. The scratch used to initiate cleavage is shown as a white line. (c) Side view, where the orientation of the (1$\bar{1}$0) wafer flat points out of the page, and the (11$\bar{1}$) surface to be exposed by cleavage points upwards. The location of the scratch and direction of the cleavage force are indicated.

The Si(111) wafer is first sectioned into strips parallel to the (1$\bar{1}$0) primary flat with a width of ~3mm, as illustrated in Figure 2.21(a). These are cleaved by scoring the sample with a diamond scribe and partitioning them over the edge of a glass slide. The sample strips are then sectioned into ~12mm pieces, shown in Figure 2.21(b), by the same diamond scribing and cleaving process. Finally, a small scratch to initiate the cleavage is scored on the top (polished) side of the wafer using the diamond scribe. The scratch extends from the edge of the sample to a length of ~1mm, illustrated by the white line in Figure 2.21(b). KOH can also be used to create a notch in the wafer to initiate cleavage[134], but we have found scribed scratches to produce cleaved surfaces of sufficient quality. Some care should be taken to ensure the scratch is straight – use of a glass slide as a straight-edge is recommended over free-hand scribing.

A force applied as shown in Figure 2.21(c) will cleave the sample to expose the (11$\bar{1}$) plane as indicated. A force of only 0.25-0.35 N (25-35 grams) is required to initiate cleavage, as measured on a digital scale. The required force is sufficiently low that it can be

supplied by any convenient transfer arm or wobble stick in the UHV system, eliminating the need for a dedicated sample cleaving apparatus.

A photograph of the mounted sample is shown in Figure 2.28(a) along with the direction of the applied force. The sample is mounted on a custom sample holder designed to hold it at the appropriate 70.5° angle such that the cleavage plane is parallel to its top surface. The clamping system of the wafer piece is illustrated by a CAD rendering shown in Figure 2.28(d). The Si sample piece is clamped between two 3.5mm x 3.5 mm x 0.3 mm pieces of 430 stainless steel sheet metal. These clamping pieces help to prevent the brittle fracture of the sample when clamped by the set screw. An 18-8 stainless steel M2 conical point set screw provides the clamping force and a hole at the end of the sample holder allows access to the screw head. The prepared sample, with the small diamond scribe scratch, is shown in Figure 2.28(b) prior to mounting in the holder.

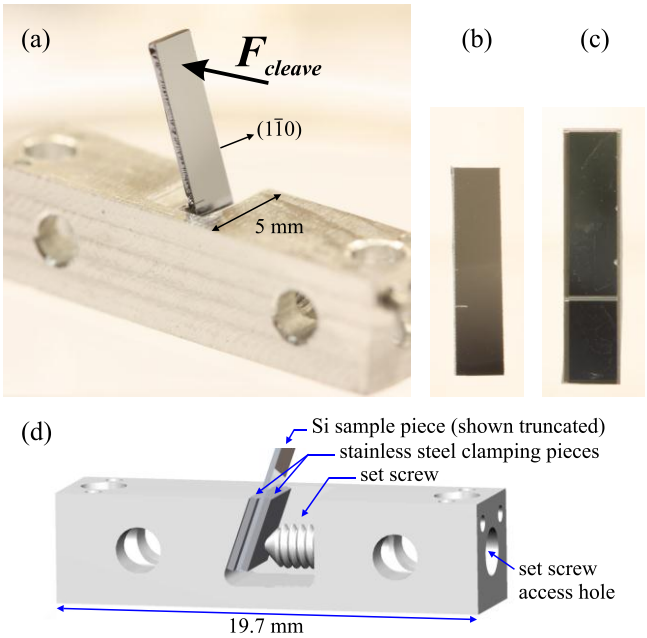

Figure 2.28: (a) Sample holder and mounted Si sample piece. (b) Si(111) sample piece with small scribed scratch to initiate cleavage. (c) Less successful Si(100) sample piece cut half-way through with diamond saw in an attempt to reduce cleavage force (see text). (d) CAD rendering of the sample holder showing details of the clamping system.

Initially, we investigated the possibility of using thicker wafers that were diced half-way through their thickness to reduce the force necessary for cleavage, as shown in Figure 2.28(c). Although the dicing was successful in reducing the cleavage force and in defining the location at which cleavage would occur, the surface quality was very poor because of the multitude of crack initiation points. The surfaces showed very small terraces, rarely

exceeding several nanometers, and were not macroscopically smooth over large distances, making STM tip approach (aligned by optical reflection) very difficult.

After loading into the UHV system, the samples are degassed overnight at ~220 °C. The samples are cooled to room temperature before cleaving to minimize drift once transferred to the STM. In order to cleave off the top portion of the wafer, the sample holder is first secured to our sample preparation stage. Then, a sample transfer fork attached to a 3 axis manipulator is used to cleave the wafer by pressing on the top edge in the direction indicated in Figure 2.28(a).

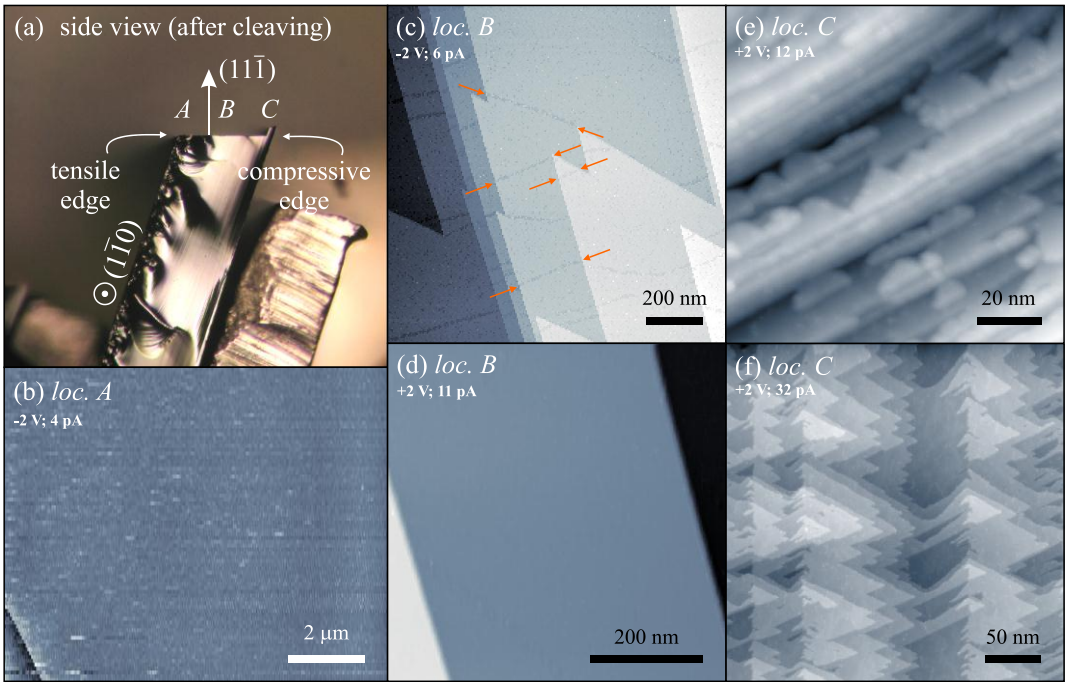

Figure 2.29: (a) Side view of sample after cleavage, in the same orientation as Figure 1(c). STM scan locations *A*, *B*, & *C* relative to the tensile and compressive edges are indicated. (b) Extremely large atomically flat terrace at location *A* extending > 10 µm, showing a single atomic step in the lower left corner. (c) and (d) Surface morphology near the center of the sample, location *B*. Arrows in (c) indicate antiphase boundaries of the reconstruction. (e) and (f) Surface morphology near the compressive edge, location *C*. STM imaging parameters indicate bias applied to the sample.

The surface topography is macroscopically rough near the scribed scratch used to initiate cleavage. At the side opposite the scratch, the surface is exceptionally smooth. We have performed STM within 1 mm from the edge opposite the scratch with excellent reproducibility. The cleaved Si(111) has a width of ~0.28 mm spanning from the tensile to the compressive edge of the sample (the force is applied by pushing on the tensile side). These edges are indicated in Figure 2.29(a).

We now briefly describe surface topographies observed at locations spanning from the tensile to compressive edges, labeled as locations *A*, *B*, and *C* on the side view of the cleaved edge in Figure 2.29(a). These are representative of topographic features observed in the half-dozen samples we have imaged by STM.

At location *A* near the tensile edge, extraordinarily large terraces are found, and can exceed 10 μm between atomic steps. Figure 2.29(b) presents a STM topograph showing a single atomic step in the lower left corner and a flat terrace exceeding 10 μm in size. The image has low resolution on the vertical axis in order to compensate for the long acquisition time needed for this scan size.

Near the center of the cleaved edge (location *B*), approximately equidistant between tensile and compressive edges, the atomic terraces show sizes on the order of hundreds of nanometers, as shown in Figure 2.29(c) and (d). The terraces in Figure 2.29(c) are separated by single atomic steps of height ~ 0.3 nm. In Figure 2.29(d), bunches of about ten steps separate atomically flat terraces. The terraces display the well-ordered 2 × 1 Pandey reconstruction [135] (not resolved at this scale), formed spontaneously upon cleavage. Antiphase boundaries between reconstructed domains are visible as darker lines which extend across terraces, highlighted by arrows in Figure 2.29(d). They are visible in this large scan frame because the domain boundaries are enlarged by rest gas molecules selectively binding to the more reactive sites at the edge of reconstructed domains. These stripes of adsorbed rest gases widen with time and eventually completely deplete the 2×1 reconstructed surface.

A rough estimation from sequential STM scans of the same area reveals that the coverage of adsorbed molecules (dark regions) expand from ~10% to ~28% over a delay of 1.5 hrs. Assuming that most of the UHV rest gas constituting the base pressure of $\sim 7\times10^{-11}$ mbar is H_2, we estimate a dose of ~0.9 L during this time (corrected for ionization gauge sensitivity for H_2 [136]) This estimation suggests a sticking coefficient, (0.28-0.10)/0.9 = 0.2, which is somewhat less than unity (neglecting gauge calibration, rest gas composition and surface binding site density).

At the compressive edge of the sample (location *C*), the surface generally shows much smaller terraces, often with small isolated single-layer high regions, seen in Figure 2.29(e) and (f). There is a larger local variability in surface structure around location *C* than locations *A* or *B*, but the surface may still be very appropriate for some surface studies.

Resolution of the 2×1 surface reconstruction is shown in the constant current STM image of Figure 2.30(a). A corrugation of ~50 pm is measured in the $(2\bar{1}\bar{1})$ direction and ~5 pm in the $(01\bar{1})$ direction at -1.94 V sample bias. Upon applying a positive sample bias of +2 V, the corrugation in the $(2\bar{1}\bar{1})$ direction is reduced somewhat to ~40 pm (image not shown).

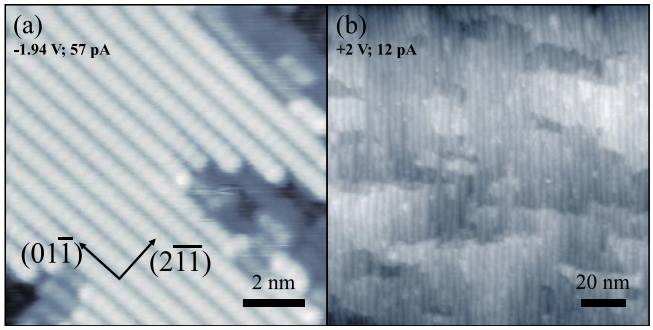

Figure 2.30: (a) Atomic resolution of the Si(111)-2 × 1 reconstruction. (b) Surface morphology of a more disordered region. STM imaging parameters indicate bias applied to the sample.

In a minority of locations of our STM studies, we have found areas that were not as well ordered as those described above. One such surface morphology is illustrated in Figure 2.30(b), consisting of a high density of steps with lateral size of ~ 3 nm and larger scale modulations of the stepped structure. Although this type of surface is less well-defined for surface science studies, STM scanning is very stable and safe – the disordered surface does not damage the integrity of the tip.

Using this preparation technique, high quality Si(111)-2 × 1 surfaces can be produced by cleavage of thin wafers. The method permits silicon surfaces to be prepared in UHV surface science systems that were not previously designed for preparation of semiconductor surfaces. The force required to initiate cleavage is suitably low such that it can be supplied by any convenient transfer arm in the UHV system. The cleaved samples show atomically flat terraces with lateral dimensions exceeding 10 μm near the tensile edge and on the order of hundreds on nanometers near the center of the sample.

2.8 Tip preparation

In the studies that follow, tungsten tips are used for FIM and SPM. Tungsten is both easily etched into sharp tips and atomically stable during imaging in the high electric fields of FIM at room temperature. We will briefly mention the tip preparation procedures used in

this work, discuss radius determination by ring counting in FIM, and present other tip preparation techniques which may be of interest for future work.

2.8.1 Etching and treatment in UHV

Tungsten tips for FIM and SPM experiments are etched in a 9M KOH solution by electrochemical etching at 3 V_{DC}. The procedure and a new design for an electrochemical bath was recently reported by our group [137], and very detailed accounts related to tip preparation can be found in the PhD thesis of Till Hagedorn [50] and the MSc work of Anne-Sophie Lucier [48, 62]. The typical concave shape of tungsten STM tips is shown in an optical microscope image in Figure 2.31 (a). This shape forms automatically during the etching process, having to do with the meniscus shape and currents in the etching solution around the tip shank. Routine success in creating sharp tips during etching is mostly dependent on obtaining a meniscus around the wire which is undisturbed by vibrations, bubbles, or debris in the etching solution, and a reliable electronic circuit which removes the applied bias when a sudden drop in electrochemical current is detected.

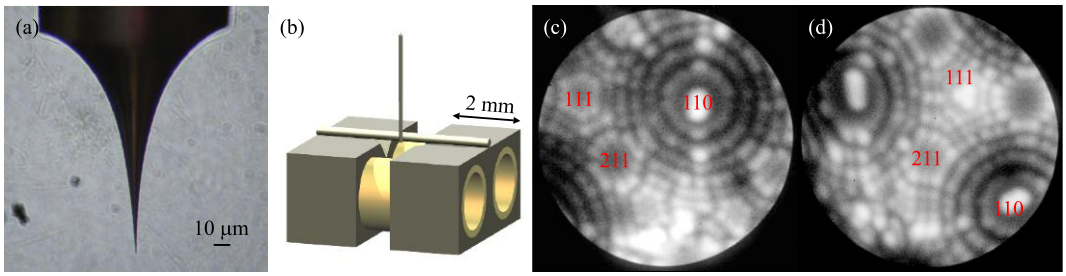

Figure 2.31: (a) optical microscope image of an electrochemically etched 0.125 mm tungsten wire; (b) tip holder design; (c) W(110) tip with a radius of 10.9 ± 0.8 nm; (d) W(111) tip with a radius of 10.3 ± 0.7 nm.

The etched tips are transferred to UHV and are annealed to an orange glow to remove the tungsten oxide layer and any physisorbed gas on their surfaces. The tip holder design, shown in Figure 2.31 (b), is particularly well suited for heating and degassing the entire tip wire. The tungsten tip wire is spot welded to a 0.25 mm diameter annealed 304 stainless steel wire (Alfa Aesar), which is in turn spot welded to the two electrically isolated halves of the tip holder. The stainless steel wire acts as a filament to resistively heat and degas the entire tungsten wire. Mounting tips to a filament is common in conventional FIM, implemented not only to clean the tips, but also in order to rapidly warm them momentarily from cryogenic temperatures to study diffusion of adatoms on their surfaces [53, 54].

After annealing, the tips are field emitted against a copper anode placed several mm from their apices. The voltage at which field emission occurs gives a good indication of their sharpness. Since electron emission necessitates a field of ~5 V/nm and ionization of helium gas requires a field of ~5 V/Å, when an appreciable field emission current (~100 nA) is observed at an applied voltage of < 1 kV, one can be confident that the tip is sufficiently sharp that an ion image can be obtained in FIM at an applied voltage of < 10 kV (the limit of our high voltage supply).

Tungsten tips with (110) and (111) apex orientations are used in these studies. W(110) tips result from etching 0.1 mm diameter polycrystalline wire (Alfa Aesar). Polycrystalline tungsten wire is highly textured from the cold drawing process and consists of long and thin ~1 × 50 μm grains oriented in the (110) direction to within a few degrees of its axis [138]. This strong crystallographic texture is common in all cold drawn bcc metals [139]. For our tips having typical apex radii of a few nm, the relevant part of the tip is effectively a single crystal. W(111) tips are etched from 0.125 mm diameter single crystal wire oriented to within 2° of the axis (Applied Physics Technologies).

FIM images of W(110) and W(111) tips are presented in Figure 2.31 (c) and (d) respectively. Low index crystal planes are identified in the micrographs. The planes are visually identified by their symmetry (two-fold or three-fold in these cases), their relative size and placement with respect to each other. Stereographic projection maps, such as the one published in Fig. 3.6 of Ref. [53], are helpful to identify the planes with respect to each other. The radii of the tips shown in Figure 2.31 are 10.9 ± 0.8 nm and 10.3 ± 0.7 nm respectively, as determined by averaging results from ring counting between all visible (110), (211) and (111) planes. The greyscale images were created using the green channel (the phosphorous screen glows green) of a RGB image obtained by averaging many individual photographs. Image contrast was adjusted using a logarithmic curve to help bring out features which are not otherwise visible in the dynamic range of print or computer displays. This processing technique seems to be unique, giving our FIM data a remarkably high printed quality.

2.8.2 Ring counting method in FIM

The most straightforward way to determine the radius of a FIM tip is to use the 'ring counting' method [53, 62, 140]. If one assumes that the apex of the tip has spherical envelope, one can count the number of atomic steps between crystallographic planes, which

show up as 'rings' in the FIM micrograph, and determine the radius by simple geometry (to follow). A spherical envelope is a good approximation within the region of the tip in which we are interested – ball models of tips created by cutting a bcc crystal in a hemisphere give good correspondence features seen in FIM images. It is worth noting that more elaborate techniques have been developed to extract the surface profile of FIM tips from features in micrographs [141, 142], essentially by using ring counting between various crystallographic poles to extract Cartesian (x, y, z) coordinates of the surface atoms. These are particularly useful if one is interested in determining the cross-sectional profile out into the far edges of the FIM image (which in our case is blocked by the aperture of the microscope cage).

Although the ring counting method is commonly used, there is still a wealth of examples appearing at conferences and in publications [143, 144] where authors (from several groups) are unable to correctly interpret features on FIM micrographs, resulting in a very large underestimation of tip radii. We now discuss where this problem arises in the context of ring counting. To proceed with ring counting, we choose a crystallographic direction (hkl) and count the number of rings n on the FIM image between (hkl) and another direction $(h'k'l')$, as shown in Figure 2.32.

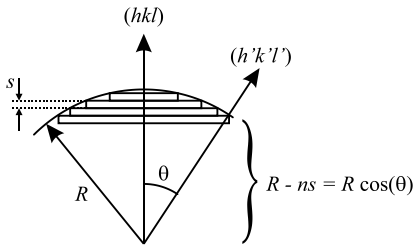

Figure 2.32: FIM tip apex with radius R showing geometry for ring counting. Planes of spacing *s* are normal to direction (*hkl*), and *n* rings are counted between poles (*hkl*) and (*h'k'l'*). The angle between these poles is θ.

Assuming a spherical envelope of the tip profile, and having calculated the plane spacing for planes perpendicular to (hkl) to be $s_{(hkl)}$, the local radius of curvature is given by

$$R = \frac{n s_{(hkl)}}{1 - \cos\theta}, \tag{32}$$

where θ is the angle between directions (hkl) and $(h'k'l')$.

Starting at the (111) pole in Figure 2.31 (d) and working over to the (110) pole, we count about 8 rings. A common error is to insert $n = 8$ into the above equation, along with the plane spacing $s_{(111)} = 0.912$ Å for the (111) direction of tungsten. As illustrated by the arrows in Figure 2.33, near the (111) pole, there exists one (111) plane per ring, but as the

angle increases toward (110), there are many more (111) planes per counted ring. The edges of individual (111) planes are no longer visible in FIM because they make up the smooth surface of the close packed (110) plane. This leads to a considerable underestimation of n, given our choice of $s_{(111)}$, and a correspondingly severe underestimation of the tip radius.

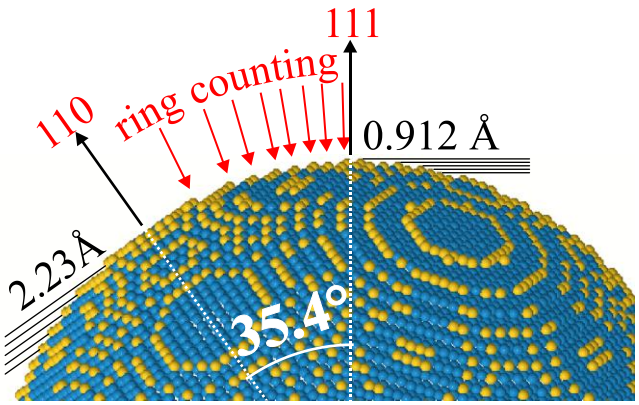

Figure 2.33: Ball model of a 9.95nm radius tip, illustrating (110) and (111) poles and interatomic plane spacings. Rings counted in the FIM image between these poles are indicated with arrows.

Carefully examining the ball model in Figure 2.33, it is apparent that there is a one-to-one correspondence between the rings and (110) planes. This is true for counting rings on relatively small tips between planes with relatively small angles between them – as tip radii increase, higher index planes become larger and start to mask individual steps, just as the (110) plane hid the (111) steps shown above. By creating a ball model of the tip, one can easily verify the correspondence between rings and single atomic steps. Good examples showing ring counting on very large tips can be found in [140].

An accurate estimation of the tip radius is achieved by using $s_{(110)} = 2.23$ Å and counting rings from the (110) axis to the (111) or (211). *Estimations from the ring counting method are only valid when the rings being counted correspond to single atomic steps*.

The average radius determined from the 6 pairs of (110)-(111) and (110)-(211) planes visible in the micrograph shown in Figure 2.31 (d) is 10.3 ± 0.7 nm. The features of this tip correspond well with those of the 9.95 nm ball model reconstruction.

To quickly estimate a tungsten tip radius in nm, one can simply multiply the number of rings from (110) to (211) by 1.66, or multiply the number of rings from (110) to (111) by 1.21 (these factors are $s_{(110)}/(1 - cos\theta)$). This inspires the mnemonic: "One one oh *to* one one one? Multiply by one two one!"

2.8.3 Other techniques – self-sputtering, N_2 etching and faceting

Here we briefly mention some investigations of other tip preparation techniques beyond the standard procedure of tungsten tip etching and FIM characterization. These techniques often appear in either the STM or FIM literature but have not enjoyed success in combined experiments, mainly because of the rarity of combined systems – there are many opportunities for cross-pollination, and we mention some of these relevant techniques below.

Self-sputtering is a technique often employed to clean or sharpen tips for STM [145-148], but its effect on their atomic-scale apex geometry is not well characterized. Self-sputtering is similar to ion milling (sputtering), but does not require a separate ion gun. It is carried out by applying a high negative potential to the tip which induces field emission of electrons from the tip apex into a low pressure of noble gas $\sim 10^{-5}$ Torr. The field emitted electrons ionize the gas atoms which then accelerate toward the tip under the applied field and bombard the surface. The process can be monitored by checking for a reduction in the field emission threshold which indicates an increase in tip sharpness.

We investigated the utility of this technique to sharpen tips which were not already suitably sharp for FIM. An indication that a tip is not suitably sharp is the lack of a field emission current when a potential up to -1 kV is applied to the tip since a potential above our 10 kV limit would be necessary to permit He ionization for FIM (section 2.8.1).

Starting with a rather blunt polycrystalline W(110) tip which field emitted 100 nA at 1100 V, we filled the UHV chamber to a pressure of 10^{-5} Torr of neon gas. At a potential of 950 V, a 50 μA current from self-sputtering was measured. The voltage applied to the tip was gradually lowered in order to keep the current stable to within a few μA. The self-sputtering was stopped once the tip reached 830 V at 50 μA. After removal of the neon gas, a 100 nA field emission current was registered at 590 V, suggesting that the tip became substantially sharper. The tip was then transferred to FIM.

A FIM micrograph of the tip apex is shown in Figure 2.34 (a). The three-fold symmetry of the (111) plane is apparent toward the top-left of the image, and the characteristic large flat (110) planes are located near the center of the image. Due to the projection geometry of the He ions being determined by the electric field, deviations from a regularly shaped smooth apex give rise to strong image distortions, making image interpretation very challenging. Due to the lack of annealing, there are many defects in this crystal which persist in Figure 2.34 (b) after evaporating several tens of layers of atoms from the tip.

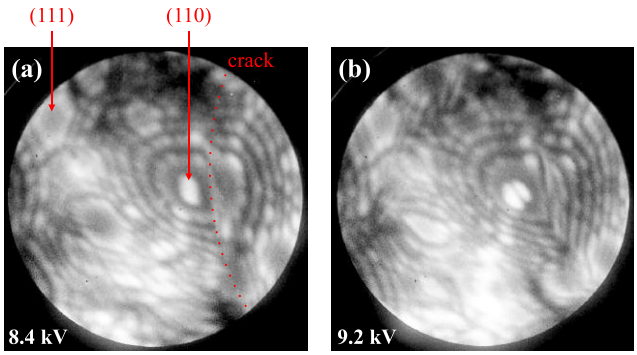

Figure 2.34: (a) FIM image of a (110) oriented tungsten tip after a self-sputtering sharpening procedure; (b) FIM image after evaporating several tens of atomic layers.

Although sharpening by self-sputtering allowed the tip to be imaged at < 10 kV, the atomic structure at the apex is far from regular. Such a locally deformed crystal structure could not have been characterized in SEM, and may also have been difficult in TEM due to the lack of periodicity of the atomic lattice across the whole tip apex. In some cases, self-sputtering may be desirable to adjust the mesoscopic tip radius to reduce long range forces during AFM imaging (section 2.4.2), but the damage to the atomic structure does not lend itself to facile characterization of the apex by FIM. For SPM experiments with well-defined tips, more regular structures are necessary.

Sharpening of tips using nitrogen gas is rather straightforward, and has been studied frequently in the context of building sharp tips for field ion emission for helium ion microscopes or electron emission for coherent electron sources and point projection microscopes. The sharpening process was discovered by Rezeq *et al.* [149], and patented by the same authors in 2008 [150].

The process occurs by adsorption of nitrogen on the tungsten tip shank, illustrated in Figure 2.35. The nitrogen cannot bind to the very apex of the tip because the electric field is too large – the gas is ionized and repelled before it can react with the tip. Nitrogen can, however, bind to the shank of the tip where the field is not as high. This happens by dissociative adsorption in which a single nitrogen atom forms a chemical bond to a tungsten atom on the tip's surface (this is discussed in Chapter 4 and is addressed specifically in Refs. [151, 152]). The W-N bond weakens the W atom's bond to its neighbours and lowers the field necessary to evaporate the W-N complex (this is well established in the FIM literature, but the burial of the N atoms under 'protruding W atoms' as shown in the patent illustration in Figure 2.35 (b) seems to be nothing more than speculation on the part of the inventors of nitrogen etching).

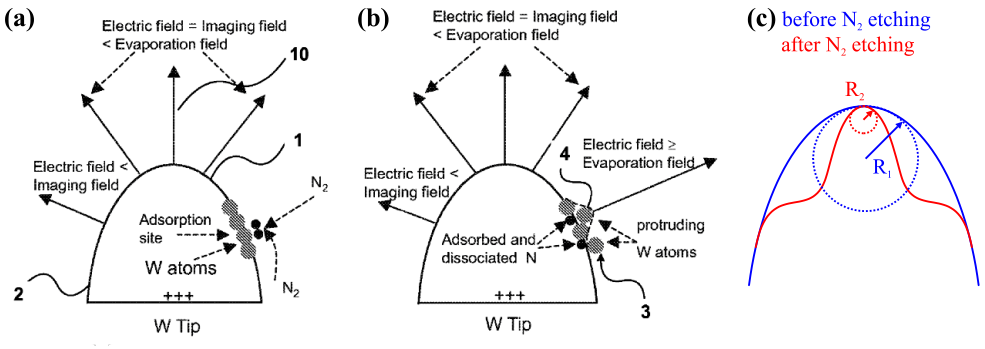

Figure 2.35: Schematic description of the sharpening process. (a) N_2 can only adsorb to the tip shank where the field is lower than at the apex. (b) The W-N bond weakens the bonding of the W atoms to the tip, and they field evaporate, leading to a preferential loss of material around the tip shank. (a) and (b) Public domain illustration from Ref. [150]. (c) Tip profile before etching (blue), and after (red), illustrating a reduction in local radius of curvature at the apex and the final 'shouldered' shape of the tip.

The weakened tungsten atoms are thus etched by preferential field evaporation from the tip shank. The resulting reduction in the local radius of curvature of the tip apex is illustrated in Figure 2.35 (c). The final profile of the tip is somewhat different than the original: a shoulder is formed where the field on the shank is no longer strong enough to evaporate the W-N (experimentally verified by SEM in [144]). At its apex, the radius is highly reduced and can be etched to terminate in a single atom.

One distinct advantage of this tip sharpening technique is that it can be monitored by helium ion FIM imaging during the etching process. A few experiments in nitrogen tip sharpening were performed with Moh'd Rezeq during his stay in Montréal for a few weeks in summer 2010. Implementing nitrogen etching on our system was not easy – in fact it required several strange workarounds which we were not expecting from our initial discussions with Dr. Rezeq. Firstly, a turbo pump must be continuously pumping the He and N_2 gases from the system so that the N_2 concentration can be lowered as required in order to regulate the etching rate. Our heated quartz tube used to supply ultra-pure He cannot produce a sufficient flux to maintain 10^{-5} Torr of imaging gas in the vacuum system while pumping. We sacrificed the imaging gas purity in this experiment and introduced He through an extra (borrowed) leak valve attached to the UHV system's load lock which was especially baked for this occasion. The gas line typically supplying noble gases to a leak valve for sputter cleaning of surfaces was vented to N_2 gas for this occasion. All gate valves between the airlock, preparation and measurement chambers were opened in order to supply the gases to the FIM in the measurement chamber.

The results of this setup are a few awkwardly controlled tip sharpening experiments that nonetheless show that in principle the technique works. In addition, this was its first demonstration on a W(111) tip (previous experiments were performed on W(110) tips).

Figure 2.36 (a)-(e) shows a sequence of FIM images during nitrogen sharpening of a W(111) tip, beginning at a radius of ~5.5 nm, and ending with a radius of ~3.6 nm by image (d). The applied voltage was reduced as necessary to slow evaporation of the tip apex while the apex radius decreased. In this experiment, the nitrogen pressure was constant at 5×10^{-7} Torr (before we had installed an extra leak valve to allow it to be independently controlled). We suspected that it was necessary to lower the nitrogen pressure since the tip apex was continuously evaporating.

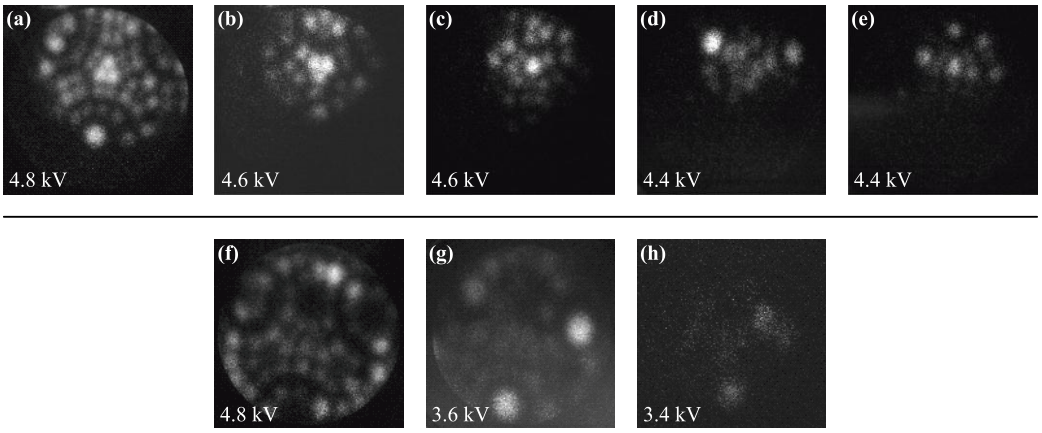

Figure 2.36: (a)-(e) Sequence of FIM images during nitrogen etching at 5×10^{-7} Torr N_2, constant pressure; (f)-(h) Sequence of FIM images during nitrogen etching where nitrogen pressure was reduced from 5×10^{-7} Torr to 3×10^{-8} Torr.

With the intent of stabilizing the final tip structure, the extra leak valve was installed to control the nitrogen pressure, but at this point, the bellows of a wobble stick on the system began leaking and limited the background nitrogen pressure to $\sim 3 \times 10^{-8}$ Torr (ironically, a vacuum leak is what led to the initial discovery of nitrogen sharpened tips). The controllable nitrogen pressure, despite the atmospheric leak background, yielded a somewhat sharper tip with notably larger magnification of the image in Figure 2.36 (f)-(h).

The atomic geometry of the apex could not be stabilized either due to (1) the ever-present background pressure of nitrogen from the leak, or (2) the lack of cryogenic cooling of our tip, which was present in previous nitrogen etching studies.

Practically, nitrogen etching results in a reliable sharpening of tip apices, however the process is difficult to implement and requires separate control of helium and nitrogen gas pressures, and may require cryogenic temperatures if single atom tips are desired. This

may serve as a useful technique to produce tips of varying radii for nanomechanics studies, however the uncharacterizable shape of the tip shoulder (Figure 2.35 (c)) could present difficulties in understanding the mechanical properties of the tip apex. The technique is certainly useful for experiments with atomically defined SPM junctions if single atom tips can be stabilized.

Faceting of crystal surfaces is another potentially valuable technique for obtaining single-atom sharp tips for SPM experiments. Many crystal surfaces can exhibit faceting – the general principle is to anneal the crystal surface in the presence of an adsorbed thin layer of another material or in an applied electric field. The modified condition under which the surface annealed is chosen to thermodynamically favour the growth of some crystal planes over others, and can thereby result in the formation of atomically sharp nano-pyramids.

Many of the initial surface science investigations of faceting systems such as the W(111) surface under adsorbed Pd (as well as other noble metals), W(111) under oxygen, and Ir(210) under oxygen were developed by Ted Madey's group under LEED and STM investigation of the surfaces of bulk crystals [153-155]. Tien T. Tsong, who worked on FIM from its inception, has done much recent work in transferring Madey's surface science systems to the apices of sharp FIM tips in order to form faceted single atom tips [156-163]. All of these studies with exception of the Ir(210) tips, involve the expansion of the (211) planes on a W(111) tip until its apex becomes a three-sided pyramid formed by the intersecting (211) planes (for reference a W(111) tip can be seen in Figure 2.31 (d)). The faceting of the Ir(210) surface under oxygen exposure forms a pyramid from the (311), $(31\bar{1})$, and (110) planes with a single atom apex pointed in the (210) direction [162].

Tip faceting by thermofield annealing (annealing under a large electric field) favours the growth of large (110) terraces. Applied to a W(111) tip, it can be used to create a pyramid in the opposite manner as described for noble metal plating – the (110) terraces expand until they intersect to form a three-sided pyramid at the expense of the (211) planes [164-167]. Thermofield annealing has the advantage of being carried out without the need of an ad-layer of oxygen or metal to be present on the tip surface.

The etching of iridium tips was given as a summer project to undergraduate student Jean-Benoît Lalanne under my supervision. Iridium tips have the possibility of surface faceting, but also provide an alternative material for fabrication of STM tips with different surface chemistry – iridium is much more inert than tungsten and is less reactive with rest

gas atoms in UHV. In addition, the atomic geometry of crystal planes arising in fcc iridium is very different than those in bcc tungsten.

An etching procedure for iridium tips was refined using $CaCl_2$ solution, which is relatively harmless compared to common molten salt solutions as we report in Ref. [60]. An electrochemically etched iridium tip is shown in SEM in Figure 2.37 (a) and (b). FIM reveals an apex radius of 16 ± 2 nm in Figure 2.37 (c), and the crystallographic directions on the surface are labeled in the ball model reconstruction in Figure 2.37 (d).

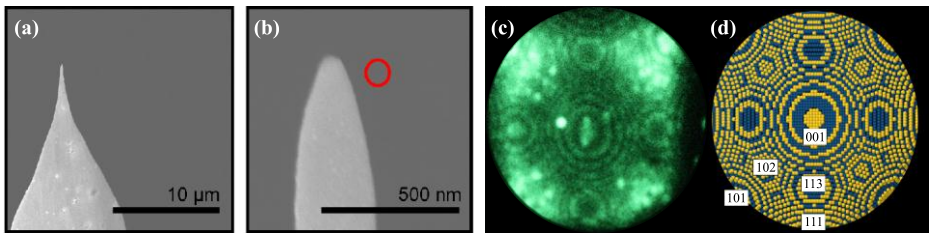

Figure 2.37: (a), (b) SEM micrographs of an iridium tip. (c) FIM image of a Ir(001) tip taken in 1×10^{-5} mbar Ne imaging gas at 8.5 kV. (d) FCC ball model of the (001) oriented tip

Practically, iridium is not a convenient tip material for our microscope: although He ion micrographs exist in the FIM literature [53], we could not obtain one at room temperature without continuously field evaporating material from the tip. Whereas the field required to evaporate tungsten atoms from tips is 5.2 V/Å, a field of only 4.4 V/Å is necessary to evaporate iridium [53], which is effectively identical to the best imaging field required to produce a He micrograph. Apparently He can be used to image iridium at cryogenic temperatures, but not at room temperature. We switched the imaging gas to neon, with a best imaging field of 3.7 V/Å, to obtain the FIM image shown in Figure 2.37 (c).

To summarize, we have investigated a number of possible techniques for the modification and engineering of the atomic structures of SPM probes. They come in different degrees of complexity and have different limitations based on material field evaporation, required control over gases, ad-layer deposition etc. A recent theoretical study has shown that iridium-coated W(111) faceted tips should be able to withstand electric fields required for FIM with He gas [168] at room temperature, overcoming many of the problems discussed previously. The pyramidal geometry of these tips would be of considerable interest not only for atomically defined SPM experiments but also in atomic-scale nanoindentation experiments due to the simple relationship between their projected contact area and penetration depth.

3. Focus on low noise and systematic reliability

Figure 3.1 (a) shows a histogram of the number of SPM images saved as a function of time of day, inspired by Stephen Wolfram's recent blog post on "The Personal Analytics of My Life" [169]. It appears from the histogram that typically no measurements occur during the morning between ~6 and ~11 am, possibly due to the time it takes to get a surface science sample freshly prepared and transferred to the SPM or a general lack of enthusiasm for this time of day. A pre-dinner-time peak reflects the rush to quickly characterize samples to see if they are worth measuring later on. After the dinnertime lull, a rapid onset of data collection occurs at ~11 pm. Why? Because the building ventilation turns off at 9 pm, and it always takes a little longer than anticipated to get the sample set up. The effect of the 9 pm ventilation shutdown on the detection noise of the tunneling current is shown in Figure 3.1 (b). The largest and lowest frequency detection noise peak at 14.2 Hz disappears when the ventilation turns off. For daytime STM, it contributes to a severe modulation of the topographic signal, and it is impractical to scan sufficiently slowly to average out several cycles of this noise in each scan pixel.

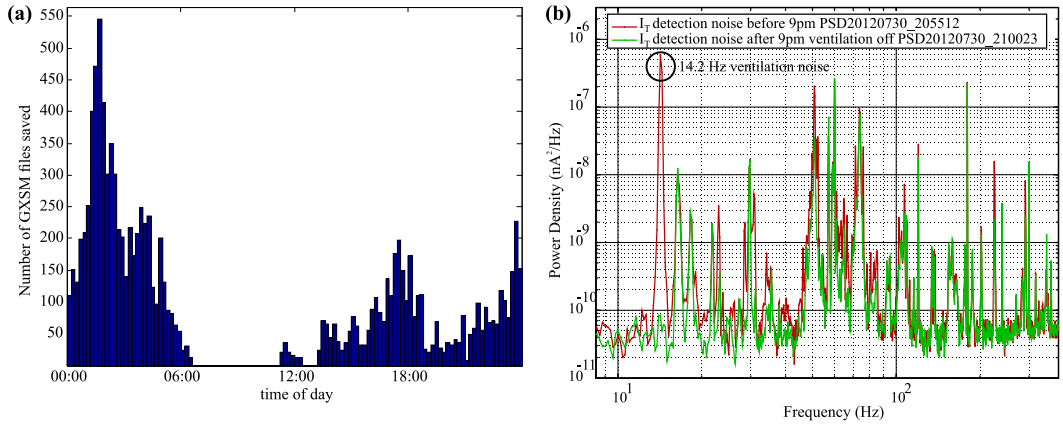

Figure 3.1: (a) Histogram showing the number of SPM images saved as a function of time of day since August 2011.

The ventilation noise is out of our direct control, but we can deal with it by measuring at times of day when it is off (the peak of the histogram is at ~2 am). Fortunately, there are many other instrumentation advances that have improved the quality of our data, independent of the time of day. Improvements to the detection noise and mechanical noise in SPM, and the renovation of the FIM to remedy problems of high voltage discharging will be discussed in this chapter. After carrying out these system improvements, everyday

reliability has improved remarkably. Successful FIM-STM-AFM measurements are now routinely, rather than exceptionally, possible.

It seems that there is little opportunity to relay progress in noise performance and reliability of SPMs, perhaps for some of the following reasons: These improvements are somewhat incremental and too specific for reporting in journals specializing in scientific instrumentation; this type of work is often carried out by lab technicians, postdocs or research associates, meaning that there is no documentation of the work in a thesis; some groups also attempt to maintain a scientific advantage by promoting secrecy regarding instrumentation or techniques. These improvements are absolutely central to enable experiments to be carried out – they are presented here in the hope that the results will facilitate others in their understanding of noise and debugging of SPM systems and help accelerate the progress of related science.

Improving detection noise in a complex experimental apparatus involving sensitive detection electronics, power electronics such as vacuum pumps, and several computers is challenging due to the multitude of possible noise sources and the burden involved in identifying them. Practically, this means stopping vacuum pumps, or unplugging some of the $\sim 10^2$ electrical components to check their effect on power spectra. Often, the same noise symptoms are caused by multiple sources. For example, noise power at line frequencies (60 Hz and harmonics) on the tunneling current signal might be caused by a combination of sources such as:

- capacitive coupling from voltage noise on nearby electrodes
- improper grounding in the tip-sample circuit
- improper grounding of other equipment connected to the vacuum system

Until the most severe noise source is found, other sources cannot be identified as they are masked under the most prominent source. Immediate improvements in noise performance are difficult to make because of this complexity: noise improvement tends to be a slow and iterative process.

In the first section, we will introduce a noise map for the SPM. This will serve to define the types of noise which will be discussed in the sections that follow. The sections on STM and AFM noise start by introducing the fundamental physical limits for current and force detection, then discuss practical detection noise limits in our experimental implementation, and present a summary of significant advances in understanding of the experimental apparatus and noise reduction. A section is devoted to mechanical noise in the tip sample

junction derived from several origins, and these sources are discussed with particular emphasis on their detrimental effect on measurements with cantilevered samples. Finally, a section on high voltage discharging in FIM presents advances in new custom high voltage coaxial wiring, vacuum breakdown elimination and data acquisition.

3.1 Noise map for combined STM and AFM

The combined current and force detection in this experimental setup makes the instrument much more complex than standard AFM or STM systems. Individual sources of noise are difficult to distinguish at first glance; it is therefore useful to lay out a framework based on the individual sources and the interplay between them. To facilitate the following discussion about noise sources and strategies for improving detection noise and system reliability, we start by presenting a map of the various noise sources in Figure 3.2.

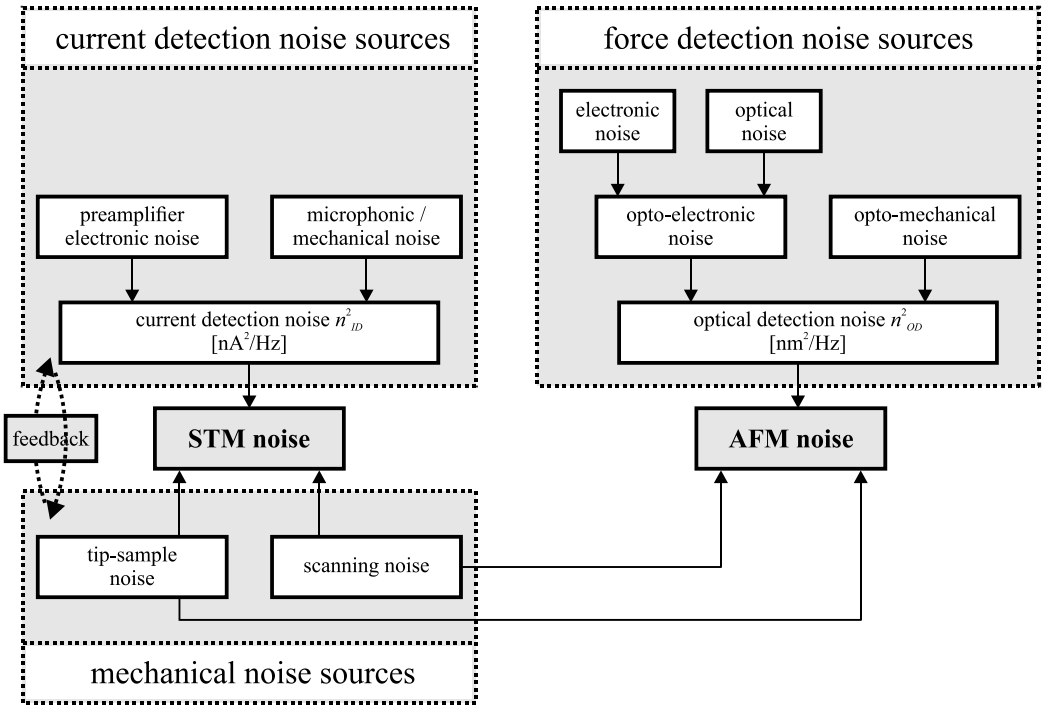

Figure 3.2: Schematic breakdown of noise sources affecting measurements in the combined STM/AFM system. This figure is adapted to the current system but is much inspired by work done with Aleks Labuda in designing an AFM for Prof. Roland Bennewitz several years ago at McGill [170].

First, it is useful to distinguish sources of detection noise from sources of mechanical noise in SPM experiments. The detection noise sources (shown in the upper portion of Figure 3.2) have to do with everything related to the detection of either currents or forces: the electronic noise of preamplifiers, the optical noise due to the laser required for

interferometry, any capacitively coupled currents, mechanical vibrations in the optical path, etc. Mechanical noise sources (shown in the lower part of Figure 3.2) contribute to true measurable current and force modulations in the tip-sample junction due to a mechanical noise. Mechanical noise sources are broken down into tip-sample noise and scanning noise; the former has to do with unwanted vibrations between the tip and sample, and the latter has to do with the atomic structure of the junction being altered by tip-sample interactions while performing an experiment. We will concern ourselves here with mechanical noise of the first type only.

Performing an experiment under feedback couples the detection and mechanical noise sources[1]. An example of this could be a 180 Hz line noise peak in the current detection noise, which under feedback, is converted into a 180 Hz modulation of the tip-sample distance (a mechanical noise). In turn, this modulation of the tip-sample distance will modulate forces in the tip-sample junction and will be detected in the force signal. When uncertainty exists regarding the source of a suspected mechanical noise, a very useful procedure is to lower or eliminate feedback to determine if the mechanical noise is sourced from detection noise.

3.2 Scanning tunneling microscopy

This section concerns itself with understanding and eliminating sources of noise in the detection of the tip-sample current in STM. We start by discussing the theoretical limit of current detection given by the Johnson noise of the large transimpedance resistor required to convert small currents into measurable voltage signals. We point out that in practice, it is quite difficult to reach this limit due to capacitively coupled mechanical and acoustic noise. The detection and de-tuning of radio noise on the tunneling current is demonstrated, followed by a discussion on grounding in the tip-sample circuit and techniques used to avoid ground loops. Noise coupled capacitively from nearby electrodes was quenched and the acoustic pickup of the current preamplifier was also improved. We conclude with a section on ground loops emerging from the poor grounding of equipment in multiple electrical circuits and the non-ideal grounding of piezo motor signals.

[1] In our case feedback is only implemented on the current channel.

3.2.1 Current detection noise limit

In STM, current is detected using a transimpedance amplifier, typically employing a large resistor on the order of 10^9 Ω by which small currents (~1 nA) are converted into measurable (~1 V) voltages. The dominant sources of noise in the detection of tunneling currents are the Johnson noise of the larger resistor, and the input noise of the opamp [72]. For a 10^9 Ω resistor, the Johnson noise amounts to $n_V = \sqrt{4k_B TR} \approx 4\ \mu\text{V}/\sqrt{\text{Hz}}$, corresponding to an equivalent current detection noise of $n_I = n_V/R \approx 4\ \text{fA}/\sqrt{\text{Hz}}$. As long as the selected opamp's input current and voltage noises are below several $\text{fA}/\sqrt{\text{Hz}}$ and $\mu\text{V}/\sqrt{\text{Hz}}$, it is relatively straightforward to build a transimpedance amplifier with a detection noise floor limited by Johnson noise of some $\text{fA}/\sqrt{\text{Hz}}$. A typical choice for a STM preamplifier opamp is the Burr-Brown (now Texas Instruments) OPA111 having low input current and voltage noises of ~0.5 $\text{fA}/\sqrt{\text{Hz}}$ and ~10 $\text{nV}/\sqrt{\text{Hz}}$.

The design of such amplifiers for STM applications has been the subject of many instrumentation papers: besides standard designs [171], certain authors have come up with innovative methods to increase bandwidth with a compensation circuit [172], lower Johnson noise by cooling the feedback resistor [173], or implement discrete junction FETs for the input stage which can operate at low temperature without degradation of performance due to loss of minority carriers [174]. Regardless of one's choice of circuit design, the difficult part is figuring out how to connect the amplifier to the STM tip without adding excess noise above the detection limit.

The current detection noise, n_{ID}^2 in Figure 3.2, is made up of the preamplifier's electronic noise (mostly Johnson noise of the resistor), and any additional microphonic/mechanical noise due to its connection to the STM. Figure 3.3 illustrates the current detection noise in red. The blue line corresponds to the expected Johnson noise limit. In some regions along the frequency axis, the red curve falls very close to this limit[1], but there exist many excess noise peaks arising from electronic and mechanical sources. Disconnecting the preamplifier from the STM shows that the electronic noise of the preamplifier is indeed much lower than the current detection noise.

[1] These quiet frequency regions are particularly valuable for lock-in measurements.

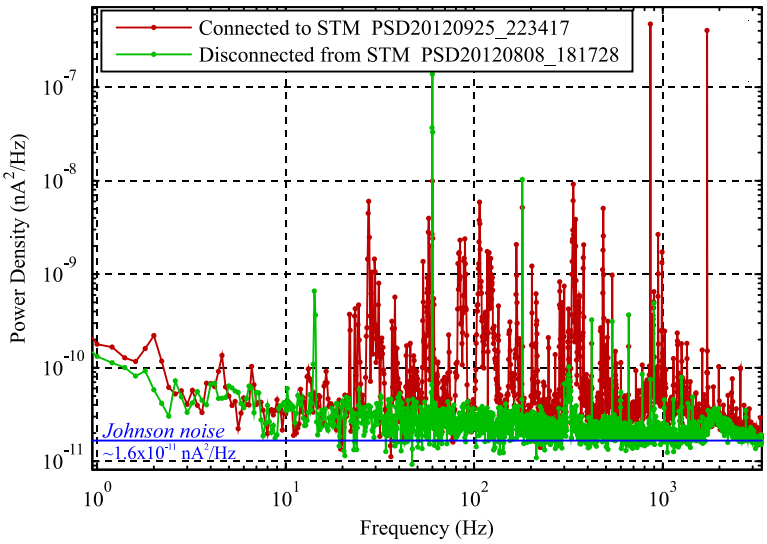

Figure 3.3: Power spectral density of the current detection noise with STM preamplifier connected to the microscope (red). When disconnected (green) it is apparent that the electronic noise of the amplifier itself is much lower than the additional microphonic / mechanical peaks. The Johnson noise set by the 10^9 Ω feedback resistor is shown by the blue line.

3.2.2 Tip-sample circuit integrity

Much of the duration of a STM experiment is spent with the tip-sample distance controlled under constant current feedback. Feedback is disabled during some measurements such as distance spectroscopy, I(z), or voltage spectroscopy, I(V), but between such measurements the tip returns to some feedback controlled set-point. Feedback is also employed during constant current topographic STM imaging. The integrity of the tip-sample circuit is therefore of extreme importance: if the tunneling current ever cuts out momentarily, the feedback controller will attempt to compensate by decreasing the tip-sample distance until the current set-point is found. This is a very dangerous situation, especially when performing an experiment dependent upon a well-defined tip apex characterized in FIM. The entire signal path from the bias voltage source to the sample[1], and from the tip to the amplifier and data acquisition equipment must be flawlessly robust.

[1] This signal path is somewhat less critical – even if the bias voltage is lost, typically when the tip is approached close enough, there will be some noise current picked up due to noise on the floating sample potential with respect to the current preamplifier's reference. This AC noise current is rectified by the feedback controller which will eventually stop the tip crash. The tip will likely not crash as far as in the case of no current being detected at all.

It is advisable to routinely check this signal path for any intermittent connections. Particularly problematic has been the connection of the current preamplifier to the vacuum feedthrough – sometimes the female MHV connector socket must be reshaped with pliers to provide a better connection, also new adapters with better spring-loaded connections from Pasternack Enterprises proved to greatly enhance reliability.

3.2.3 Radio detuning

A tunneling current noise power spectrum is shown in Figure 3.4 – the red curve illustrates the typical detection noise present in the system before December 2010. The acquisition of power spectra was common before this date, and the shape of the red curve was very familiar: a large, broadband detection noise hump across 100-2500 Hz which fell off with the bandwidth of the preamplifier. This noise is right in the middle of relevant STM signal bandwidth. Several attempts to figure out what contributed to this noise hump were made by unplugging various pieces of connected equipment suspected to be sources of noise, as well as attempting to run the preamplifier on battery power. The detection noise could not be improved.

Upon connecting the tunneling current signal to amplified audio speakers, it became immediately obvious that this large bandwidth of detection noise was coming from the radio. The radio station is not really identifiable – it sounds as if there is perhaps more than one station competing on a weak signal. It is also not clear what non-linear element in the tunneling current detection system contributes to the demodulation of the radio signal (which must be AM, as FM demodulation requires a phase locked loop). The fact that radio was being tuned in on the tunneling current signal suggested that perhaps the noise could be eliminated by de-tuning the station by changing the antenna length, i.e. the length of the wire leading to the STM tip.

The green curve in Figure 3.4 shows the result of adding a 30 cm length of BNC cable to the exterior of the vacuum chamber. Extra mechanical vibrations are transduced in the 10-20 Hz range, circled, but the large signal power coming from the radio signal is gone. As a more permanent solution with improved performance at low frequency, a length of wire was inserted in a metal enclosure with BNC ends and a tin plated copper braid was used to additionally shield the wire inside the box. The result of this radio detuner is shown in blue in Figure 3.4.

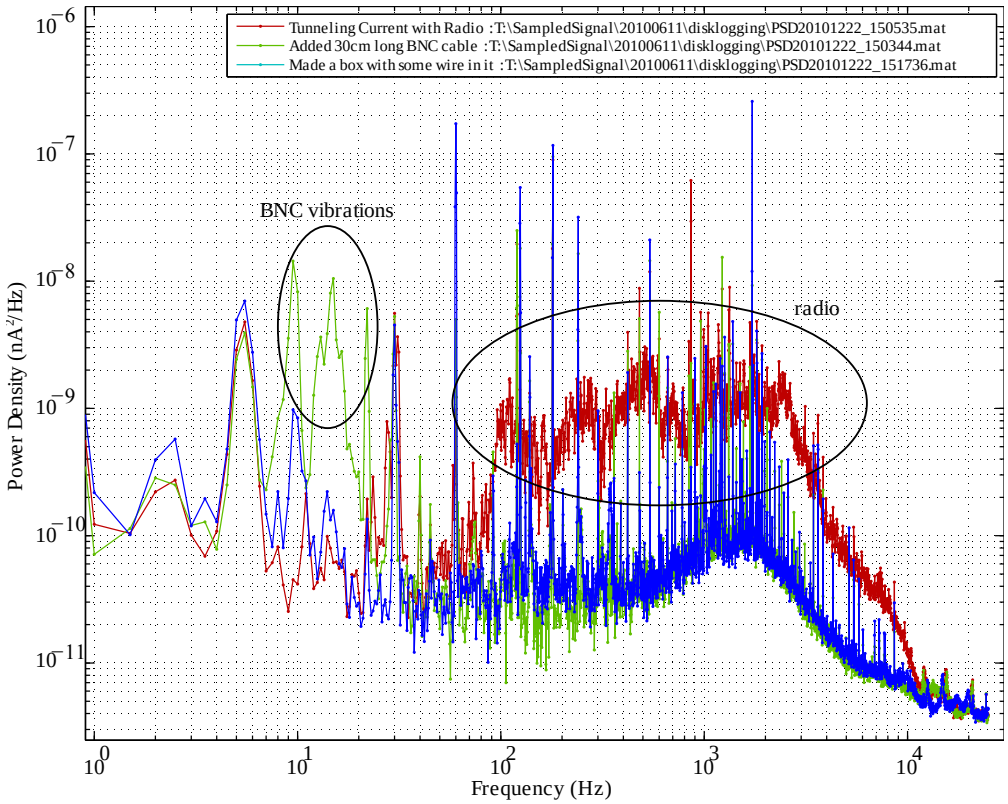

Figure 3.4: PSD of the tunneling current detection noise. Red: demodulated radio contributes to a large hump in detection noise between 100-2500 Hz.

3.2.4 Grounding in the tip-sample circuit

Proper grounding of equipment is a topic that often comes up in discussing noise. "Ground loops" are often mentioned, but many people have the idea that a "ground loop" has to do mainly with a ground connected in a circle that picks up an induced current due to fluctuating magnetic fields. In most systems, ground loops are caused by improper or inadvertent return of electrical current over ground lines, not necessarily by magnetic fields which pass through their loops. If one is trying to measure a signal voltage with respect to a ground with a current flowing through it, the finite resistance of the ground cable will contribute to a voltage drop (IR drop) across the ground cable, thereby corrupting the measurement of the signal voltage.

To put it concisely, we quote the current Wikipedia page on ground loops [175]:

> In an electrical system, a ground loop usually refers to a current, almost always unwanted, in a conductor connecting two points that are supposed to be at the same potential, often ground, but are actually at different potentials.

In practice, we seek to eliminate unnecessary currents passing through signal grounds by minimizing potential differences between pieces of equipment. We can also implement measures to make signal measurements less afflicted by them.

In the context of the tip-sample circuit, consisting of the current path from the bias voltage source to the sample, across the tunneling gap, then from the tip to the current preamplifier and back to the bias voltage source, there are two important issues to discuss: referencing of the bias voltage to the microscope, and referencing of the current preamplifier with respect to the bias voltage source.

The first issue has to do with the bias voltage fundamentally being controlled by the output of a digital-to-analog converter (DAC) somewhere on a rack of control electronics. This voltage must be brought to the vacuum chamber and referenced properly to the microscope ground potential. To eliminate the possibility of ground loops (return current over the signal's ground line), the implementation of a unity gain bias voltage amplifier was proposed by Prof. Rolf Möller during a several week stay in our lab just before my arrival as a graduate student[1].

The idea is to mount an instrumentation amplifier at the vacuum chamber which measures the bias voltage delivered from the rack with respect to its ground, illustrated in Figure 3.5 (a). Both inputs of the instrumentation amplifier are high impedance, $\sim 10^{10}$ Ω, so no ground loops can form on the bias ground line. The INA128 instrumentation amplifier used in the circuit also has a reference terminal to which its output voltage is referenced. We attach the INA128's reference terminal to the V_{TGND} (tunneling voltage ground) wire which attaches to the microscope body inside the vacuum chamber. The circuit's DC power supply is referenced to the V_{TGND} voltage through a RC network as shown. Pins 1 and 8 of the INA128 can be used to apply a gain to the voltage between the + and – inputs as per the function $G = 1 + \frac{50k\Omega}{R_G}$; in our case no resistor is installed, so G=1. The INA128 is mounted on an 8-pin IC socket to allow for quick exchange if damaged – if the FIM high voltage sparks to the sample stage, the INA128 can be destroyed. It is important to check that the voltage at the amplifier's output is correct before any STM experiments (generally this is no longer a problem since FIM high voltage sparking has been made exceedingly rare, as per section 3.5).

[1] This is the only improvement to the system described in this chapter which is not directly my work; it has been included since it relates closely to this section on STM noise.

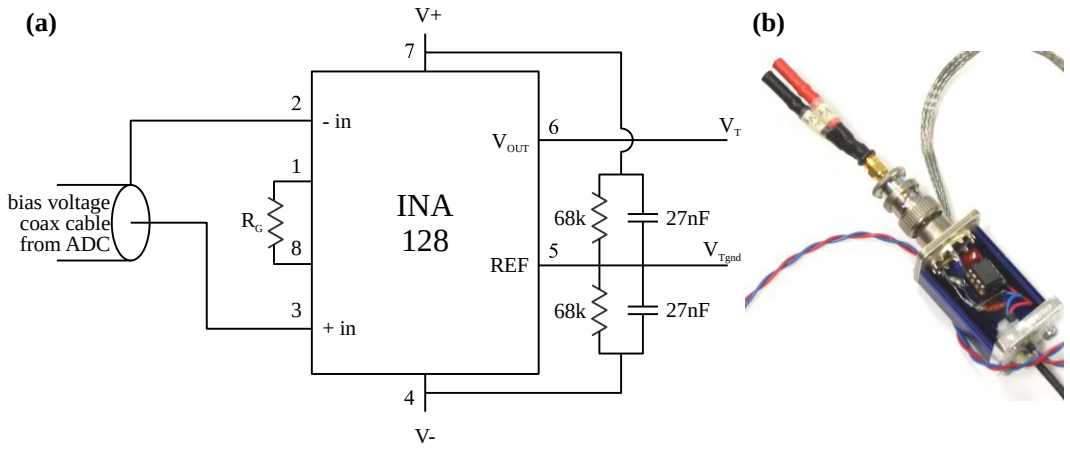

Figure 3.5: (a) Bias voltage buffer amplifier schematic. The gain is set to unity by setting $R_G = \infty$, i.e. open circuit. (b) Photograph of the bias voltage amplifier. The INA128 chip is mounted to an 8-pin IC socket for easy replacement in case of damage.

The second tip-sample circuit grounding issue is deciding how to best reference the bias voltage amplifier, discussed above, to the tunneling current preamplifier. Figure 3.6 shows the configuration of the bias voltage amplifier and current preamplifier with respect to the microscope body and tip-sample junction. For the sake of discussion, the bias voltage amplifier is shown as a battery voltage source, and the current preamplifier circuit is simplified. The preamplifier output is given by [176]

$$\begin{aligned} V_{out} &= V_{IGND} + I \cdot R_f \\ &= V_{IGND} + \frac{V_T - V_{IGND}}{R_{TS}} \cdot R_f \,. \end{aligned} \tag{33}$$

In the second equation the tunneling current has been re-expressed as the tunneling bias voltage with respect to the preamplifier virtual ground, $V_T - V_{IGND}$, divided by the tip-sample gap resistance, R_{TS}.

The first term of Eq. (33) shows that any voltage difference between 'true' ground and the tunneling current preamplifier's ground reference V_{IGND} will appear directly on the output voltage of the preamp (ideally $V_{IGND} = 0$ V). The second term shows that fluctuations in the preamplifier's virtual ground will cause the actual bias voltage across the tip-sample junction, $V_T - V_{TGND}$, to vary – this causes a disturbance of V_{out} with a multiplicative factor of $\sim 0.01 < \frac{R_f}{R_{TS}} < 1$ (for typical tunneling conditions). As a result, one should make sure that no unwanted currents are flowing between these grounds so their potentials are as equal as possible.

Efforts had been made previously to implement a star grounding topology [177] on the system: One star ground located at the electronics racks connected by a low resistance

cable to another star ground at the top flange of the vacuum chamber. This apparently helped in properly referencing some of the microscope control signals to the instrument in the vacuum chamber. Figure 3.6 (a) illustrates the original star ground referencing strategy: the bias voltage amplifier and the current preamplifier are connected to the chamber star ground (red lines). Although the recommended star topology is respected, this connection actually caused additional line noise on the tunneling current signal. In this case, the chamber star ground is located in the middle of the connection between the bias voltage amplifier and the current preamplifier. It is likely that currents passing between the chamber and rack star grounds favoured one path which added a potential difference between these components. The new modified grounding scheme is seen in Figure 3.6 (b).

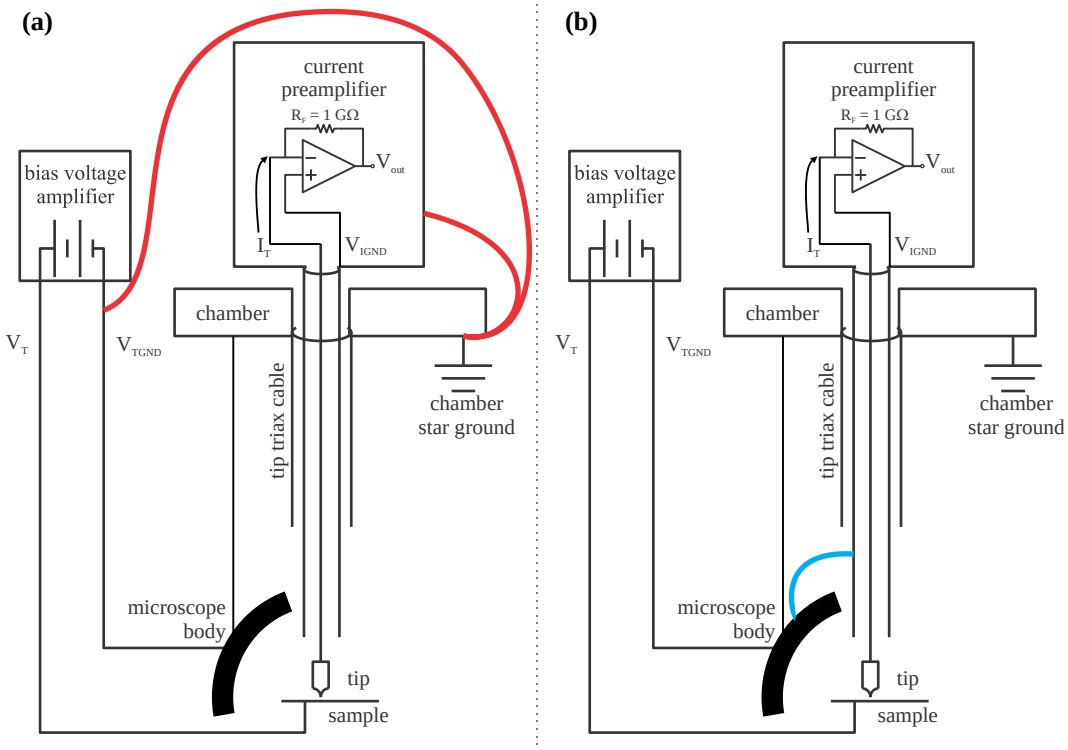

Figure 3.6: Grounding schematic of the tip-sample circuit (a) as found; (b) modified to reference ground potentials

Although the new grounding scheme does not follow the ground topology, it suggests several important aspects of grounding in a STM tip-sample circuit:

1. The bias voltage V_T should be carefully referenced with respect to the virtual ground of the current preamplifier (Eq. (33)).
2. Ground loops to the control rack can be avoided using a bias voltage preamplifier, shown in Figure 3.5.

3. The ground of the current preamplifier (the tip's virtual ground) should be referenced well with respect to the microscope body to reduce capacitively coupled currents ($I = C\frac{dV}{dt}$).

3.2.5 Capacitive noise

In an attempt to remove detection noise at line frequencies, the signal path from tip to preamplifier was examined for possible sources of capacitively coupled noise. Capacitively coupled alternating currents can be picked up if there is a significant capacitance between the tunneling current wire and some component with a time varying voltage difference, $I = C\frac{dV}{dt}$, or if there is a time varying capacitance between the tunneling current wire and some component at high voltage, $I = \frac{dC}{dt}V$ (less common of a problem if well shielded).

A significant portion of the line noise peaks in the tunneling current power spectrum was sourced from capacitively coupled noise near the STM tip stage. The ~ 5 × 5 mm tip holder magnetically attaches to the STM tip stage, which is connected to the wire that brings the tunneling current out of the vacuum chamber. The STM tip stage is separated from a metal plate which has a thermocouple attached to it ("thermocouple plate") by a ~ 1 mm thick Macor ceramic spacer, as shown in Figure 3.7. This thermocouple is intended to monitor the temperature at the tip when the microscope is cooled with liquid nitrogen. Its wires are generally left floating, or are attached to a floating thermocouple reader outside the vacuum system. The capacitance between the thermocouple plate and the tip stage, assuming a ~ 25 mm^2 parallel plate capacitor with a plate spacing of 1 mm and a Macor dielectric with dielectric constant $\varepsilon_r \approx 6$ [178], is approximately:

$$C = \varepsilon\frac{A}{d} \approx 6\,\varepsilon_0\,\frac{25\text{ mm}^2}{1\text{ mm}} \approx 1.3\text{ pF}\,. \tag{34}$$

To put this number into context, one can consider the case of a 60 Hz voltage noise capacitively coupled through the 1.3 pF capacitance. The maximum derivative of a sinusoidal time varying voltage with frequency f and amplitude V_0 of the form $V(t) = V_0\sin(2\pi f)$ is $2\pi V_0$. Inserting this into $I = C\frac{dV}{dt}$ gives a current amplitude of

$$I_0 = CV_0 2\pi f\,. \tag{35}$$

From Eq. (35), one can estimate that a capacitive current with amplitude 1 pA, a significant fraction of low pA tunneling currents, only requires a 60 Hz voltage noise with 2 mV amplitude! The required voltage amplitude to couple 1 pA gets correspondingly smaller as

we consider the integer harmonics of 60 Hz. It is essential to make sure that the potential at the thermocouple plate is well defined with respect to the potential at the tip. Connectors with ground braids have been built for this purpose and are responsible for a significant reduction in detected line noise.

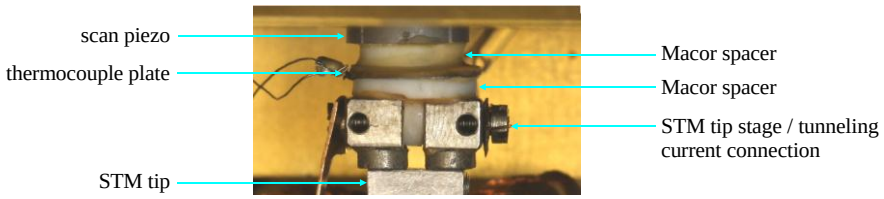

Figure 3.7: Photograph of the STM tip holder. The scan piezo is seen slightly protruding from the coarse approach motor in this photograph. A 1 mm thick Macor ceramic spacer separates the scan piezo from the thermocouple plate, which is in turn separated from the STM tip stage by another 1 mm thick Macor spacer.

3.2.6 Acoustic pickup in preamplifier

During STM imaging on cantilevered samples which have fundamental resonance frequencies of 1-2 kHz (section 2.5.2, page 29), acoustic noise in the lab can be detected by the STM preamplifier and can couple under feedback to the resonance of the cantilevered sample leading to unstable imaging and tip crashing. Unstable imaging is quite problematic when the Varian MiniTask pumping station[1] used for another AFM in our lab is running due to the broadband acoustic noise of its diaphragm pump. One can fortunately arrange with colleagues to turn off this pump temporarily during measurements (highly recommended).

The acoustic coupling of the current preamplifier was improved to some extent as we report here. The red trace in Figure 3.8 shows the tunneling current detection noise with the preamplifier disconnected from the microscope, but still resting on the chamber so that vibrations coupled by the vacuum system are detected. We see the characteristic 860 Hz and 1720 Hz peaks arising from the fundamental rotation frequency and first harmonic of the STM chamber's turbo pump. Other vibration peaks are seen at ~ 30 Hz, between 100-300 Hz, and many between 1000-2000 Hz. In the olive coloured curve, the preamplifier was hung on a rope from a hook attached to the ceiling to isolate it from vibrations coming from the vacuum system – the remaining peaks in the 1000-2000 Hz region are presumably coupled by acoustics. Some success in the suppression of these peaks was achieved by adding foam inside the enclosure of the STM preamplifier to prevent its components from

[1] A turbomolecular pump and dry diaphragm roughing pump in one unit.

vibrating. Several rounds of adjusting the foam and moving around wires inside the box yielded the improvements seen in the blue and green curves.

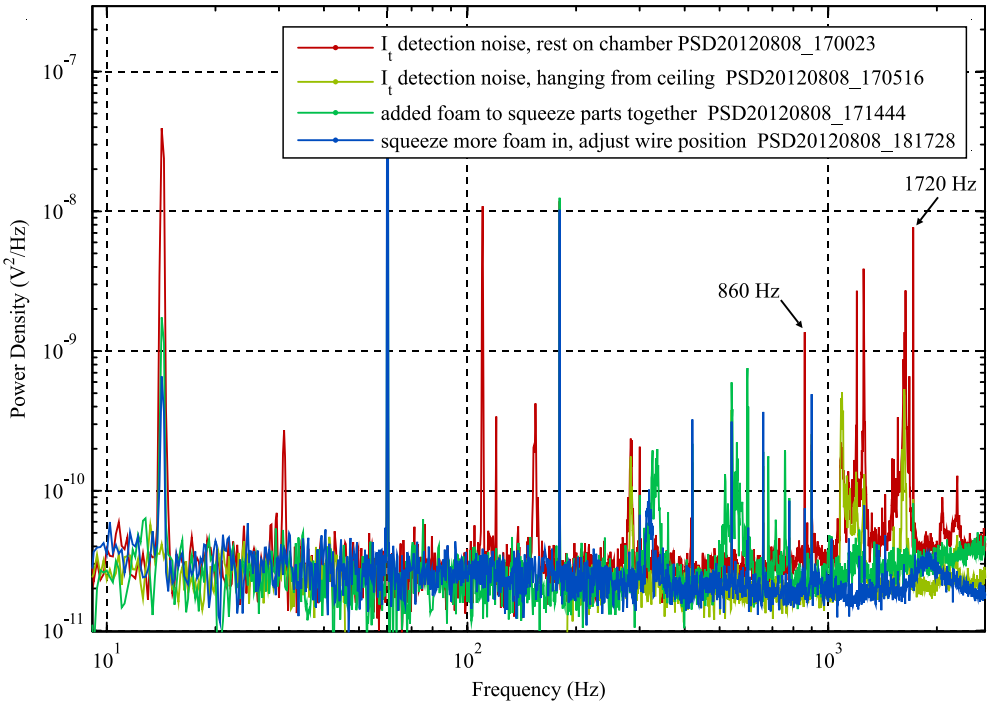

Figure 3.8: Effect of acoustic noise on the tunneling current detection noise and improvements made by adding foam inside the current preamplifier. See text for additional description of the data.

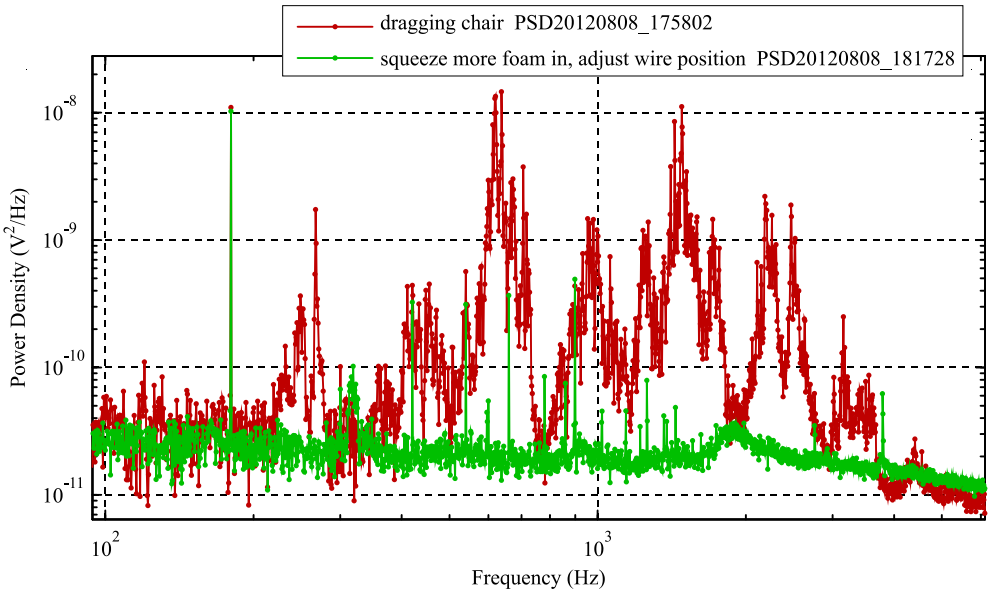

Figure 3.9: Acoustic noise picked up by dragging a wooden chair across the floor.

Despite these improvements, the STM preamplifier is still sensitive to acoustic noise in the lab, which we demonstrate by dragging a wooden chair noisily across the floor in Figure

3.9. The message here is that it's relatively easy to couple acoustic noise to the tip-sample junction through the STM preamplifier.

Finally, we demonstrate the acoustic detection of the Varian MiniTask's diaphragm pump in the tunneling current signal, even after the improvements obtained in Figure 3.8. Figure 3.10 illustrates the tunneling current detection noise with the Varian MiniTask on and off. There is a set of wide peaks almost exactly 50 Hz apart at 1070, 1120, 1170, 1220, 1270 Hz which disappear when the diaphragm pump is turned off. These are in a frequency range which may coincide with cantilevered samples – one should be aware of their presence.

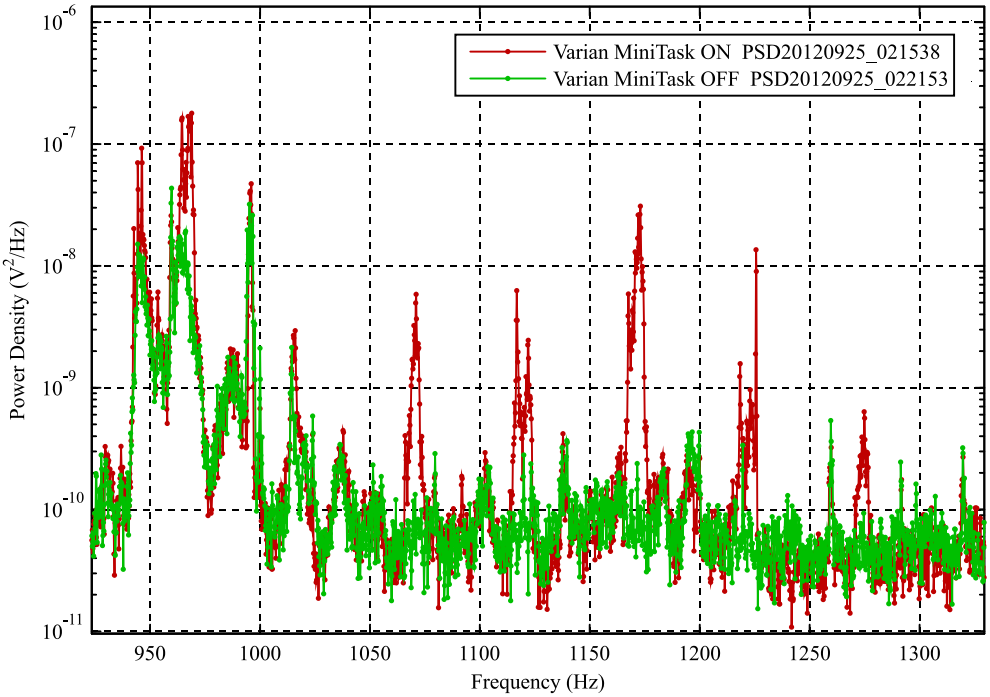

Figure 3.10: Acoustically coupled peaks on the tunneling current signal coming from a diaphragm pump in a Varian MiniTask pumping station.

3.2.7 Equipment grounding

The UHV system and combined microscopes require many different pieces of equipment to be plugged into several supply circuits on 110 and 230 V lines. Given that several circuits in the building are used for this purpose, it's important to make sure that any potential differences between circuit grounds do not flow through our equipment and contribute to line noise arising from ground loops. An effective solution to grounding equipment connected to different circuits is to replace the ground pin of power bars by a wire connecting to the system's star ground. The system may still be connected to one (and only

one) building ground – it is the potential differences between building grounds which must be avoided. Isolated power bars had been implemented in two places on our system. Due to the complexity of the apparatus, it took a few years for me to realize exactly where everything was plugged in – and an exercise in sifting through lots of power cables revealed that one unwanted building ground was still attached to the system. Unplugging the equipment on this one problematic circuit gave a stunning reduction in line noise peaks in the tunneling current detection noise. This is seen by the disappearance of many of the line frequency peaks from the red curve of Figure 3.11.

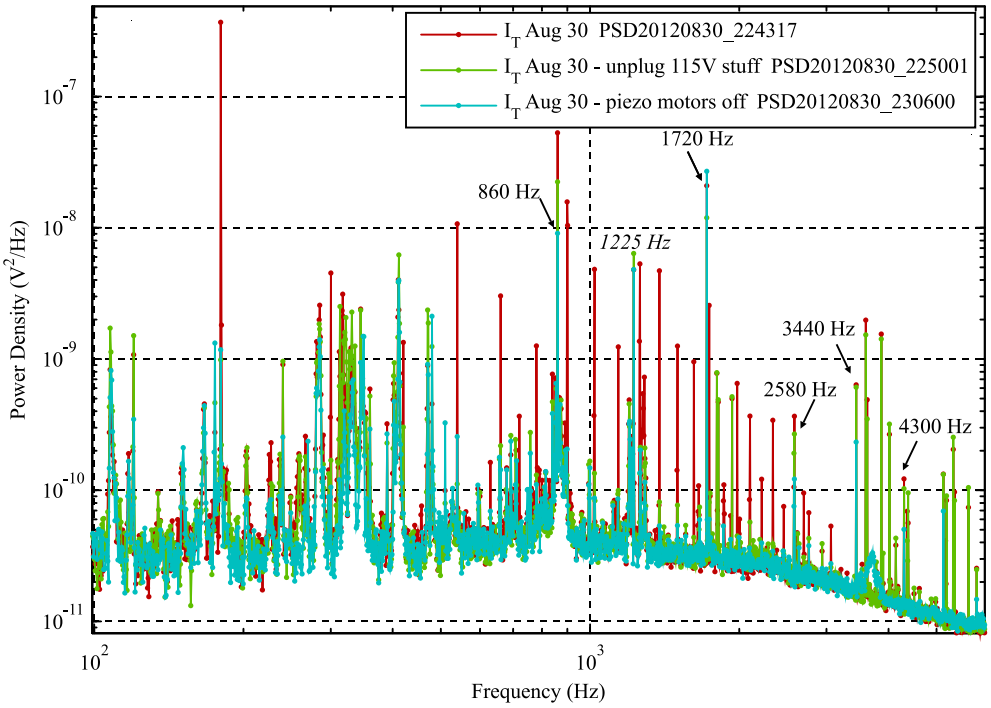

Figure 3.11: Tunneling current noise improvement after unplugging equipment from an offending circuit ground and after grounding piezo motor signals in an improved manner. See text for details.

The green curve in Figure 3.11 still shows several remaining line frequency peaks in the 1000-5000 Hz range. These were associated with the coarse piezo motor signals being grounded at the rack rather than at the chamber (this will be further discussed in section 3.4.3, page 105). Grounding these motor signals near the microscope suppressed most of the remaining harmonics of 60 Hz, and a few other strange noise peaks seen in Figure 3.12. The remaining largest noise peaks above 1 kHz in the tunneling current signal are due to the turbomolecular pump and harmonics (indicated as 860, 1720 Hz, etc.) and the peaks around 1225 Hz likely caused by the acoustically coupled diaphragm pump.

It is easier to notice the disappearance of the noise peaks separated at 60 Hz on a linear frequency scale. The regularly spaced red peaks in Figure 3.12 are much attenuated in the green curve, and then nearly completely disappear in the turquoise curve with improved grounding of the piezo motors.

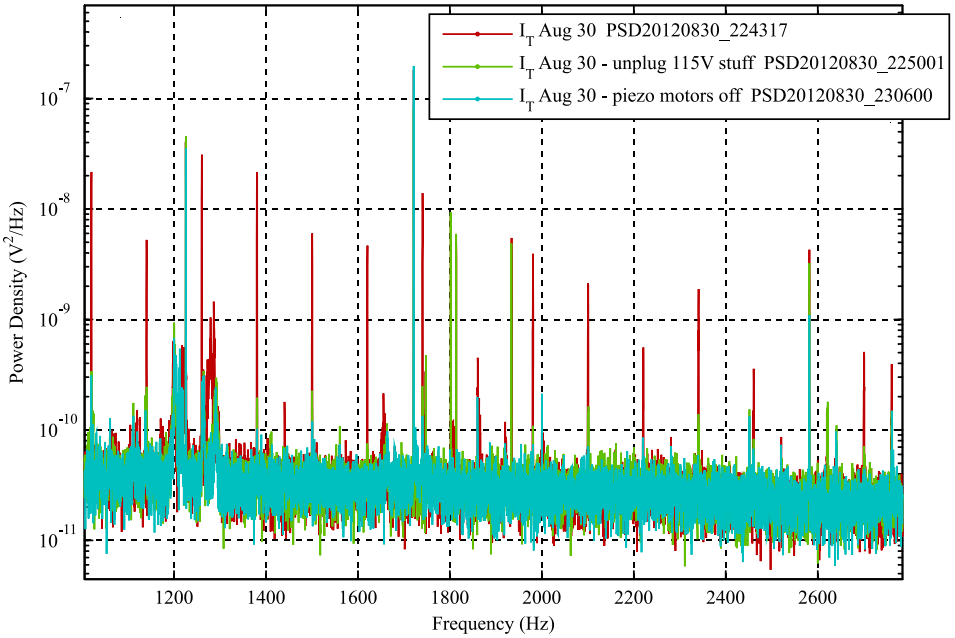

Figure 3.12: Improved tunneling current detection noise plotted on a linear scale, details in text.

3.3 Atomic force microscopy

In this section, we focus on improving the force detection noise in AFM. We cover the fundamental shot noise limit of the interferometer setup as well as the practical limit of the interferometer phase noise. In two examples, we illustrate the fact that measurement sensitivity (e.g. nm/V) is not necessarily a figure of merit – different optical alignments of the interferometer with the same sensitivity can show very different signal-to-noise ratios. This is demonstrated for interferometer phase noise and common mode laser noise.

3.3.1 Fundamental detection noise limits

The ultimate noise limit for force detection by interferometry is dictated by shot noise on the photocurrent, arising from the Poisson statistics of discrete photons [71]. The shot noise power on the photocurrent is

$$n_I^2 = 2eI\,, \tag{36}$$

where e is the electron charge and I is the average current. In our interferometer setup described in section 2.6, the photocurrents detected by two photodiodes are subtracted to yield the cantilever deflection signal. The average value of the photocurrents for typical measurements is $I = V_0/R_T = 5\text{ V} / 300\text{ k}\Omega \approx 16.7\ \mu\text{A}$. R_T is the value of the photodiode preamplifier's transimpedance resistor, and the average output voltage V_0 is roughly 5V, as seen in the interferometer calibration curve in Figure 2.14 (page 36). The interferometer sensitivity, $S_{\delta u}$ in Eq. (28) (page 35), and the transimpedance resistance can be used to convert the current noise power to displacement noise power as follows:

$$\begin{aligned} n_{\delta u}^2 &= 2S_{\delta u}^2\, n_V^2 = 2S_{\delta u}^2\, R_T^2\, n_I^2 \\ &= \frac{\lambda^2 e R_T}{8\pi^2 V_0}. \end{aligned} \tag{37}$$

The factor of 2 reflects the addition of noise power from the two photocurrent signals. We have also used the fact that the peak-to-peak voltage V_{pp} of the interference fringe is related to the average voltage of the photodiodes by $V_{pp} = 4V_0$.

In our experiment, the shot noise floor for displacement detection is $\sim$8.6 fm/$\sqrt{\text{Hz}}$ (or equivalently $\sim 7.4 \times 10^{-11}$ nm^2/Hz). Displacements can be converted to forces by the cantilever spring constant at the tip location of $k_T \sim 100$ N/m, so this corresponds to a $\sim$1 pN force resolution in a 1 Hz bandwidth[1].

The interferometer detection system is not shot noise limited, however. We now discuss the practical laser detection noise limits referring to the power spectral density plotted in Figure 3.13. The data shown here is calibrated by the interferometer sensitivity to reflect the displacement noise power in units of nm^2/Hz. The shot noise limit we discussed above is plotted as a blue line at 6.7×10^{-11} nm^2/Hz (this value corresponds to the actual $V_0 = 5.5$ V for this measurement). The white noise limit in our experimentally obtained noise power spectrum is a full order of magnitude higher than the shot noise baseline. The electronic noise due to the photodiode preamplifier and other electronics (measured with the laser off, not shown) is on the order of 10^{-12} nm^2/Hz, well below our measured data. The white laser noise reported by Stalder with the same interferometer was significantly higher than ours, owing to perhaps a different laser diode, and indicated by the orange arrow at 4×10^{-8}

[1] A geometric factor is also needed to describe the displacement at the beams with respect to the displacement at the tip location, see Eq. (13), but it is of order unity.

nm²/Hz. Stalder also observed that the white laser noise was about an order of magnitude larger than his shot noise estimate and attributed it to phase noise of the laser diode.

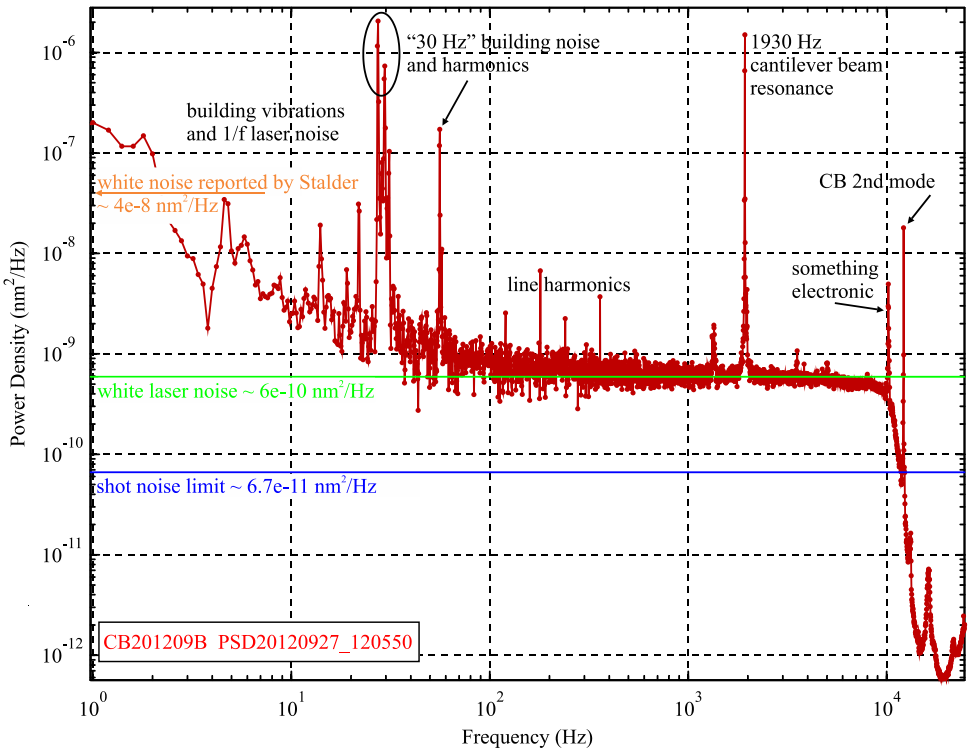

Figure 3.13: Displacement noise power spectral density measured by interferometry from a cantilevered sample. The calculated shot noise limit is shown in blue, an order of magnitude below the measured white laser noise. Sources of various noise peaks are labeled.

The characteristics of the white laser noise will be discussed shortly. First, we point out some of the characteristic features of the noise power spectrum in Figure 3.13. The low frequency regime has a 1/f tail and several peaks coming from building vibrations of various magnitudes. There is a large cluster of peaks around 30 Hz with a width of several Hz coming from mechanical building noise sources, some with harmonics around a factor of 2 higher in frequency. Noise peaks around 30 Hz are likely due to AC motors (pumps, elevators, ventilation) which have a rotation speed slightly lower than half the line frequency depending on the applied torque [179, 180]. Some harmonics of 60 Hz line noise are seen above the white laser noise from 120 – 360 Hz. The cantilever beam from which the laser beams reflect has a resonance frequency of 1930 Hz, and also shows a peak from its second mode at 12165 Hz, just beyond the 10 kHz roll-off frequency of the data acquisition antialiasing filter. Some strange electronic peaks of unknown origin are detected around 10 kHz.

Returning to the subject of the excess white noise, we now consider its scaling with optical power. In the case of shot noise, the photocurrent noise power is proportional to the average photocurrent $n_{I-shot}^2 \propto I$ (Eq. (36)). Since distance sensitivity (nm per photocurrent) is inversely proportional to the average photocurrent, $S_{\delta u} \propto I^{-1}$, the **shot noise contribution** to the displacement noise power **decreases with increasing photocurrent**:

$$n_{\delta u-shot}^2 = S_{\delta u}^2 \, n_{I-shot}^2 \propto I^{-1} \, . \tag{38}$$

On the other hand, **classical noise sources** that scale as $n_{I-class}^2 \propto I^2$, when calibrated into displacement noise power by $S_{\delta u}$, are **independent of laser intensity**:

$$n_{\delta u-class}^2 = S_{\delta u}^2 \, n_{I-class}^2 \propto I^0 = 1 \, . \tag{39}$$

The independence of the white displacement noise on photocurrent can be verified by intentionally mis-aligning the exit beams of the interferometer with respect to the photodiodes, such that a portion of the beam intensity is lost. This is demonstrated in Figure 3.14, where a 1.7× reduction in photocurrent was attained between the red and green curves. If shot noise were the source of the white noise floor, one would expect a corresponding 1.7× reduction in displacement power spectral density (Eq. (38)), which is not observed. The blue arrows and dotted lines show the magnitude of the expected drop.

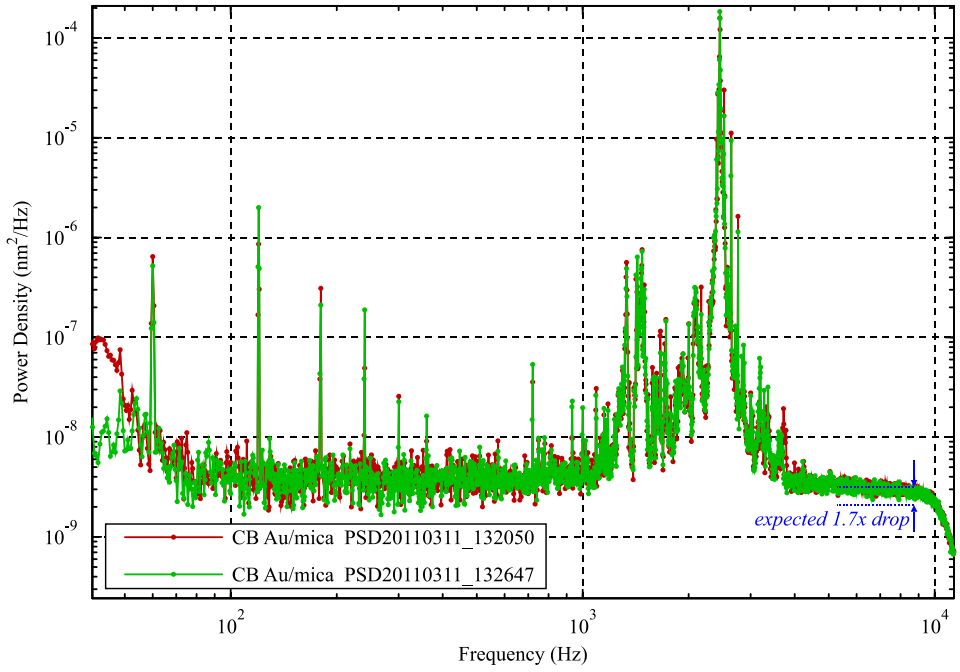

Figure 3.14: Displacement noise power spectra for the same sample in two interferometer alignment configurations with different photocurrents. If the white noise background was due to shot noise, a 1.7× drop in the baseline would be expected. Note that excessive sample vibrations are evident in the low kHz region because the power spectra were taken when the microscope was set up for repair on a lab table without vibration isolation.

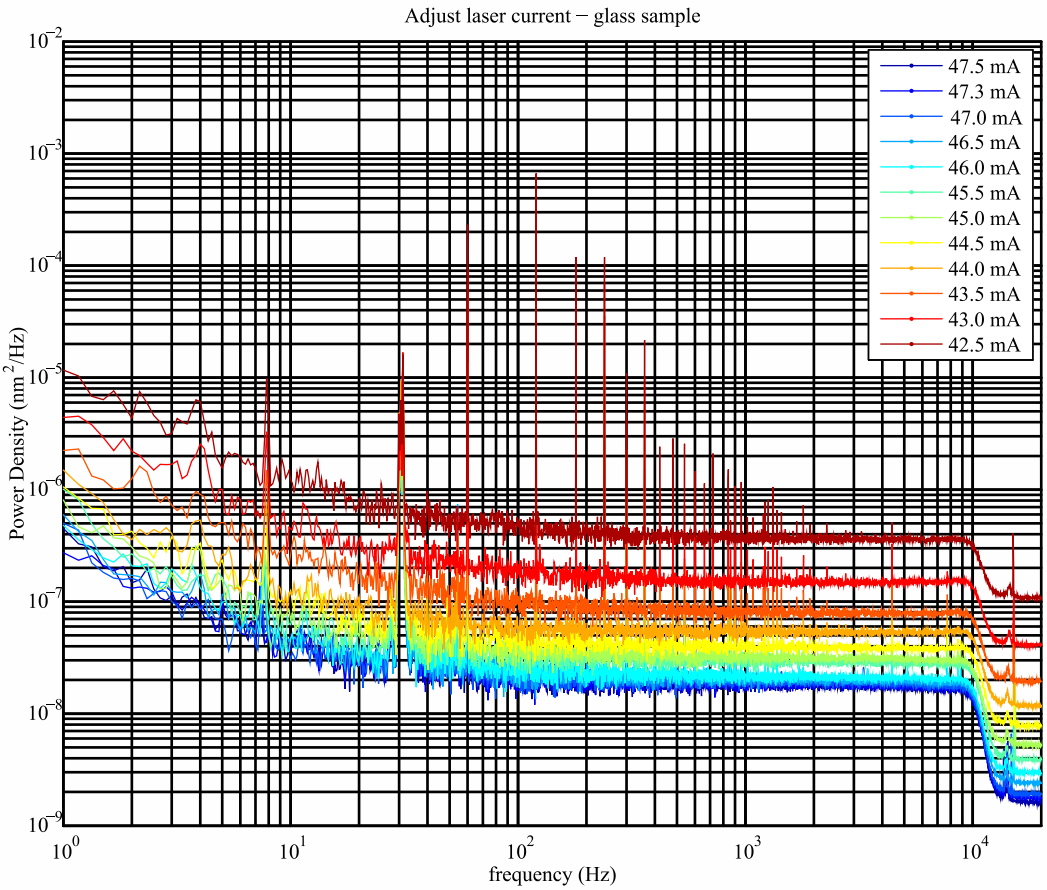

Figure 3.15: Interferometer displacement detection noise as a function of laser diode operating current. Up to ~46 mA, a decrease in laser noise is observed for increasing operating current.

The independence of the white noise baseline on photocurrent suggests that there is a phase difference noise in the interferometer which has a white spectral density. As Stalder points out [44], the phase difference that the interferometer measures is (from Eq. (27))

$$\phi = \frac{2\pi}{\lambda}\, d = kd\,, \tag{40}$$

where k is the wave vector of the laser light. Any fluctuations in k will also add noise to the measured signal:

$$\delta\phi = \delta(kd) = (\delta k)d + k(\delta d)\,. \tag{41}$$

Laser diode phase noise (frequency instabilities) will contribute to fluctuations in wave vector. Eq. (41) makes it apparent that in order to minimize the effect of laser diode phase noise on the phase difference between the two beams, one must minimize the path difference d between the beams. Practically, we don't have much control over this path difference, so the frequency stability of the laser diode is the most accessible experimental

parameter. It has been observed that increasing the laser power decreases the white noise baseline, as illustrated by Figure 3.15. The increase of laser current seems to stabilize the frequency of the laser diode. A decrease in laser noise is observed up to 46 mA, after which the baseline is rather constant. The maximal operating current of the laser diode is 48 mA.

3.3.2 Problems with phase noise

We furthermore report on a particularly peculiar problem relating to the white laser phase noise that was observed (and corrected to some extent) with the interferometer. During some experiments carried out to characterize new types of cantilever beam samples in late 2010 and early 2011, it was observed that the interferometer signal was often abnormally noisy – characterized by a dramatic increase in 1/f noise as well as the white phase noise baseline. The time domain signals drifted furiously around in a manner which made the recoded data rather useless, as shown in Figure 3.16.

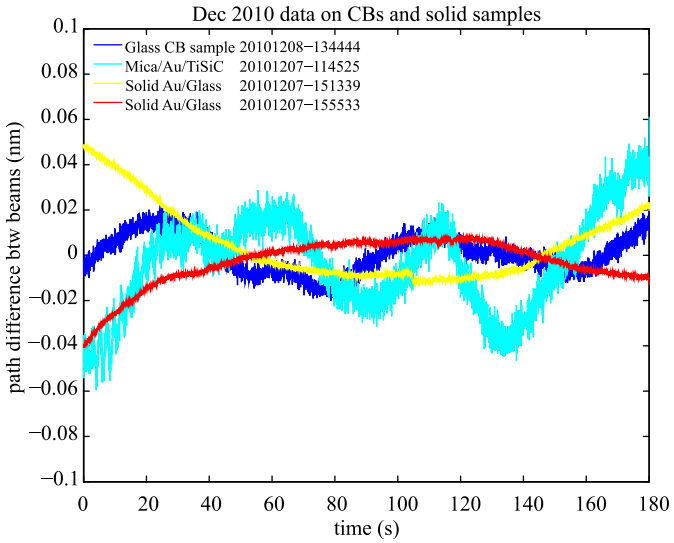

Figure 3.16: Time domain interferometer signals showing noisy (light and dark blue) and quiet (yellow and red) interferometer behaviour. A first order polynomial has been subtracted from this data to emphasize variations from slow linear drift.

All kinds of sources were considered: something bizarre about new glass cantilever beams, dysfunctional thermoelectric laser diode temperature control, improperly aligned vibration damping, power fluctuations of the laser which heat cantilevers by the bimetallic effect [181], etc. After trying multiple samples, re-aligning the interferometer countless times, taking vast amounts of data, and staring at a mountain of senseless plots, it became apparent that the only correlation between "noisy" and "quiet" interferometer behaviour

with any experimental parameter was the **sign of the interferometer fringe**. It was as if an occult hand had adjusted the interferometer detection noise based on whether the operating point was the positive or negative slope of the interference pattern. Worth noting is that the sign of the interferometer fringe has never been a parameter that has ever been recorded in previous experiments; typically one would write down only the peak-to-peak value of the interferometer fringe from an oscilloscope readout because the calibration sensitivity is equal on both sides of the fringe. The fact that Matlab routines were developed to collect every single calibration curve meant that the direction of the fringe response in relation to the sign of the path difference was saved.

The calibration curve in Figure 2.14 (page 36) shows the fringe response (black) going in the **opposite** direction as the driven path difference (green). By adjusting the angle of the sample very slightly ($\arctan(\lambda/4d_b) = \arctan((780\text{nm}/4)/1\text{mm}) \approx 0.01°$) to change the path difference by $\lambda/2$, one can operate the interferometer on the other side of the fringe, such that the green and black curves have the **same** slope.

The only physical mechanism we could think of to explain the dependence on fringe sign was that perhaps there was a dependence on the absolute phase of the outgoing beams due to interference with the incident beams. This could occur if light from the incident beam leaked around the mini-prism (Figure 2.10, page 31) and re-combined with the outgoing light. A copper foil shield was carefully added around the edges of the mini-prism to ensure light could not leak around it. All of the interferometer optical components were re-aligned during this repair in March 2011. Although the "noisy" / "quiet" behaviour did not return to the same extreme, it can still sometimes be observed (mechanism unknown). It is recommended that the interferometer be aligned on both positive and negative fringes to determine if one is better for noise performance.

Although this result is admittedly physically unsatisfying in terms of understanding (at the moment), it is of great practical importance to operation of the STM/AFM. It is also an excellent example of two experimental configurations that have the same sensitivity (nm/V) but a very different signal-to-noise ratio. One must always remember that sensitivity is not a good figure of merit – noise (in calibrated units) must always be examined.

3.3.3 Differential interferometer and common-mode noise

We have introduced the differential interferometer in section 2.6 in the context that the output signal is sensitive only to differential mode phase changes and not common mode

phase changes in the optical path (Eqs. (24) and (25)). There is another differential aspect to this interferometer which is slightly more subtle but absolutely crucial to appreciate for noise performance. The interferometer output signal is obtained by differencing the laser signal on the two photodiodes, PD_A and PD_B. The calibration curve of Figure 2.14 (page 36) shows the red and blue interference patterns on both photodiodes, and the black interferometer output signal which is the difference between them, that is,

$$V_{int} = V_{PD1} - V_{PD2}\,. \tag{42}$$

The fact that the output signal is a subtraction of the two photodiode signals means that laser noise appearing equally on both signals (such as 1/f and line noise intensity fluctuations) will cancel as long as $V_{PD1} \approx V_{PD2}$. The differential nature of the output signal means that common mode laser noise (common to both beam polarizations) is rejected. This is exactly the case with optical beam deflection setups where the top and bottom segments of a split photodiode are differenced [182]; the best common mode noise rejection is reached when the DC values of the photocurrents are perfectly balanced.

Despite having intimate familiarity with noise in beam deflection AFM, the analogy with our differential interferometer was not obvious to me for some time. The new photodiode preamplifier with a gain of up to 100× inadvertently required the intensities to be well-matched whenever the gain was turned on[1], to the noise benefit of data taken by Hagedorn and El Ouali [49, 50], before the common mode laser noise rejection was appreciated.

We plot the interferometer detection noise (in arbitrary units) in Figure 3.17 for various initial phase offsets driven by the calcite piezo. The interferometer is aligned with balanced photodiode intensities at a calcite offset voltage of 0 V which corresponds to the curve with the lowest noise. The offset voltage is changed up to 1 V in each direction. As this is done, the intensities of the photodiodes become unbalanced and the common mode rejection is spoiled, permitting a much larger portion of 1/f and line noise to corrupt the signal. In this measurement, the 1 V calcite offset produces a maximal change in the interferometer phase of about $\pi/16$, corresponding to a reduction in sensitivity of only ~2%: the measurement is still being performed well within the linear region of the fringe response. The sensitivity of the measurement is hardly affected, but the noise changes dramatically.

The examples of phase noise affected by the sign of the interferometer fringe (section 3.3.2) and common mode rejection are reminders that sensitivity is not an indicator of

[1] When a high gain is applied, the photocurrents must be balanced in order for the difference signal to be within the ±10 V data acquisition range.

signal-to-noise. Power spectral densities calibrated into the measurement units (in this case, displacement) reflect directly the signal-to-noise ratio that is achieved.

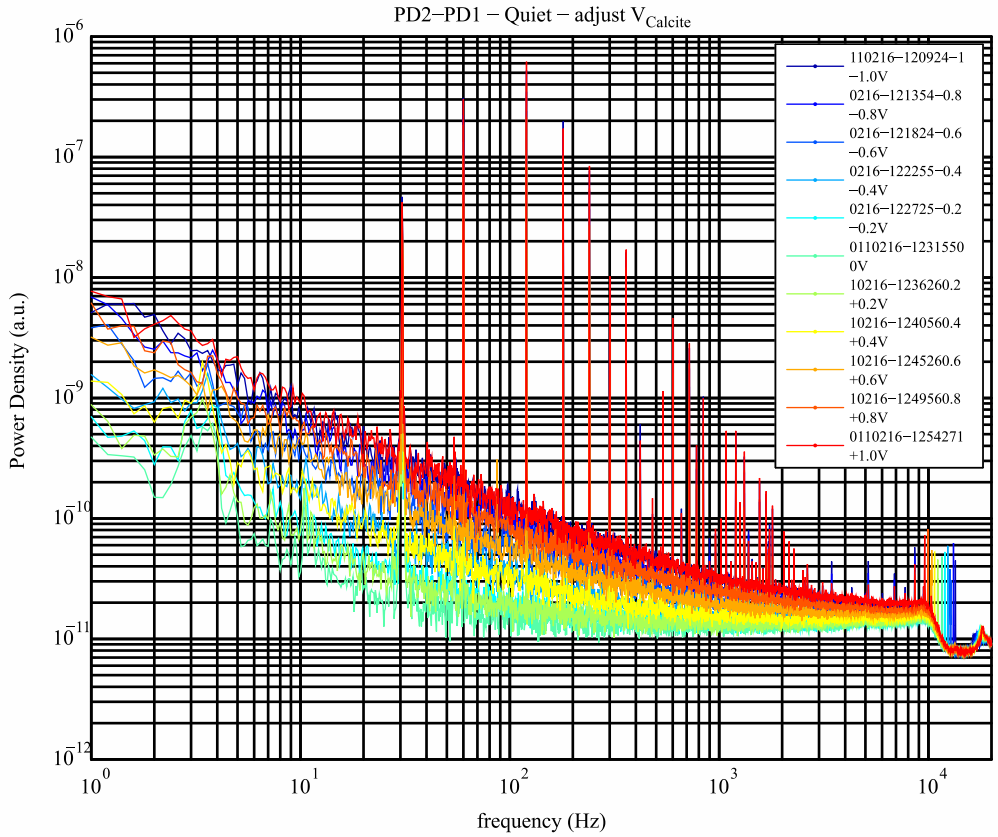

Figure 3.17: Interferometer noise power spectra as the phase offset is varied. The photodiode intensities are perfectly balanced in the green curve labeled 0 V, and have a phase offset of maximum $\sim\pi/16$ (curves labeled 1 V) where a significant amount of common mode laser noise is detected in the form of 1/f and line peaks.

3.3.4 Equipment grounding

In section 3.2.7 (page 89), we described improvements to equipment grounding by eliminating multiple power circuit grounds and by grounding piezo motor control signals near the vacuum chamber rather than at the electronics rack. These efforts also improved the deflection noise power spectral density, as demonstrated in Figure 3.18. Most of the red noise peaks are eliminated by removing the extraneous ground connection (green). Additional attenuation of peaks near 1000 Hz was achieved by grounding piezo motor signals at the microscope (turquoise). The most significant peaks left in the power spectrum after these improvements are the turbomolecular pump's first harmonic, and the second resonance mode of the cantilever beam.

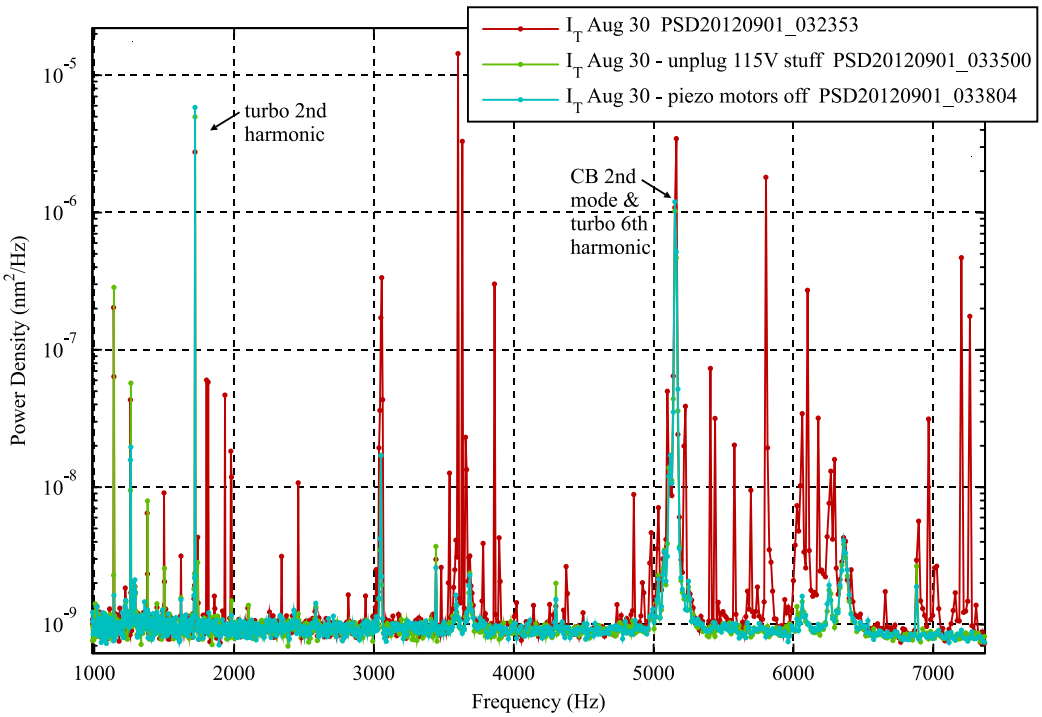

Figure 3.18: Deflection noise power spectrum illustrating improvements from power circuit grounding and piezo motor signal grounding.

3.3.5 Power shutdown

The last major step toward in improving the deflection detection noise relies on an understanding of the cluster of peaks found around 30 Hz, illustrated in Figure 3.13 (page 93). The following possible causes of this noise have been considered:

- Our system's rotary vane pumps (tested – doesn't make much difference).
- Magnetic levitation turbo pump's bearing controller (tested – no).
- Building vibrations coupled through vacuum bellows and other cables (tested by removing as many connections as possible – no).
- Opto-mechanical noise arising from noise on the piezo walkers or other electro-mechanical components (tested by disconnection of amplifiers, etc. – no).
- Resonance of the bellows from which the STM is suspended in UHV for vibration isolation – Stalder thesis [44] mentions stuffing with steel wool to damp them (filled exterior of bellows with ethanol/methanol mixture to try to damp them with a fluid – no change).
- Transverse modes of bungee cords suspending the system (tested by mass loading them in the center – no significant change).

- ❖ Strange laser polarization noise (sounds unlikely, and also the 30 Hz peaks are also present on the current detection noise, so probably of mechanical origin).

We conclude that these mechanical noise peaks must be coupled through the bungee cords suspending the vacuum chamber. They might also be resonantly enhanced by some component – the suspension bellows as mentioned earlier, or maybe a mechanical resonance of the fiber optic. My suspicion is that the mechanical noise is transduced by a mechanical motion of the optical fiber. Stress on the birefringent fiber causes a polarization change of the light, resulting in the observed interferometer signal.

On September 27, 2012, we had the rare opportunity to have a 600 V supply line under repair for several hours which serves several buildings in our area of the McGill campus. This gave us a chance to test whether the noise was caused by our equipment, or by other things in the building. All vacuum pumps were shut down and disconnected as per a usual power shutdown. The UPS serving to protect the magnetic bearing turbomolecular pump was used to power all the necessary electronics to operate the interferometer[1] during the power shutdown. Data was recorded on a battery powered laptop.

The power spectrum captured at 12:26 am before the shutdown, illustrated in red in Figure 3.19, shows the typical 30 Hz cluster of noise peaks, line noise peaks at 60, 120 and 180 Hz, and the first mode of the cantilever at 1926 Hz. In preparation for the power shutdown, all equipment running in our lab had already been turned off and unplugged, eliminating the possibility that any changes in detection noise came from our equipment. We also tested data acquisition on the UPS to check that any changes did not originate from the electrical supply.

The power shutdown occurred at 1:30 am, at which point all ventilation systems and rumbles audible in the laboratory shut off. Within seconds of the shutdown, some motor started running again, showing some noise power around 30 Hz. The audible noise was loudest on the 4th floor outside the elevators. At 1:45 am, this noise stopped, and the building fell completely silent. The deflection noise power spectrum during the complete power shutdown is shown in green in Figure 3.19.

This is evidence that the 30Hz noise cluster comes from the building and not our equipment. It also distinguishes between optomechanical and optical noise: the noise is not

[1] This consisted of the laser diode, thermoelectric cooler, photodiode amplifier, antialiasing filter, high voltage amplifier for calcite phase adjustment, and National Instruments data acquisition hardware for a total of 180 W for an available running time of ~32 min on the UPS.

due to laser polarization fluctuations (optical noise), it is due to mechanical noise affecting the optical path.

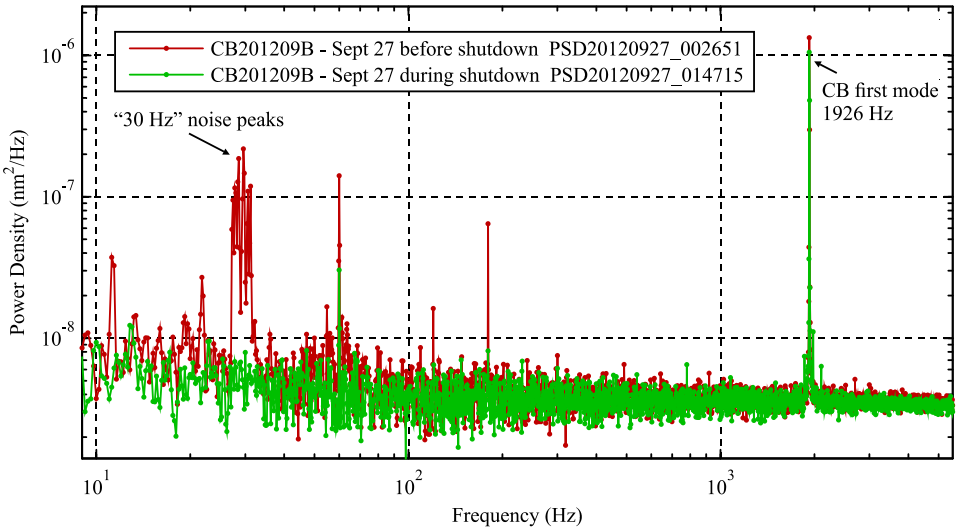

Figure 3.19: Deflection power spectrum before building power shutdown (red), and during shutdown (green).

3.4 Mechanical noise in the tip-sample junction

In this section, we start by discussing the deleterious resonance of cantilevered samples during indentation experiments to motivate the need for a mechanically quiet tip-sample junction. Electrical noise in the grounding of piezo motors was found to be a large contributor to unwanted tip-sample vibrations. These tip-sample vibrations were characterized using interferometry and the STM tunneling current. Finally, we review the cantilever beam's resonant coupling to the turbo pump, other harmful effects of the turbo pump vibration, and the excitation of the cantilever beam by line noise on the scan piezo high voltage amplifier.

3.4.1 Cantilever beams and mechanical noise

The cantilevered samples introduced in section 2.5 (page 27) make our scanning probe microscope particularly vulnerable to the effects of mechanical noise. We have shown in the case of current and deflection detection noise that line noise and acoustic noise can contribute noise power at well-defined frequencies. If this noise power couples to the motion of the z piezo under feedback, it can be driven into dangerous oscillations. A similar situation holds true for mechanical noise but without necessitating feedback: any

substantial mechanical noise contributing to a relative motion between the tip and sample at a frequency matching that of the sample will drive it to oscillate.

The situation might be regarded as "unlucky" when the frequencies of tip-sample noise and cantilever beam resonance match so precisely. In fact, the act of bringing a tip in contact with the sample changes the resonance frequency through a wide range, so it is hard to avoid such coupling. In Figure 3.20(a), a plot reproduced from Mehdi El Ouali's thesis [49] shows the time trace of the cantilever deflection during a nanoindentation experiment. The cantilever deflects smoothly and then becomes extremely excited around the middle of the curve, oscillating by up to ~ 2 nm.

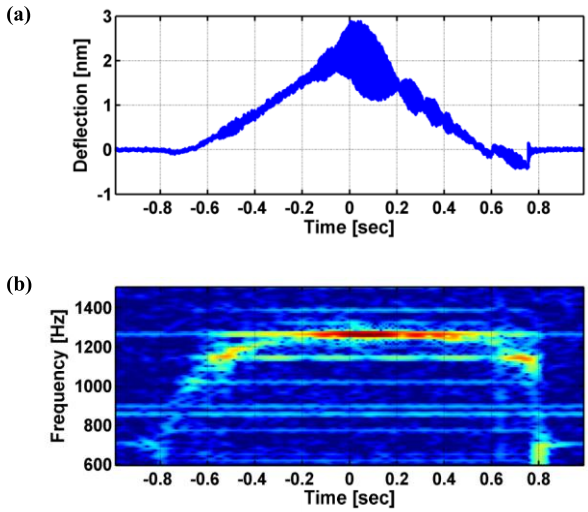

Figure 3.20: (a) Deflection of the cantilevered sample during nanoindentation. (b) Power spectral density evolution of the deflection signal (values are coloured with a jet colormap: dark blue = low, red = high). Figure courtesy of M. El Ouali [49].

Figure 3.20(b) shows the power spectral density evolution of the deflection signal during indentation: each vertical column represents the power spectrum derived from a window in time during the indentation. The free resonance frequency of the cantilever beam is around 700 Hz at the beginning of the indentation (on the low side). As the tip approaches the sample, tip sample force gradients (section 2.4.2, page 21) will cause the resonance frequency to change. The resonance frequency briefly decreases during the attractive force gradient regime (hardly visible in Figure 3.20(b)), then begins to rise sharply as the tip enters rigid mechanical contact. Throughout Figure 3.20(b), we can see horizontal stripes consisting of detection noise peaks at particular frequencies. Some of these may be harmless to the cantilever – they are not all mechanical in nature. However, as the cantilever passes just above 1000 Hz and around 1150 Hz, for example, it couples to

mechanical noises which contribute to driving it. Most catastrophic is the cantilever beam's transition over a ~1250 Hz peak, when it becomes very strongly excited.

Mechanical noise between tip and sample can be problematic for a rigid STM setup, but it does not uncontrollably excite resonances of a sample. In the case of cantilevered samples with resonance frequencies that change considerably during measurements, it is absolutely crucial to keep the mechanical noise between the tip and sample to a minimum.

3.4.2 Interferometric measurement

The AFM interferometer can be used to directly measure vibrations between tip and sample. This was carried out as an extension of work started to characterize piezo creep, in which a large stainless steel wire was installed in place of a tip and rigidly pushed into contact with a cantilevered sample, such that the deflection of the sample followed the tip motion exactly. Power spectra with the tip in and out of contact with the sample revealed that many noise peaks between 1 – 10 kHz contributed to an extra ~1.5 Å RMS relative motion between the two – a rather large mechanical noise at the length scales of interest to us. The disappearance of the noise also occurred when the STM Z coarse approach motor was unplugged (while the tip was still in rigid contact with the sample). The power spectrum of the deflection signal is shown with the Z piezo motor connected (red) and disconnected (blue) in Figure 3.21(a).

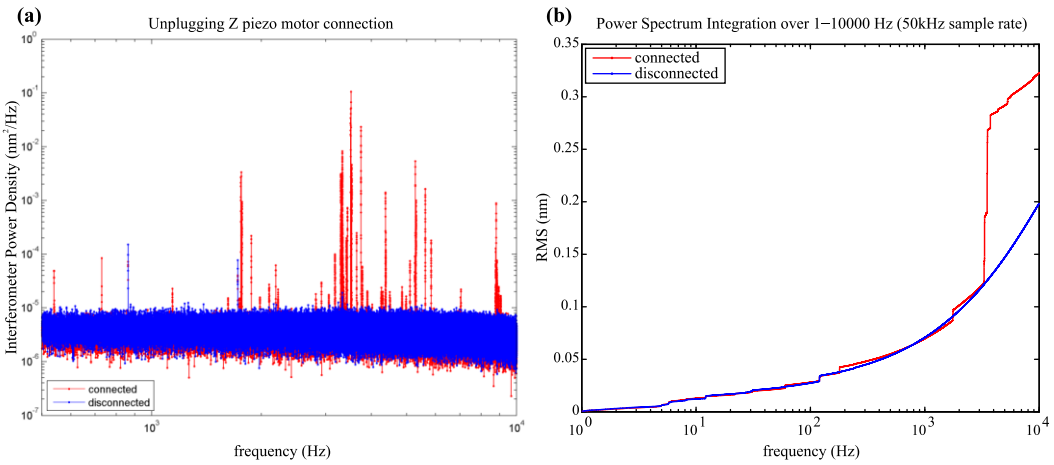

Figure 3.21: (a) Power spectra of the deflection signal with the Z piezo motor connected (red) and disconnected (blue). (b) Integrated power spectrum showing that the noise peaks contribute to a ~ 1.5 Å increase in tip-sample vibration.

The solution to this problem is to ground the Z motor whenever it is not required to be connected. An automatic relay connection/disconnection system was implemented, as

described in Appendix C. This system involves a few timing circuits to connect the piezo motor through a relay, allow a delay for the relay contact to settle, then trigger the motor pulse signal, followed by the disconnection of the relay. The relay was implemented only on the Z channel of the piezo motor, since this was the only offending channel as determined by the power spectrum measurement. However, the power spectrum in Figure 3.21(a), was taken with the interferometer in a "noisy" state, which was unknown at the time (section 3.3.2, page 96). More recent measurements using the tunneling current and the interferometer in the "quiet" state revealed that **all** motors required improved grounding.

3.4.3 Tunneling current measurement

The tunneling current can be used as a sensitive indicator of the tip-sample distance due to its rapid decay of ~ 1 decade per Ångstrom (section 2.4.1, page 19). In order to measure tip-sample vibrations, distance feedback must be turned off or considerably reduced. The tip-sample junction must also be atomically stable so that atomic scale processes do not contribute to fluctuations of the tunneling current. This is difficult to achieve on Au(111) due to a very mobile adatom population, but was possible on Cu(100) and Si(111).

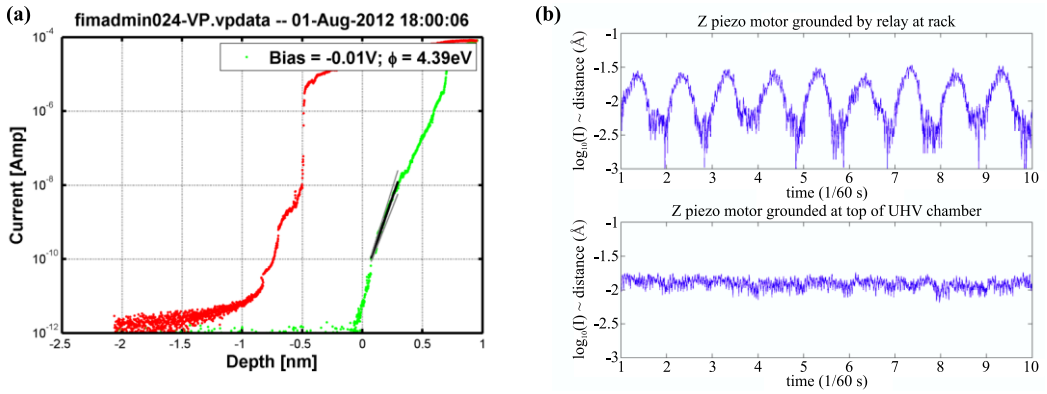

Figure 3.22: (a) Characterization of the apparent barrier height on Cu(100) used to convert tunneling current modulations to distance modulations. (b) Distance modulations derived from the tunneling current in the absence of feedback with the Z piezo motor grounded at the rack (top), and at the UHV chamber (bottom).

In Figure 3.22(a), we characterize the distance dependence of the tunneling current. In repeated measurements, the apparent barrier height extracted from a fit to the tunneling current between 0.1 and 10 nA was found to be on the order of 4 eV, as expected for a clean metal-metal junction. Turning feedback off, we measure the variation of tunneling current and convert this to distance variations. The top half of Figure 3.22(b) shows a distance

variation of ~ 1 Å between tip and sample at a frequency of 60 Hz – the horizontal axis is plotted in units of 1/60 s to emphasize this. From this measurement, it is apparent that a line frequency modulation of the tip-sample distance occurs when the Z motor is grounded at the rack by the relay implemented in section 3.4.2 (even though high frequency noise was suppressed). The noise does not occur if the Z motor is grounded at the top of the UHV chamber, shown in the lower half of Figure 3.22(b).

Grounding of all piezo motors (X, Y, Φ, Θ, Z) was implemented by a set of 5 relays installed near the top of the vacuum chamber. These relays are actuated automatically when needed, or through a manual bypass (see Appendix C). The relays are shown in a photograph in Figure 3.23 along with some other parts nearby on the top vacuum flange.

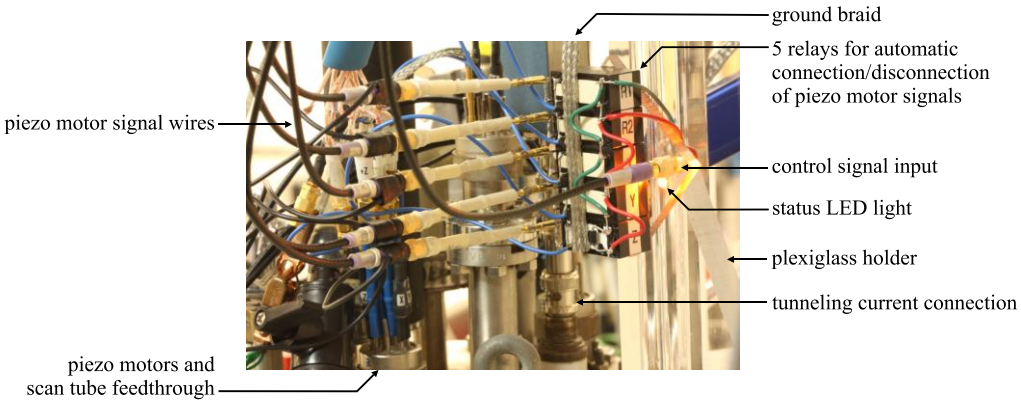

Figure 3.23: Photograph of the 5 relays that are used to ground all piezo motors automatically when not needed.

3.4.4 Cantilever beam resonance coupling

We saw in section 3.4.1 that our cantilever beams can problematically couple to noise at their resonant frequencies. We return to discuss the elimination of the last few noise sources that are problematic for the cantilevers.

The turbomolecular pump's first harmonic at 1720 Hz is often very close to the resonance frequency of our cantilever beams, owing to their geometry. We show an example of a sample with a resonance frequency of 1584 Hz used in a nanoindentation experiment in Figure 3.24 (b). As the tip is pressed into the sample, the resonance frequency increases, and as it crosses 1720 Hz, a large excitation is seen on the blue force channel (circled in red). The excitation is also present in the measured current (green), due to the conductance of the junction being modulated by the mechanical vibration of the cantilever. The turbo pump frequency is crossed again near the end of the indentation

which also excites the sample. The mechanical excitation of the sample makes experiments difficult to interpret: Is the threshold force for initiating plastic deformation affected by the oscillations of the cantilever? Will the observed adhesive force be accurate if the sample is excited as the tip is retracted from the sample?

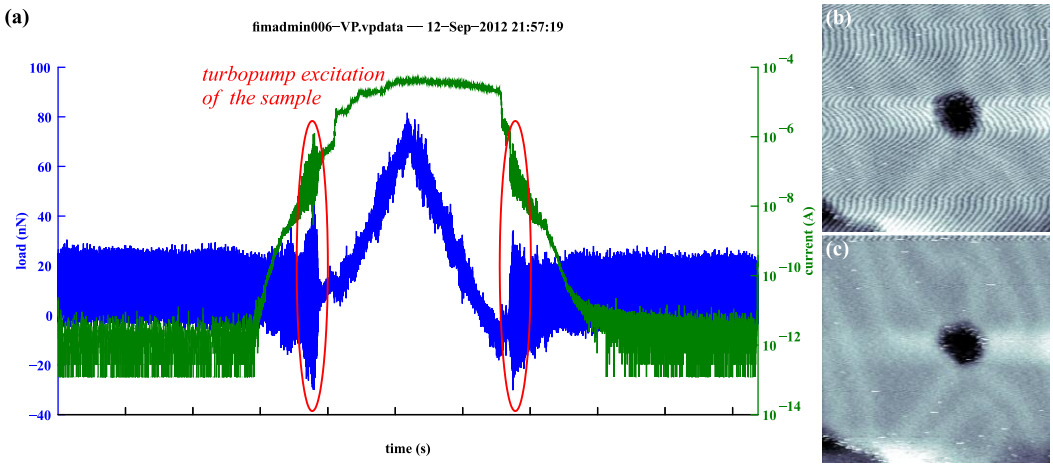

Figure 3.24: (a) Indentation curve showing force (blue) and current (green) as a function of time. The sample becomes excited by the turbo pump near the beginning and end of contact. (b) STM image taken on a different sample at 6 pA, -0.6 V; (c) STM image of the same region as (b) but at a different setpoint of 6 pA, -1.3 V .

Even when the tip is not in contact with the sample (beginning and end of the curve), it remains affected by the oscillations of the turbo pump. This sample should be replaced with one that has a frequency higher than that of the turbo pump. This is possible when our 50 μm thick mica beams are cut to a length of 5 mm or less (Eq. (19), page 29). Higher harmonics of the turbo pump don't seem to be as catastrophic to samples, so for the moment, designing them to have a resonance frequency around 2000 Hz is a reasonable solution. A real solution would be to turn off the turbo pump during measurements, but one would need to continue pumping with some other pump, such as an ion pump or non-evaporable getter pump. The latter choice would be ideal as it would also help to purify the He gas during FIM imaging. Non-evaporable getter pumps also have extraordinarily high pumping speeds (~200 l/s, about the same as our turbo pump) and are very small (can be installed in a 2.75" vacuum flange).

We move on to another sample, this one with a resonance frequency 1938 Hz – higher than the turbo pump's 1720 Hz excitation. STM images on this sample are shown in Figure 3.24 (b) and (c). The image shown in (b) is corrupted by sample vibrations, showing up as wiggly stripes down the image. By changing the STM setpoint from 6 pA at -0.6 V to 6 pA at -

1.3 V, the tip-sample distance, and therefore force gradient, is changed. The imaging becomes much steadier, shown in (c).

In this example, it is not clear exactly what is driving the cantilever beam, but the manner in which it is translated into stripes in the STM image is rather interesting: The wiggles seen in (b) are due to the STM feedback following a large signal at ~218 Hz in the current channel (seen in the power spectral density, not shown). 218 Hz is the difference frequency between the cantilever resonance and the turbo pump first harmonic. The non-linear I(z) behaviour of the STM junction serves to mix the 1720 Hz and 1938 Hz peaks, providing a substantial current signal at 218 Hz which is right in the middle of STM bandwidth. The STM feedback then responds to this signal with a real tip-sample modulation at 218 Hz which is visible as stripes in the topographic image. This is yet another detrimental effect of the turbo pump vibration; this time it affects imaging in a relatively convoluted way.

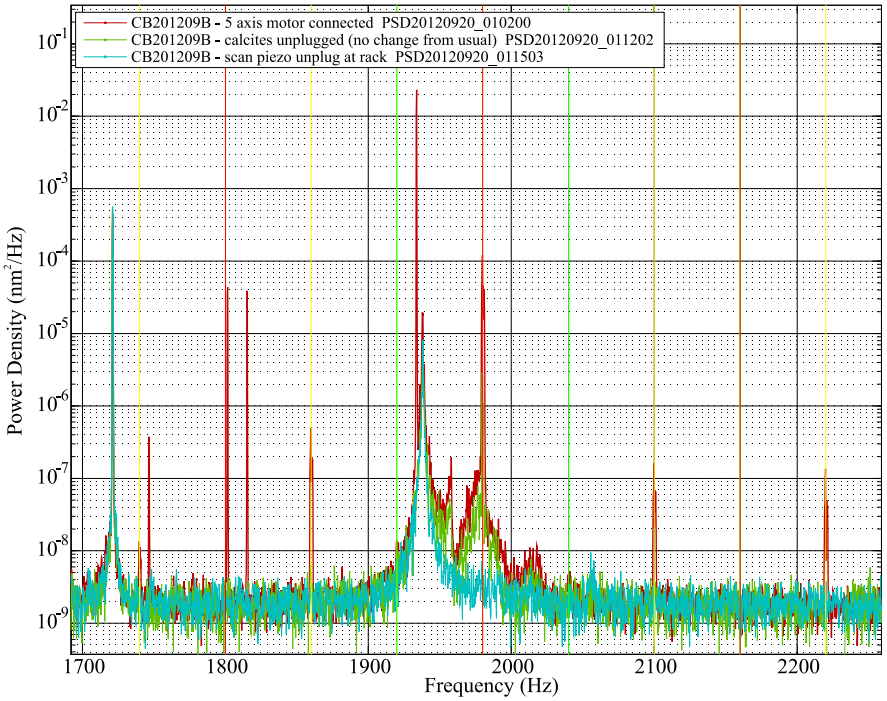

Figure 3.25: Deflection power spectrum of a cantilevered sample showing the effect of grounding the 5 piezo motors (red → green), and of unplugging the scan piezo (green → turquoise)

The last source of sample excitations to be discussed is line noise on our high voltage amplifier (custom electronics commissioned by McGill from the University of Basel ca. 2004). A power spectrum of the deflection signal is shown in Figure 3.25. In this figure, the benefits of proper grounding of the 5 piezo motors are illustrated in the difference between the red and green curves, where many noise peaks at line frequencies disappear, along with

some peaks at other strange frequencies such as 1934 Hz. The turbo pump is seen at 1720 Hz, and the first mode of the sample is at 1938 Hz. In the green curve, a large peak remains at 1980 Hz, the 33rd multiple of 60 Hz. This excitation is seen when the tip is retracted from the sample, and was finally attributed to the mechanical shaking of the scan piezo coupling to the cantilever through the microscope body – even when the tip is retracted! The only reason that we have the sensitivity to see this noise peak, or the sensitivity to be bothered by it, is because the cantilever resonance is very close by. The turquoise curve shows the power spectrum with the scan piezo unplugged, showing its disappearance.

Attaching a different high voltage amplifier (Ergonomics or Nanonis, borrowed from other SPM experiments) showed that the line peak was unique to our amplifier. However, the broader resonances around 1980 Hz (red and green curves) were more pronounced with the other amplifiers. The white noise on the output of our Basel-built amplifier is lower than the other amplifiers (this is because its overall gain is less, so the corresponding voltage noise is smaller); we attribute the broad peaks to the white noise excitation of mechanical resonances in our STM by the piezotube.

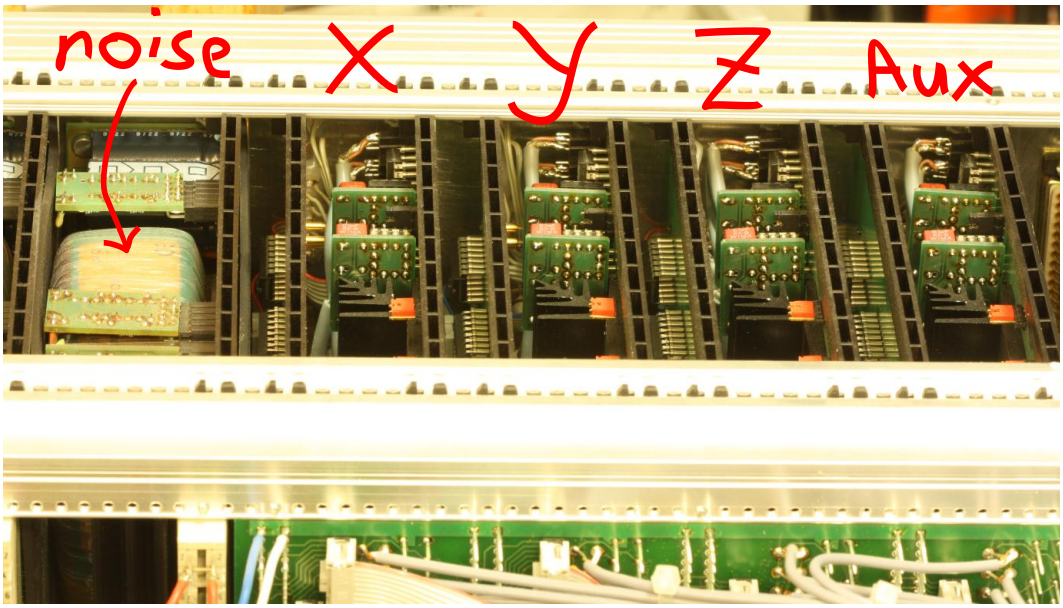

Figure 3.26: Photograph of the interior of the high voltage amplifier with noisy power supply and X, Y, Z, Aux high voltage amplifiers labeled.

Knowing that the noise was coming from our high voltage amplifier, we set about to determine if one particular channel was contributing to it more than others. Indeed, the X channel was most noisy, followed by Y, then Z. As shown in Figure 3.26, the X channel is

closest to the source of noise – a power supply board hosting a big toroidal transformer (a second one e

xists just to the left of this one). Upon investigation, this particular power supply board was not actually being used to power anything, so it was unplugged. The X channel signals were then internally re-wired to be amplified on the Aux board (the farthest from the noise source), which was unused. A mu metal shield between these components might solve the problem in the case that four channels need to be operated simultaneously…

This has hopefully relayed some important sources of noise that may exist to mechanically drive the tip-sample junction. Solving these issues contributes to more reliable experimental results and a larger fraction of usable samples.

3.5 Field ion microscopy

The simultaneous design requirements of low-noise STM and high-voltage FIM operation in this instrument present significant practical challenges. On the one hand, coaxial cabling is desirable for low-noise STM current detection, but offers a considerable design challenge when a 10 kV potential must also be carried by this cable. High voltage breakdown in vacuum also contributes to problems – even a small continuous discharge somewhere in the system will create a source of ions or electrons which are collected by the microchannel plate and phosphorous screen, giving it a uniform green glow and rendering FIM useless. In more dramatic situations, sparks occur between various parts of the apparatus rendering FIM impossible (these can also damage electronics).

The reliability of the FIM has been an issue for many years, and numerous lab books are filled with frustrated complaints on the topic. After solving other reliability issues with the SPM, it was clear by mid-2010 that the FIM was severely limiting experimental productivity. In desperation, I even designed a separate FIM to be accessible with the existing sample transfer tools in the UHV system. This separate FIM would require the tips to be manually transferred to it from the STM, and then translated along a rail to the position of a new microchannel plate and phosphorous screen. This separate FIM would allow properly specified high voltage design to be carried out without compromising STM performance or FIM reliability, as well as adding the possibility of cryogenically cooling tips during FIM.

The new FIM design was put on hold (after most of it was machined) during the visit of Prof. Moh'd Rezeq in summer 2010. Prof. Rezeq suggested that we temporarily re-wire the existing FIM/STM with bare copper wire insulated by Teflon tubing to accomplish reliable

FIM operation during his visit (in which we investigated nitrogen sharpening of FIM tips as per section 2.8.3). An improved version of this wiring was built based on a custom coaxial cable made from Teflon tubing and copper shielding braid. A new way of attaching it to the STM also had to be found, described in 3.5.1.

Once these problems were solved, high voltage breakdown near the tip holder was still a recurring issue. The breakdown at the tip holder was eliminated once the physical origin of voltage breakdown along insulating surfaces was understood, as discussed in 3.5.2. One issue that makes this work so tedious is the fact that one cannot simply pump the vacuum system and switch on the high voltage to test each configuration. The microchannel plate and phosphorous screen must be active (biased to high voltage) to report on any green glows originating from electron or ion emission in the system. However, the chamber must be baked fully to first degas the microchannel plate and phosphorous screen – this effectively means a delay of a week for each configuration to be tested!

3.5.1 High voltage coaxial wiring

The original STM/FIM tip wire connected to a length of Kapton insulated coaxial cable (KAP3, MDC Corp) which served to bring the tip wire out of the microscope body and then connect to a larger triaxial cable which attaches to the vacuum feedthrough. Several attempts were made to re-build the KAP3 cable connection with subtle improvements, but none provided a reliable solution.

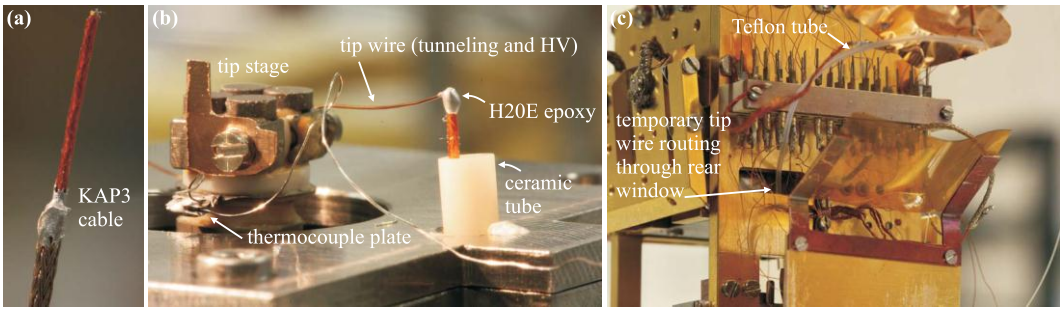

Figure 3.27: (a) 0.97mm diameter KAP3 coaxial cable, stripped and shield ends secured with H20E epoxy. (b) Connection of the tip stage to the stripped end of the KAP3 tube with H20E epoxy. Ceramic tube by which the KAP3 passes through the coarse approach unit. (c) Temporary solution showing Teflon tube insulated copper wire passing through the rear microscope window.

In the original configuration, the KAP3 wire was fed through ceramic insulators passing through the Z coarse approach unit designed by Till Hagedorn (described in Ref. [50]). Sparks were often observed coming from around the ceramic insulators, so the cable was

replaced, with the added feature of securing the trimmed cable shielding with Epotek H20E conductive epoxy to avoid sharp protruding filaments from the shielding braid, Figure 3.27 (a). The ceramic insulating tubes were also re-machined and replaced, seen in Figure 3.27 (b), and a short bare copper wire was neatly attached to the end of the KAP3 cable using H20E epoxy. This configuration worked several times, and then began sparking near the ceramic tube. Two major issues remained with the design: KAP3 is only rated to 2kV DC – perhaps the dielectric was breaking down, but also the KAP3 cable passes through a sharp right-angle in the Z coarse approach block – this makes the wire very difficult to install and likely damages the dielectric when it is maneuvered around the corner.

A temporary solution consisting of a bare copper wire shielded by a Teflon tube (which was key in inspiring the permanent solution) was implemented in summer 2010. The 1/16" OD Teflon tube was passed through a small window in the rear of the STM/FIM, as shown in Figure 3.27 (c). The Teflon insulator solved the high voltage breakdown problems related to the wiring, but added noise to current detection in STM due mechanical vibrations transduced by the capacitive coupling of the unshielded tip wire with respect to the high voltage piezo tube wires (~100 V) which pass through the same window.

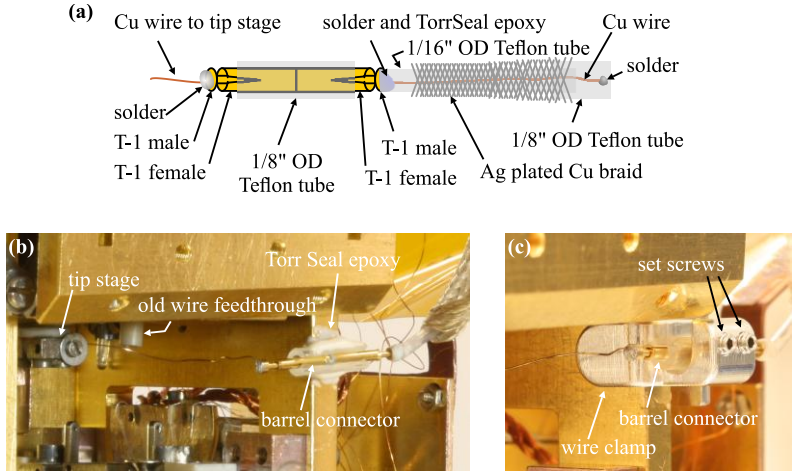

Figure 3.28: (a) Schematic assembly of a custom Teflon tube insulated double barrel connector based on T-1 machined contacts. The custom coaxial cable based on Teflon tubing is electrically shielded with a Ag plated Cu braid. The larger 1/8" Teflon tube can be pulled over the 1/16" Teflon tube to access a solder point. (b) Photograph of the test implementation in which the double barrel connector was attached to the microscope wall with Torr Seal epoxy. (c) Photograph of the permanent installation using a custom built wire clamp which has set screws to secure the Teflon tube and barrel connector.

With the empirical demonstration that a Teflon tube has a high enough dielectric strength to withstand 10 kV on the copper wire, a coaxial cable and double female barrel connector were designed to connect to the tip stage. Shown schematically in Figure 3.28 (a)

is the design of a double barrel connector based on T-1 style machined contacts made of a gold plated copper alloy suitable for UHV (Accu-Glass Products), and a coaxial cable based on two Teflon tubes and 1/8" inner diameter silver plated copper braid shield (Accu-Glass Products). Regular rosin flux solder is used sparingly to make electrical connections after holding the molten solder on the hot iron tip for ~30 s until the flux is burned off[1].

A photograph of the barrel connector temporarily connected to the microscope body by Torr Seal epoxy is illustrated in Figure 3.28 (b). This connection worked flawlessly for high voltage. However, the mechanical stability of the Teflon tube in the Torr Seal was poor because the epoxy did not provide any clamping force, adding detection noise to STM. A custom clamp designed to hold the Teflon tube and barrel connector to the microscope body was built and installed in the system in September 2012, shown in Figure 3.28 (c).

3.5.2 High voltage breakdown

Figure 3.29 presents some typical photographs of high voltage breakdown around the tip stage. Generally, a steady green glow is observed on the phosphorous screen which may fluctuate in intensity and suddenly flash bright green, corresponding to the occurrence of vacuum breakdown. Figure 3.29 (c) shows the bright green glow of the phosphorous screen reflecting off the stainless steel walls of the UHV chamber surrounding the front viewport. The flashes were captured on camera by opening the shutter for many seconds at a time and waiting for vacuum breakdown to occur. The photographs give some clues as to what part of the microscope is causing problems. In each of the photographs in Figure 3.29, the flash happens on the tip stage (at high positive voltage) and the nearby thermocouple plate.

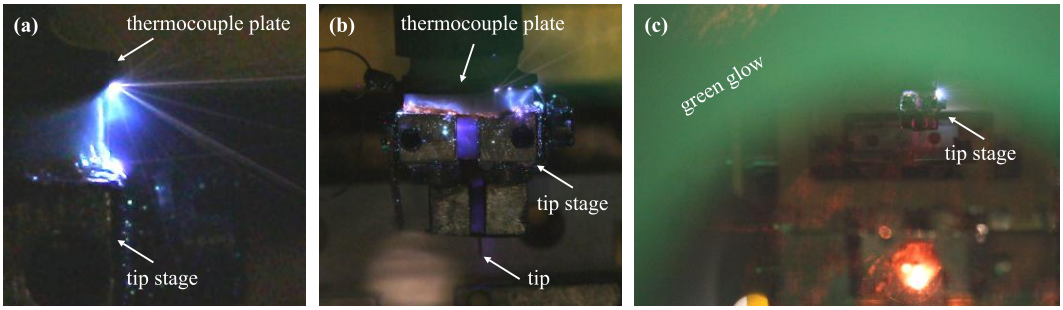

Figure 3.29: Vacuum breakdown near the tip stage.

[1] Although this is not "good" UHV practice, it had become a typical procedure on our microscope, and vacuum performance has apparently not suffered.

High voltage breakdown tends not to be covered in standard textbooks on vacuum technology such as Refs. [183, 184]. After some research, it became apparent that the field of vacuum breakdown is particularly relevant to vacuum tube technology, and many interesting and relevant references can be found from the 1950s. Two excellent book chapters on breakdown in vacuum are found in Refs. [185, 186], from which we obtain most of the specifics summarized here.

Given that our discharging behaviour is not changed by the presence or absence of He gas, we are not dealing with the breakdown of a gas described by Paschen's Law [71, 187]. Also, our $\sim 10^{-10}$ mbar base pressure is much less than the regime described by Paschen's Law, describing breakdown behaviour in the range of 1 mbar over a distance of 1 cm.

Electrodes in vacuum high voltage equipment must be supported on insulators (obviously), so it is inevitable that high voltage gradients develop across the surface and bulk of these insulators. For a given electric field, breakdown is most likely to occur across an insulator's surface, then through the bulk, then across a vacuum gap. It is well recognized in the vacuum tube literature that the onset of surface discharge in vacuum is controlled by mechanisms happening at the junction of vacuum, insulator, and metal, known as the triple junction. It is generally agreed upon that field emission at the cathode triple junction is the source of trouble, and then a set of various mechanisms can be hypothesized to describe what happens subsequently (most of which are good attempts to explain the data, but no single theory describes quantitatively or qualitatively all of the observed phenomena).

For instance, one could imagine that the field emitted electrons bombard the insulator's surface, emitting an avalanche of secondary electrons and desorbed gas molecules. The gas molecules, ionized by the electrons, drift toward the cathode and further enhance the field (space charge), thereby encouraging more field emission. This runaway process could lead to an avalanche of vaporized insulator material which would permit a plasma breakdown of the gas along the insulator surface.

There are several empirically determined design principles which are useful to know for surface breakdown:

- The choice of electrode material has little effect on the breakdown voltage.
- Lengthening the path by surface roughening does not work in high vacuum.
- The type of rest gas in unimportant in high vacuum.

In a system plagued by breakdown, one can attempt to increase the threshold for flashover by surface conditioning. This is carried out by gradually increasing the voltage until sparkover occurs, then decreasing the voltage to the operating point. Presumably this may reshape or remove some of the field emission sites and could increase the breakdown voltage by a factor of ~2× (whisker formation at the cathode leading to field emission has been observed in TEM [188, 189]). Surface conditioning doesn't work when flashover leaves residues on the surfaces, however. In our experience, surface conditioning has on occasion helped to increase the breakdown voltage by ~10 %, but sometimes this leads to complete failure of the insulating surface, draining enough current across the electrodes that the current limited power supply cannot exceed ~100 V.

From a design point of view, there are numerous ways to decrease the field at the cathode triple junction. For instance, reducing the dielectric constant of the insulator will proportionally decrease the value of the electric field inside any voids at the electrode junction. Judicious geometric design of the triple junction can also provide a factor of ~4× improvement in breakdown voltage, and we present a few representative results from Refs. [185, 190].

Figure 3.30 (a) shows the cross-section of a Pyrex cylinder between two copper disc electrodes. The design with the flat cathode has a breakdown voltage of 25 kV, whereas the inset cathode design, where the glass cylinder is placed inside a slot in the cathode (with radius of curvature 0.8 mm), has a breakdown voltage of 90 kV. Due to the placement of the triple junction within the body of the cathode, the field is greatly reduced, hampering the field emission initiation of surface breakdown. The geometric effect of the triple junction is also clear in Figure 3.30 (b) where a borosilicate glass tube is sealed to a Kovar[1] cylinder with a void-free inside-outside seal on top, and a butt joint on the bottom. The breakdown voltage depends on the sign of the applied voltage, and is maximized when the anode is placed at the butt joint (110 kV), rather than the cathode (32 kV). One may also implement fancier insulator or electrode designs at the cathode such as those illustrated in Figure 3.30 (c). In the undercut design, the insulator directly adjacent to the cathode is undercut so that field emitted electrons will accumulate as a space charge near the cathode electrode and serve to decrease the electric field at the cathode. The cathode may also be extended into the dielectric to redistribute the field and reduce its value at the triple junction.

[1] A nickel-cobalt alloy designed to match the thermal expansion of borosilicate glass.

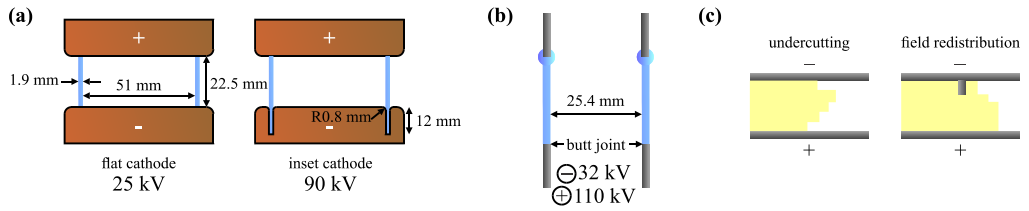

Figure 3.30: (a) Pyrex tube in between copper electrodes having a flat cathode and improved inset cathode design. (b) Kovar tubes joined by a borosilicate glass cylinder with one inside-outside seal and one butt joint – the design works best with the cathode at the inside-outside seal. (c) Techniques such as undercutting the insulator near the cathode surface to trap space charge and redistributing the field by extending the cathode electrode can help to maximize breakdown voltage.

Knowing that the cathode junction is most critical to breakdown, examining our setup in Figure 3.29 suggests that the thermocouple plate probably acts as a source of field emitted electrons (against the positive tip stage potential) which initiate breakdown. Although modification of the existing design would be rather tricky and time consuming, a very practical option is to simply remove the surface of the cathode by encapsulating it in epoxy – there is no reason that the thermocouple plate needs to be exposed. In order for breakdown to occur between the thermocouple plate and the tip stage, bulk breakdown of the epoxy encapsulation would be required (which is much more difficult than field emission and surface flashover). Epotek H77 non-conductive epoxy was chosen for its fantastic vacuum performance[1], and good dielectric strength. Since the epoxy is very runny when heated for curing, several coats were applied to ensure a complete encapsulation of the thermocouple plate. The changing viscosity of the epoxy makes is somewhat difficult to control when curing, giving rise to the admittedly untidy appearance of the encapsulation. Photos taken before and after the encapsulation of the thermocouple plate are shown in Figure 3.31.

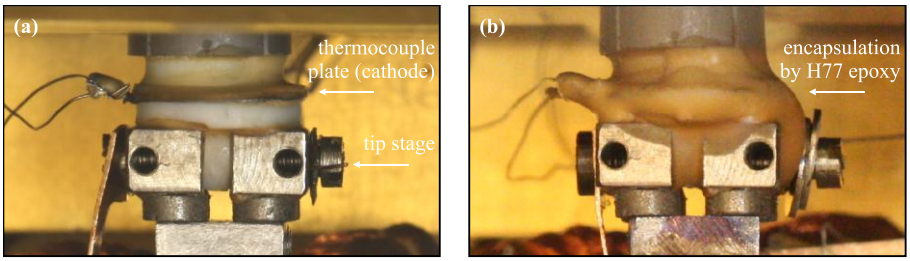

Figure 3.31: (a) The thermocouple plate is an exposed cathode electrode. (b) The encapsulated thermocouple plate can no longer field emit electrons when the tip stage is biased to a high positive voltage.

[1] An excellent database on the outgassing of materials in vacuum is maintained by NASA at http://outgassing.nasa.gov.

Removal of the cathode electrode completely solved the routine problem of high voltage breakdown at the tip stage. An understanding of the mechanisms of high voltage breakdown in vacuum was crucial to its diagnosis and solution.

3.5.3 Data acquisition for FIM

A working FIM can quickly generate large amounts of image data, along with pages of lab notebooks filled with tip imaging voltages. As it is never an ideal situation to record images and applied voltages in different places, a high voltage divider was built so that the FIM high voltage could be recorded by a computer controlling the image acquisition. We briefly describe the high voltage divider and data acquisition here.

The high voltage divider was designed to divide by 1000 using a 1000 MΩ and 1 MΩ resistor[1], such that the 10 kV range could be acquired by a corresponding analog voltage up to 10 V. 10 kV is a rather large voltage to put across a 1000 MΩ resistor, which must have a wattage rating of $> V^2/R = 0.1$ W and also be able to withstand the 10 kV potential difference without dielectric breakdown. Ohmite's Maxi-Mox series is especially designed for high voltage applications up to 50 kV. Here we use the 20 kV rated MOX-2-12-1007FE available from Newark. This is a rather large resistor at 54 mm length for the 20 kV version, and they extend up to 130 mm long for the 50 kV rated resistors!

The circuit diagram of the divider is shown in Figure 3.32. A second 1000 MΩ resistor is added before the low voltage output to add extra output impedance just in case something sparks across the first 1000 MΩ resistor. An additional safety feature is a gas discharge tube placed across the 1 MΩ resistor which shunts the resistor in the case where the potential exceeds 75 V, illustrated in red in Figure 3.32.

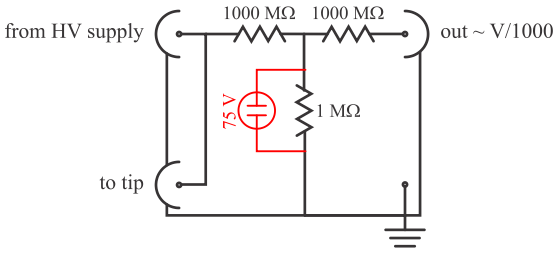

Figure 3.32: 10kV high voltage divider for FIM voltage acquisition.

[1] The divider therefore actually divides by 1001…

Due to the high input impedance of the divider's output, it cannot directly drive the input of our National Instruments USB-6259 BNC card. It is therefore attached to the data acquisition card via a unity gain buffer amplifier built with a TL074 chip (10^{12} Ω input).

Control of our Canon EOS XSi digital SLR camera is achieved in Matlab using Breeze Systems DSLR Remote Pro which is triggered to take pictures using the command line. Matlab acquires the FIM voltage from the National Instruments card, and then triggers a photograph to be taken and writes the applied voltage to the digital photograph's EXIF data 'UserComment' field. This method allows for easy data browsing and the impossibility of separating image and voltage data!

Computer acquisition of the image data in custom built software enables convenient access to camera control for shutter speed and crop settings. The acquisition of images directly to the PC also means that data processing can be performed on the fly during experiments, such as the display of a log contrast image to provide the user with a more detailed preview while acquiring FIM data and an averaging preview which can average *n* previous images for a better signal-to-noise image preview. Image differencing is also performed to visualize increases (blue) and decreases (red) in image intensity between subsequent frames which makes field evaporated atoms show up as red dots, shown in Figure 3.33.

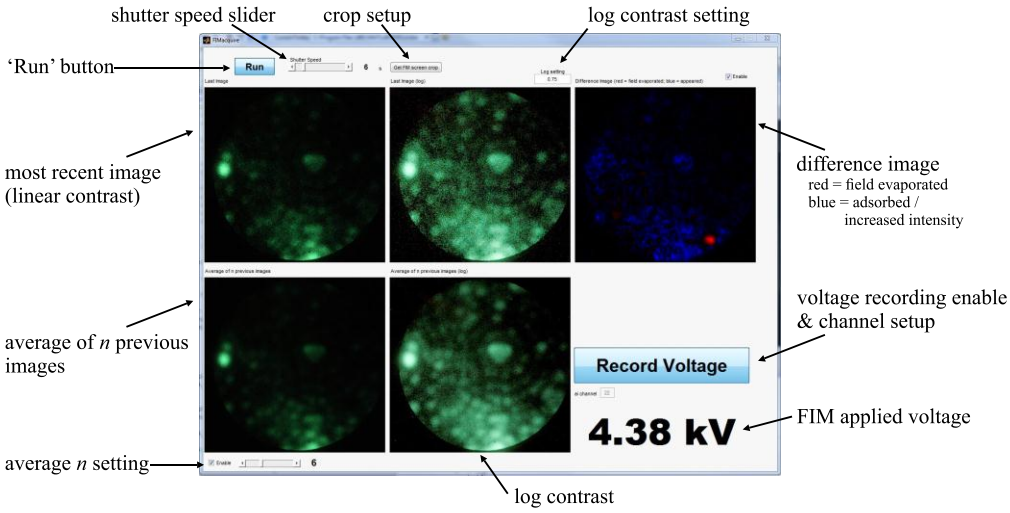

Figure 3.33: Screenshot `FIMacquire`, the Matlab-based FIM data acquisition program and camera controller.

3.6 Summary and outlook on reliability

3.6.1 Summary

Habitual acquisition of noise power spectra and a familiarity with typical noise signatures helps to diagnose problems and identify noise sources.

In our system, the current detection noise in STM is not limited by the Johnson noise of the preamp's resistor – demodulated radio, acoustic, ground, and capacitive noises all contribute to a substantially larger detection noise baseline but can be largely eliminated by detailed study of power spectra.

The interferometer detection noise was shown to be practically limited by classical laser phase noise scaling with optical power, not shot noise. The differential noise character of the interferometer was demonstrated, and a strange behaviour of phase noise was unveiled, giving practical suggestions for low-noise operation (check both fringe signs). We emphasized the use of calibrated power spectra to reflect signal-to-noise and pointed out that sensitivity is often not a good figure of merit. A rare complete power shutdown allowed the investigation of the still limiting ~30 Hz cluster of mechanical noise peaks.

Our cantilevered samples change resonance frequency considerably during indentation measurements and thus necessitate a mechanically quiet tip-sample junction. Substantial improvements were achieved by proper grounding of piezo motors and eliminating line frequency excitation of the scan piezo, but the turbo pump still contributes mechanical and detection noise which can cause sample excitations that affect imaging and indentation.

Feedback coupling between detection noise and the mechanics of the tip-sample junction can also provoke mechanical noise from detection sources.

New custom coaxial wiring designed for FIM and STM has allowed FIM to be carried out without sparking and still allows for stable STM operation. An understanding of the initiation of surface breakdown was instrumental in correcting sparking near the tip stage. Finally, high voltage data acquisition was implemented for FIM operation.

3.6.2 Outlook

Efforts to understand the noise sources in STM and AFM have led to a systematic improvement of the quality of our experimental data. Features in the detection noise power spectra are now no longer so mysterious: the sources of much of the line noise, radio noise,

and mechanical noise (sourced from electronic noise or building vibrations) have been identified. To emphasize the improvements in deflection detection noise, we show in Figure 3.34 a power spectrum of the deflection noise taken several years ago on the same instrument (reprinted from Mehdi El Ouali's thesis [49]). The insert shows a power spectrum from the recent building power shutdown in Figure 3.19 to scale with El Ouali's data. In 2008, we had no idea where all the observed detection or mechanical peaks at line frequencies came from, as well as all the clusters of peaks in the kHz range arising from piezo motor amplifiers. In fact, at that time, it was a challenge to identify the cantilever's resonance buried in all of these peaks! Today, we observe a nearly phase-noise limited deflection power spectrum.

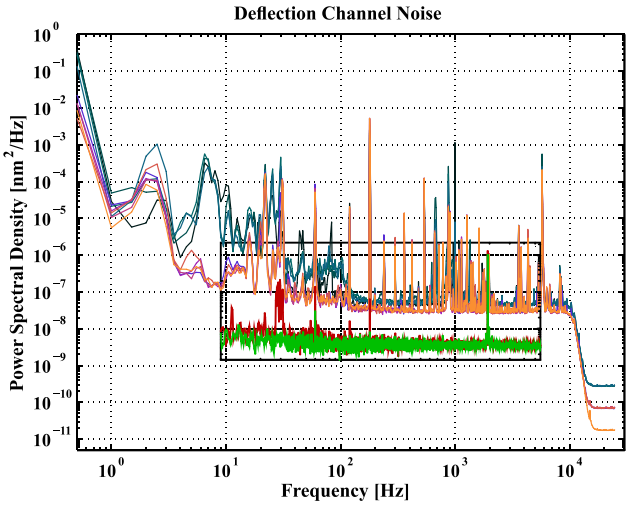

Figure 3.34: Deflection noise power spectrum reprinted with permission from [49]. Inserted is the deflection noise power spectrum data from the building power shutdown presented in Figure 3.19.

There are still some severely limiting noise sources which we now understand but for which we have no immediate solution. These comprise (1) 30 Hz building vibration peaks, (2) turbomolecular pump 1720 Hz noise, (3) mechanical noise in current detection.

The 30 Hz building vibrations were shown to be sourced from equipment elsewhere in the building and probably transduced through our bungee cords. The passive mass-spring damping of the vacuum system hanging from the bungees has a very low resonance frequency due to the long extension length of the bungees. Hanging a mass m from a spring of stiffness k extends the spring by a length $\Delta x = F/k = mg/k$. The figure of merit for

passive vibration isolation by hanging a mass from springs is therefore just the extension length of the springs, as the resonance frequency depends only on the extension Δx[1]:

$$f = \frac{\omega}{2\pi} = \frac{1}{2\pi}\sqrt{\frac{k}{m}} = \frac{1}{2\pi}\sqrt{\frac{g}{\Delta x}} \approx 0.5\ (\Delta x\ [\mathrm{m}])^{-1/2}\ \mathrm{Hz}\,. \tag{43}$$

For a spring extension of 1 m (on the order of what we have), the resonance frequency is 0.5 Hz, which offers vibration isolation performance close to that of commercial isolators. In our case, the 30 Hz peaks may also couple through higher transverse or longitudinal modes of the bungees. Depending on the source of the noise peaks, a floor-based support system may offer less mechanical noise than our ceiling-anchored bungees (if the noise is sourced from say elevator motors located on the roof). One could also consider relocating the UHV system to a basement laboratory, for example. One could then obtain a flat, phase noise limited detection noise power spectrum. These ~30 Hz low frequency detection noise peaks severely limit AFM noise performance and would be necessary to fix for molecular electronics studies where sub-nN force resolution is needed.

The STM chamber turbo pump must be running during experiments to maintain good vacuum pressure, but causes a large mechanical tip-sample noise peak at 1720 Hz. This can couple directly to the cantilever beam resonance during indentation experiments, forcing samples to be designed with resonance frequencies higher than 1720 Hz. It can also produce a low-frequency tunneling current noise (we saw 218 Hz) by mixing with the cantilever resonance frequency in the non-linear tunneling junction. Ideally, one would install a non-evaporable getter pump (no moving parts) on the vacuum chamber and turn off the turbo pump during SPM measurements.

Finally, I suspect that many of the remaining STM detection noise peaks are due to mechanical vibrations, shown in Figure 3.3, and could be solved by improving the wiring to the STM tip. For a start, one could try removing the unshielded wire leading from the barrel connector to the STM tip stage (Figure 3.28 (b)) to determine if this portion of the circuit should be better shielded or mechanically stabilized.

On top of the improvements to the SPM, the FIM now works without discharging issues. After correcting the high voltage breakdown problems, the FIM has worked completely reliably since summer 2011 and has been used in over 185 FIM measurements (Aug 2011 to

[1] Credit to A. Labuda for having pointed this out to me rather recently.

Sept 2012) without sparking or discharging issues. The FIM/STM/AFM is ready to welcome in a new era of experimental productivity.

4. Atomically defined tips: from FIM to SPM

The utility of the FIM for preparing and characterizing tips destined for SPM experiments was considered by Hans-Werner Fink of IBM Zürich in the context of STM shortly after its invention [35]. The main advantage of an atomically defined tip apex is clear: If the exact atomic arrangement of the apex is known, the electronic structure of the tip and the lateral resolution of the STM are predetermined. The same detailed knowledge of the apex termination, as well as the tip radius, is useful for Atomic Force Microscopy (AFM) experiments, and important in the interpretation of results from combined STM and AFM experiments.

Furthermore, since the transport properties of a molecular junction are sensitive to the atomic arrangement of the contact electrodes [33], FIM characterized tips are excellent candidates for constructing and studying well-defined junctions in STM/AFM. One motivation for our work is the construction of an atomically defined metal-molecule-metal junction by contacting a C_{60} molecule using the known atomic structure of a FIM tip apex and investigate its mechanical and electrical properties through force and current spectroscopy. A starting point for this pursuit is to figure out how to reliably transfer an atomically defined FIM tip to a SPM experiment and be sure that the atomically-defined apex structure from FIM is in fact maintained in the tip-sample junction.

Many questions need to be addressed concerning the implementation of FIM tips in SPM: Will the atomically defined tip be modified by impurities in the FIM imaging gas? If so, can this be avoided? Although UHV is very clean, it still has a finite rest gas pressure – how long will the atomically defined tip remain atomically defined in vacuum? How much time do we have to perform our atomically defined SPM experiment? How can we approach the tip to the sample and ensure that it doesn't crash or become modified upon interaction with the substrate?

Performing SPM with tips characterized in FIM is an exercise in extreme dynamic ranges in short periods of time: Tips and samples must be translated from a relative separation of $\sim$ 1 m down to a controlled separation of $\sim$ 1 Å without overshooting (crashing the tip). Electrical connections must be switched over between the two modes of microscopy and the applied voltages change from order 1 V in STM to 10 kV in FIM. The vacuum pressure must also change from $\sim 10^{-11}$ mbar to 10^{-5} mbar of He and back. It's a tour-de-force that requires plenty of lab equipment to work very reliably.

This chapter begins with a comprehensive review of combined FIM and SPM experiments appearing in the literature. We then address the integrity of FIM tips with regard to the imaging gas and UHV rest gas during the delay time required for a SPM experiment, and support this with experimental data. The formation of tunneling gaps with FIM tips in STM on several types of substrates will also be described.

4.1 Review of combined FIM/SPM literature

A handful of groups have worked to combine FIM and SPM from the mid-1980s to the late 1990s. We review the work of the principal groups in this field in an approximately chronological order and conclude with a brief summary including an outlook on current experimental progress.

4.1.1 Kuk & Silverman (AT&T Bell Laboratories, New Jersey, USA)

The first report of combined FIM and STM techniques was from Kuk and Silverman working at AT&T Bell Laboratories in New Jersey. Their only results appear in a two-page Applied Physics Letter about the measured corrugation height of the rows of the (1×5) reconstructed Au(100) surface with a W(100) tip at room temperature [191]. The same results also appear in a well-cited paper about STM instrumentation published in 1989 [179]. The authors do not present a convincing discussion about maintaining tip integrity throughout the experiment, and the quality of the FIM data is primitive (due to image acquisition tools available at the time). In this work, it was assumed that the tip was unchanged, but our experience with FIM suggests that it can be rather easy mistakenly assess that tips are unchanged because their crystalline structure is self-similar: Inadvertently removing a layer or two of material will expose an identical looking tip[1]. This was, nevertheless, a demonstration that a combined FIM/STM instrument can be built.

[1] This is one reason that monitoring the entire FIM process by high dynamic range digital photography is necessary.

4.1.2 Sakurai (Tohoku University, Japan)

Toshio Sakurai's group from Tohoku University in Sendai, Japan published quite extensively about combined FIM and STM in a technique they refer to as field ion-scanning tunneling microscopy (FI-STM). By 1989, Sakurai had built a series of room temperature FI-STMs [192]. A review article on the FI-STM technique appeared in Progress in Surface Science in 1990 [193]. In the early 1990s, the group focused on silicon surfaces and worked to study the surface bonding of C_{60} molecules [194-196] and alkali metals [197]. Their use of FIM is not even mentioned in several of these publications, and no FIM images appear in any. When tip characterization by FIM is mentioned, it is only used as a confirmation that the tip is clean and sharp enough to ensure reliable atomic resolution. The role of the tip's atomic structure in STM imaging was not an explicit concern in this work.

4.1.3 Tomitori (Tokyo Institute of Technology, Japan)

Some very diligent combined FIM/STM work was carried out by Masahiko Tomitori while based at the Tokyo Institute of Technology, Yokohama, Japan between ~ 1990-1996. Tomitori used FIM to evaluate a new coarse approach mechanism being designed for fast tip approach, then investigated the application of FIM tips to obtain better reproducibility in scanning tunneling spectroscopy (STS).

The first work investigating STM tip approach was performed in air on freshly cleaved highly oriented pyrolytic graphite (HOPG), and the PtIr alloy tips were transferred to and from vacuum for FIM characterization [198]. The goal was *not* to implement atomically defined tips in air; they wanted to ensure that the tip apex did not crash into the substrate inadvertently during coarse approach. Tomitori underlined the necessity in performing the tip approach within the bandwidths of the STM feedback loop and current preamplifier – exceeding these bandwidths could result in crashing the tip without any sign of a current spike arising from mechanical contact. Approaching the tips too quickly was found to render the tip apex non-observable in FIM; a large amount of carbon, hydrogen and oxygen had also been transferred to the tip apex, detected by a Time of Flight (ToF) mass spectrometer.

In 1996, Tomitori reported results of STS with a 'build-up' tip in UHV. The motivation here was to try to develop an experimental procedure to obtain reproducible STS data by controlling the tip geometry – that way, the STS technique could be more straightforwardly

applied to unknown samples. The tips consisted of a W(111) wire whose apex was shaped into a triangular pyramid of W(112) facets by thermofield annealing, also known as the 'build-up' method (discussed in section 2.8.3). The tips were characterized by FIM with Ne gas in a separate chamber. Tip characterization was also possible in the STM chamber, but only by field emission microscopy (FEM)[1]. Tip preparation by thermofield annealing could be carried out in either chamber.

The field emission pattern is characterized by a three-fold symmetry arising from the W(111) plane (because of its low work function, it emits a larger current than other planes). FEM is sensitive to work-function changes arising from adsorbed atoms and molecules, and to the general symmetry of the tip apex. FEM was used as an indicator of tip integrity since it did not require introducing any imaging gas which could destroy the fine structure of the tip – this seems to be the first reported concern regarding tip integrity with respect to the imaging gas.

STS was carried out on the Si(111)-7×7 surface in 64 × 64 point arrays in order to average over the surface unit cell, and spectra were found to be reasonably repeatable with the build-up tips as long as the bias range was kept within -2 to +2 V. Tips retained similar patterns in FEM with slightly modified voltage thresholds for imaging (perhaps indicating a minute tip change). Expanding the STS bias range to -3 to +3 V altered the STS spectra radically, and FEM showed large changes present on the tip, attributed to the transferral of Si atoms from the substrate.

These two studies by Tomitori provided valuable early insights into the implementation of atomically defined tips in STM: Feedback and current detection bandwidths must be respected to avoid tip crashing on approach, FEM might be a less awkward way than FIM to check for tip changes due to the absence of potentially corrosive imaging gas, and STS can be implemented without significant tip changes as long as the bias voltages are kept within a small enough range (± 2V).

[1] FEM operates in a similar manner to FIM, but a field emission current is detected rather than field ionized gas atoms. A spatial map of the field emission current is visualized on a MCP/phosphorous screen when the tip is negatively biased.

4.1.4 Weierstall & Spence (University of Arizona, USA)

A combined STM with a ToF atom probe was built during Uwe Weierstall's postdoctoral appointment at the University of Arizona with well-known electron microscopist John Spence. They called the instrument the Scanning Tunneling Atom Probe (STAP), and it was intended to be a means of providing the STM with chemical identification in a kind of "atomic tweezer". The goal of this instrument was to transfer a chemically unknown species from the sample to the tip, say by pulsing the STM bias voltage, switch over to ToF mode and identify the chemical species ejected from the tip. Their first report in 1996 demonstrated the proof of concept of the STAP [199]. The atom probe's mass-to-charge detection was calibrated by W^{3+} and W^{4+} field evaporated from tungsten tips, and the authors presented a preliminary result measuring a handful of Si atoms transferred from a Si(111)-7×7 surface to a tip apex, as identified both in STM imaging and ToF mass spectrometry.

A second and final paper from this instrument was published in Surface Science in 1998 [200]. Although FIM characterized tip apices were not an objective of their work, some aspects of this second paper are relevant to our implementation of atomically defined tips. ToF revealed that some care had to be taken in order to not overshoot the tunneling current setpoint upon initial approach and transfer Si atoms from mechanical contact, as noted by Tomitori. The authors report statistics on an impressive number of experiments: After improving their tip approach procedure, in ~ 80% of about 50 experiments, W tips could be scanned and returned for ToF analysis without having picked up Si atoms. In ~ 20% of cases, a tip change occurred while scanning, often accompanied by a sudden improvement in STM resolution, and this correlated with the detection of Si transferred to the probe tip.

Although single-ion sensitivity is possible with their chevron microchannel plate, the open area for detection is only ~ 60%. Nevertheless, the statistics are quite convincing that W tips can be approached to tunneling proximity in STM without the transferal of atoms from the substrate, but tip changes seen during imaging correlate with atom transfer. FIM imaging of the tip is missing from these studies, but they are quite valuable from the standpoint of considerations of material transfer affecting our atomically defined tip apices.

4.1.5 Leisch (Graz Institute of Technology, Austria)

Manfred Leisch's group at the Graz Institute of Technology, Graz, Austria built a position sensitive atom probe detector to be used in conjunction with a commercial Omicron STM-1.

Only two publications came from this work. In the first, appearing in Fresenius' Journal of Analytical Chemistry in 1999, the authors state their interest in performing experimental research on the mechanical interaction between materials on the atomic scale [201]. The focus on nanomechanics was inspired by early work in atomistic simulation which appeared during the 1990s to address atomic scale wetting, adhesive bonding, connective neck formation, and plastic deformation [40]. The experimental investigation of mechanical interactions between tips defined in FIM and other specimens was not new – this had been investigated to some extent in the 1960s, but the lack of control over interaction forces between the tip and contacting specimen made it difficult to avoid obliteration of the delicate FIM tip. Leisch and co-workers identified that the techniques developed for proximal probes (STM and AFM) were ideal for controlling mechanical interactions with FIM tips at atomic length scales.

The first publication described preliminary contact experiments between a W(110) tip and Au sample (likely polycrystalline). Contact was made in two ways: In the first, the tip was approached toward the sample until the current preamplifier "overflow" was detected; in the second, the tip was indented from tunneling distance into the substrate to a depth of about 1 nm. The sample bias was 1 V. In the first contact experiment, it is not clear from the description at what current the preamplifier "overflowed" – in our experience with tip-sample mechanical contacts, a 1V bias will cause catastrophic melting of the sample and annihilation of the tip apex if a large current (> several μA) is allowed to flow through the junction[1]. The linear preamplifier of the STM should limit the current flowing through the contact, and effectively lower the bias voltage across the STM junction[2]. The contact experiment showed a sub-monolayer transfer of Au from tip to sample which remained relatively well-confined to the tip apex, determined by the position-sensitive atom probe.

[1] Such is the case with our logarithmic preamplifier.

[2] During indentation, the output of the linear preamplifier will reach a DC power rail (probably ±15 V or ± 12 V) somewhere around the maximum detectable current, 100 nA for the Omicron STM-1. At this point, the virtual ground of the tip, provided by the inverting input of the opamp, can no longer be 0 V – for it to be, the opamp would have to output a voltage much larger than the power rails. Since V_{out} is finite and limited by the power rails, the voltage on the tip is that of the middle of a voltage divider made up of the tip-sample junction resistance and the transimpedance resistor between the sample bias and current preamp's output which is saturated at a voltage rail: $V_{tip} = V_{sample} + \frac{R_{TS}}{R_{TS}+R_F}\left(V_{rail} - V_{sample}\right)$. Since $R_{TS} \ll R_F$, the bias at the tip will approach that of the sample, and the potential across the tunneling gap will collapse. This is a fortunate damage-limiting feature.

The indentation experiment to 1 nm depth yielded a damaged tip in FIM (not consistent with our experiments), as well as transferred Au.

In their second paper appearing in 2003 [202], additional experiments were presented regarding contacts to Au and a stepped Ni(997) surface. The descriptions of the atom probe data and the FIM images taken before and after tip-surface interaction are not convincing – the presence of many hydrocarbons in TOF but not in FIM is an unexplained discrepancy, and some of the 'same' tips before and after STM experiments look completely different. A useful result is the estimate of the number of Au atoms transferred to the tip during indentation: 66 atoms at 1nm depth, 80 atoms at 3nm, and 87 atoms at 5nm (the detected number of atoms should probably be multiplied by 1.67 to account for the 60 % open area of the microchannel plate detector). These numbers were found to be in rough agreement with wetting phenomena observed in atomistic simulations. Another important observation was that characterization of the substrates by STM scanning causes changes to the tip structure.

4.1.6 Summary and experimental outlook

Several groups have put significant effort toward the marriage of FIM and STM techniques. However, these studies present quite preliminary results, and very few groups have published any more than two papers – somewhat surprising considering the investment in such sophisticated vacuum equipment. Perhaps these projects were abandoned because the complexity of the apparatus hindered experimental productivity.

The most practical insights come from the work of Tomitori and Weierstall & Spence regarding the conservation of tip integrity during STM. Leisch's work, though not always well expressed, presents a selection of intriguing results from tip-sample contacts.

Scanning probe techniques have reached a high level of maturity and sophistication in the last ~10 years. Experiments on the cutting edge of AFM and STM often turn to modeling to explain the measured forces and currents between tips and samples. The atomic scale geometry of tips is a free parameter which can be tweaked to fit the data [63], and in some cases, in unrealistic ways [24]. Several groups have recently built, or are in the process of building AFM/STM systems with FIM tip characterization facilities. Although these groups don't have any published data yet, they regularly present posters at conferences.

André Schirmeisen, who worked on our FIM/AFM/STM system at McGill has implemented FIM on a AFM based on a quartz tuning fork (qPlus sensor). His group has

worked to characterize the electrostatic force parabola (Eq. (8), page 22) with input about the tip radius from FIM. It is not clear what the future direction for this work will be.

Franz Gießibl at the University of Regensburg commissioned Omicron to build a FIM in the preparation chamber of a commercial low-temperature (4 K) qPlus-based AFM/STM. They have not been able to acquire FIM images from tips (reason unknown), but a symmetric pattern can be seen on the screen, which is probably a field evaporation image. They used this setup to prepare clean W tip apices by field evaporation, and used them in a recent experiment published in Science claiming that the crystallographic orientation of the W tip apex could be changed by mild mechanical contact with a Cu substrate [203]. The peculiar and absolutely unsatisfying explanation for this data begs experimental verification of the tip apex structure in FIM, or at least theoretical backing of a proposed deformation mechanism. Much work will have to be done on this system once the FIM is operational in order to verify that tips can be transferred hastily between the microscopes in separate UHV chambers without damage by UHV rest gases.

Rolf Möller from Uni Duisburg is currently building a 4 K temperature qPlus-based AFM/STM with an in-situ FIM – similar in concept to our combined FIM/SPM instrument. The goal of this work is to implement atomically defined probes in state-of-the-art AFM measurements. This is probably the most promising experimental system underway at present: The tip will remain at 4 K during FIM and SPM limiting the diffusion of material both on the substrate and the tip, and the vacuum pressure will probably be excellent due to the cryogenic pumping effect of the rest of the microscope body. There may be an issue with He gas remaining physisorbed to the tip at low-temperature with this design, but this could be remedied by heating the tip momentarily.

To summarize, FIM can be an excellent tool for characterizing the general apex shape of STM tips, and ensuring that they are clean for measurements. The implementation of atomically defined probes in STM is still an active pursuit.

4.2 FIM tip integrity

A prerequisite for a SPM experiment with an atomically defined tip is a tip whose apex is stable. First, the tip must be made of a material whose atomic structure does not change by self-diffusion at room temperature – a W(111) tip is appropriate for this purpose. Furthermore, the vacuum system and the procedures carried out for FIM or during sample

transfer must not be a source of contaminant atoms or molecules which could adsorb to the tip and alter its structure.

Because we don't have a ToF mass spectrometer to analyze the chemical composition of the tip apex, all of our observations regarding tip integrity are based on FIM images of tip apices. It is therefore a good idea to know something about the adsorption of gases on the tips, and what is known with regard to the FIM imaging of gas-dosed tips. Section 4.2.1 reviews the literature on the adsorption mechanisms of common gases, their appearance in FIM images, and their corrosive effects to the tip material. Section 4.2.2 confronts impurities in the imaging gas from an experimental standpoint, and demonstrates how their corrosive qualities can be mitigated. Section 0 addresses the formation of a tunneling gap in STM experiments on several substrates.

4.2.1 Gas adsorption on FIM tips

The interaction of gases with metal surfaces was studied extensively in FIM by Erwin Müller (the inventor of FIM) at Penn State University, Gert Ehrlich at the University of Illinois at Urbana-Champaign, and Holscher and Sachtler at Shell Research in the Netherlands in the early 1960s. We summarize the experimental findings for the typical rest gases in UHV system (N_2, CO, O_2, H_20, and H_2), and provide a more detailed review of the adsorption and corrosion behaviour, along with associated references, in Table 1.

Nitrogen adsorbs on tungsten by dissociation, that is, as a single N atom chemically bound to a W tip atom. When imaged, it appears brighter and larger than regular tip atoms. The N-W bond weakens the W bond to its neighbours, which means that the W and N can field evaporate at fields lower than those necessary for imaging. Missing W atoms could be an indicator of N adsorption.

Carbon monoxide was found to be less corrosive than N_2, however it was still found to remove substrate atoms when field desorbed, leaving behind vacancies. Oxygen corrodes tungsten in a manner similar to nitrogen, though Müller claims less aggressively. Again, the presence of oxygen is inferred by missing atoms. Water was shown to remove tungsten atoms down to liquid He temperatures.

The adsorption of hydrogen has no corrosive effect on tungsten tips, nor can it be detected in FIM imaging. However, changes in field emission are detectable upon hydrogen adsorption.

We now summarize references and experimental results for both tungsten and iridium (where available) tips in Table 1.

Table 1: Adsorption and corrosion behaviour of various gases on tungsten and iridium FIM tips.

Gas	Tungsten tips	Iridium tips
N_2	Adatoms appear bright, larger. Adatoms observed on highly corrugated planes and at steps - not within the close packed (110), but at the edges. More adatoms near (310) rather than (111) – this anisotropy is attributed to difference in N_2 dissociation rate. [204] Nitrogen binds strongly to W. Perturbed by the act of adsorption, the W can be field evaporated off at regular imaging fields for that of W. [151] N binds on top of W sites (the N_2 molecule is dissociated, measured by mass spectrometry). Most N field desorbs before the ion emission is bright enough to be photographed (missing atoms could be sites of previously adsorbed N). W atoms were removed at fields lower than useful for imaging. [152] W-N complexes field desorb as a unit, reported in the first paper on the time-of-flight atom probe. [57]	N_2 adsorbs as a molecule (without dissociation) between Ir atoms. Much less corrosive to Ir than it is to W (weaker bond). [152]
CO	Found to be less corrosive than N_2. During FIM, CO is most corrosive when dissociated due to O adsorption on W which removes W substrate atoms. CO is dissociated by the energetic electrons removed from the He+ during the FIM process. Adding H_2, as a source of even higher energy electrons (in addition to the He imaging gas) enhanced the dissociation rate of CO. [152] CO adsorption was found to rearrange substrate atoms. At 300 K, this leads to surface corrosion leading to vacancies underneath adsorbed molecules. Chemisorbed CO leads to "promoted field desorption" whereby the adsorbed species evaporates before it can be imaged, leaving behind a vacancy. [205]	Much less corroded than W. [152]
O_2	Seems to be less corrosive than N2, but not as extensively studied. [152] W-O complexes are field desorbed together, observed in Ar ion FIM. [206] W-O complexes field desorb as a unit, reported in the first paper on the time-of-flight atom probe. [57] In He ion FIM, adsorbed oxygen cannot be directly observed on the surface; its presence is inferred from corrosion damage. [207]	
H_2O	Studied in Mulson's PhD thesis. Shown to remove W surface atoms (as well as Pt), even when surface is kept at liquid He temperature. [152]	
H_2	Adsorption causes significant changes to the Field Emission pattern of the tip. However, no change can be detected in FIM. During FIM, a perturbation of the adsorbed H_2 layer is attributed to the bombardment of electrons coming from ionized He+ imaging gas. [208] H_2 did not have a corrosive effect, and could also not be detected. [152]	H_2 could not be imaged, but removal of atoms, particularly in the bright (110) zone boundary, is attributed to H_2 adsorption. [152]

In summary, a weakening of the metallic bonding of tungsten atoms under most types of adsorbed gases leads to the removal of tip atoms in FIM imaging. In the case of N_2, imaging

is possible (but not always) at fields required for He ion FIM. FIM is completely blind to hydrogen adsorption – it is neither detected in images, nor does it remove substrate atoms.

4.2.2 Imaging gas impurities

The following section and sections 4.2.3, 4.3, 4.3.2, 4.3.3, 4.3.4, and 4.4 are based in part on text and figures from

Paul, W., Miyahara, Y. & Grütter, P. H. Implementation of atomically defined field ion microscopy tips in scanning probe microscopy. *Nanotechnology* **23**, 335702 (2012).

Dedicated FIM systems intended for diffusion studies have very stringent vacuum requirements. They are often made of glass to minimize the presence of hydrogen and are designed for high temperature bakeout (limited to 300°C by the micro-channel plate (MCP)) [54]. These systems are usually baked out several times, and the MCP is bombarded for many days by 200eV electrons to remove gas trapped in the channels. Gas molecules desorbed from the MCP under electron bombardment can contribute a significant source of rest gas in UHV due to the MCP's large surface area, so they are often turned off when not needed [209]. Imaging gases are admitted through Vycor or quartz tubes and titanium getters and cold traps are also used extensively. These systems must be clean enough to avoid rest gas atoms landing on the atomic planes being studied for diffusion during the experiment. Due to the complexity of our combined FIM-SPM apparatus, the system cannot be as thoroughly clean as the dedicated FIM systems described.

In our FIM studies, helium is used as an imaging gas. It is admitted through a heated quartz tube to provide an ultra-clean source of helium. However, due to the slow leak rate of the quartz tube, the system cannot be pumped actively with a turbomolecular pump. All pumping during FIM is done passively with a liquid nitrogen cooled titanium sublimation pump (TSP). Diffusing the helium gas through heated quartz introduces minimal impurities into the vacuum system, but the imaging gas purity is still limited by the outgassing of the vacuum system and the MCP.

Regardless of the source of the imaging gas (quartz tube, or leaked in directly from a gas line), impurities are likely to be in higher concentration while the imaging gas is admitted. It is important to keep these impurities from reacting with the tip apex atoms during FIM and while pumping the imaging gas after FIM. We demonstrate the very rapid etching of the tip apex due to imaging gas impurities by preparing a clean tungsten tip in Figure 4.1(a) and

momentarily lowering and raising the imaging voltage from 5.1kV to 0V and back. This voltage ramping process took 40s.

The many changes to the atomic structure of the tip are highlighted in Figure 4.1(b) in a manner employed by Müller to identify individual changes among the many atomic sites of a tip [210]. A colour superposition image is constructed by illuminating the initial image in green and the final image in red. They are aligned and re-exposed (digitally in Matlab) to produce the superposition image. Areas that show up in green correspond to atoms that have field evaporated, whereas atoms that show up in red correspond to adatoms that have appeared. Missing atom sites (green) should also be considered as sites where an adsorbed gas atom had previously been bound: As we discussed in section 4.2.1, most adsorbed species weaken the bonding of underlying tungsten atoms and remove them upon field desorption (which may happen before an adequate field is reached to produce a helium FIM image) [151, 152].

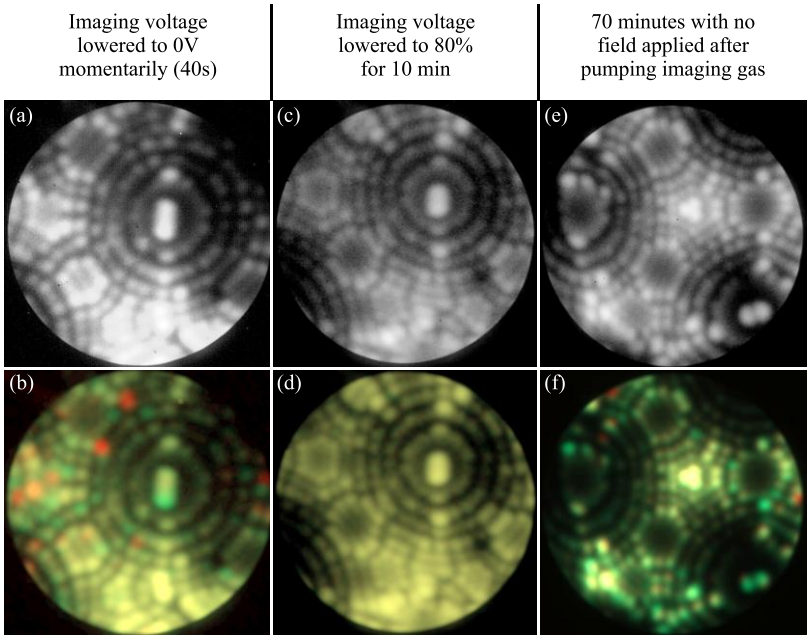

Figure 4.1: (a) (110) tip at 5.1 kV; (b) colour superposition image of (a) with the FIM image after the imaging voltage was momentarily lowered and raised – about 30 atomic sites show modifications; (c) (110) tip at 5.0 kV; (d) colour superposition image of (c) with the FIM image after waiting 10 minutes with the voltage lowered to 4.0 kV – no changes are observed to the atomic structure; (e) (111) tip at 6.0kV; (f) colour superposition image of (e) with the FIM image after waiting 70 minutes in UHV.

The ~30 changes visible on the tip's ~120 nm^2 surface area in ~40 seconds are discouraging to the prospect of preserving an atomically defined tip apex. Fortunately, helium has a much higher ionization energy than all other gases [211], and as long as a sufficient field is applied to the tip, other gas species will be ionized with a greater rate and

accelerated away from the tip before they can react with the tungsten atoms on the apex. Experimentally, we find that reducing the tip voltage to about 80% of the imaging voltage is sufficient to keep contaminant gases from reacting with the tip during extended periods of time. The somewhat reduced magnitude of the field helps ensure that no atomic changes to the tip occur due to field evaporation. We call this the "force field" and demonstrate it on a tip in Figure 4.1(c) which is exposed to the imaging gas and its impurities at 80% of the imaging voltage. Ten minutes later, no changes are observable in the colour superposition micrograph of Figure 4.1(d).

The "force field" method should be applied to ensure that the tip apex remains clean between FIM and SPM. The "force field" voltage is applied to the tip while the helium is pumped from the chamber and maintained until the UHV system returns to base pressure. Processes that result in increased pressure transients such as flashing the TSP and refilling its liquid nitrogen reservoir can be done while the "force field" is on to avoid contamination of the tip apex.

After performing a scanning probe measurement with the FIM tip, it is necessary to perform FIM again to check the integrity of the apex. During the He filling process, we are faced with the choice of whether or not to apply the "force field". If the "force field" is applied before turning on the MCP and leaking in helium, field desorption events occurring at voltages lower than the "force field" voltage will not be imaged, and cannot be counted. Working quickly with a fresh TSP shot, we have found that it is possible to keep the tip reasonably clean during the FIM start-up sequence without the "force field". This way, the number of adsorbed atoms during the experiment interval may be overestimated, but field desorption events below the "force field" voltage can be recorded.

To summarize, we propose the following FIM protocol to preserve the tip apex from imaging gas impurities in SPM experiments:

(1) Prepare a clean tip by field evaporation in FIM
(2) Reduce applied voltage to ~80% ("force field")
(3) Pump imaging gas, refill liquid nitrogen cold traps, flash TSP while "force field" is on
(4) Ramp down "force field" voltage when pressure has recovered
(5) SPM experiment

During the interval of the SPM experiment, the FIM tip will be subject to contamination by the UHV rest gas. The vacuum requirements necessary to keep the apex of a tip clean during such an experiment are now considered. A typical trimer apex of a W(111) tip is shown in a FIM image in Figure 4.2(a). The trimer apex is illustrated schematically in Figure 4.2(b). A dashed hexagon is drawn around the perimeter of the first and second layer of a (111) trimer apex. We consider the likelihood of rest gas molecules impinging on this 1.16nm^2 area. In this discussion, we address only the probability of various gas species impinging on the apex. Many subtle effects regarding sticking coefficients are at play such as the anisotropic adsorption coverage of gases on a tip surface due to the difference of dissociation rates on different atomic planes [204]. The following estimations represent an upper limit of tip contamination as they do not include adsorption probabilities.

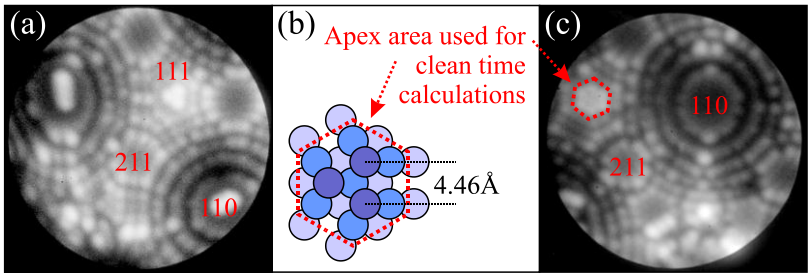

Figure 4.2: (a) Typical W(111) tip ending in a trimer prepared by field evaporation. (b) trimer apex model illustrating the area used for the calculation of clean time. (c) The area corresponding to the hexagon illustrated in (b) is shown around the (111) pole of a W(110) tip.

The rest gas composition in UHV is first estimated using a residual gas analyzer (RGA) in our preparation chamber. The location of the RGA is different from the location of the FIM/SPM measurements, but we assume that the gas composition will be similar for this similarly pumped vacuum chamber (with the possible overestimation of H_2O partial pressure because of the more thorough FIM/SPM chamber bakeout). The gas composition is calculated by the SRS RGA Windows software, and is presented in Table 2. For a total pressure reading $P_{gauge} = 5 \times 10^{-11}$ mbar, the individual partial pressures p_i of the component gases are calculated as

$$p_i = n_i \frac{P_{gauge}}{\sum_i \frac{K_i}{K_{N_2}} n_i} , \tag{44}$$

where n_i is the pressure fraction of the gases and K_i/K_{N_2} is the ionization sensitivity [136] of the gauge to the various gases.

The flux of each gas species can be calculated from their respective masses and partial pressures by combining the Boltzmann velocity distribution of the gas particles with the ideal gas law [212]:

$$F_i = \frac{p_i}{\sqrt{2\pi m_i kT}}. \tag{45}$$

Table 2: Table of typical UHV rest gas species, their partial pressures, fluxes, and calculated contamination times and probabilities for a 1.16 nm^2 tip apex.

Species	Mass, m (amu)	Ionization Sensitivity, K_i/K_{N_2}	Pressure Fraction, n_i	Partial Pressure, p_i (mbar)	Flux, F ($nm^{-2}\ s^{-1}$)	**1:20 apex contamination time(min)**	**P(k>1) gas atom on apex during a 60 min delay**
H_2	2	0.42	88.0%	9.4E-11	1.0E-03	0.7	98.5%
H_20	18	0.9	4.6%	4.9E-12	1.8E-05	41	7.1%
N_2	28	1	2.3%	2.4E-12	7.0E-06	100	2.9%
CO	28	1.2	1.7%	1.8E-12	5.2E-06	140	2.1%
CO_2	44	1.4	1.1%	1.2E-12	2.7E-06	270	1.1%
He	4	0.16	0.1%	1.1E-13	8.1E-07	890	0.3%

Given a flux per unit time and area, F, and assuming that the arrival of gas molecules is independent of time and location, the probability of obtaining k arrivals in an area A in time τ is given by a Poisson distribution [213]:

$$P(k) = \frac{e^{-FA\tau}(FA\tau)^k}{k!}. \tag{46}$$

We are interested in the probability of obtaining more than one arrival, i.e. $k > 1$, which is easily obtained using the normalized nature of the distribution:

$$P(k > 1) = \sum_{k=1}^{\infty} P_k = 1 - P_0 = 1 - e^{-FA\tau}. \tag{47}$$

We describe the rate of contamination of the tip apex area in 2 ways: In the first, we calculate the duration of an experiment such that in 5% of experiments of this duration, one would count more than one gas molecule impinging on the apex. The second is the probability of more than one gas molecule impinging on the apex during a 60 min delay. The results of these calculations are shown in Table 2. Note that other unidentified gases (not listed) make up 2.2% of the gas composition, meaning they have approximately the same statistics as N_2.

Due to its low mass and large pressure fraction, hydrogen has a high flux and correspondingly very large probability of contaminating tips. In addition, hydrogen gas

cannot be imaged in FIM and is known to have no corrosive behaviour when adsorbed on tungsten tips [152], so its presence goes undetected with the methods employed here.

The next most prevalent gas species (H_2O, N_2, and CO) are at a nearly acceptable background level if an experiment is completed within a short period of time (~1 hour). These species are also known to etch tungsten atoms, so changes to the atomic structure would likely be detectable in FIM [151, 152, 204, 208]. However a more convincing confirmation of a contamination-free tip would be the experimental repeatability of the electronic properties of its tunneling junction with an atomically clean surface, measured by STS.

We illustrate typical rest gas contamination of a tip in Figure 4.1(e) which was preserved with a "force field" until the UHV system had returned to base pressure. The "force field" was then turned off, and the tip was left in UHV for 70 minutes (a reasonable SPM experiment duration). The colour superposition image in Figure 4.1(f) shows ~30 changes to atomic sites. The number of changes is overestimated due to the contamination during the FIM start-up sequence. Assigning an approximate mass of 28 amu, the changes to the tip during this interval indicate an effective contaminant pressure of $\sim 2\times10^{-11}$ mbar. This number is consistent with the calculations in Table 2 and the expected overestimation of contamination due to the FIM start-up sequence.

From these rest gas calculations, it is clear that experiments must be performed quickly, even in a clean UHV environment. This has important consequences for the design of a combined FIM/SPM experiment: Since the sample should not be subjected to contamination from the imaging gas, the tip or sample must be transferred in a reasonable time frame, and the coarse approach of the tip to the sample surface must be done quickly.

4.3 Tunneling gap formation

Having established the "force field" protocol for preserving FIM tip apices, and shown that they can be kept atomically clean for a reasonable length of time, we now consider the challenges in forming the tunneling gap between a FIM tip and a surface. The object of these experiments was to determine if we could transfer FIM tips to and from a tip-sample junction without apex alterations. We start by describing tip approaches to cantilevered Au(111) samples, which were found to behave poorly. In order to exclude the possibility of tip alterations due to the flexible samples, solid STM samples were investigated next: Au(111), HOPG, and Si(111), among others.

The initial coarse approach is monitored optically, and the tip can be brought to a distance of 5-10 μm from the surface by observing its reflection off the sample.

The bandwidth of our tunneling current preamplifier is ~ 2 kHz [70], and the response time of the STM controller feedback loop is also set on the order of ~ 1 ms. Since the tunneling current increases at a rate of about one decade per Angstrom, it is necessary to ensure that the approach speed does not exceed 1000 Å/s so that the feedback loop can detect and correct the tip position without serious overshoot. We manage to achieve negligible current overshoot with a tip approach speed of ~ 200 Å/s.

We prepare trimer tip apices before each experiment by field evaporation (with the exception of a rather asymmetric apex used in one experiment which supported unusually stable tetramer tips). The tip is brought to tunneling interaction with the sample within 30-50 minutes of the time the "force field" voltage is turned off. Once in tunneling range, we wait about one minute for z-piezo creep to settle, and then perform small 10x10 nm scans at slow can speeds to check the sample slope. The tip is maintained within tunneling distance of the sample for 4-5 minutes before it is withdrawn and FIM is performed again (images are acquired with lower applied voltage to capture adsorbed atoms). With the exception of the measurement on cantilevered samples, the tunneling current throughout the experiment is recorded at a sample rate of 50 kHz (with an external 8th order antialiasing filter at 10 kHz) using a National Instruments USB-6259 BNC controlled by Matlab. The tunneling current recorded for the cantilevered sample was bandwidth limited to 512 Hz.

4.3.1 Cantilevered Au(111) samples

The approach of an atomically defined FIM tip to a Au(111) cantilever beam (of the type described in section 2.5 (page 27) and illustrated in Figure 2.4 (page 19)) is summarized in Figure 4.3. In Figure 4.3(a), we plot the force and current at the moment of first approach for a total duration of 1 second. The sample bias voltage was set to -0.05 V and the current setpoint was 20 pA. A slight feedback overshoot to ~70 pA exists when the tunneling current is first detected. About 0.15 s later, some instabilities are measured on the tunneling current – keeping in mind that in this data set, the current is low-pass filtered to 512 Hz, so instantaneous values could be much higher. In the force channel, it is apparent that the cantilever becomes excited at about the same time as the tunneling current instabilities, highlighted by a red bracket. The Fourier transform is taken of small windows of data throughout the force signal, and the power spectral density evolution is shown in

Figure 4.3(b). In this plot, time runs from bottom to top, and each row represents the cantilever deflection power spectrum at a different time during the acquisition. Odd harmonics of 60 Hz are measured over a large bandwidth, highlighted by the blue arrows – this data was taken before the final improvements in detection noise were made (section 3.3, page 91). Apparently the line noise may also have a mechanical component and it appears that the cantilever beam, upon a slightly negative frequency shift, becomes excited by the line noise (red bracket).

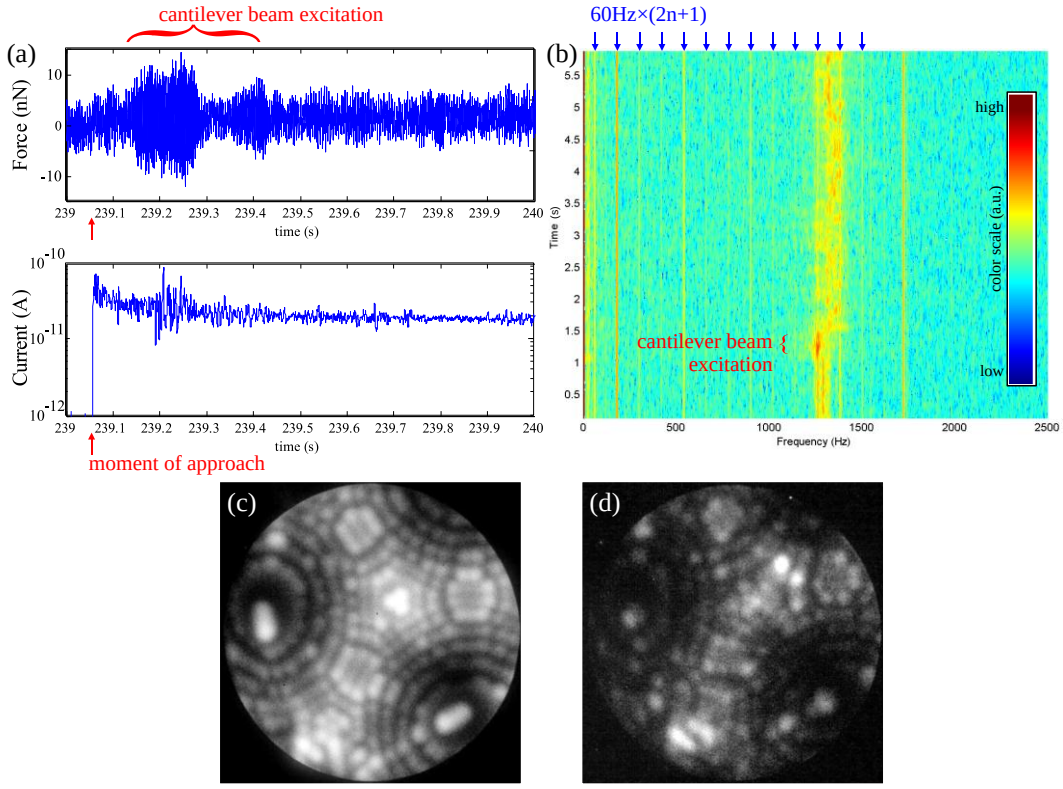

Figure 4.3: Approach of a W(111) FIM tip to a Au(111) cantilever beam: (a) Force and current signals over 1 second duration upon initial approach. (b) Power spectrum evolution of the force (time goes upwards in this plot). (c) FIM before at 6.0 kV (20120228 #109-123). (d) FIM after at 5.1 kV (20120228 #169-184).

Another interesting feature of this data is the apparently repulsive force between tip and sample, increasing by ~ 4 nN at the moment of approach. The frequency shift of the cantilever beam is positive after the approach of the tip, suggesting that at this tunneling current setpoint, the force minimum of the force-displacement curve has been passed (Figure 2.6, page 24).

The tip apex is shown before and after the approach to tunneling in Figure 4.3(c) and (d). It is clear that merely approaching the tip to the cantilever beam within tunneling proximity serves to severely modify the atomic structure of the tip apex. The tip maintains the same

radius, and the atomic structure of some of the crystal planes appears quite similar, but we cannot claim that the trimer apex is conserved. Nor can we claim that the SPM tip-sample vacuum gap is formed between a W apex and Au surface.

Following this experiment, it is not clear if the mechanical oscillations of the cantilever beam were responsible for the transferal of material to the tip. Perhaps the tip modifications were a result of physisorbed gases diffusing down the tip shank along the field gradient into the tip-sample junction and causing the tip modifications.

In order to test the second hypothesis, we performed the experiment again having freshly annealed the W tip to ensure the tip shank was properly degassed. The results are summarized in Figure 4.4.

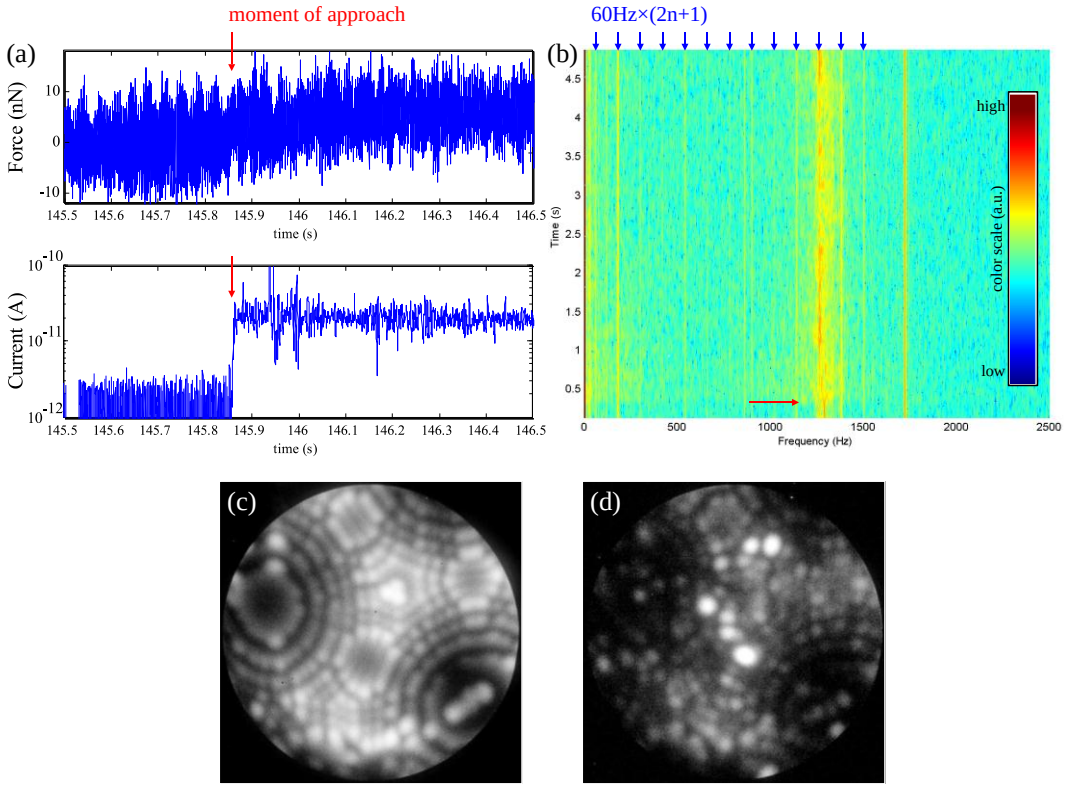

Figure 4.4: Approach of a W(111) FIM tip to a Au(111) cantilever beam: (a) Force and current signals over 1 second duration upon initial approach. (b) Power spectrum evolution of the force (time goes upwards in this plot). (c) FIM before at 6.1 kV (20120228 #359-384). (d) FIM after at 5.3-5.6 kV (20120228 #410-425).

Similar to the previous approach experiment, the FIM tip apex has been severely modified. The force channel does not show as large cantilever excitations as measured previously. The tunneling current in this experiment still showed some instabilities (again, within a bandwidth of 512 Hz).

The origin of tip alterations is still not clear from this data. We decided to simplify the experiment by studying FIM tip approach to non-cantilevered Au(111) samples to avoid spurious sample oscillations.

4.3.2 Au(111) (non-cantilevered sample)

The approach of an atomically defined tip to a Au(111) surface is illustrated in Figure 4.5. In this experiment the Au(111)/mica sample was affixed rigidly to a stainless steel sample holder with Pelco silver paste. As soon as the tunneling gap is established (6 pA, -0.08 V on the sample), many spikes are seen on the tunneling current up to ~40pA. The spikes are continuous throughout the experiment, and this behavior is representative of the 4 other experiments of approaching atomically defined W(111) tips to non-cantilevered Au(111). After the FIM tip is withdrawn from the tunnel junction, the apex is severely modified by adsorbed atoms.

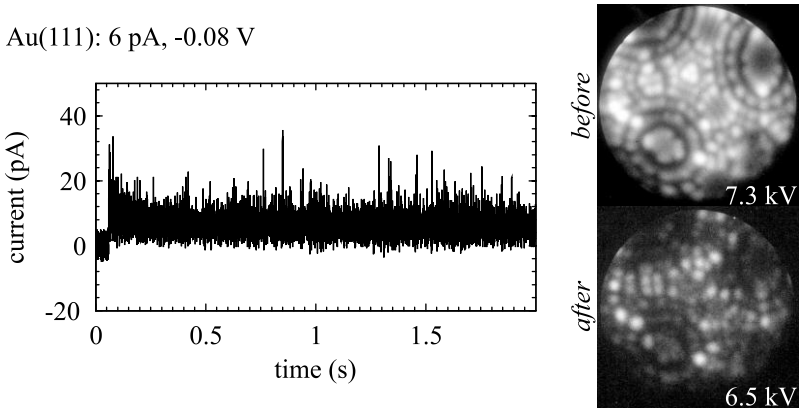

Figure 4.5: Current trace upon approach to Au(111) and FIM tip apices before and after.

4.3.3 HOPG

HOPG was investigated as an alternative substrate to elucidate the cause of the tip apex contamination. The samples were cleaved in air and quickly inserted into vacuum and then degassed overnight at 150 °C in UHV to remove physisorbed gases. The tunneling current (6 pA, -0.1 V on the sample) behaviour on HOPG was generally much quieter, but during the two experiments on HOPG, occasional bursts of noise were observed, such as the one ~90 s into the experiment, shown in Figure 4.6. Again, the FIM tips withdrawn from the two tunneling experiments performed on HOPG were covered with adsorbates.

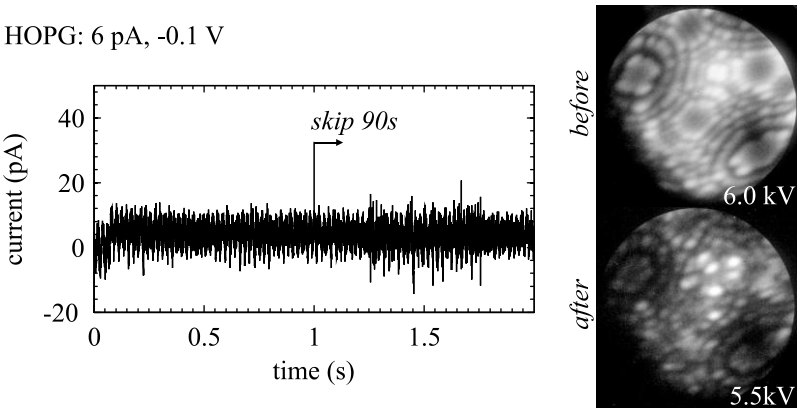

Figure 4.6: Current trace upon approach to HOPG and FIM tip apices before and after.

4.3.4 Si(111)

Clean Si(111)-2x1 surfaces were prepared by cleavage in UHV less than 30 minutes before the tunneling junction was established (as described in section 2.7.7, page 58). A trimer tip was prepared in FIM and approached until a current of 6 pA at +2 V sample bias was achieved. This experiment was performed with two tips on two different cleaved Si(111) samples, and no spikes in tunneling current were detected, which is apparent in the current trace in Figure 4.7. The overshoot of the tunneling current upon approach is also very minimal. The tip apex returned unchanged from the tunneling junction in the two experiments performed on Si(111).

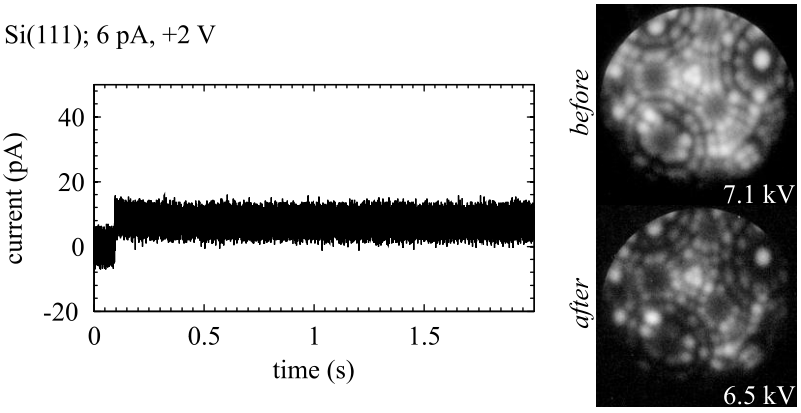

Figure 4.7: Current trace upon approach to Si(111) and FIM tip apices before and after. The brightness of the 'after' image is lesser than the 'before' image because of the reduced applied voltage.

4.3.5 Other surfaces

GaAs can be prepared by cleavage in UHV to expose the GaAs(110) plane. Compared to Si(111), it is much more straightforward to prepare as the cleavage plane is perpendicular

to the wafer. The approach of FIM tips to GaAs(110) was investigated twice, both times yielding similar results. The tunneling current, shown in Figure 4.8(a) and (b) is much better behaved than on Au(111) surfaces. Occasional spikes in the tunneling current shown in Figure 4.8 (b) are observed, as well as streaks in the STM image, Figure 4.8 (c), indicating tip changes. The FIM images of the W(111) tip show that the apex has been altered during the tunneling experiment, Figure 4.8(d) and (e).

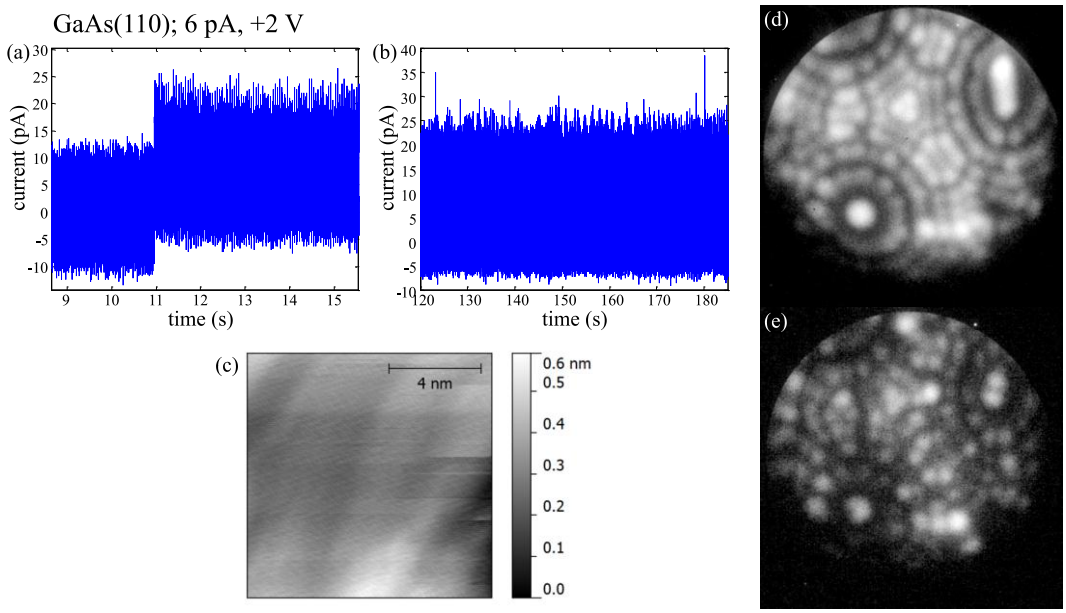

Figure 4.8: (a) and (b) Current traces upon approach to GaAs(110). (c) STM image of the surface. (d) FIM tip before approach, 7.1 kV (20120506 #63-77). (e) FIM tip after approach, 6.5 kV (20120506 #105-116).

In order to perform simultaneous STM and AFM rather than just STM, we require a sample which can be cantilevered. Cleaved semiconductor surfaces are not appropriate for cantilevering because substantial forces must be applied to expose the fresh crystal surface. Thin semiconductor beams made of silicon might constitute a reasonable sample for our studies, although silicon surface preparation by flash annealing of thin beams to near-melting temperatures constitutes a prohibitively open-ended project for the present time. We turned to the investigation of InSb(001), a semiconductor surface which can be prepared by sputtering and annealing cycles (section 2.7.6, page 55). In theory, a cantilevered sample for force detection could be fabricated by careful thinning of this single crystal, or by mounting a small sample to a cantilever beam made of some other material such as glass (demonstrated in Figure 6.26, page 234).

Approach of FIM tips to InSb(001) surface showed many spikes, qualitatively similar to those measured on Au(111). The FIM tips also returned covered with adsorbed atoms – this

is not entirely surprising considering our experience with STM on InSb(001) which indicates that surface atoms are mobile at room temperature (Figure 2.26(d)&(e), page 57).

4.4 Discussion and summary

We suspect that the return of altered tip apices from tunneling experiments with Au(111) results from the transfer of mobile adatoms on the sample surface at room temperature. The presence of a STM tip can substantially lower the energetic barrier for diffusion of adatoms toward the tip and for atom transfer to the tip [214-216]. Another possible source of the adsorbed atoms that must be considered is physisorbed gas diffusing from the tip shank (perhaps collected during FIM cycles) to the tip-sample junction along the field gradient. Fortunately, it seems that the source of the tip contamination is *not* from the tip shank since the tips approached to Si(111) return with identical apices.

HOPG was investigated because of its stronger covalent bonding within the plane, and therefore very different surface diffusion properties than the close packed metallic Au(111). Unfortunately the preparation of HOPG by cleavage in air followed by degassing in UHV may not be sufficient to form an atomically clean surface free of diffusing contaminants, which ultimately change the FIM tip apex structure. Small flakes of carbon left on the surface after cleavage may also be responsible for the observed apex changes. The exact species of the transferred atoms cannot be determined in our system.

The return of unaltered FIM tips after tunneling to Si(111) is not completely surprising. The surface is very reactive and should therefore be free of diffusing adatoms. Its preparation by cleavage in UHV immediately before the experiment also guarantees that it is free of contamination.

To summarize, a protocol has been introduced for preserving the tip apex of FIM tips using a "force field". This serves to keep the apex unchanged while pumping the FIM imaging gases, and carrying out dirtier vacuum processes. The time limitations for performing an experiment in typical UHV rest gas conditions without apex contamination were estimated to be reasonable for all gas species except molecular hydrogen. Hydrogen is not observable in FIM and desorbs without changing the underlying tungsten tip structure. Other gases are either observed as larger, brighter atoms or serve to remove underlying tungsten atoms.

We find that the implementation of atomically defined tips in SPM experiments at room temperature is limited by the choice of substrate. Spikes in the tunneling current signal

correlate with changes in tip apex structure in FIM. We also conclude that changes to the atomic structure of the tip are due to adatoms or physisorbed gas molecules transferred from the sample, and not from the tip shank.

Guidelines for implementing FIM tips in SPM experiments have been established, as well as the first convincing demonstrations of tip-sample interactions without modification of the atomic geometry of tip apices as determined by FIM.

5. SPM with atomically defined tips

In the preceding chapter, we discussed the transfer of atomically characterized tips from FIM to a STM junction without modification by the FIM imaging gas impurities or the UHV rest gas. Unaltered tip apices were returned to the FIM for imaging after tunneling interactions with Si surfaces, but not when approached to Au(111), HOPG, InSb(001) or GaAs(110) at room temperature. The modification of the tip structure was attributed to mobile adatoms or molecules transferred from the surface to the tip.

This chapter continues our work on implementing atomically defined tips in SPM, seeking to understand the details of atom transfer in the tip-sample junction in tunneling experiments with Au(111), the identification of tip changes in FIM, and the threshold for tip modification when performing STM as well as scanning tunneling spectroscopy (STS) on Si(111)-2×1.

Section 5.1 presents data from the approach of W(111) and W(110) apex tips to the Au(111) surface at temperatures of 298 K and 158 K, and yields important insights into the choice of tip orientation for SPM studies with atomically defined probes. Section 5.2 addresses the statistics of spikes measured in the tunneling current, and presents an attempt to understand the energetics of adatoms in the tip-sample junction by observation of tunneling current instabilities. STM and STS with atomically defined tips on Si(111)-2×1 is the subject of Section 5.3: We discuss the lifetime of the atomically defined tips, tip rearrangements while scanning with fresh tips, changes to STM resolution and tip convolution, and identification of tip changes in STS. We end with recommendations for achieving truly atomically defined nanoscale junctions in SPM.

5.1 Tip apex orientation and temperature

The key components of our tip-sample system are a FIM characterized tungsten tip and a flat Au(111) single crystal surface, illustrated Figure 5.1. Figure 5.1(a) shows a W(111) oriented tip apex having a radius of 8.2 ± 0.5 nm, and ending in three atoms (trimer) on the (111) plane. The tip is brought into close proximity with a surface by monitoring the tunneling current – the atomic geometry of the tip and sample surface is illustrated as a ball-model in Figure 5.1(b). The flat Au(111) surface, as imaged by topographic STM, is shown in Figure 5.1(c). The tip is approached to the sample surface in the procedure outlined in

section 4.3 (page 138), with feedback parameters and approach speeds chosen to avoid overshoot upon initial approach.

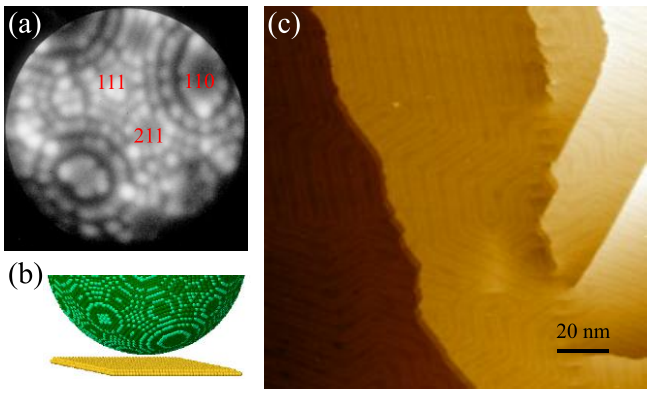

Figure 5.1: (a) Typical W(111) trimer tip prepared by field evaporation having a radius of 8.2 ± 0.5 nm, imaged at 7.3kV in FIM; (b) Ball model (side view) of a W(111) tip and Au(111) surface; (c) STM image of a clean Au(111) surface (8 pA, -0.95 V sample bias).

5.1.1 W(111) tips / Au(111) surface

After clean FIM tips are approached to Au(111) surfaces, spikes are always observed in the tunneling current. At room temperature, the spikes reach a maximum of ~40 pA, and lead to a completely changed tip structure after remaining within tunneling proximity of the sample for a few minutes, as illustrated in Figure 5.2(a). FIM tip approach experiments were additionally performed at a temperature of 158 K[1]; a representative snapshot of the current trace and FIM tip structure before and after tunneling at 158 K are shown in Figure 5.2(b). The vertical axes of the current traces have the same limits, emphasizing that the current spikes in the lower-temperature data are much larger, reaching ~130 pA. The FIM tip retracted from the tunneling junction at 158K appears to have a nearly identical apex,

[1] The microscope was cooled with liquid nitrogen, reaching a base temperature of 158 K at both the sample and tip. The cryogenic design of the microscope is particularly poor – its small liquid nitrogen reservoir must be filled every few hours, causing a substantial temperature fluctuation of the microscope of several degrees and a very short stable measurement time. The minimum of the thermal drift between contraction and expansion of the tip-sample gap was found during one STM study. There is only a ~15 minute operational window where the tip-sample thermal drift is < 2 nm/min (going from a contacting tip-sample gap to an expanding gap). This is a tolerable drift rate which would not necessarily require additional correction during distance spectroscopy or nanoindentation measurements having a duration of a few seconds each. However, it is common to find the tip-sample gap drifting at rates of > 1 nm/second during measurements at 158 K. If the drift happens to be in the wrong direction, this limits the measurement time to a few minutes before the tip is crushed by the approaching sample!

with the exception of an additional atom appearing very bright next to the original trimer apex. The lower-right atom in the trimer also appears brighter.

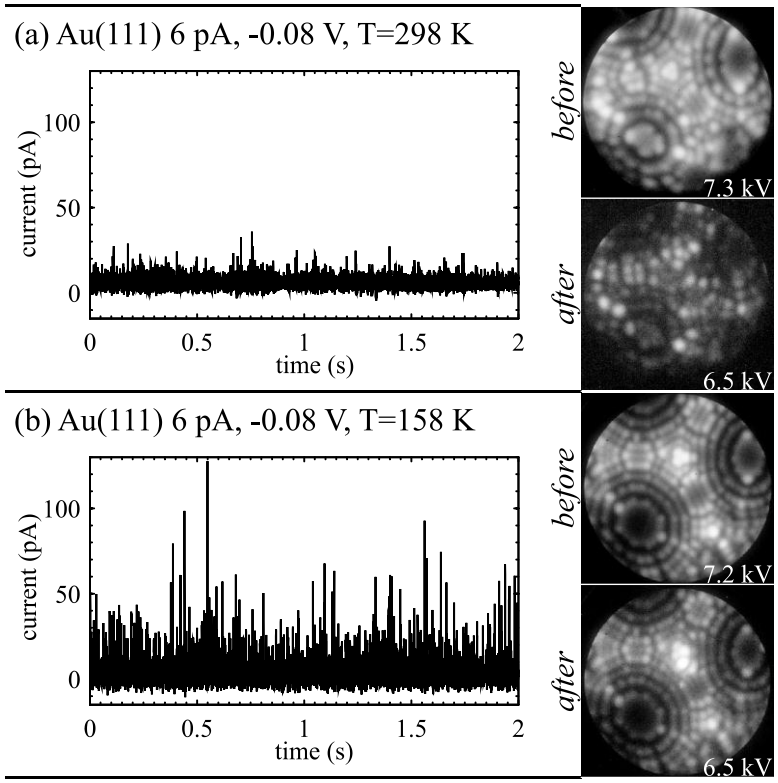

Figure 5.2: FIM tip apices before and after, as well as a snapshot of the measured tunneling current when approached to Au(111) at temperatures of (a) 298 K, and (b) 158 K.

The minor modification of the tip apex near the (111) plane provides two satisfying results: It demonstrates that the tip's (111) apex is indeed oriented perpendicularly to the sample and is the part of the tip which interacts with the sample[1]. The minor tip changes furthermore confirm that the adatoms we observe on FIM tips after tunneling originate from the sample. This supports our previous supposition based on the absence of tip changes when approaching the reactive cleaved Si surface.

Several additional insights can be gained by closely monitoring the sequence of field evaporation of the tip apex when it is returned to FIM for imaging. The FIM image in Figure 5.2(b) was actually acquired slightly after the onset of imaging conditions, and corresponds

[1] One cannot tell from FIM how well the crystallographic axis of the tip is aligned with respect to the macroscopic tip wire due to FIM image distortions caused by asymmetric microscope design (causing a variable shifting of the center of the image toward the top). As provided, the W(111) single crystal wire is specified to have a miscut of < 2° from the axis (section 2.8.1, page 62).

to the second image of the field evaporation sequence shown in Figure 5.3. Each image of the sequence is an average of several photos during which the apex configuration was stable. We present a logarithmic contrast (top) and linear contrast (bottom) version of each image in the field evaporation sequence. Logarithmic contrast serves to aid with the visibility of a larger dynamic range over the entire image, and the linear contrast gives a representation of the actual image contrast when viewed on the screen.

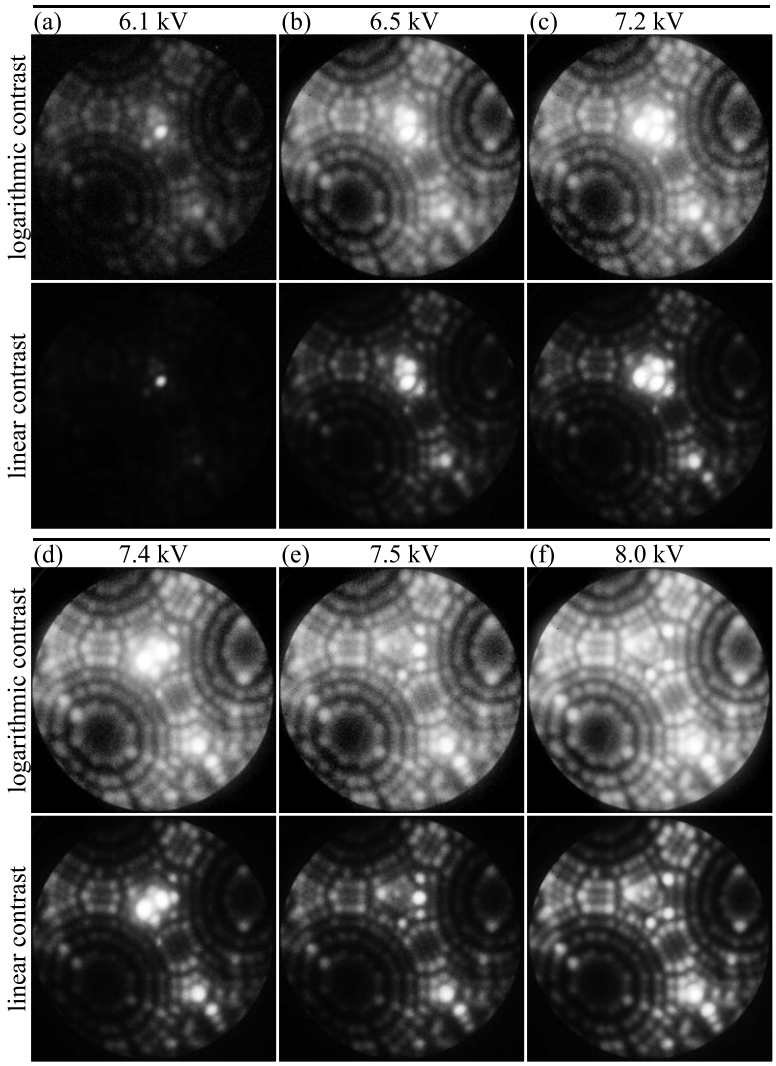

Figure 5.3: Field evaporation sequence of the W(111) tip apex after tunneling to the Au(111) substrate for several minutes at 158 K.

The tip becomes visible in FIM at an applied voltage of about 6.1 kV, as shown in Figure 5.3(a). It appears from a first inspection of the logarithmic contrast image that the W(111) apex trimer is intact and an additional adatom is adsorbed just next to it. Upon increasing the voltage to 6.5 kV, one of the trimer atoms appears much brighter – an intensity

comparable to its adsorbate neighbour. At 7.2 kV, a nearby atom to the left of the trimer begins to be imaged very brightly – the extreme contrast of these bright atoms compared to the image intensity of the rest of the tip can be appreciated best in the linear contrast image. At 7.4 kV, the earliest imaged adsorbate is removed by field evaporation. At 7.5 kV and up to 8.0 kV, several more atoms are lost to field evaporation from the center of the tip apex. The rest of the atoms on the tip apex began to field evaporate in a usual homogeneous manner at ~ 8.5 kV (not shown).

The highly localized field evaporation we measure on the W(111) tips at 158 K differs substantially from the usual field evaporation of clean W(111) tips. The localized field evaporation occurs at a comparatively low tip voltage, suggesting that the adsorbed atoms promote evaporation at lower fields, as well as the removal of the underlying W atoms (a common theme of adsorbed atoms on W tips, discussed in Chapter 4). It is not known whether Au and W evaporate as a unit as N-W and O-W have been shown to do by time of flight (ToF) mass spectrometry measurements.

Certainly, there are some field-induced rearrangements of the tip apex atoms that occur during FIM imaging, evidenced by select atoms suddenly appearing brighter before their removal by field evaporation. One could imagine interesting atomic mechanisms involving place exchange of W and Au atoms leading to a local protrusion to enhance brightness before one or several of the atoms involved in the bright spot are field evaporated. The existing theoretical literature on field evaporation and tip structures in FIM is mainly concerned with homogeneous materials, not tips with small amounts of adsorbed dissimilar metals. Unfortunately, the inspection of FIM images alone cannot reveal all the details about the transferred material or the field evaporation processes.

From this sequence of images, one can conclude that there are at least several adsorbed Au atoms on the tip – inspecting only the first image, Figure 5.3(a), might lead to the conclusion that only one Au atom was transferred to the tip. Apparently some of the transferred atoms can be hidden around the tip apex, perhaps at atomic plane edges just beside the apex, or in the very open and corrugated (111) surface of the bcc W crystal. A carefully recorded sequence of field evaporation images is therefore a useful experimental tool to verify the integrity of the tip apex: If indeed no tip changes occur during STM, no adsorbate promoted field evaporation would occur, and the field evaporation of the (111) apex would commence at a comparable field to the rest of the tip structure (~8.5 kV in this case).

As mentioned previously, the quantity of transferred Au atoms is not known with great precision from FIM images alone. Another concern regarding the estimation of the number of transferred atoms is that the field evaporation of some fraction of adsorbed atoms may occur at fields lower than required for ionizing the He imaging gas in FIM. Bulk Au cannot be imaged in He ion FIM, so if a small cluster of Au formed at the tip apex, one would expect the bulk-like Au atoms to be removed before the onset of imaging. This process might leave behind only the last layer of Au which would be more strongly bonded to the W tip atoms. Certainly, the best way to experimentally determine the number of transferred atoms and to investigate field evaporation mechanisms is to implement a ToF mass spectrometry measurement. Although the open area of MCP detectors is only ~60%, one could gather statistics reasonably easily on the quantity and spatial location of transferred atoms. The mechanisms of field evaporation (whether or not W and Au are evaporated together) could also be determined by ToF measurements.

From the spatial extent of the tip changes observed in FIM at these two temperatures, we can estimate rough upper and lower bounds for the activation energy of Au atoms diffusing over the W tip surface. We note that the diffusion barriers on different planes of the same crystal are in reality very different – what we extract here is an effective energy whose estimation should be dominated by the largest of the barriers of the relevant planes of the tip (in this case, the W(111) plane).

For a particle on a two dimensional surface, the mean square diffusion distance in time τ is[1]

$$\langle r^2 \rangle = 4tD_0 \exp\left(-\frac{E_a}{k_B T}\right), \tag{48}$$

where D_0 is a diffusion prefactor (takes into account the attempt frequency and jump distance), E_a is the activation energy of the diffusion jump process, k_B is the Boltzmann constant, and T is the temperature. For an experimental delay time of $\tau \approx 1000$ s and assuming a typical prefactor of $D_0 = 10^{-3}$ cm^2/s, we plot in Figure 5.4 two exponential curves expressing the expected root-mean-square (RMS) displacement at temperatures of 158 K and 298 K.

From the room temperature FIM image in Figure 5.2(a), we can estimate a lower bound for the RMS displacement of transferred Au adatoms – they are observed essentially 'everywhere' on the tip, indicating a RMS displacement greater than 10 nm. This provides

[1] The derivation of this expression is discussed in Appendix A.

an estimate of the upper bound of the activation energy for the diffusion process of ~0.74 eV. If the energetic barrier were higher, the adatoms could not have been displaced all over the tip. From the FIM image at 158 K, Figure 5.2(b), it appears that the damage to the tip extends to a lateral width of only ~2-3 nm (atoms on the W(111) plane are spaced by 0.46 nm). We estimate the lower bound for the activation energy based on a RMS displacement of 1 nm at 158 K to be ~0.46 eV. It is possible that the RMS displacement due to adatom diffusion is actually less than 1 nm: If a cluster of Au formed on the tip apex, the mechanism by which the damage spread to a width of ~2-3 nm may not be diffusion of Au on the W tip, but the rearrangement of a small Au cluster on the tip as adatoms are collected.

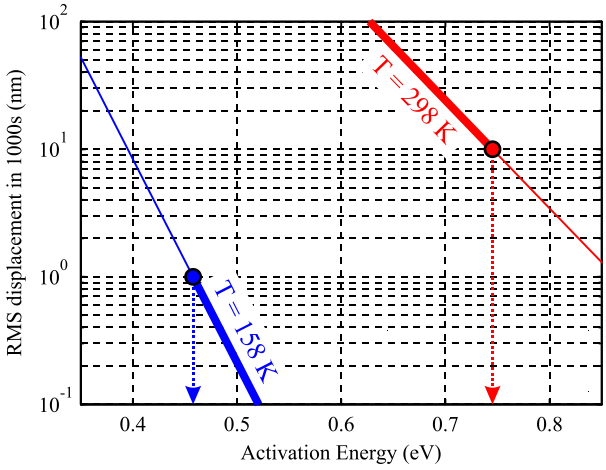

Figure 5.4: Expected RMS displacement of diffused adatoms at T = 158 K (blue) and T = 298 K (red) during 1000s as a function of activation energy. Upper and lower limits of the displacement estimated from FIM data dictate a range for the activation energy for adatoms to escape from the vicinity of the tip apex.

5.1.2 W(110) tips / Au(111) surface

In a manner similar to the W(111) tip, tunneling currents measured between W(110) tips and Au(111) surfaces exhibit continuous spikes. In FIM, the evidence of transferred atoms is much more difficult to discern than for W(111) tips because of their atomic structure made up of smooth planes. We examine changes to the W(110) tips, as characterized by FIM, after approach of the tip to mechanical contact and tunneling to Au(111) at 158 K, and after rest gas adsorption in UHV at room temperature.

Figure 5.5 summarizes the first of two experiments in which a W(110) tip was approached to mechanical contact with the Au(111) substrate at a temperature of 158 K.

The W(110) tip was fabricated with polycrystalline tungsten wire, so it is expected that the (110) pole of the apex is aligned to within ±10° of the wire axis[1]. The tip apex was characterized by FIM before approach to the sample, shown in Figure 5.5(a) with the low index planes labeled.

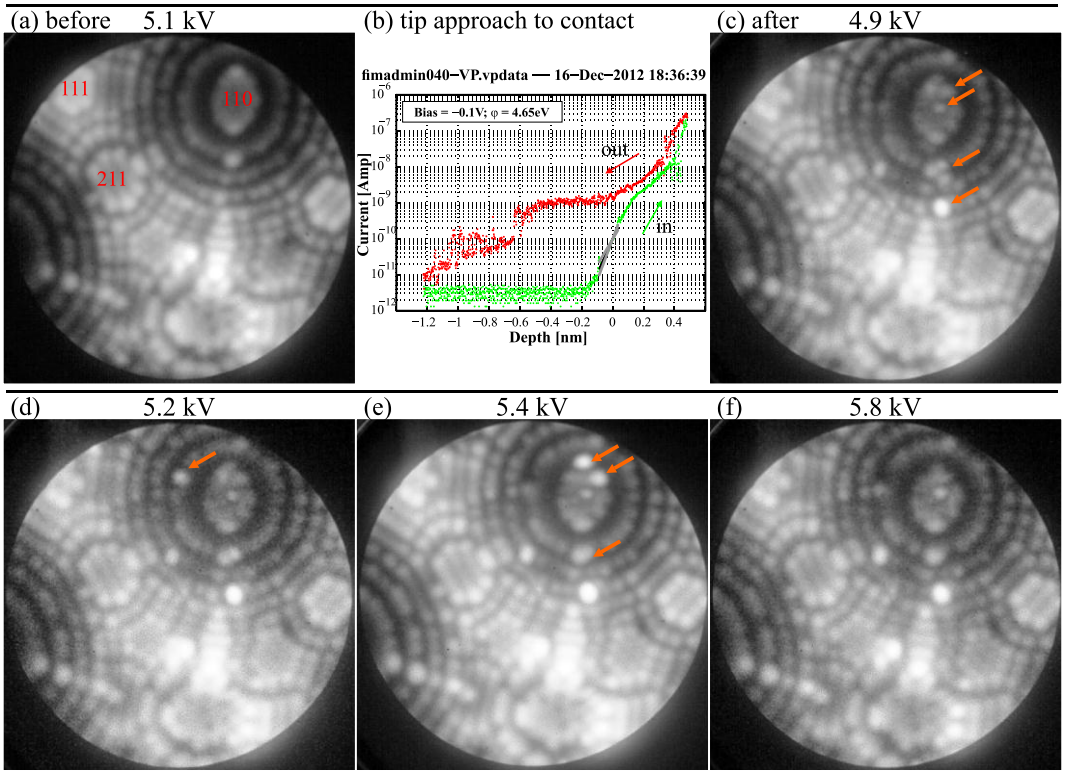

Figure 5.5: (a) FIM image of the ~12 nm radius W(110) tip apex. (b) Current-distance curve acquired during approach to contact showing a large hysteresis between in and out directions. (c-f) Field evaporation sequence of the tip imaged in FIM after the approach to contact.

After the initial approach to tunneling proximity with the Au(111) surface, the tip apex was moved toward the surface to incrementally larger displacements while monitoring the current behaviour until a signature of mechanical contact was obtained. For small displacements from the tunneling setpoint, a plot of the current as a function of tip displacement, I(z), will reveal the exponential distance behaviour expected for a tunneling junction (Eq. (7), page 20). The current recorded upon approach and retraction, 'in' and 'out' directions, should overlap unless there are any major changes occurring in the tip-sample junction. The I(z) curve plotted in Figure 5.5(b) shows the exponential increase on the 'in' curve (green) with an apparent barrier height of ~4.7 eV, on the order expected for a

[1] This number is estimated from the X-ray diffraction pole figure of the {110} reflections for cold drawn tungsten wire measured by Greiner and Kruse [138].

clean metal-metal contact [67]. The fit to the data is shown by the black line from 15 to 200 pA. At ~10 nA on the 'in' curve, an instability occurs and the junction conductance abruptly increases. Upon withdrawal of the tip from the sample, a large ~0.5 nm hysteresis is present, interpreted as the drawing and breaking of a wire of Au atoms pulled up from the sample. After this signature of mechanical contact, the tip was returned to FIM for characterization.

The FIM imaging sequence after mechanical contact is shown in Figure 5.5(c-f) during which the imaging voltage was gradually increased. In Figure 5.5(c), some of the changes to the tip apex are indicated by orange arrows – a few atoms have adsorbed onto the apex (110) plane, as well as the edge of (110) planes two to four atomic steps down from the apex. The edges of the (110) planes, particularly layers 2 and 3 from the (110) pole, also appear slightly more disordered, indicating changes to the atomic structure at their edges. Changes to the tip at the edges of (110) planes are particularly difficult to discern as the FIM does not provide resolution of the atomic structure at the plane edge. Upon increasing the imaging voltage, some adsorbed atoms begin to appear brighter (indicated with arrows in Figure 5.5(d-e)) before field evaporating – qualitatively similar to the behaviour of atoms seen on the W(111) tip in Figure 5.3.

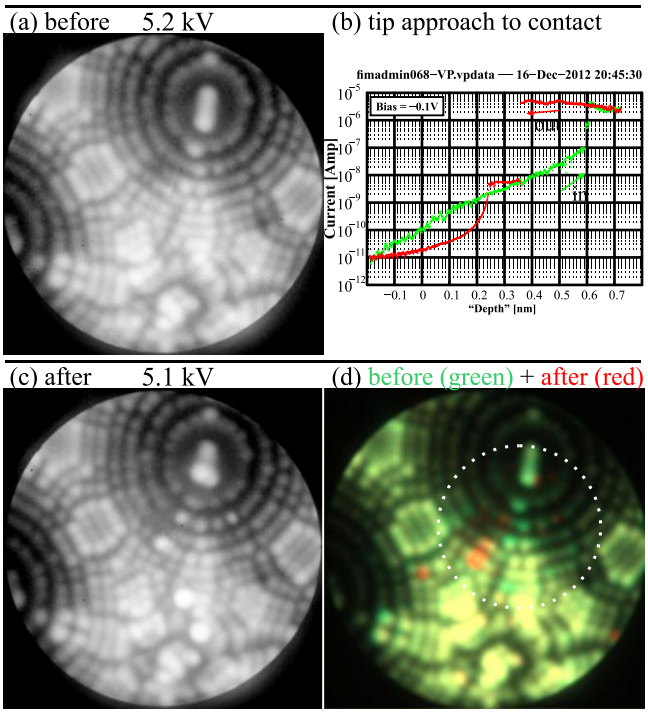

Figure 5.6: (a) FIM image of the ~12 nm radius W(110) tip apex. (b) Current-distance curve acquired during approach to contact (see text regarding inaccurate distance scale). (c) FIM image after contact experiment. (d) Colour superposition image of FIM images taken before (green) and after (red) the approach to contact.

A second experiment was performed in the same manner, summarized in Figure 5.6. The FIM images of the tip before and after contact are shown in Figure 5.6 (a) and (c), and the I(z) curve acquired during approach is plotted in Figure 5.6(b). The distance scale (and thus the slope of the I(z) curve) in Figure 5.6(b) is *very* inaccurate due to the thermal drift of the microscope being >1 nm/s during this particular measurement, requiring the I(z) curve to be carried out very quickly before the sample withdrew from the reach of the tip apex. The hysteresis and wire drawing are still indicative of mechanical contact, especially as the conductance of the junction suddenly drops during the 'out' curve. The strange shape of the red curve near its end (depth < 0.24 nm) is due to the settling time of the current preamplifier after the second break of the contact.

A superposition image of the FIM images before and after contact is shown in Figure 5.6(d). Special attention was paid to aligning the camera so that the images could be accurately compared. The 'before' image is illuminated in green, and the 'after' image in red, so that atoms appearing in green are those that have field evaporated, and those appearing in red are newly adsorbed. It seems that the changes to the tip structure are concentrated in the region indicated by a dotted white circle, centered about three (110) steps down from the (110) pole.

The rather large spatial extent of the tip changes seen in these contact experiments suggest that the transferred atoms have diffused a substantial distance on the tip, in contrast with our observation for the W(111) tip, in which tip changes were concentrated to a very small region at the apex. We know that the contact area between the gold and tungsten tip is small – on the order of one to several atoms. The maximum conductance during the first contact experiment is ~0.05 G_0, and the maximum conductance in the second experiment is ~0.9 G_0. Ab initio transport calculations carried out to support our previous nanoindentation experiments indicated that a modified Sharvin conductance of ~0.2 G_0 per atom is expected due to the k-space mismatch of conduction electrons in W and Au [43]. Further effects of crystalline disorder could reduce this value further. In any case, the contact region is *much* smaller than the ~7nm wide dotted circle in Figure 5.6(d). The diffusion rate of material away from the contact area is expected to be significantly faster on the W(110) plane compared to the W(111) plane – activation energies for single atom diffusion are ~2× lower than those measured for the same atomic species on the (111)

plane. Some typical activation energies obtained from FIM studies of single atom diffusion are summarized in Table 3.

Table 3: Activation energies for W, Pd, Ni adatom diffusion on W(110) and W(111) surfaces. From ref. [54].

Surface / Adatom	W	Pd	Ni
W(110)	0.93 eV	0.51 eV	0.49 eV
W(111)	1.85 eV	1.02 eV	0.87 eV

Although energy barriers for the diffusion of Au on W surfaces have not been measured experimentally, the scaling of the activation energies for other elements should be indicative of the behaviour expected for Au. The large atomic corrugation between binding sites on the bcc (111) surface compared to the bcc (110) requires a larger energy difference between the energy minimum and saddle point, hence increasing the energetic barrier for diffusion of any atomic species. The (110) plane is the closest packed bcc crystal plane, allowing for transferred material to displace significantly, even at a temperature of 158 K.

Knowing that Au adatoms are transferred to STM tips during tunneling interactions, W(110) tips were approached to tunnel to Au(111) substrates for several minutes to investigate the visibility of transferred atoms in a much more benign experiment than approach to mechanical contact. Two experiments were performed in which tips were approached to a setpoint of 25 pA at -0.1 V sample bias, and kept within tunneling range for five minutes. Minor changes to the 110 plane edges are seen after tunneling, shown in Figure 5.7(b) by orange arrows and in a colour superposition image in (c). Again, the (110) tip apex makes the identification of tip changes particularly difficult because of the lack of atomic resolution and the low diffusion barriers which permit the relocation of transferred atoms.

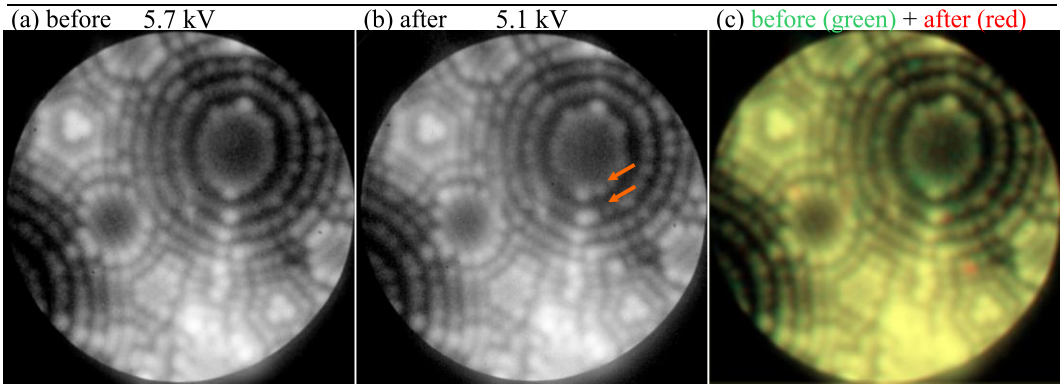

Figure 5.7: (a) W(110) tip apex before tunneling experiment. (b) W(110) tip apex after tunneling to Au(111) for five minutes. (c) Colour superposition image highlighting differences in the atomic structure of the tip.

Finally, we comment on the resolution of adsorbed atoms in general on the W(110) planes by examining a field evaporation sequence of a tip left in UHV conditions and subjected to rest gas contamination over several days. At the beginning of the initial FIM imaging sequence, starting at 5.7 kV in Figure 5.8(a), a significant number of adsorbed gas atoms have already been removed, and the (111) and (211) planes have begun to appear free of bright adsorbed atoms. The (110) plane at the tip apex seems to have some brighter adsorbed atoms on its edge, and one might conclude that this was the full extent of the damage to this area of the tip. Upon slowly increasing the field, atoms at the edge of the (110) are field evaporated from the tip, and reveal an enhanced contrast in in the central region of the plane. Figure 5.8(d) shows that the middle of the (110) planes is far from atomically perfect and contains many adsorbed gas atoms.

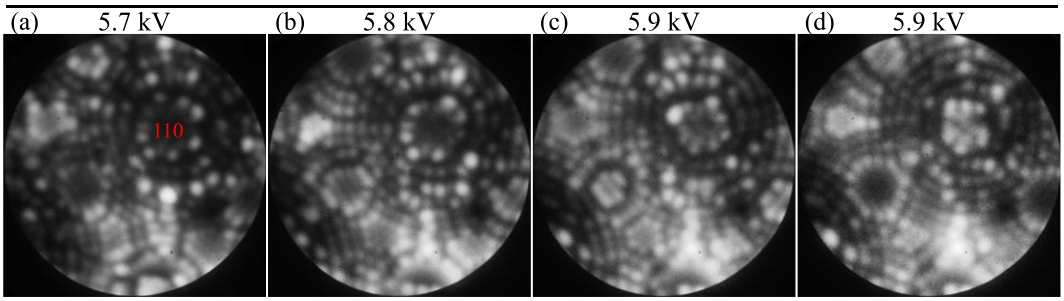

Figure 5.8: A field evaporation sequence of a W(110) tip left to adsorb UHV rest gases for several days. The (110) plane is shown to hide adsorbed atoms, which begin to be imaged as the edge atoms are carefully removed.

Due to the fact that the (110) planes are large and flat, the local electric field is not large enough to ionize He over the adsorbed atoms in the middle of the (110) plane in Figure 5.8(a). The (110) planes can conceal adsorbed atoms, making the close monitoring of field evaporation a necessity to discern changes to the tip's atomic structure.

To summarize, we have shown that the transfer of atoms occurs from Au(111) substrates to W tips. Transferred material diffuses to a great extent on W(111) tips at room temperature, but is confined to the (111) apex when cooled to 158 K. W(110) tips were brought into mechanical contact with Au(111) at 158 K, and it proved to be more difficult to identify adsorbed atoms on these tips due to the larger extent of diffusion on the (110) plane. Large, flat (110) planes hinder the characterization of the tip's atomic geometry due to the lack of atomic resolution and the fact that adsorbed material can be hidden within the planes. W(111) tips provide both high diffusion barriers and atomic resolution in FIM, making them most appropriate for SPM studies with atomically defined tips. However, the

transfer of atoms from Au(111) samples to W tips cannot be eliminated at temperatures accessible to our system.

5.2 Adatom diffusion under and transfer to the STM tip

The statistics of the tunneling current spikes between W tips and Au(111) samples are discussed, along with physical interpretation in the context of adatom diffusion. The possibility of measuring surface diffusion parameters with well-defined tips in STM is discussed. Appendix A contains an introduction to adatom diffusion on surfaces for greater context.

5.2.1 Tunneling current spikes: characterization

We now turn to the subject of the tunneling current spikes observed when clean FIM tips are approached to tunneling proximity with Au(111) surfaces – what information is contained within these spikes, and what can be learned regarding adatom motion and transfer to the tip?

The tunneling current spikes have a nearly identical peak shape, illustrated in Figure 5.9. Their width of ~0.4 ms is of the expected order based on the bandwidth of our tunneling current preamplifier. The consistent peak shape suggests that the instantaneous current spike, due to an adatom diffusing into and out of the junction, is very short in time. Each current spike is subjected to identical broadening from the detection electronics.

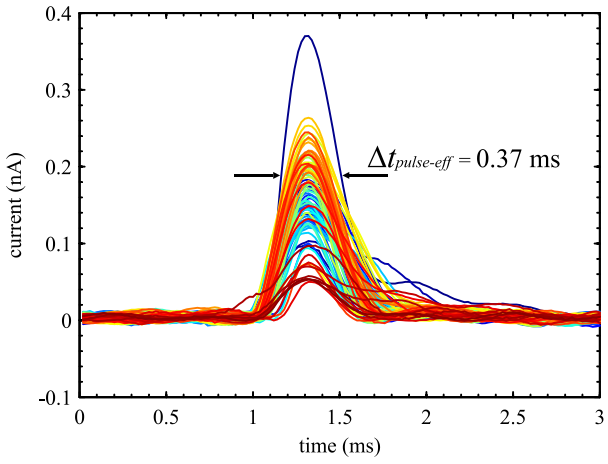

Figure 5.9: Tunneling current spikes detected while tunneling to a Au(111) substrate at 158 K. The peaks have a nearly identical shape suggesting that they are subjected to identical broadening due to the finite bandwidth of detection electronics.

Pictured in Figure 5.10(a) is the scenario of a diffusing adatom on the sample surface, depicted by a periodic potential landscape. The adatom gas density determines the rate of arrival of adatoms into the STM junction $\Gamma_{arrival}$. An adatom arriving under the tip will reside there momentarily. For a very short time, Δt_{atom}, the conductance of the tunneling junction is modified, allowing a much larger current than usual, I_{atom}, to pass through. The instantaneous current has the form of a rectangular pulse of width Δt_{atom} and height I_{atom}, as illustrated in Figure 5.10(b). The pulse detected by our relatively low-bandwidth current preamplifier is smaller in height and wider in time, as shown by Figure 5.10(c).

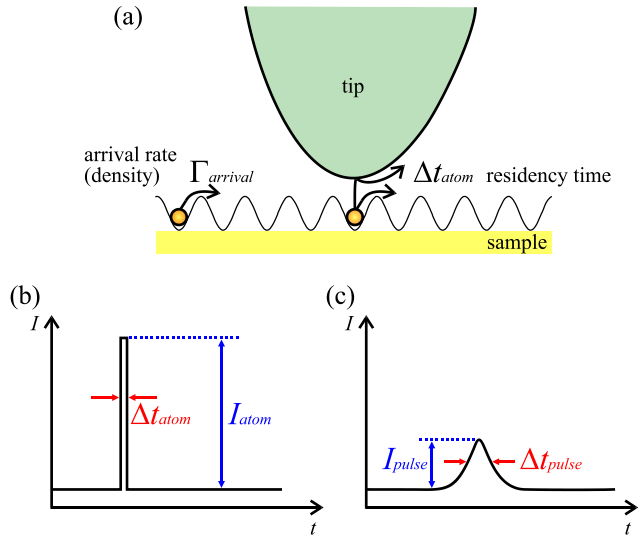

Figure 5.10: (a) Schematic cartoon of adatom diffusion in a periodic surface potential landscape and residing under the tip for some short time before escaping either to the tip or elsewhere on the sample. (b) The instantaneous current pulse due to the increased junction conductance is short in time and large in magnitude. (c) The detected current pulse is broadened by detection electronics, but will have the same integrated area as the pulse in (b).

The conservation of charge imposes a precise relationship between the instantaneous current spike and the broadened current pulse. The only place for electric charge to flow is through the current preamplifier, therefore the area of the instantaneous and broadened peaks must be equal:

$$Q = I_{atom}\Delta t_{atom} = \int_{t_1}^{t_2} I_{pulse}(t)dt\,. \qquad (49)$$

Because all of the detected pulses have the same shape, we can obtain their integral by multiplying the peak height by an effective width $\Delta t_{pulse-eff}$ (this makes it possible to obtain an integral for smaller peaks which fall into baseline noise). We find this effective width by plotting the numerically integrated peaks as a function of the maximum peak current, and taking the slope of this plot, shown in Figure 5.11. The obtained effective width

of 0.369 ± 0.013 ms compares favourably with a visual inspection of the full-width at half-maximum of the peaks shown in Figure 5.9 (where we have indicated this 0.37 ms effective width to scale).

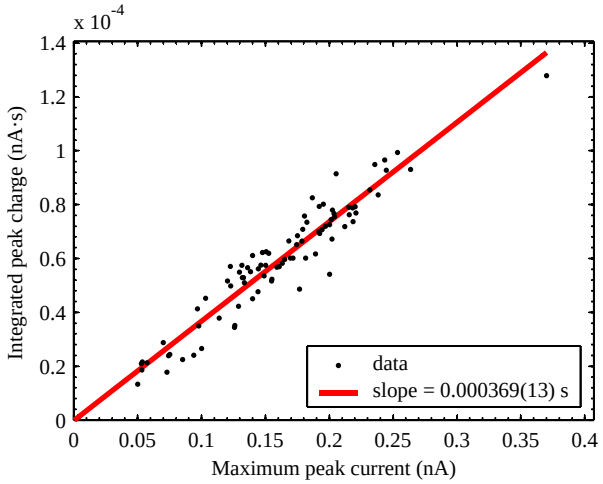

Figure 5.11: Plot of the integrated peak charge as a function of the maximum peak current. The slope gives the effective width which can be used to estimate the peak's area from its maximum value.

Replacing the integral in Eq. (49) with $I_{pulse}\Delta t_{pulse-eff}$, we obtain an expression for the residency time of an atom in the tunneling junction based on the pulse heights:

$$\Delta t_{atom} = \frac{I_{pulse}}{I_{atom}}\,\Delta t_{pulse-eff}\,. \tag{50}$$

In Eq. (50), a value must be estimated for the instantaneous current, I_{atom}. An adatom on the surface will be on the order of one lattice plane closer to the tip than the surface on which it resides, i.e. ~2.5 Å. Assuming the decay of the tunneling current to be one decade per Ångstrom, I_{atom} should be on the order of $10^{2.5}\times$ greater than the tunneling current baseline in the absence of the adatom.

Thermally activated adatoms will leave the tunneling junction at a rate given by the Arrhenius equation

$$\nu = \frac{1}{\langle \Delta t_{atom} \rangle} = \nu_0 \exp\left(\frac{-E_a}{k_B T}\right), \tag{51}$$

where ν_0 is an attempt frequency, E_a is the activation energy of the escape process, k_B is the Boltzmann constant, and T is the temperature. For an Arrhenius behaviour, we expect the distribution of residency times to be exponential: each attempt at frequency ν_0 has an equal probability of escape, $P_{esc} = \exp(-E_a/k_B\,T)$, thus the probability of the adatom still residing in the junction after n attempts (corresponding to time $\Delta t = n/\nu_0$) is $(1-P_{esc})^n$. A histogram of the maxima of the measured current peaks in the data recorded at 158 K

(Figure 5.2(b), page 149) is shown on a logarithmic scale in Figure 5.12. The distribution of current peaks, and thus the residency time, is exponential over at least two orders of magnitude.

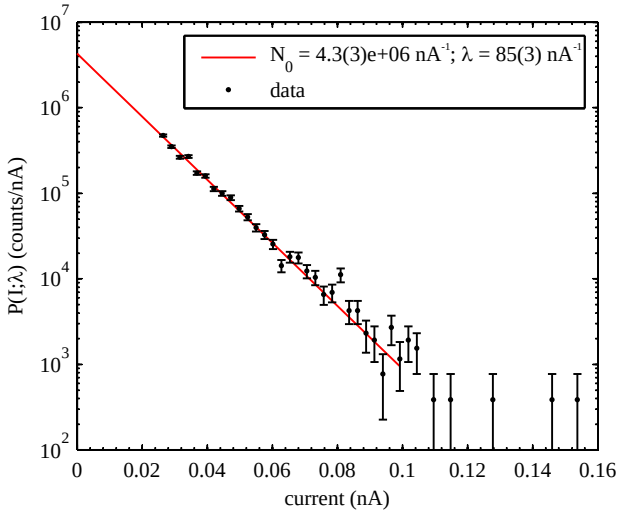

Figure 5.12: Log scale histogram of the number of tunneling current spikes as a function of spike height, showing an exponential distribution over at least two orders of magnitude.

By fitting the data in Figure 5.12 to an exponential probability distribution,

$$P(I;\lambda_I) = N_0 \exp(-\lambda_I I)\,, \tag{52}$$

a mean pulse current of $\langle I_{pulse}\rangle = \lambda_I^{-1} = 11.8 \pm 0.4$ pA is obtained. This corresponds to a mean residency time of $\langle \Delta t_{atom}\rangle = 2.3 \pm 0.1$ μs.

Rearranging Eqs. (50) and (51), the activation energy for the escape process is given by:

$$\begin{aligned} E_a &= k_B T \ln(\nu_0 \langle \Delta t_{atom}\rangle) \\ &= k_B T \ln\left(\nu_0 \frac{\Delta t_{pulse-eff}}{I_{atom}} \langle I_{pulse}\rangle\right). \end{aligned} \tag{53}$$

Assuming an attempt frequency of 10^{12} – 10^{13} Hz, an activation energy in the range of 0.20 – 0.23 eV is determined.

Finally, we consider whether any information about the arrival rate of adatoms, $\Gamma_{arrival}$, can be obtained from the tunneling current data. Given that the mean pulse current is about 10 pA, many of the spikes will pass below our detection threshold – simply measuring the time between the pulses detected above a threshold of ~25 pA will greatly overestimate the mean time between events. However, the total number of events in the exponential probability distribution of current pulses can be obtained by the fit parameters of the distribution (obtained by normalizing and analytically integrating Eq. (52)):

$$N_{tot} = \frac{N_0}{\lambda}. \tag{54}$$

The rate of the current spikes can be calculated by dividing this total number by the acquisition time interval. A rate of $\Gamma = 300 \pm 20$ Hz is obtained for the data in Figure 5.2(b).

For the room temperature data, an analysis of the tunneling current spikes presented in Figure 5.2(a) yields a mean pulse current of 3.6 ± 0.2 pA, corresponding to a 0.70 ± 0.04 μs residency time below the tip. The activation energy of the escape process is estimated to be 0.35 – 0.40 eV assuming an attempt frequency of 10^{12} – 10^{13} Hz. The mean pulse rate is found to be 1040 ± 300 Hz (note, however, that the measured pulse rates are not reflective of the true adatom arrival rate due to tip interactions as discussed below).

5.2.2 Discussion

From the exponential distributions of tunneling current spikes obtained in several experiments at 158 K and 298 K, we obtain activation energies of $E_{a_{158\,K}} = 0.19 \pm 0.01$ eV and $E_{a_{298\,K}} = 0.360 \pm 0.014$ eV. The uncertainties quoted represent the standard deviation of the six measurements at 158 K and four measurements at 298 K. Here, we have taken the attempt frequency to be 10^{12} Hz (see Appendix A). The measurement of two different activation barriers is somewhat unexpected for the similar experimental configurations – perhaps we are measuring two different escape mechanisms at these temperatures with differing energetics. A process requiring 0.36 eV will have a $\sim 3 \times 10^5$ smaller rate at 158 K than at room temperature, leading to very small statistics compared to the 0.19 eV process. Meanwhile, the detection of a 0.19 eV process at room temperature would require the measurement of ~0.1 pA current spikes, which is well below our current detection noise limit.

Order-of-magnitude variations in our assumptions for the instantaneous peak current, I_{atom}, and the attempt frequency, ν_0, contribute to errors in determined activation energies of $k_B T \ln(10)$. This translates to 0.03 eV at 158 K, and 0.06 eV at room temperature. If temperature could be varied slightly in these experiments, an Arrhenius analysis could be carried out by plotting the measured mean residency time as a function of 1/Temperature. Not only would this alleviate the required assumption of the attempt frequency, but it would also make the obtained E_a independent of the estimation of the instantaneous tunneling current value (Eq. (50)). If the mean time were wrong by some factor α because of the

instantaneous current estimation, it would appear at the intercept of the Arrhenius analysis, not in the slope:

$$\ln\left(\frac{1}{\langle \Delta t_{atom} \rangle}\right) = \ln(\nu_0) + \ln\left(\frac{1}{\alpha}\right) - E_a\left(\frac{1}{k_B T}\right). \quad (55)$$

The mechanism causing the tunneling current spikes has not been addressed – it is assumed that the energy barriers we measure are for the adatom to escape from the tunneling junction, which could happen by diffusion to other lattice sites on the surface, or by transfer to the tip. Spikes in the tunneling current could also result from rearrangements or adatoms diffusing on the tip itself. Comparison of the expected rate of adatom arrival (based on an estimated adatom gas density) to the measured rate of spikes may help discern the source of the events, and may help to illuminate the source of noise spikes in STM imaging.

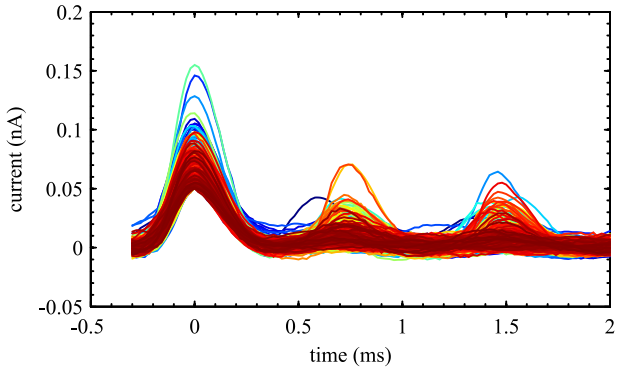

Figure 5.13: Time trace of the current for all spikes > 50 pA showing a regular time interval between many of the sequential spikes.

It turns out that the arrival rate of adatoms deduced earlier from the integration of the exponential curves (Eq. (54)) does not represent the true value for the unperturbed surface because of the influence of the STM tip. It is apparent that in several of our measurements, the tunneling current spikes are correlated in time. Figure 5.13 shows a plot of all detected peaks above 50 pA in the data collected at 158 K, centered together at time 0 ms. A periodic trend is immediately detected – spikes are often followed by other spikes at regular time intervals of ~0.75 ms. The reason for this could be a very small mechanical noise which serves to modulate the tip-sample separation very slightly, resulting in a regular tilting of the adatom energy landscape. Measurements of tip-sample vibrations at constant height on Si(111)-2×1 and Cu(100) suggest that the tip-sample gap stability is better than 20 pm. In atomistic simulations, changes in tip-sample-separation of ~30 pm have been shown to collapse barriers for diffusion or atom transfer by up to ~0.2 eV [216]. Although the arrival

of spikes is correlated in time, we expect that the escape process should be unaffected by this due to its relatively instantaneous timescale.

The extraction of the energy barrier for intrinsic adatom diffusion and the density of the adatom gas requires a non-interacting tip. From the direct observation of material transfer in FIM, we know that there must be a reasonable force exerted by the tip on adatoms which lowers the energetic barrier for transfer sufficiently that a finite number are transferred to the tip during measurements. Experiments performed at several tip-sample distances and applied voltages should clarify the role of the tip in the statistics of tunneling current spikes[1]. One might envisage the tip's effect on the diffusing adatom's potential landscape shown in red in Figure 5.14, in which two effects suggested in experimental and simulation work are illustrated. The strong electric field in the tip-sample junction is expected to interact with the adsorbate dipole moment, leading to a broad potential well superposed on the atomic corrugation [18, 217]. In addition, the height of the energy barriers between binding sites on the surface are expected to decrease with the proximity of the tip [216].

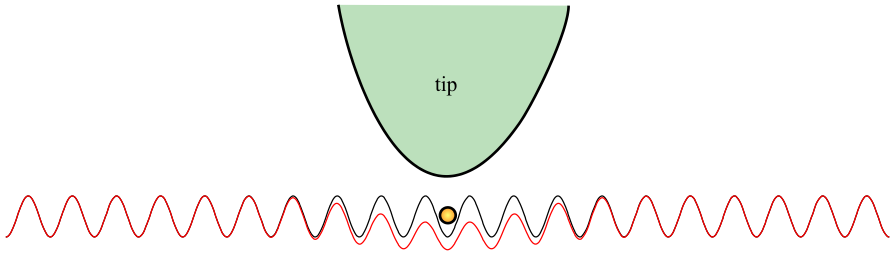

Figure 5.14: Illustration of the tip's effect on the adatom potential landscape – a broad potential well superposed on the periodic landscape, and decreased energetic barriers close to the tip location.

In a more sophisticated model, one may have to consider effects such as the resolution of the tip – an instantaneously high current might be measured while the adatom visits several sites under the tip, not just one. The known geometry of our tunneling tips provides a good starting point for such estimation. If one were interested in extracting the adatom gas density, one would also have to consider the return of the same adatom into the junction due to long-range tip interactions.

To summarize, we have characterized the exponential distribution of tunneling current peak heights observed when tunneling to Au(111) substrates at 298 K and 158 K. The mean peak heights were related to the residency time of an adatom in the STM junction through

[1] At the moment we have focused on reasonable low-current, low-bias tunneling conditions with the main goal of assessing FIM tip integrity in STM experiments.

the conservation of charge and an estimation of the peak tunnel current. From the residency time, the activation energy for adatom escape can be estimated. We have shown that even if not all events are above the detection noise, one can in principle integrate the exponential distribution and infer the mean rate of spikes. The influence of the STM tip, the detailed mechanisms of adatom escape, and the refinement of approximations remain open questions for future work in both experiments and atomistic modeling using the FIM tip structure as a well-defined starting point.

5.3 STM and STS with FIM-defined tips

Since we have shown in Chapter 4 that FIM tips can be approached to Si surfaces and return unaltered, we have investigated the Si(111)-2x1 surface with FIM tips by STM and STS to determine the limits of FIM tip integrity during such experiments. Since exceedingly little is known about atomically-characterized FIM tips in STM junctions, we seek answers to the questions such as: How long does it take for a tip change to occur? What are the characteristics of these tip changes? What instigates tip changes? What reasonable imaging conditions (bias voltage / tunneling current) need to be used to avoid tip-sample interaction? What is the range of bias voltages for STS for which the tips are atomically stable? Can we measure the I-V behaviour of a perfectly atomically defined nanojunction?

We first start with an introduction to STS, then report on our results of STM and STS investigations of the Si(111)-2x1 surface with FIM-defined tips.

5.3.1 Introduction to scanning tunneling spectroscopy

By varying the potential difference between the tip and sample of the STM, different eigenstates of the sample and tip become accessible for tunneling electrons. The investigation of the local density of electronic states (LDOS) with the STM is known as scanning tunneling spectroscopy (STS). We have waited until now to introduce these concepts because they are relatively irrelevant in our typical use of the STM to characterize the topography of metal surfaces where the local density of states is relatively featureless and where Eq. (7) does a reasonably good job of explaining the observed topography. Many surfaces do not contain a flat LDOS, such as those of semiconductors, so a more detailed model of electron tunneling needs to be considered. With these more 'exotic' surfaces, it becomes even more apparent that STM images do not reveal the 'position' of the atoms in

constant-current topographic mode. Rather, topographic images reflect an iso-surface of constant integrated LDOS over the bias voltage range. Due to the highly spatially-variable LDOS, which may represent bonding or anti-bonding states, the observed 'bumps' in a STM image should not necessarily be interpreted as the positions of atoms. Spatially resolved STS is a powerful technique to measure the LDOS around dopants, impurities, adsorbed molecules, steps, defects, etc., all of which can be important active sites in physical and chemical processes.

Results from STS measurements are well-described by the expression for tunneling current derived with the Wentzel-Kramers-Brillouin (WKB) method [218, 219]

$$I(z,V) = \int_0^{eV} \rho_s(E)\rho_t(E-eV)T(z,eV,E)dE\,, \tag{56}$$

where we integrate over the bias voltage range, V, between the Fermi levels of the two electrodes, ρ_s is the LDOS of the sample, ρ_t is the LDOS of the tip, and T is the transmission matrix element given by Eq. (57). The integral over the density of states of the tip and sample is illustrated for a positively and negatively biased sample in Figure 5.15. Electrons contributing to tunneling are illustrated by red arrows. In the above expression for I, we have removed the Fermi functions which serve to broaden the integration limits at finite temperature. From the WKB approximation, T has the form:

$$T(z,E,eV) = exp\left(-\frac{2z\sqrt{2m}}{\hbar}\sqrt{\frac{\phi_s+\phi_t}{2}+\frac{eV}{2}-E}\right). \tag{57}$$

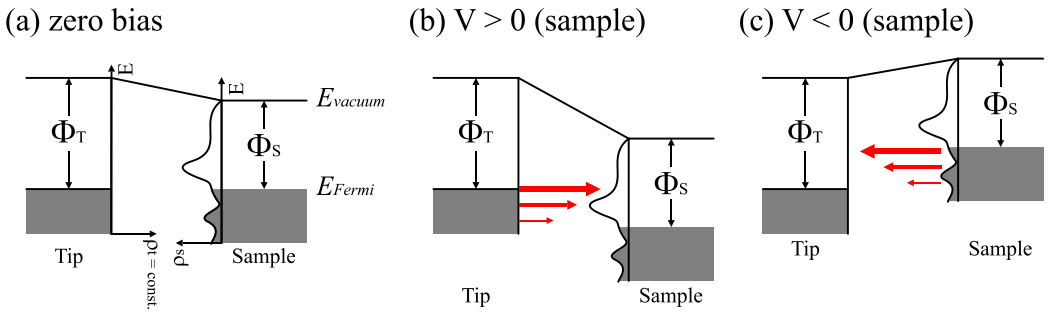

Figure 5.15: Density of states involved in the tunneling process, showing a featureless tip DOS, and a feature-rich DOS of the sample at (a) zero bias, (b) positive sample bias, probing empty sample states, (c) negative sample bias, probing filled sample states.

Working toward the goal of extracting the density of states of the sample, we take the derivative of the tunneling current I, Eq. (56), with respect to the voltage V:

$$\frac{dI}{dV} = \rho_s(eV)\rho_t(0)T(eV,eV) + \int_0^{eV} \rho_s(E)\rho_t(E-eV)\frac{dT(E,eV)}{dV}dE\,. \tag{58}$$

As a first attempt to isolate ρ_s, we invoke a common set of approximations first proposed by Stroscio *et al*. [220]. First, one assumes a constant $\rho_t(eV)$ (after all, the tip was etched out of a metal), and further assumes that the voltage dependence of the tunneling barrier, contributing to $T(z, E, eV)$, only contributes a smooth background in the second term of Eq. (58) on which the spectroscopic information is superimposed. These approximations suggest that the first derivative of the tunneling current is proportional to the product of ρ_s and T:

$$\frac{dI}{dV} \approx \rho_s(eV)T(eV, E)\,. \tag{59}$$

The transmission matrix element T can be removed to first order by dividing dI/dV by the quantity I/V – it roughly cancels due to its exponential nature (most of the integral comes from the 'top' part of the integration window from 0 to eV):

$$\frac{dI/dV}{I/V} \approx \frac{\rho_s(eV)T(eV)}{\frac{1}{eV}\int_0^{eV}\rho_s\,(E)T(E)dE} \approx \frac{\rho_s(eV)}{\frac{1}{eV}\int_0^{eV}\rho_s\,(E)dE}\,. \tag{60}$$

This procedure is commonly known as 'normalization' of dI/dV and can be used to extract an approximate LDOS from either numerically differentiated $I(V)$ data, or from dI/dV acquired directly with a lock-in technique. Because T has an exponential dependence on the bias voltage, a very large dynamic range is required to capture dI/dV over a substantial bias range. Experimentally, this can be done by acquiring dI/dV at several tip-sample separations, shown in Figure 5.16(a), reprinted from [221]. The curves acquired at different tip-sample separations can be normalized by dividing by the static conductance I/V, yielding the very well overlapping $(dI/dV)/(I/V)$ spectra in Figure 5.16(b) (the three curves are for several sample doping levels).

One convenient way to avoid the inconvenience of acquiring data piecewise at multiple tip-sample separations is to acquire dI/dV directly by a lock-in technique while maintaining a constant average current I_0 under feedback (slower than the lock-in modulation voltage). By doing so, the tip-sample distance varies slowly throughout the measurement to keep I_0 constant. This technique is known as constant current STS. An important advantage of constant current STS is that it safeguards against excessive currents which may damage the sample. However, a significant limitation is that this technique cannot cross zero bias under feedback.

Several groups have discussed interpretation of constant current STS spectra, which show somewhat similar features to those taken at constant current, but are quantitatively different. Kosolowski [222, 223] and Ziegler [224] have contributed significantly to the

understanding of these effects. Both of their approaches take into account the second term of Eq. (58), and Ziegler presents a method to use the tip excursion signal, $z(V)$, recorded along with dI/dV to recover ρ_s. Compared to constant distance data, peaks are shifted slightly to lower-magnitude bias, their position depending on the width of the peaks themselves and on any constant LDOS background which is present. Peak heights will be attenuated toward higher bias, and an increasing background will appear toward low bias arising from the slope of $z(V)$ being larger at low bias.

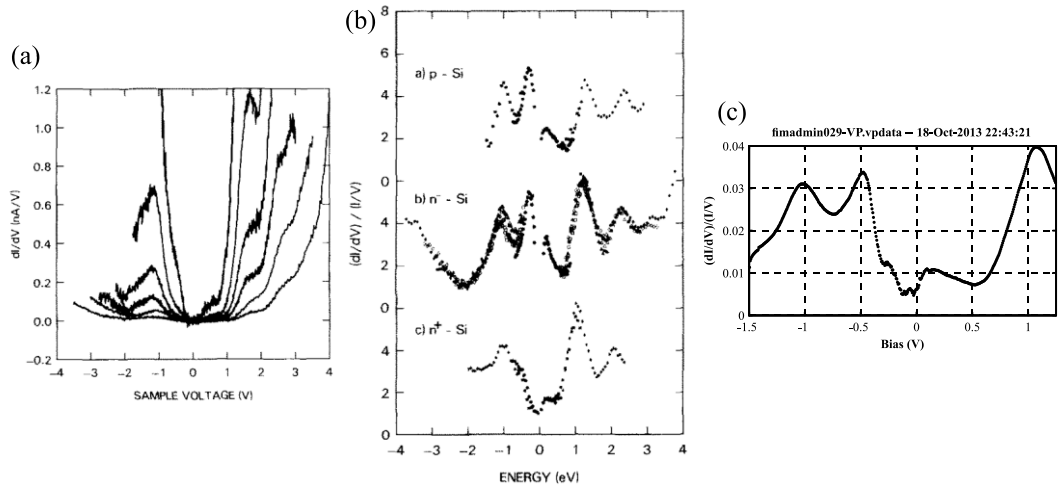

Figure 5.16: (a) dI/dV measured on Si(111)-2×1 at several tip-sample separations. (b) dI/dV normalized by I/V for several doping levels of Si wafer for the Si(111)-2×1 surface. (c) (dI/dV)/(I/V) acquired on our STM for one tip-sample separation on the Si(111)-2×1 surface – an average of 10 locations on the surface. (a) and (b) are reprinted from Ref. [221].[1]

With the support of atomistic modeling, FIM tips could provide a well-characterized tip DOS for the extraction of a true ρ_s, and would offer a routine starting ρ_t to aid in the repeatability of measured spectra. The transmission matrix element's dependence on energy tells us that the majority of tunneling electrons will come from the Fermi level of the negatively biased electrode, depicted by the arrows of varying size in Figure 5.15(b) and (c). This means that a non-flat tip DOS will be more apparent when it is being probed by the electrons of the sample at negative sample bias. It is the measurement of low-lying filled-states of the sample which will have the largest signature of the tip's electronic structure.

Finally, if one wishes to compare spectra from multiple measurements with FIM tips, one must have access to a reliable sample LDOS to measure. For this, we turn to Si(111)-2×1,

[1] Reprinted from Surface Science, Vol 181, R. M. Feenstra, J. A. Stroscio & A. P. Fein, "Tunneling spectroscopy of the Si(111)2 × 1 surface", Pages No. 295-306, Copyright 1987, with permission from Elsevier.

incidentally one of the very earliest surfaces to be studied with STS [220, 221, 225] (and now of revived interest due to recently discovered buckling structures of the reconstruction [226-228]). The spectra reprinted in Figure 5.16(a) and (b) correspond well with our STS spectrum in (c) obtained by numerical differentiation. Because ρ_s is spatially varying, one must be sure to take several spectra over the surface unit cell to obtain an averaged LDOS – our measurement in (c) represents an average of ten locations across the surface. Another consideration to preparing a repeatable ρ_s is that the sample must be cleaved well on the (111) plane and properly reconstructed – spectra taken on a stepped surface, or over surface defects will *not* be the same as on pristine 2×1 reconstructed areas.

The consideration of surface quality is well illustrated in Figure 5.17 where we start with a STM image of a 2×1 reconstructed area in (a), measure dI/dV and z (the tip sample separation) during constant current STS in (b), indent the surface in (c) and measure a completely different STS behaviour in (d). The final state of the surface in (e) shows a 3 Å high blob which unsurprisingly has a completely different LDOS from the sample. In the constant current STS spectra, we show individual spectra in different colours, and their average in black. In (b), we see two peaks associated with the bottom and top of the π^* unoccupied band of surface states [220, 221] near 0.5 eV and 1.25 eV, the lower of which is exaggerated in intensity due to the constant current mode of STS. These spectroscopic features also influence the tip-sample-separation curve, where the tip retracts faster at the points of larger LDOS. In (e), instabilities in the STM junction during spectroscopy are reflected by very a sudden change in both dI/dV and $z(V)$ behaviour.

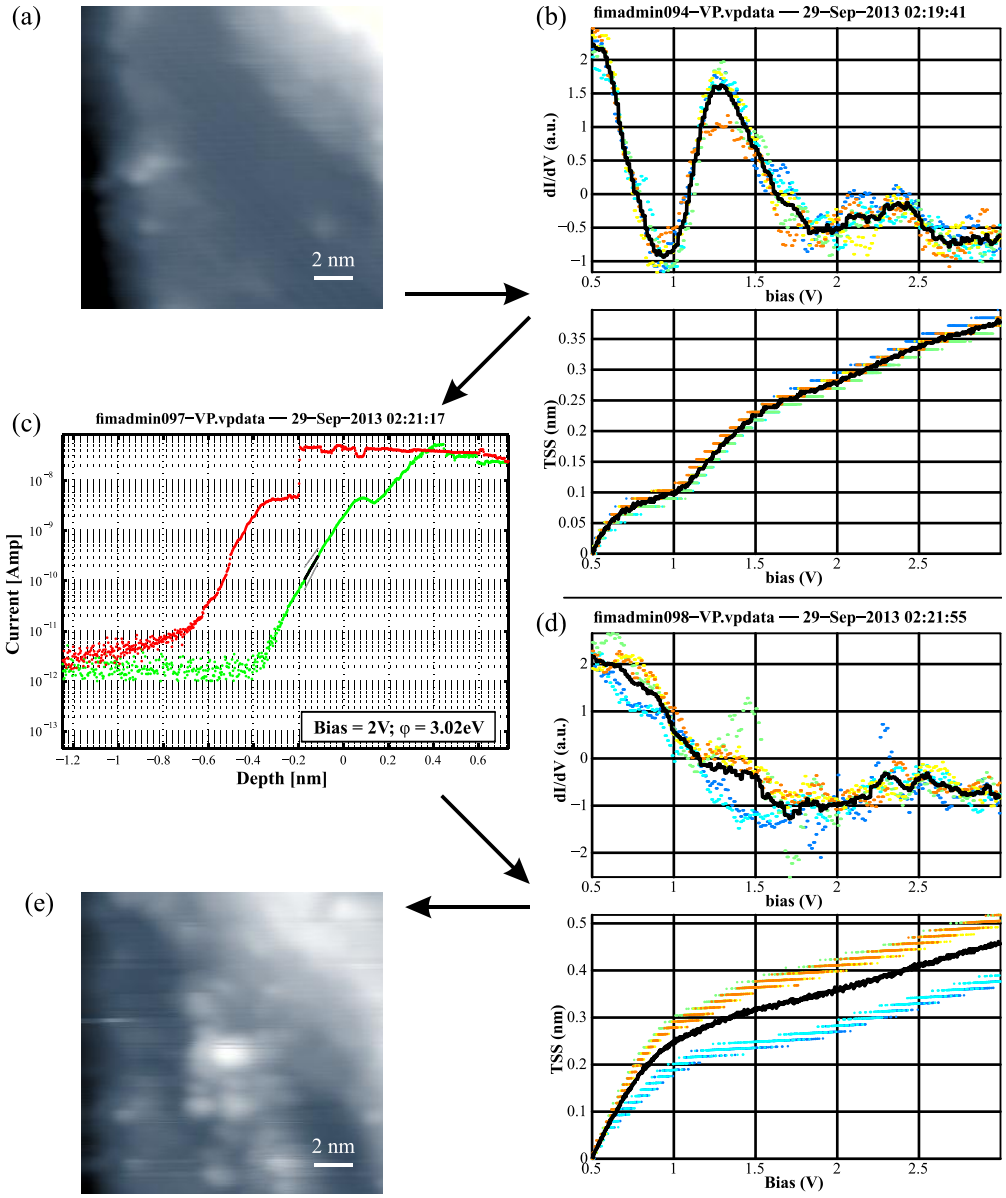

Figure 5.17: Illustration of the measurement of the surface LDOS and the importance of imaging to verify sample integrity. (a) STM image of the Si(111)-2×1 surface (24 pA, +2 V). (b) dI/dV and z traces from constant current STS taken in the middle of the 2×1 region. (I_0 = 25 pA) (c) Current-distance curve during a 1 nm indentation of the surface, showing a ~3 Å hysteresis. (d) dI/dV and z traces from constant current STS taken at the location of the indentation. (I_0 = 25 pA) (e) STM image showing a 3 Å protrusion on the surface due to the mechanical contact with the tip (24 pA, +2 V).

5.3.2 STM with FIM-defined tips

The results of seven experiments with freshly cleaved Si(111) surfaces have given us a good sense of the potentials and challenges of using atomically defined tips in STM. In our careful experiments, tips were approached to the surface with the techniques established in

Chapter 4, and a continuous log of the tunneling current was acquired for later examination of tunneling current spikes or instabilities. It turns out that even at very mild tunneling conditions (~10pA, 2V), spikes are observed at a rate of about one per minute while scanning Si(111)-2×1. In this section, we will first address the spatial resolution of the fresh W(111) tips. Then, we will discuss the spikes in the tunneling current observed in these experiments – their typical magnitude, correlations with discontinuities in STM scan height and instantaneous changes in STM resolution. Finally, we demonstrate the reverse-imaging of the tip apex structure by convolution with point defects on the Si(111)-2×1 surface, and discuss these image artifacts in relation to the real space atomic structure of the FIM tip.

Figure 5.18(a) shows a STM image taken with a FIM tip which has undergone very minimal changes – it was taken relatively early in the experiment, and only one large current spike occurred to ~0.43 nA before it was acquired. The lateral resolution of fresh tips is not particularly good, but this is to be expected due to their three-atom apex on the W(111) plane with 0.46 nm interatomic spacing (Figure 5.1(a), page 148, for example). It is only with some transfer of material during scanning or indentation of the tip apex into the surface that the tip can resolve the 2× rows of the 2×1 surface reconstruction (the 1× periodicity requires more tip conditioning until resolution is achieved, such as in Figure 2.30(a), page 63).

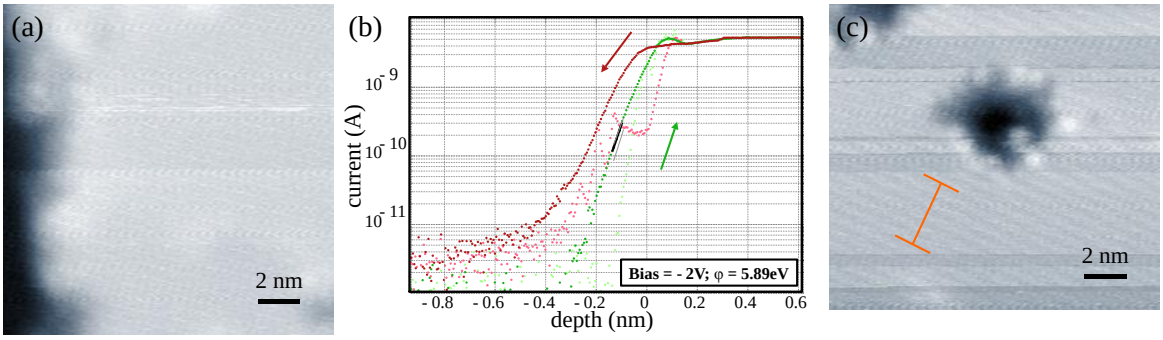

Figure 5.18: (a) STM image of the Si(111)-2×1 taken with a relatively fresh W(111) FIM tip (10 pA, -2V). (b) Two current-distance traces taken during indentation of the surface (#1 = dark, #2 = light colours). (c) STM image of the surface after indentation with improved resolution, but multiple tip changes. The orange marker indicates the region used to evaluate the sample corrugation, measured to be 6.9 ± 0.3 pm (15 pA, -2V).

In Figure 5.18(a), tip changes are evident by ~10 pm jumps in scan height at certain points during imaging (the slow scan direction is top to bottom, so they show up as a sudden change in brightness of scan rows). Two tip indentations were then performed to ~0.8 nm beyond the tunneling setpoint. The first is shown in dark red/green (in/out) and the second in light red/green in Figure 5.18(b). The 1-2 Å hysteresis and the sudden changes in current

when the tip is withdrawn the second time are clear indicators of material adhesion. After the indentation, the STM resolution is improved, allowing for the resolution of the reconstruction rows with a corrugation of 6.9 ± 0.3 pm measured in the region indicated by the orange marker in Figure 5.18(c). A ~5nm wide hole is left in the surface. Tip changes appear again as horizontal stripes across the image from sudden changes in tip height on the order of 10 pm.

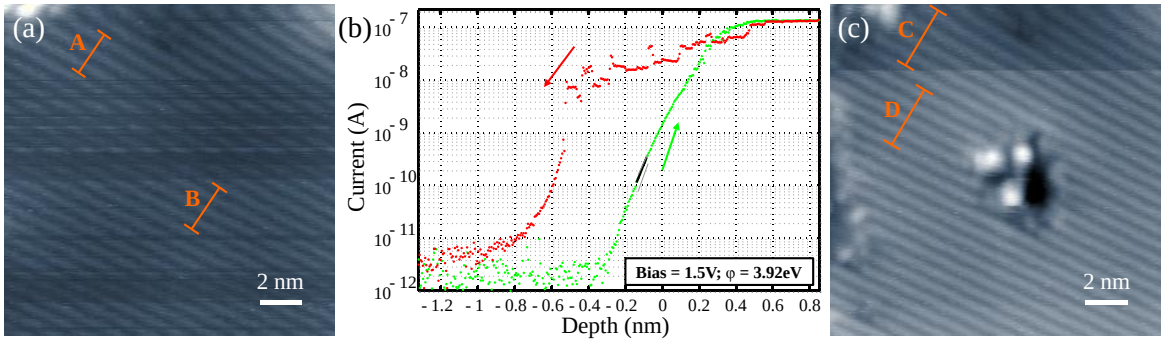

Figure 5.19: (a) STM image of the Si(111)-2×1 surface with frequent tip changes. The corrugations of the 2× reconstruction rows along profiles A and B are 13.9 ± 0.3 pm and 13.8 ± 0.5 pm. (60 pA, +1.5 V) (b) Current-distance curve acquired during indentation of the surface. (c) STM image of the surface damage resulting from indentation. Corrugations along C and D are 13.5 ± 0.5 pm and 18.2 ± 0.3 pm. (60pA, +1.5V)

Indentation of the tip can also be used to stabilize the apex if sudden changes are frequent during imaging, such as the 10 pm jumps in Figure 5.19(a). After the indentation, STM imaging is much more stable with the exception of one jump, corresponding to a 15 pm lengthening of the tip. The resolution is also improved in this jump, making for a ~35 % larger corrugation of the reconstruction rows. The corrugations measured along profiles A, B, C, and D in Figure 5.19 are 13.9 ± 0.3 pm, 13.8 ± 0.5 pm, 13.5 ± 0.5 pm, and 18.2 ± 0.3 pm, respectively.

Another example of spontaneous tip changes to a fresh tip is illustrated in Figure 5.20, where the first and second frames of constant current STM scanning are shown in (a) and (b). The surface here is atomically flat with some local point defects (imaged as protrusions), and shows a larger scale rumpling of amplitude ~0.5 Å[1]. After just over a minute of scanning the surface, a 80 pA current spike was detected at the location circled in (a), contributing to a sudden 14 pm extension of the tip, apparent from the averaged line

[1] Further imaging of the surface confirmed that it was indeed clean and 2×1 reconstructed, but this one (and only one) particular sample showed the rumpling, the origin of which is still undetermined.

profile plotted in (b). At this point in the experiment, the tip must no longer have the atomically defined structure which was characterized in FIM. A few more changes occur in the remainder of this image, none of which drastically affect the STM resolution.

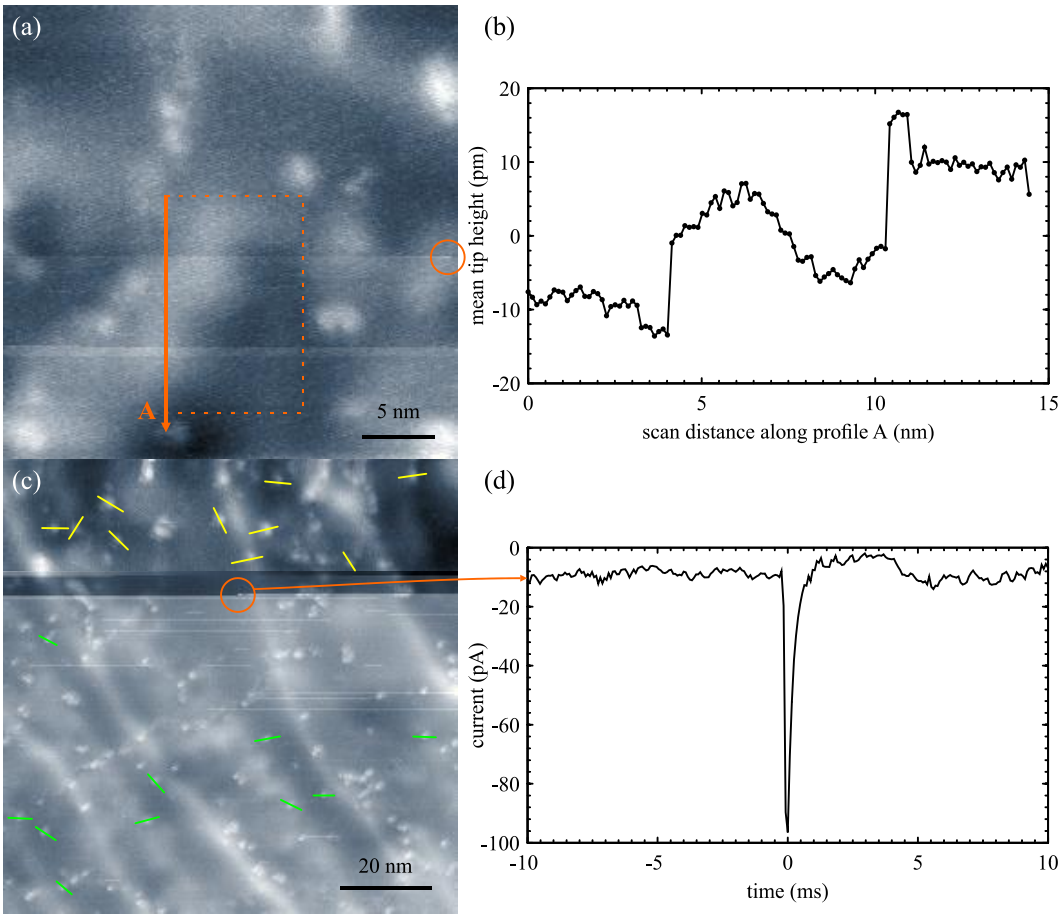

Figure 5.20: (a) First acquired STM image with a fresh W(111) trimer tip. (8 pA +2V) (b) Discontinuities in tip height along scan profile A show that the tip is being lengthened (c) Second STM image with the tip showing a sudden extension of the tip with a corresponding increase in resolution. Yellow and green profiles indicate those used to characterize resolution (see text). (8 pA +2V) (d) Spike in the tunneling current measured at the point of the tip change.

In the second image taken with this tip, shown in (c), a very large tip change occurred suddenly at the circled point, corresponding to a 95 pA spike recorded in the tunneling current, plotted in (d)[1]. This event lengthened the tip by 130 pm (much more than the usual ~10 pm variations), and a rather impressive improvement of the resolution of point defects is noticed just by inspection of the image. The resolution improvement is quantified by

[1] Note that the other contrast change which occurs several lines above this is due to the adjustment of the scan tilt while scanning – the image had to be piecewise adjusted in contrast and re-stitched for presentation.

analyzing ten profiles across the point defects before and after the tip change, indicated by yellow and green lines respectively. The full-width at half-maximum is improved from 17.2 ± 1.6 Å to 10.6 ± 0.6 Å after the tip change. The tip is apparently not entirely stable after this event, as evidenced by about a dozen intermittent tip changes appearing as streaks across the image. These seem to be reversible and last less than the duration of a scan line (1 second), and correspond to a 35 pm height change.

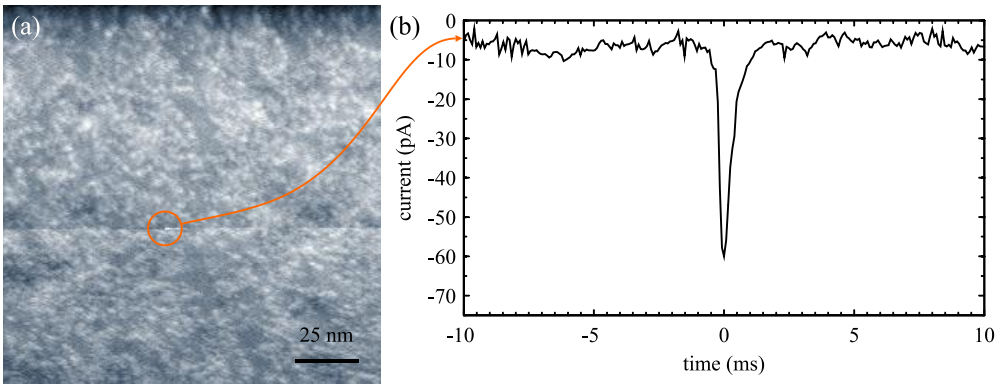

Figure 5.21: (a) Image of a poorly reconstructed Si(111) terrace with a clean W(111) FIM tip during which the first tip change occurs. (7pA +2V) (b) Tunneling current spike measured at the point of tip change.

We present another first-detected tip change in Figure 5.21 with a corresponding 60 pA spike in the tunneling current. The tip lengthened by 40 pm in this event which occurred after five minutes of STM imaging.

The surface topography in Figure 5.21(a) looks rather strange for a clean surface. It is apparently one atomically flat terrace with not much order within it. After another spike in tunneling current to 125 pA and a change in scan location, the topographic image in Figure 5.22(a) was recorded. Apparently only relatively small patches of the sample show the 2×1 reconstruction, leaving many point defects. This happens to be in the middle of the gargantuan > 10μm atomically flat terrace we measured in Figure 2.29(b) (page 61), where we wonder if the kinetics of the reconstruction process become frustrated due to the lack of nearby atomic steps. Irrespective of the mechanism, these point defects, probably unpaired Si dangling bonds, serve to report on the condition of the tip apex.

Repeated throughout Figure 5.22 (a) is a motif made up of two blobs, one slightly brighter than the other with a center-to-center spacing of 1.5 nm. Figure 5.22 (b) shows a larger image containing both the motif and two rotated domains of the 2x1 reconstruction – the less obvious one is rotated by 120° and is located in the top-left corner of the image. A dumbbell-shaped ball-and-stick representation of the motif is also drawn in Figure 5.22 (b).

This feature occurs repeatedly throughout the image due to the tip structure consisting of two atoms dominating the detection of the tunneling current which are convolved with point-like dangling bonds on the Si surface. We can relate the real-space directions of the scan image and the size of the convolution kernel to the FIM image of the tip[1]. The ball-and-stick representation is shown in Figure 5.22(e) and has been scaled to the magnification of the FIM image of the tip, determined by the 0.46 nm spacing of atoms on the W(111) plane. This gives us an idea of the size scale of the tip modifications in relation to the tip's atomic structure before STM. The convolution feature appears to be rather well aligned with the crystallographic direction of the (211) plane to the left of the apex.

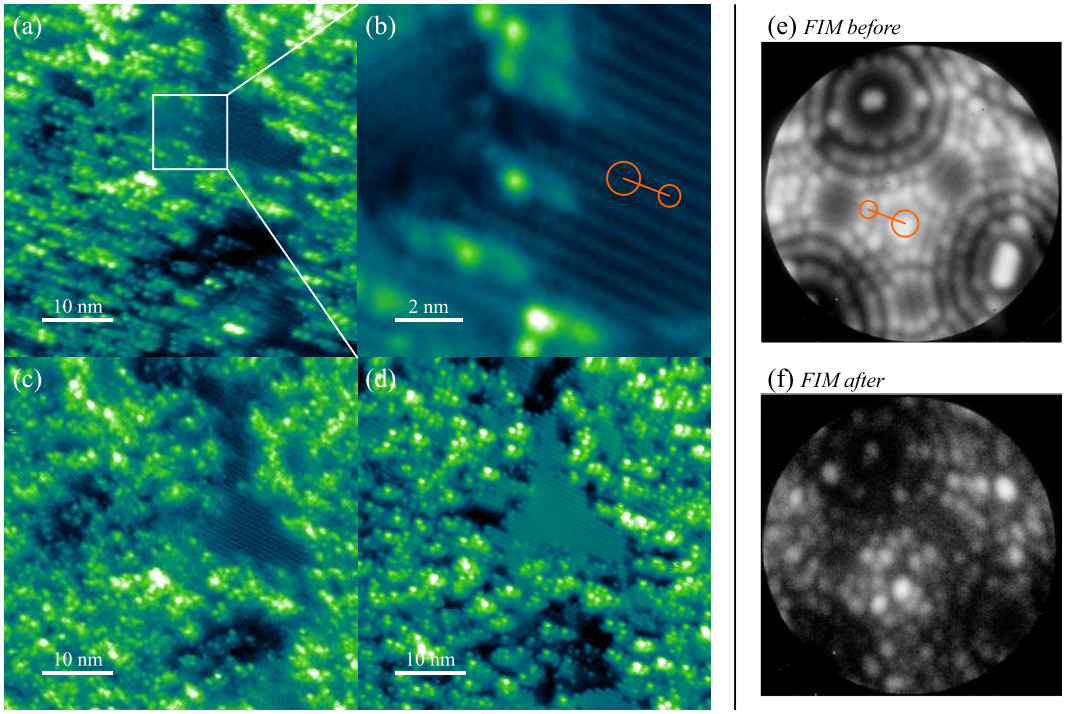

Figure 5.22: (a) STM image showing a partially reconstructed Si(111) terrace. (15 pA, +2 V) (b) higher magnification image of a region shown in (a) highlighting the tip convolution feature. (15 pA, +2 V) (c) Filled state STM image of the same area after tip changes. (15 pA, -2V) (d) Empty state STM image of the same area. (15 pA, +2V) (e) FIM image before STM experiments with tip convolution model scaled to the appropriate size and direction. (6.4 kV) (f) FIM image after extensive STM experiments. (6.2 kV)

[1] The +X scan direction is toward the Rutherford Physics Building rm 404 lab windows (Montréal west), and the +Y scan direction is toward the front window of the STM chamber (Montréal south). This can be checked by borrowing a ×40 high voltage amplifier (Nanonis HV amp from the ULT-SPM in the basement is appropriate) and running a ~10 μm raster scan: the motion of the tip can be seen by looking through the telescope. In order to make FIM images and STM scans have the same spatial axes, one must flip our standard FIM images upside-down and backwards (this has been done in Figure 5.22). To compare the convolution effect due to scanning, the kernel should be flipped upside-down and backwards as well.

After substantial surface scanning, STS measurements, and one indentation, the repeated motif of the tip has changed dramatically, shown in Figure 5.22(a) and Figure 5.22(b) (empty and filled state images, respectively). After these experiments, the tip was returned to FIM, and the first several images at the onset of He ionization were averaged for display in Figure 5.22(f). There is not much that can be determined about the atomic geometry of the tip, as we cannot characterize the loss of material due to field evaporation before the onset of imaging. However, it is apparent that the tip is not structurally damaged in any dramatic way – there is evidence that the (211) planes, though covered with adsorbed atoms, are still existent. This suggests that any mechanical damage to the tip is limited to a depth of a few W(111) plane spacings from its apex, that is, a few Ångströms (the W(111) plane spacing is 0.9 Å, see Figure 2.33, page 67).

Another very clear example of tip convolution is illustrated in Figure 5.23 from our only experiment with a W(110) tip. This tip was unique among these experiments both in its crystallographic orientation and its preparation by self-sputtering (section 2.8.3, page 68) giving a distorted FIM image due to the mechanical damage. Nevertheless, the tip was cleaned by field evaporation and was used in our early testing of STS techniques. A striking four-lobed blob is apparent in the high magnification image of Figure 5.23(b), in which the 2×1 reconstruction rows are also resolved. Figure 5.23(c) shows that this motif is repeated throughout the image – a dotted circle marks the location of the feature imaged in (b). After some STS measurements and an indentation which left a small cluster on the surface, the tip structure is shown to be markedly different by its convolution features in Figure 5.23(d).

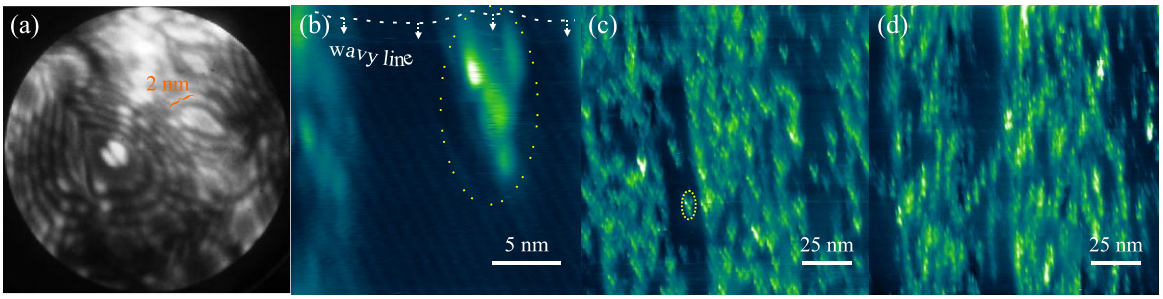

Figure 5.23: (a) FIM image of the self-sputtered W(110) tip before the STM experiment. (9.2 kV) (b) STM image showing 2× reconstruction rows and the large tip convolution feature. (11 pA, +2V) (c) Larger scale image showing the same convolution feature. (11 pA, +2 V) (d) Different tip convolution feature measured after tip indentation and STS measurements. (11 pA, +2V)

Interpretation of the FIM magnification of the self-sputtered tip is hindered by the inhomogeneous electric field due to its irregular shape – as a point of reference, however, we note that the width of the (211) terrace identified in Figure 5.23(a) is about 2 nm. The

convolution is on the order of 5nm wide and 10 nm long, so it is not clear what part of the tip may be large enough to produce this.

As a slight parenthesis, we comment on a very odd image artifact which has stumped several SPM experts who have examined it – it is highlighted in Figure 5.23(b). There is a wavy line running across the image, the shape of which is outlined by an offset dashed line – it appears almost as if someone has laid a string over the topography. Tips dragging molecules along scan lines could create streaks along the fast scan direction, however the departure from the fast scan direction is most peculiar. In addition, where it becomes wavy and departs from the horizontal, there is evidence of slight current overshoot/undershoot in the feedback error signal (not shown), indicating that the tip actually took this trajectory. We leave it as an exercise to the reader to propose an explanation.

To summarize, fresh W(111) trimer tips approached to Si(111)-2×1 surfaces show rather poor resolution at first, which is improved by spontaneous tip changes (usually tip lengthening), or by intentional indentation of the surface. Spontaneous tip changes generally happen within several minutes of scanning the surface, leaving relatively little time to characterize the tip in its pristine state. Tip changes can be identified by sudden changes in topographic scan height in images. The tip changes correlate with spikes of order 100 pA in the tunneling current, and often are accompanied by changes in imaging resolution, quantified by the reconstruction corrugation and lateral resolution of point defects. The condition of the tip is also reflected in the tip convolution with point defects, presumed to be silicon dangling bonds on the surface. The size of the convolution features and their orientation with respect to the scan axes can also be related to the atomic geometry of the FIM tips.

5.3.3 STS with FIM-defined tips

In experiments with atomically defined tips, there is a shortage of time to allow the microscope to thermally stabilize after transferring the sample – the sample must be cleaved in the preparation chamber, transferred, and approached within 20-30 min of pumping the FIM imaging gas. The resulting thermal drift between the tip and sample coordinates in our measurements on cleaved silicon range from $\sim 0.2-0.4$ Å/s, always in the direction of increasing tip-sample separation. In this situation, constant current STS is much more practical than constant height STS as the drift is compensated by the feedback loop. Results of constant current STS on clean and reconstructed regions of Si(111)-2×1 are

presented here. We start with the effect of tip indentation on filled state (negative sample bias) spectra for a relatively clean FIM tip, then look at the repeatability of empty state (positive sample bias) spectra with different tips. Since it is ultimately desirable to measure STS in the absence of any tip changes, we discuss several indicators of tip changes which can be used to monitor the tip apex integrity. Finally, we demonstrate the limits of constant current spectroscopy near low bias, where the tip-sample-separation decreases to the extent that the tip and sample collide.

We discussed in section 5.3.1 that the signature of the tip DOS should be most prominent at negative sample bias due to the majority of the tunneling electrons coming from the Fermi level of the sample. We start with a relatively clean tip in the state shown in Figure 5.22(b), after two spikes were detected in the tunneling current from the time of its initial approach to the surface, which yielded a two-lobed tip convolution with a spacing of 1.5 nm. The constant current STS measured with this tip for negative sample bias is shown in Figure 5.24(a) in blue, and represents an average of ten spectra taken in a line across the surface (to average over variations of the LDOS in the surface unit cell). The steep rise toward -1 V is attributed to the lower edge of the π band of the surface state, seen in the constant height spectra in Figure 5.16(b) and (c). Following an indentation to a depth of 1 nm, a marked increase of the dI/dV signal is seen in the red curve for low magnitudes of the bias voltage. We presume that this is a signature of a different tip DOS because the STS measurement after indentation was also performed in a region of pristine 2×1 surface.

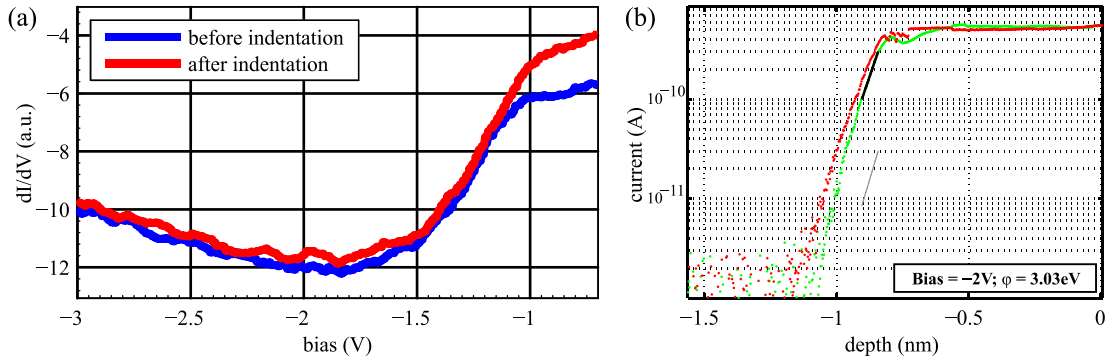

Figure 5.24: (a) Constant current negative sample bias STS measured before and after indentation. Both spectra were acquired on pristine 2×1 areas. (I_0 = 15 pA) (b) Current-distance curve acquired during indentation of the surface, used to alter the apex of the tip.

Constant current STS spectra for positive biases are shown in Figure 5.25 for two different days of experiments, each corresponding to the average of ten locations over the surface. The red and blue curves were taken sequentially with the same tip and sample with

one STM scan in between. In these spectra, the tip was in the condition produced by the handful of tip changes discussed in Figure 5.20. The origin of the dI/dV vertical offset is not clear. The green spectrum was taken with a different tip-sample system where the tip had been largely modified from its initial state by the indentations previously shown in Figure 5.18. Despite the very different tip treatments, the spectra reflect the expected surface DOS peak at 1.25 V (top of the π^* band), and what may be a bulk DOS peak at 2.25 V.

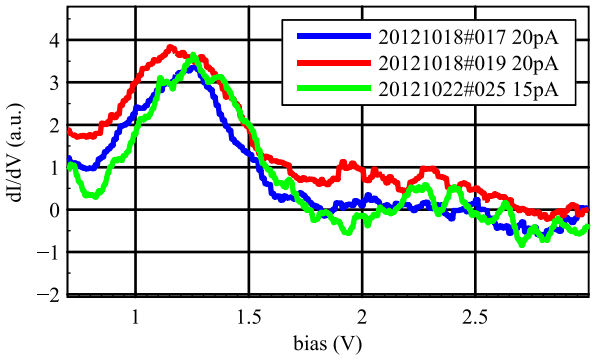

Figure 5.25: Constant current positive sample bias STS spectra measured in different experiments. Constant current settings indicated in the legend.

We now address tip changes during constant current STS: Sometimes, the tip rearranges as the bias voltage is varied under feedback, and it is important that these changes be detectable in experiments with atomically defined tips. The tip-sample-separation during a particularly poorly-behaved spectroscopy experiment is shown in Figure 5.26(a); the individual colours represent the curves from ten individual spectra, while the black curve is their mean[1]. Tip rearrangements are clearly reflected in sudden changes of the tip-sample-separation, such as those in the yellow, dark blue, and medium blue curves. Plotting the current during the constant current STS spectrum should yield a constant value due to the enabled feedback, however in the case of tip changes, spikes are discerned quite well in the data, illustrated in Figure 5.26(b). Although the bandwidth of the acquired data is not as high in the GXSM controller as with our MATLAB logs of the tunneling current (GXSM averages samples together and returns a fixed number of points), the tip changes contribute large enough current spikes that they can be detected directly here.

[1] The quantized values reflect the bit values of the digital-to-analog converter, although GXSM is reported to output a dithered version which increases the resolution by 1-3 bits [80]. The quantized values are sloped due to the subtraction of the estimated tip-sample drift.

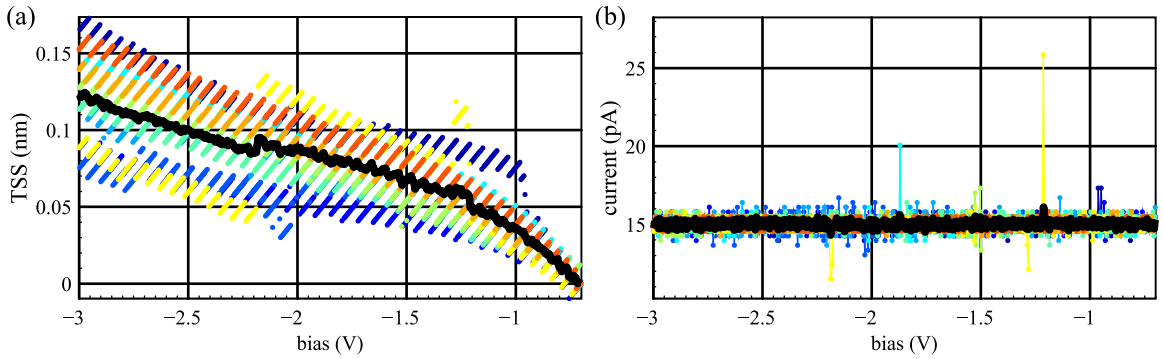

Figure 5.26: (a) Tip-sample-separation recorded during a constant current STS experiment with individual curves (coloured) showing large discontinuities. (I_0 = 15 pA) (b) Current recorded during the same constant current STS experiment showing spikes due to tip changes.

We end this section on STS with an exploration of the bias voltage limits of constant current STS. A topographic image of a ~15 nm wide terrace is shown in Figure 5.27(a), on which we perform repeated STS measurements, starting with the bias voltage range [+0.5 +2.5] V for which three individual spectra (non-averaged) are shown in Figure 5.27(b). Two more individual spectra were performed in the range [+0.2 +2.5] V, which agree very well with the previous. Their excellent agreement is attributed to the low lateral resolution of the tip which is large enough to average over the 2×1 surface unit cell – tips which have better spatial resolution will exhibit larger discrepancies between individual curves because each curve samples a more *local* LDOS. Upon decreasing the lower limit of the bias range to +0.1V, shown in orange, the tip crashes into the surface. This is reflected in a sudden withdrawal of the tip in the tip-sample-separation curve (not shown), a highly altered STS spectrum, and a hole visible in STM topography, Figure 5.27(c). This provides a useful lower bound for the bias range of constant current STS on the Si(111)-2×1 surface.

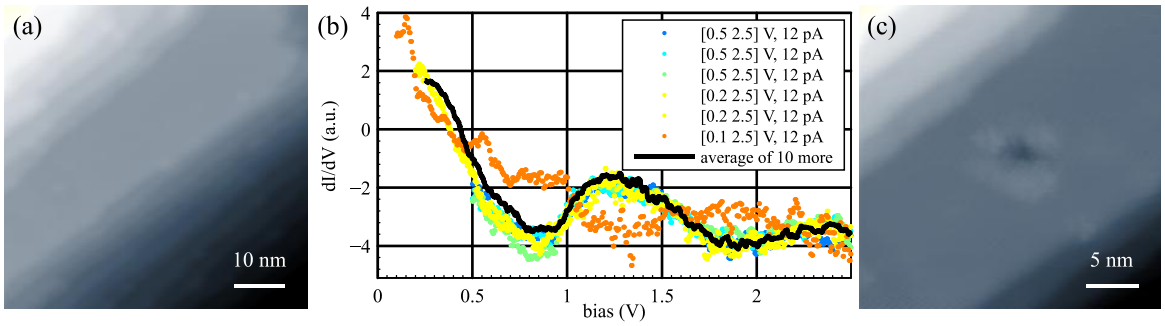

Figure 5.27: (a) STM image of a flat terrace of Si(111)-2×1. (12 pA, +2V) (b) Constant current STS spectra while decreasing the lower limit of the bias window toward 0V until a tip crash occurs. (I_0 = 12 pA) (c) STM image showing the indentation due to the tip crash in constant current STS at +0.1V.

In summary, we have measured changes in negative bias constant current STS spectra on the Si(111)-2×1 surface due to indentation induced tip changes. Unfortunately, no spectra could be performed with pristine tips due to the occasional tip changes discussed in section 5.3.2. Positive bias spectra seem to be reproducible regardless of the details of the tip treatment, though this should be investigated with better statistics. Tip changes during constant current STS can be identified by observing discontinuities in the simultaneously acquired tip-sample-separation signal and spikes in the current signal (which should otherwise remain constant). Constant current STS at positive sample bias was shown to be safe down to a bias voltage of +0.2 V; smaller bias voltages lead to indentation of the sample.

5.3.4 Discussion and outlook on FIM tips for STM and STS

We have demonstrated STM imaging with pristine FIM tips, although for very short periods of time. Tip changes have been characterized in STM images by discontinuities in tip height, spikes in the tunneling current, and changes to STM resolution. STS can be performed safely under constant current mode, which is most convenient due to the tip-sample thermal drift in experiments with rapidly transferred samples. Tip changes can also be monitored in STS by discontinuities in tip-sample separation and spikes in the tunneling current.

This still leaves us wondering what material could be used as a substrate in order to keep the tips atomically defined if Si(111)-2×1 only provides stability for a short time? Certainly, a STM operating at liquid helium temperature would quench effectively all diffusion and atom transfer processes relying on thermal activation, but at room temperature, we may still have some options. One option is inspired by the observation of exquisitely stable STM imaging of poorly-cleaved silicon surfaces, such as the one shown in Figure 5.28.

Although the surface topography of the poorly cleaved sample is rough compared to flat terraces, the sample is still reasonably flat – the vertical contrast limits are actually only 4 Å and 5 Å in (a) and (b) respectively. These images were also without doubt acquired with the pristine W(111) timer tip as it was characterized in FIM. Sudden discontinuities in tip height and large spikes in the tunneling current are completely absent from imaging on these rough surfaces. The lack of tip changes is attributed to the un-reconstructed surface – a somewhat randomly cracked silicon crystal will leave many unpaired dangling bonds which should be much more chemically reactive than the 2×1 reconstructed surface. We

suspect that this surface roughness and reactivity helps to bind any impinging gas molecules and prohibit the diffusion of any adatom species on the surface.

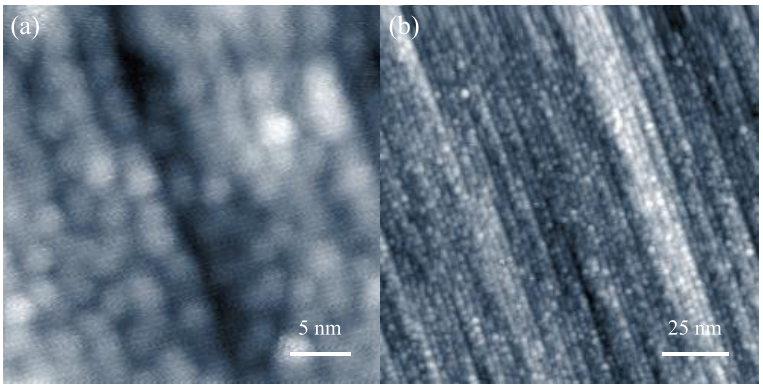

Figure 5.28: STM images of a poorly cleaved Si surface showing a high density of steps. (a) 6 pA, -2 V; (b) 12 pA, -2V.

This hypothesis is supported by two additional observations: Firstly, if one closely inspects the tip changes which occur in STM images, such as the one in Figure 5.20(c) (page 174), one observes that the location of the tip change is not correlated with any obvious features of the surface. Nothing static is being removed suddenly from the surface – we do not image a partial protrusion which suddenly disappears from the topography when it is transferred to the tip. This indicates that the transferred material is mobile on the surface. Secondly, mobility of molecules on the surface is evidenced by our observation, reported in section 2.7.7 on the preparation of cleaved Si(111)-2×1 (page 58), that rest gases lead to the depletion of the reconstruction after many hours in UHV. It was noted that molecules bind preferentially to domain boundaries which are more reactive, leading to expanding areas of adsorbed molecules over the surface – the 2×1 reconstruction does not disappear in the middle of a well ordered region. This, and our estimated sticking probability of order 0.2 (section 2.7.7, page 58), indicate that diffusive transport of molecules must occur on the 2×1 reconstructed surface. We therefore conclude that whatever is transferred to the tip was probably mobile on the surface.

In this case, what can be done? A more reactive or corrugated surface is needed – an obvious choice is Si(111)-7×7[1]. With its partially filled dangling bonds ready to capture and chemically react with impinging molecules, it should be able to keep our tips safe. Additionally, extraordinarily high diffusion barriers between the surface reconstruction's

[1] Preparation of the Si(111)-7×7 surface would requiring high temperature annealing currently unavailable in our apparatus as well as meticulous contaminant-free sample handling.

half unit cells, owing to the extreme atomic corrugation, should keep any adatoms still wishing to diffuse well confined on the surface [229].

5.4 Summary

In this chapter, we have characterized atomically defined tips in FIM and transferred them using the techniques and understanding developed in Chapter 4 to STM tip-sample junctions with Au(111) at 158 K, Au(111) at room temperature and with freshly cleaved Si(111)-2×1 at room temperature.

We concluded that W(111) tips are much better suited to atomically defined SPM experiments because they show atomic resolution in FIM and have high enough diffusion barriers at 158 K to prohibit the movement of transferred material. Tip changes can therefore be characterized in FIM after the SPM experiment by employing carefully monitored field evaporation. W(110) tips do not provide atomic resolution in FIM due to their large flat terraces, and additionally, their lower diffusion barriers permit the relocation of transferred atoms.

The current spikes measured while tunneling to Au(111) substrates were characterized by an exponential distribution of their peak heights, which we believe reflects the short lifetime of an adatom momentarily residing in the tunneling junction. Using the conservation of charge, we related the bandwidth-limited pulse heights to the residency time and discussed activation barriers for removal of the atom from the STM junction. We discussed the challenges associated with obtaining intrinsic diffusion parameters from measurements of current spikes in STM, and noted that a variable temperature experiment could be used to remove some assumptions made in the present implementation.

Finally, STM and STS on Si(111)-2×1 were investigated, showing that tip changes are still problematic to the implementation of truly atomically defined tips. An understanding of the characteristics of the very first tip modifications has been established from STM imaging. STS measurements have indicated that the effect of the tip LDOS may be measurable at negative sample bias voltages, but this must be further investigated with an unaltered W(111) tip. Disordered regions of the cleaved surface provided flawless STM stability against tip changes. This observation, along with those of the tip changes in STM imaging of 2×1 areas and the manner in which rest gas adsorption depletes the 2×1 reconstruction

suggest that an even more reactive surface must be found to guarantee the atomic integrity of FIM tips in STM at room temperature.

6. Atomic-scale nanoindentation

Understanding the initial plastic yield of materials at the atomic scale is of fundamental importance for the design of new nanostructured materials [230] and elucidating the origins of wear and friction [231, 232]. This chapter focuses on indentation experiments carried out with FIM characterized tips. The size of the tips characterizable in FIM corresponds directly to the length scale accessible in molecular dynamics modeling, therefore these experiments provide high quality data suitable for direct comparison with simulation. The preparation of tip apices by field evaporation in FIM also means that the chemical nature of the tip is known, which is certainly not the case for nanoindentation in ambient conditions, nor for UHV AFM indentation using traditional silicon cantilevers. The chemical composition of the tip surface is a factor which greatly affects adhesion during atomic-scale indentation and should be taken into account when comparisons with atomistic simulations are made.

Compared to traditional nanoindentation, our experiments offer excellent force resolution down to the nano-Newton regime, making it possible to capture the earliest indications of plasticity in force-displacement curves. The indentation depth is also precisely determined, which is not possible in traditional atomic force microscope (AFM) indentation due to problems with quantitative beam deflection calibration and large piezo displacements causing creep and hysteresis. Our AFM-based indentation is not affected by these issues because of its interferometric detection method where displacements are directly calibrated to the wavelength of laser light and relatively small piezo displacements ensure minimal piezo hysteresis.

We begin by introducing indentation and plasticity in section 6.1 to give the reader a sufficient background to appreciate the contrast between “macro”-nanoindentation and our atomic-scale experiments. In section 6.2 we focus on transient phenomena observed in the indentation of fresh tungsten FIM tips into gold surfaces, attributed to the wetting of the tungsten tip by gold atoms. The transition between elastic and plastic loading of an indentation contact is studied in section 6.3 – we examine in detail the intriguing features of the force-displacement and current-displacement curves, as well as STM images of the surface post-indentation. The indentation curves with the fresh tips discussed in this section are unique – we measure an anomalous negative-hysteresis loop, indicating that during indentation of fresh tips, some mechanical energy is transferred to the force transducer from the indentation volume.

We show high-resolution STM imaging of the residual impressions left by indentation in section 6.4 and discuss the rearrangements of the surface reconstruction near the indentation site, and what this implies regarding the type of defect left in the surface. STM imaging of the residual impressions also shows that they change over a timescale of minutes, and we report evidence that the symmetry of residual impressions reflects the symmetry of the {111} slip systems in the substrate. In section 6.5 we investigate incipient plasticity in Au(111), reporting on the formation of the smallest permanent indentation at the transition from elastic to plastic loading. Elastic and plastic indentations are identified both in the residual impression image and by features in their force-displacement curves such as the sink-in depth, pop-ins and hysteresis energy.

6.1 Indentation and plasticity review

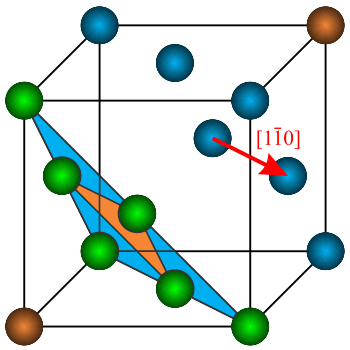

Figure 6.1: Illustration of the {111} ⟨1$\bar{1}$0⟩ slip system in a fcc metal. The blue atoms sit atop the sites indicated by blue triangles, and the orange atoms are atop the site indicated by the orange triangle. Together, the green, blue, and orange layers form the ABC stacking of the close packed fcc (111) planes.

In classical dislocation theory, a material yields due to the motion or generation of dislocations [233]. In a perfect crystal, the theoretical yield stress is the shear stress required to move one plane of atoms with respect to another. This process is known as slip, and occurs along a slip plane – generally between crystal planes which are spaced farthest apart and contain the highest density of atoms. The slip direction is usually the direction with the shortest translation vector. The combination of slip plane and direction is known as a slip system; for fcc metals, the slip system consists of a {111} slip plane and a ⟨110⟩ slip direction. There are 4 possible {111} slip planes containing 3 possible ⟨110⟩ slip directions in each. The {111} ⟨1$\bar{1}$0⟩ slip system is illustrated in Figure 6.1. With respect to the atoms in the green plane, the blue plane must be translated in the ⟨1$\bar{1}$0⟩ direction (red arrow) to

reach an equivalent lattice site. Slip in the $\langle 1\bar{1}0 \rangle$ direction occurs via the intermediate stacking fault site shown on the plane of green atoms by the orange triangle; the $\langle 1\bar{1}0 \rangle$ slip is carried out by two Shockley partial slips in $\langle 112 \rangle$ directions.

The boundary between the slipped and unslipped parts of the crystal is defined as a dislocation. The translation vector which is required to bring the dislocation back to perfect crystalline registry is known as the Burgers vector and uniquely describes the dislocation.

In order to produce a dislocation by a slip process, one must provide enough shear stress on the slip plane to move one plane of atoms over another. In a simple model of two atomic planes sliding with respect to each other, the theoretical shear stress is on the order of $\tau_{theo} \approx G/2\pi$ [233], where G is the shear modulus.

During an indentation measurement, a force is applied in the direction perpendicular to the surface. The loading of the crystal results in a complex sub-surface stress field – it is the magnitude of this stress field, resolved along a slip plane, which determines the load at which the material yields by a slip process.

6.1.1 Indentation measurements

Indentation can be a relatively simple mechanical test to characterize material properties, particularly hardness, and has been in use in this manner for over a century [234] . Hardness refers to a material's resistance to plastic deformation, and as a material property, it is particularly hard to define due to the dependence of the yield point on the volume being probed, the indenter geometry, etc. In a most straightforward indentation measurement, it corresponds to the force per area supported by the material during fully developed plastic deformation. For years, the contact area in indentation measurements had been extracted by examination of the residual impression by optical microscopy, and the hardness obtained as $H = P/A$, where P is the applied load, and A the projected (cross-sectional) contact area.

A desire to shrink the length scales of indentation was motivated by the prospect of probing the mechanical properties of just *one* crystalline grain of a material at a time. A major hurdle in shrinking the indentation size was the accurate determination of contact area after unloading [235]. This prompted the development of depth-sensing instrumentation, where the load and penetration depth are both recorded during indentation. With knowledge of the tip geometry, one can infer the contact area from the penetration depth. Nanoindentation is the application of depth-sensing indentation to small

displacements, typically on the nanometer scale. Commercial instruments working in ambient conditions have force and depth resolutions of ~300 nN and 0.25 nm respectively [236].

The features of a typical elastic-plastic force-displacement curve (known as a *P-h* curve[1]) are now discussed with reference to Figure 6.2(a). We consider a material in which plastic deformation occurs continuously during loading. The loading curve (blue), shows a rise in force with a non-constant slope reflecting the changing contact area. At maximum depth, the average contact pressure, $p_{ave} = H = P_{max}/A_{max}$, can be interpreted as the hardness, where A_{max} is the projected contact area. The contact is then unloaded (black), and the force reduces to zero at a depth of h_f. The work done in creating the plastic damage is the difference between the work done to load the contact and work released in the elastic unloading of the contact – this integrated area is shown shaded in yellow.

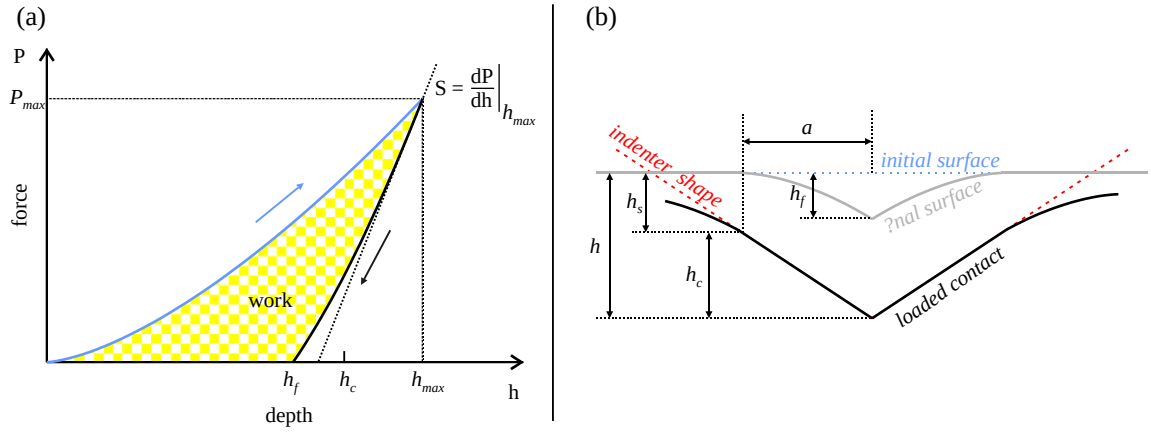

Figure 6.2: (a) Schematic force-distance (P-h) curve during indentation of an elastic-plastic material. (b) Side-view diagram of an indented surface showing the initial surface profile (blue), profile of the loaded contact at maximum penetration (black), the final surface profile (grey), along with various indentation parameters (see text).

The most significant advances in extracting material hardness and elastic modulus from force-displacement curves came from Doerner and Nix [234] and Oliver and Pharr [237, 238]. Oliver and Pharr extended previous work from a flat punch approximation to arbitrary indenter geometry by fitting the unloading curve to a power law $P = \alpha\left(h - h_f\right)^m$.

[1] *P-h* curves: where *P* and *h* clearly denote *ph*orce and depth respectively. In this chapter we will use 'force' and 'load' synonymously, as well as 'depth' and 'displacement' synonymously. The former terms are more common in the SPM community, whereas the latter terms are more common in the indentation community.

The unloading slope at maximum load, $S = \left.\frac{dP}{dh}\right|_{h_{max}}$ is used to infer the elastic sink-in depth, h_s, shown in Figure 6.2(b), using

$$h_s = \epsilon \frac{P_{max}}{S}, \tag{61}$$

where ϵ is a constant that depends on the indenter geometry (0.75 for a spherical indenter). The depth of the actual contact (below the depth of the elastically sunken surface) is $h_c = h_{max} - h_s$. The contact area at maximum depth can be inferred from the area function corresponding to the indenter geometry. For a sphere, the contact area is

$$A_{max} = \pi a^2 = 2\pi R h_c - \pi h_c^2, \tag{62}$$

where a is the radius of the contact circle, shown in Figure 6.2(b). From the unloading slope and the contact area at maximum load, the reduced modulus of the contact can be found using

$$E^* = \frac{1}{\beta} S \frac{1}{2} \frac{\sqrt{\pi}}{\sqrt{A_{max}}}. \tag{63}$$

The reduced modulus is defined as

$$E^* = \left[\frac{1 - \nu_s^2}{E_s} + \frac{1 - \nu_i^2}{E_i} \right], \tag{64}$$

where E_x and ν_x are the Young's moduli and the Poisson ratios of the sample (subscript *s*) and indenter (subscript *i*). Eq. (63) has been shown to apply for any axisymmetric indenter with a smooth profile [239].

Two important assumptions inherent to the Oliver-Pharr analysis are that the indentation is carried out in the absence of adhesion and that there is no pile-up of material around the indenter as a result of plastic damage. Adhesion and pileup are both concerns in our experiments, therefore we expect the Oliver-Pharr method to overestimate *E* and *H* due to the underestimated contact area of this approach. The Oliver-Pharr analysis of the continuum picture of nanoindentation still helps to define important features of the indentation process.

We now discuss the discretization of plasticity, which is a phenomenon observable in nanoindentation measurements at depths less than ~400 nm [235]. In Figure 6.3, force-displacement curves are shown for the nanoindentation of Al films of different crystallographic orientations. The initial loading curve shows a smooth elastic behaviour, but at certain loads, sudden horizontal bursts in displacement are seen, known as "pop-ins". The pop-ins are interpreted as the initiation of plasticity due to their departure from elastic

loading, and are expected to occur when the shear stress under the indenter is of the same order as the theoretical shear strength of the specimen.

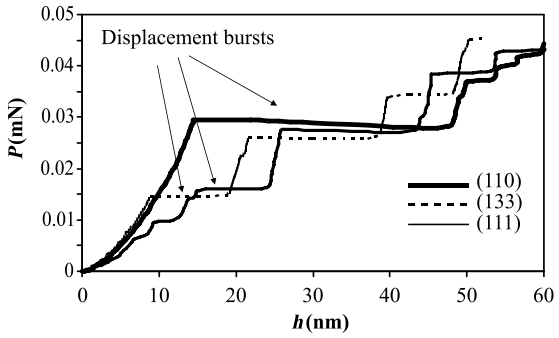

Figure 6.3: Force-displacement curve from nanoindentation of single-crystal Al films of thickness 400nm having different orientations (on Si substrates). The horizontal displacement bursts which depart suddenly from elastic behaviour are known as "pop-ins" and are interpreted as discrete plastic events. From Ref. [235].[1]

Pop-ins appear as horizontal displacement bursts in typical nanoindentation measurements because most commercial instruments are designed to operate under load control – the load is ramped at a constant rate, and a feedback mechanism ensures that the indenter travels until the depth at which the contact can again support the requested load. Load control of an indentation measurement is a rather alarming mode of control: After a certain yield event, the subsequent yield point may occur at a lower load once the contact is re-loaded. Indentation under load control will miss these events and will drive extra energy into the system, as has been pointed out by a few researchers [240]. The physically optimal measurement would be to implement a purely displacement controlled experiment wherein the indenter remains at a fixed depth during a pop-in event, measures a sudden change in force, and proceeds to re-load the contact upon continuation of the indentation. The displacement controlled scenario is illustrated in Figure 6.4(a), where the discrete plastic event is shown as a vertical drop in force. True displacement control implies that the force transducer and mechanical loop between indenter and sample have infinite stiffness – the depth does not change at the pop-in event.

Figure 6.4(b) shows a discrete plastic event occurring under load control, which was shown for real nanoindentation data in Figure 6.3. The force transducer has effectively zero

[1] Reprinted from Acta Materialia, Vol 55, A. Gouldstone, *et al.*, "Indentation across size scales and disciplines: Recent developments in experimentation and modeling", Pages No. 4015-4039, Copyright 2007, with permission from Elsevier.

stiffness as no change in contact load occurs the plastic event. In our measurements, the cantilevered sample has a finite stiffness (see section 2.5, page 27). A pop-in is characterized by a simultaneous drop in force and increase in penetration depth, as illustrated in Figure 6.4(c). The slope of the pop-in is the compliance of the force transducer which links forces to tip-sample displacements. Indentation experiments are controlled by moving the tip toward the sample at a constant rate – the position of the tip is known as z_{piezo}, which differs from the indentation depth by an amount equal to the bending of the cantilever. The indentation depth is obtained by subtracting the cantilever's deflection at the location of the tip, u_t (Figure 2.8, page 28), from z_{piezo}:

$$h = z_{piezo} - u_t \, . \tag{65}$$

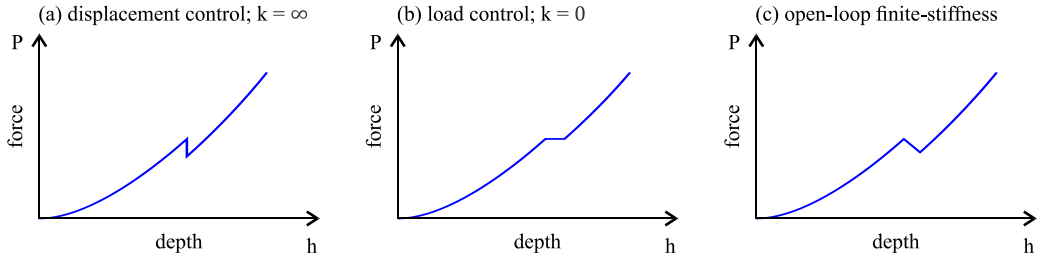

Figure 6.4: Control schemes for nanoindentation showing the appearance of discrete plastic events as (a) a sudden drop in load in displacement control, (b) a sudden displacement excursion in load control, (c) a simultaneous drop in load and increase in penetration depth in an open-loop finite-stiffness measurement.

An example indentation curve acquired during one of our experiments is shown in Figure 6.5 which serves to introduce some typical features of indentation. The colour code used to plot the data is consistent throughout this thesis: On the loading, or **'in'** curve, force is blue and current (or conductance) is green. On the unloading, or **'out'** curve, force is black and current (or conductance) is red.

We now discuss the features labeled A-G in Figure 6.5: The depth zero of the indentation, indicated by A, is set to the crossing of the 1 GΩ tunneling point of the current data (1×10^{-5} G_0 in Figure 6.5). A jump-to-contact is observed in the current at point B where the conductance of the junction jumps to ~ 3 G_0. Pop-ins are observed at the points labeled C on the loading force curve (not all pop-ins are circled). At ~50 nN on the unloading force curve, a pop-out is observed at point D, interpreted as a discrete event which reverses a plastic process introduced during loading of the contact. The large adhesion of the metallic contact is observed at E. The red conductance trace shows a large hysteresis, indicating that

a wire is drawn upon unloading which finally breaks at point F at a conductance of just over 1 G_0. If the drawn atomic wire is sufficiently short, sometimes a tunneling current is measured after its breaking point. In the example shown, no tunneling behaviour is present – the slow decay toward the detection baseline, labeled G, is due to the long settling time of the logarithmic current preamplifier after returning to the linear current regime below 1 nA.

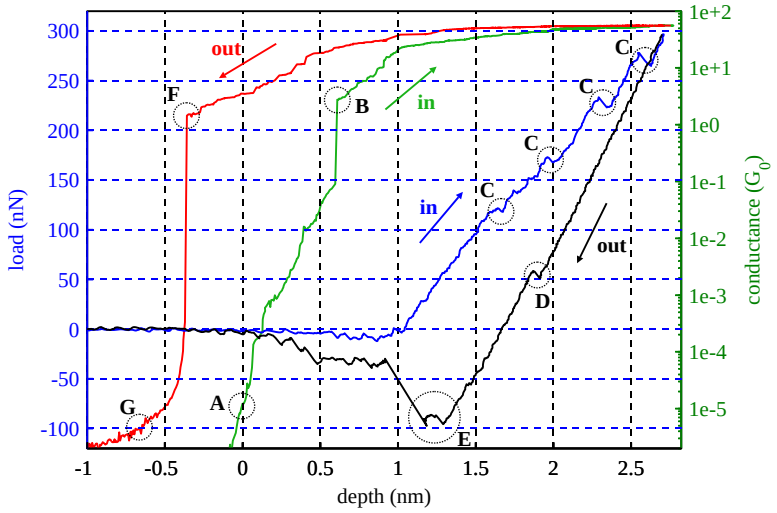

Figure 6.5: A load-displacement curve identifying the colour code used and several important features of indentation experiments (see text).

In the subsequent results, we will measure the junction conductance in units of the conductance quantum $G_0 = 2e^2/h$ because it is a convenient unit to use for contacts at this length scale. The ballistic conductance of an atomic wire of single atom width is very close to 1 G_0 (for Au, Ag, Pt, Cu), and arises from the laterally confined quantum modes of the wire (single eigenchannel transmission) [241-246]. We often measure atomic wires breaking near 1 G_0, but exact correspondence to 1 G_0 cannot be expected due to loss of transmission at the W-Au interface [43].

Systematic uncertainties in our experiment determine forces to ~10%, as discussed in Chapter 2. Piezo sensitivity governing the tip position is a function of scan position due to strain in the element, but is constant within 5%. Uncertainty in the penetration depth and force, as well as the correlated noise between force and penetration depth give rise to a ~ 30% uncertainty in the hysteresis energies reported by numerical integration. The slight temperature dependence in calibration of our current preamplifier should yield a calibration within 2.5 % at a conductance of 1 G_0 and within 7.5 % at a conductance of 10 G_0.

6.1.2 Atomic-scale plasticity

The small length scales of our experiments imposed by the very small ~4-12 nm tip radii involved require an atomistic perspective of plasticity. One of the earliest atomic-scale simulations of indentation was performed by Landman *et al.* [40] for a nickel tip indenting a gold surface. The molecular dynamics results showed a jump to contact instability occurring as a sharp increase in the attraction between tip and sample, when gold atoms from the substrate displaced by ~2 Å toward the tip and became chemically bound to it. The simulations showed that hysteresis in the force-displacement curve is a result of adhesive bonding. During indentation, non-monotonic increases in the tip-sample load resulted from a flow of gold atoms relieving indentation stresses by wetting the sides of the indenter and piling up around its edges. Slip processes were also observed on sub-surface {111} planes. Separation of the tip and sample was accompanied by inelastic processes in which the topmost gold layer remained adhered to the tip and an adhesive neck formed which thinned by ductile extension before breaking at a distance of 9-10 Å.

As we can see, the atomistic features of indentation as described by Landman *et al*. are markedly different from the continuum description. Another landmark work in the atomistic understanding of plasticity was a paper by Kelchner, Plimpton, and Hamilton [247], addressing the dislocation structures generated in Au(111) under indentation by a smooth sphere. A major contribution of this work was a new visualisation parameter used to identify and colour code different defect structures within the bulk, called the centrosymmetry parameter. This parameter vanishes if opposite nearest neighbours are perfectly symmetric – deviations from symmetric opposite nearest neighbours are summed, yielding a scalar value which can be used to easily distinguish and selectively visualise surface atoms, stacking faults, and partial dislocations. In terms of the mechanisms of nanoscale plasticity, their simulation showed that dislocations were nucleated by slip along {111} planes below the surface and displaced from the indenter's axis of symmetry. This was an initially surprising result given that the principal shear stress calculated from Hertz theory [248, 249] is expected *on* the indenter axis at a depth of $z = 0.78a$ below the free surface, where a is the indenter radius. A re-examination of the continuum solution with consideration of the projection of the shear stress onto {111} planes showed that the largest shear stress resolved onto {111} planes occurs off axis. The configuration of these dislocations is effectively identical to the results shown in Figure 6.6 for the indentation of Cu(111) studied by Zhu *et al*. [250] – in this particular snapshot from the simulation, three

dislocation embryos have formed on two different slip planes (the largest and smallest ones coalesce soon after this frame). The two resulting dislocation loops grow rapidly and emerge at the surface. Kelchner *et al.* always found twofold symmetric structures; two of the three possible {111} slip processes were enough to accommodate the deformation imposed by the indenter.

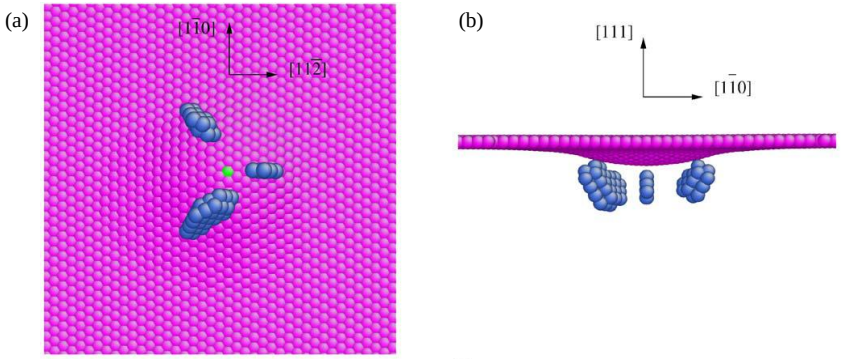

Figure 6.6: Molecular dynamics simulation of nanoindentation of Cu(111) by a spherical indenter. (a) View from under the surface, looking up. (b) Side view along [11$\bar{2}$]. From Ref. [250].[1]

The mechanism by which dislocations are nucleated in a material is of fundamental interest to the design of new nanostructured materials and elucidating the origins of wear and friction. The beginning of plastic behaviour during indentation is referred to as incipient plasticity – it is the first deviation from elastic behaviour in the load-displacement curve, often attributed to the first detected pop-in event. In the examples of Au(111) and Cu(111) discussed above, dislocations were nucleated homogeneously, that is, within a region of material of crystalline perfection. The alternative scenario that can transpire is one of heterogeneous nucleation, where the critical stress required to nucleate the dislocation is reduced by some local imperfection. Heterogeneous nucleation can result from (among many things) thermally promoted transient defects, point defects, or indenter surface roughness.

Wagner *et al*. investigated the effects of temperature and indenter surface roughness in the indentation of Al(111) [38]. It was concluded from their work with a 50 nm radius spherical indenter that the load required to nucleate a dislocation on the {111} slip plane was reduced at room temperature relative to 0 K due to transient "hot spot" defects which

[1] Reprinted from Journal of the Mechanics and Physics of Solids, Vol 52, T. Zhu, *et al.*, "Predictive modeling of nanoindentation-induced homogeneous dislocation nucleation in copper", Pages No. 691-724, Copyright 2004, with permission from Elsevier.

were concentrated near the regions of highest local shear stress – shown in Figure 6.7(b). The defects are caused by large thermal fluctuations of atoms away from highly coordinated sites. At elevated temperature, the depth at which the dislocation nucleated was also significantly shallower. The authors proceed to investigate the difference between a spherical indenter and a more realistic atomically rough indenter shape formed by carving out a spherical piece of diamond lattice in the ⟨111⟩ direction (also with a 50 nm radius). For the rough indenter at 0 K, Figure 6.7(c), a dislocation loop nucleates at the surface, aided by the indenter surface roughness, and proceeds to grow into the bulk as plasticity develops. At 300 K, Figure 6.7(d), small dislocation loops form at the surface due to indenter roughness, but before indentation stresses are adequate for them to propagate into the crystal, thermally induced defects help to nucleate dislocations within the bulk in approximately the same manner as for the smooth indenter at 300 K.

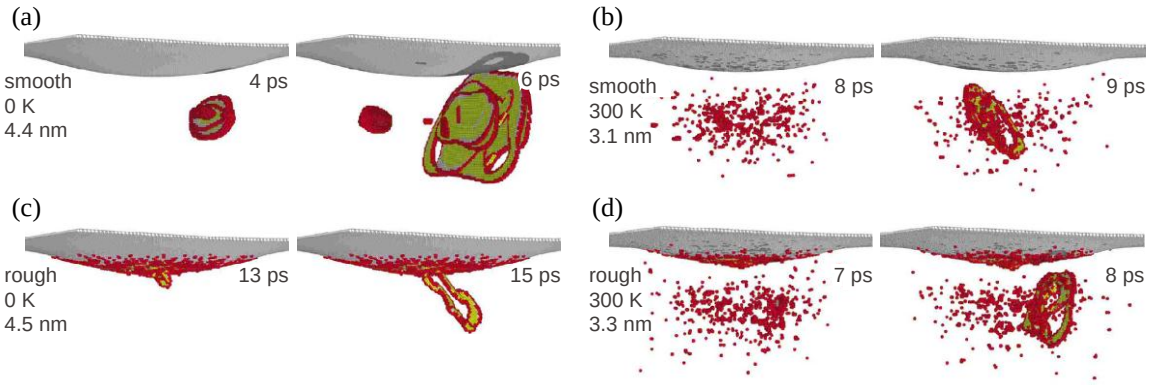

Figure 6.7: Defect structures during indentation of Al(111) coloured by the centrosymmetry parameter – surface (grey), partial dislocation (red), stacking fault (yellow). The four configurations results from indentations at temperatures of 0 K and 300 K and for smooth and rough indenters, as indicated. From Ref. [38].[1]

The picture of heterogeneous nucleation has been compellingly conveyed by the experimental work of Schuh *et al*., who noted that the load at which the first pop-ins were detected on single crystalline Pt(110) is highly stochastic [251]. By carrying out measurements in which the temperature and indentation rate were varied, the authors extracted an activation energy of ~0.28 eV and an activation volume of ~10.2 Å^3. The minute activation volume, of the order of a point defect, is a clear indication of heterogeneous nucleation – for homogeneous nucleation to occur, a cooperative process of

[1] Reprinted with permission from Wagner, R. J., Ma, L., Tavazza, F. & Levine, L. E. "Dislocation nucleation during nanoindentation of aluminum." *J. Appl. Phys.* **104**, 114311 (2008). Copyright 2008, American Institute of Physics.

atomic motion is required with a correspondingly large activation volume comprising many atomic volumes. This experiment didn't necessarily give insight to the type of point defect involved, but it conclusively supported the notion that plasticity should be thought of as a thermally activated and heterogeneous process (for this particular system, at least).

Another question which requires more experimental attention is whether the first pop-in detected during nanoindentation actually corresponds to the onset of plasticity, or if there are plastic processes which occur below the detection noise limits. In fact, indentation experiments of aluminum within a TEM column showed that small events barely distinguishable from the 0.5 μN noise floor caused dislocations to be nucleated and propagated through the grain being indented [252]. The authors also insisted on the importance of displacement control, and suggested that the manner in which many nanoindenters find the specimen surface – by approaching the indenter until a load above their noise threshold is detected – may already inject plasticity into the sample.

Surface oxides [253, 254], surface steps [255], and pre-existing dislocations or defects [256] contribute to a modification of the load required to initiate plasticity. The sensitivity of incipient plasticity to atomic-scale cleanliness and crystalline perfection makes investigation in UHV particularly worthwhile. The resolution of STM also allows extremely detailed surface characterization of the indentation sites. FIM characterization of the indenter not only allows its radius to be well characterized, but also its atomic scale roughness (due to its crystalline nature) which plays a large role in the breakdown of continuum mechanics in small asperity contacts [36, 39].

In the experiments described in the following sections we focus on phenomena uniquely measurable by the combination of FIM, STM and AFM. Performed at the same length scale as atomistic simulations, our results help to establish an experimental understanding of plasticity at the atomic scale.

6.2 Transient phenomena: tip wetting and conductance drop

The very first indentations measured with a clean tip are unique due to the transfer of sample material inherent in the adhesion process as described by Landman *et al*. [40], as well as the unavoidable material transfer we observe when tips are approached to tunneling proximity with Au(111) (Chapter 5). The care with which our tungsten tips were approached to samples in these experiments far exceeds what has been achieved previously

on the same experimental apparatus [45, 49], so initial tip wetting phenomena are here measurable for the first time.

6.2.1 Experimental results

W(111) tip apices were prepared by field evaporation in FIM and approached to tunneling interaction with Au(111) samples at a setpoint of 9 pA at –0.05 V sample bias. Upon finding the sample surface, the tunneling setpoint was reduced to 3–4 pA at –0.25 V sample bias to minimize the frequency of spikes in the tunneling current (and thus transfer of material). This setpoint was maintained under feedback for ~3 minutes in order for piezo creep to stabilize. The tip was then moved under feedback to a new location on the sample for each indentation, where it was approached toward the sample by 3 nm from the tunneling condition which was 25 pA at –0.05 V. The indentation sites were spaced by 25 nm in a 5 × 5 array. The surface topography was not imaged before the indentations so that indentation could be started with a minimally modified tip.

The resulting indentation curves from two such experiments are summarized in Figure 6.8 in the left and right columns. The general phenomena described here have been repeatedly observed in over a dozen experiments with different indenter radii – we present two sets of results with tips of nearly identical radii to emphasize the repeatability. FIM images of the tip apices used in these experiments are inset in (a) and (d) showing radii of 9.0 ± 0.7 nm and 9.5 ± 0.8 nm, determined by ring counting between the visible pairs of (110), (111) and (211) planes (section 2.8.2, page 65).

In (a) and (d), we plot the force upon loading the contact ('in' direction) for all 25 indentations, colour coded according to the legend inset in (a). The first loading curve is plotted in black over the coloured curves to emphasize the transient changes. Examination of the loading curves reveals that the rise of the repulsive force between the clean tip (black curve) and the surface provides a left-hand bound to the rest of the indentations. The depth axis is zeroed to the distance of a 1 GΩ tunneling gap, so what we observe here is the displacement of the onset of repulsive contact *relative* to the point at which a tunneling current is measured. This is explained by the adhesion of gold atoms to the tip, adding a compressible yet conductive layer of variable thickness to the apex. The offset between tunneling and repulsive loading eventually becomes rather stochastic and reflects the compression of various amounts of substrate material adhering to the tip before the rigid body W(111)/Au(111) contact occurs.

The corresponding unloading curves are shown in (b) and (e) for these experiments. Upon unloading, the first curve in (b) shows an unloading stiffness of ~370 N/m whereas the subsequent contact unloadings are much less stiff – the latter half of the curves in this set have an unloading stiffness of ~292 ± 11 N/m (the uncertainty represents the standard deviation in the distribution of fitted stiffness values). The stiffness determination is not particularly accurate because the fit region must be manually selected to avoid events such as pop-ins / pop-outs, and adjustment of the fit region readily changes the determined values by ~5 %. A continuous stiffness measurement obtained by AC modulation of the z piezo may provide a better means of measuring this value throughout indentation. The unloading curves end with an enormous attractive adhesion force reaching a maximum magnitude of −157 nN in the first curve of (b). The adhesion reduces quite rapidly to a much smaller value of ~ −50 nN after several indentations.

The conductance measured during indentation of the substrate is shown in (c) and (f) where both loading and unloading directions are plotted on the same graph. The sample bias was -0.05 V. The loading conductance curves pass through the depth zero point during the tunneling regime, and at maximum depth, the conductance generally reaches a near-maximum value. It is common for atomic rearrangements in the unloading curve to improve the junction conductance from its value at maximum depth by up to 20 %. The junction conductance decreases abruptly from ~88 G_0 to ~18 G_0 at the point where the adhesion force jumps from −154 to −24 nN. This jump is labeled by points A and B in both the force (b) and current (c) plots. The sudden rearrangement is accompanied by a change in penetration depth due to the compliant cantilevered sample, so we plot a time trace of both force and current in the insets showing that this event is effectively instantaneous in time (here, limited by the bandwidth of our digital acquisition antialiasing filter). The conductance decreases until the atomic wire breaks at a conductance of ~ 1 G_0 at a length of > 1.5 nm.

In subsequent indentations, the maximum conductance is markedly decreased and reaches a maximum of only 48 G_0 for the last indentation curve (see the progression of blue to red curves near maximum depth in (c) and (f)). Also, hysteresis in the current channel in subsequent indentations is much smaller, showing that the atomic wire breakage happens earlier. These later curves often return to the tunneling regime after wire breakage, indicating that the contact has not snapped to as large a separation as it did initially.

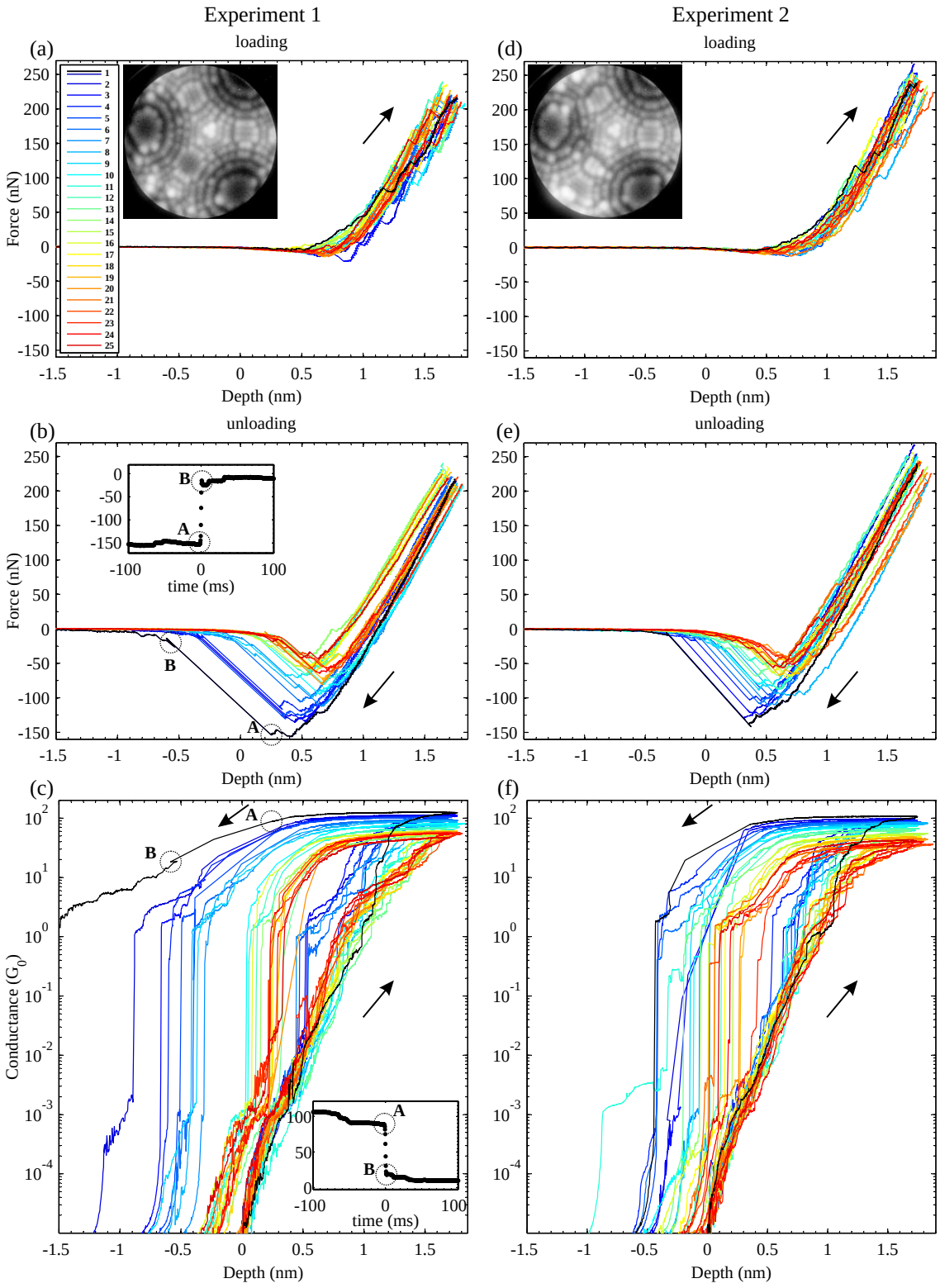

Figure 6.8: Summary of the first 25 indentation curves of a fresh W(111) tip in a Au(111) substrate in two separate experiments. (a) & (d) Force upon loading. (b) & (e) Force upon unloading. (c) & (f) Conductance upon loading and unloading at -0.05 V sample bias. Insets show FIM images taken at (a) 6.3 kV and (b) 6.2 kV. Insets in (b) and (c) show time traces corresponding to the discontinuities observed between points A and B.

STM images of the indentation sites were taken after indentation, shown in Figure 6.9. One particular curiosity is the 8th to last indentation in experiment 2 which did not leave any permanent impression, and appears as if it should have been located at the site of a screw dislocation – a pop-in was registered in the force-displacement curve, but apparently plasticity was somehow reversed. Monoatomic islands of pile-up are located near most indentation sites, but in 8 of 50 locations, no pile-up is imaged. The pile-up could result from material ejected from the indentation site, from the wire neck breaking during unloading, or a combination of both effects. In passing, we find that producing indentations in arrays is extremely useful for the identification of indentation sites because it leaves a regular pattern on the surface – even in the presence of thermal drift causing a skewed pattern of holes and piezo hysteresis and creep affecting image linearity, it remains possible to unambiguously identify indentation sites.

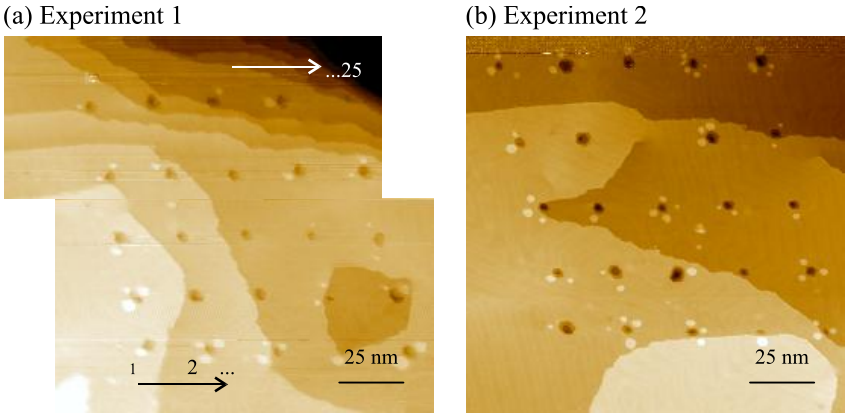

Figure 6.9: Topographic STM images of the indentation arrays produced in two experiments summarized in Figure 6.8. Both arrays were performed from left to right and bottom to top, as indicated by the numbering in (a). The bottom half of image (a) is displaced due to a change in scan offset location carried out in the middle of the scan to allow the full array to be imaged. (a) 12 pA, -0.05 V (b) 10 pA, -1 V

The reduction of maximum conductance and adhesive force for these two experiments is plotted as a function of indentation number in Figure 6.10. The conductance and adhesion behaviour is in good quantitative agreement between the two experiments, although the second experiments seems to start with an initially lower conductance and adhesion. It is difficult to say whether this deviation is statistically significant – defining an initial condition for the tips is hindered by the fact that their approach to tunneling proximity with the substrate allows for the transfer of material to the tip. Any discrepancies in the duration of tunneling or feedback conditions could be accounted for by a different initial condition of the tip apex, altered by material transfer.

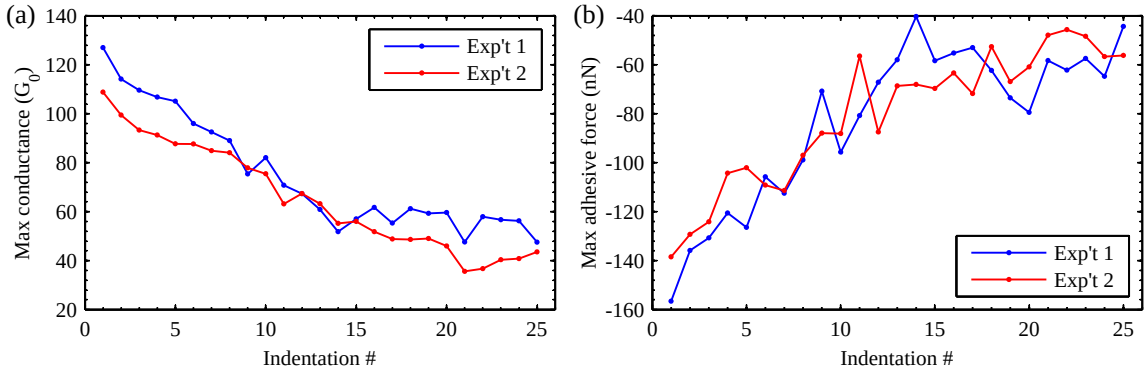

Figure 6.10: (a) Maximum conductance and (b) adhesive force measured in the indentation curves shown in Figure 6.8.

Another intriguing feature about this behaviour is that it takes a substantial number of mechanical contacts between the tip apex and gold surface to alter the observed behaviour. We speculate that it takes repeated indentations to reach equilibrium values of the conductance and adhesive force because of the diffusion of gold atoms away from the tip apex. After many indentations, a sufficient reservoir of gold on the tip may be established such that the behaviour becomes repeatable. One could design an experiment with different pause times between indentations, or different indentation depths to test this hypothesis.

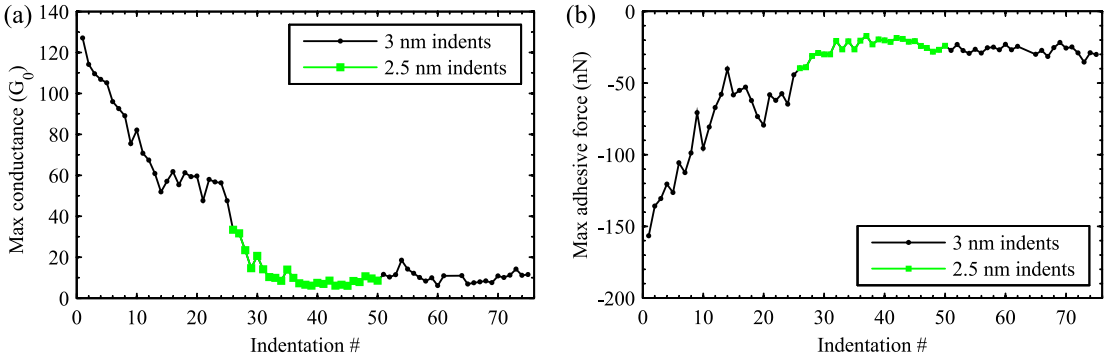

Figure 6.11: Maximum conductance (a) and adhesive force (b) tend toward a constant value after repeated indentation. Data from Experiment 1, including two subsequent 5 × 5 indentation arrays.

A plateau in the conductance and adhesion behaviour beyond the first 25 indentations is illustrated for Experiment 1 in two subsequent 5 × 5 arrays carried out to 2.5 nm and 3 nm depth setpoints. In Figure 6.11 we show the maximum conductance and adhesive force in (a) and (b) respectively. The conductance and adhesive force in the last indentation array have average plateau values of $\langle G \rangle = 11 \pm 3\ \mathrm{G_0}$ and $\langle F_{ahd} \rangle = -27 \pm 3$ nN, where the uncertainties express the standard deviation of the measurements.

The change in junction conductance behaviour can be appreciated in another way by plotting the conductance as a function of the indentation load during the loading curves. This is shown for Experiments 1 & 2 in Figure 6.12(a) and (b) respectively, with the data from the very first indentations plotted in black. It seems as though the first curve provides a lower bound to the obtainable conductance at a given repulsive load until about $10^0 - 10^1$ G_0, at which it becomes the best conducting junction at any load.

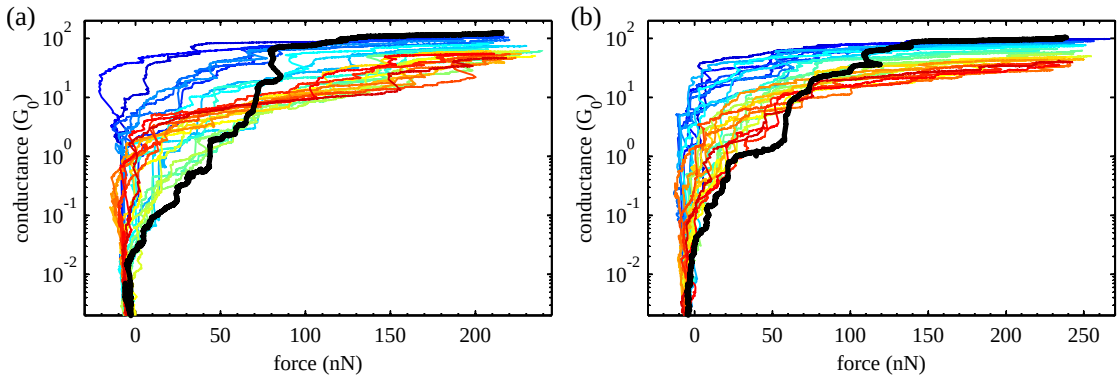

Figure 6.12: Conductance as a function of indenter load measured during the loading curves for the indentations shown in Figure 6.8. The very first indentation of the W(111) tip is shown in black, and the subsequent curves are coloured with the same scheme as Figure 6.8. (a) Experiment 1, (b) Experiment 2.

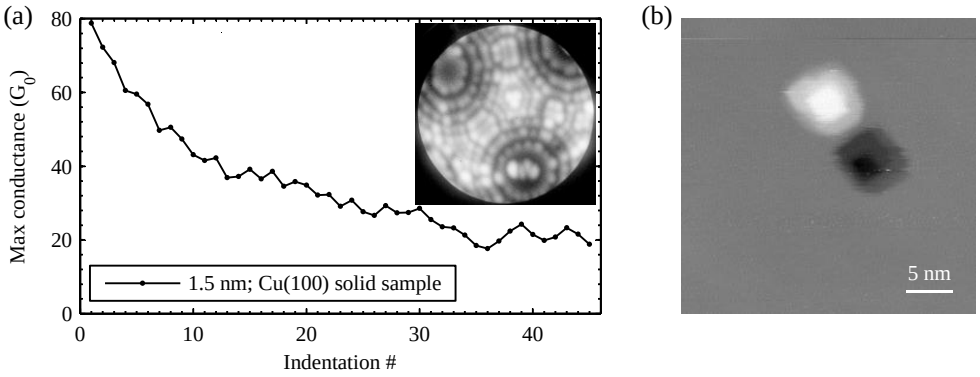

Figure 6.13: (a) Maximum conductance during indentation sequences on Cu(100). (b) Typical square shaped hole and pileup reflecting the symmetry of the substrate.

To investigate the universality of this phenomenon, indentations were also performed on a Cu(100) single crystal with a W(111) tip. Due to the fact that the sample was a 2 mm thick single crystal (i.e. not a compliant cantilever), a lower depth setpoint of 1.5 nm was chosen; this depth roughly corresponds to the maximum penetration depth in the Au(111) experiments (after subtracting for the cantilever deflection). The maximum conductance of

the first indentation was ~80 G_0. After 25 indentations, the maximum conductance began to plateau around ~20 G_0, as shown in Figure 6.13(a). We note that a dozen STM images and 2 small indentations were performed before the indentation array shown here, adding some uncertainty to the initial state of the tip.

6.2.2 Discussion and summary

We conjecture that the added material on the tip in the later indentations serves to lower adhesion by facilitating atomic rearrangements on retraction – rather than the gold substrate adhering directly to the tungsten tip, a buffer layer of gold mediates the rearrangement of atoms during pull-off. Molecular dynamics simulations are currently underway to investigate the atomistic mechanisms in contact separation of fresh and gold-wetted tungsten tips.

There is a severe geometrical mismatch between the bcc tungsten lattice of the tip and the fcc gold lattice. The W(110) planes are the most closely packed of the bcc crystal, and are most closely matched to Au(111) lattice constants. We wonder if the additional gold layer adds further interface or defect losses [43] for ballistic transport through the junction due to additional layers of lattice mismatch between tip, Au interface layer, and Au bulk. Knoppe and Bauer studied the electronic structure of ultrathin single, double and multi-layer Au films on W(110) using angle-resolved ultraviolet photoelectron spectroscopy (ARUPS) and showed that for Au films of 3 or less layers, there is a strong deviation from bulk-like electronic structure [257]. First-principles calculations of transport through the system of tens or hundreds of thousands of atoms involved in our indentations is unfeasible. However with some understanding of the interface structures from molecular dynamics, one might be able to more confidently approximate the ballistic transport losses through simpler models of the interfaces. A cartoon of a plausible scenario of a wetted contact interface during indentation is shown in Figure 6.14. One should expect regions of quasi–Au(111) to form, such as on the W(110) planes, which cannot geometrically be in registry with the W(111) apex, nor with the substrate Au(111). A disordered transition between the W(111) apex and Au(111) surface is also likely. Concerns such as vacancies, dislocations and disorder are also illustrated, which have been raised in previous work regarding junction conductance of a loaded contact [43]. Though we cannot exclude the possibility of contaminant atoms affecting the adhesion and conductance behaviours, we do not expect

this effect to be dominant due to the respectable UHV conditions corroborated by the clean surfaces and step edges imaged in STM.

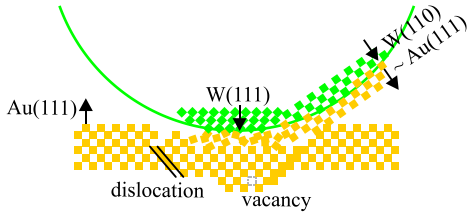

Figure 6.14: Illustration of geometrically impossible lattice matching between quasi-Au(111) on the W(110) planes, the W(111) apex and the Au(111) surface which may be enhanced upon tip wetting adding electron scattering sites to the junction. Dislocations, vacancies and disorder are also expected to affect junction conductance.

In summary, fresh tungsten tips were shown to have the smallest distance between the tunneling point and onset of repulsive load, pointing to the addition of a soft layer of gold to the tip apex after repeated loading. The wetting of the tips showed up to a ~12–fold reduction in maximum junction conductance and ~6–fold reduction in adhesive force, reaching plateau values after ~30 repeated indentations. A decreasing junction conductance was also measured for repeated indentation of Cu(100). We hypothesize that the added material is mobile and that multiple indentations are required to saturate a reservoir on the tip apex. We anticipate a better understanding of the junction lattice matching and interfaces with the results of molecular dynamics work on this system.

6.3 Transition from elastic to plastic loading in the first indentations of FIM tips

We have seen that the very first indentations of a tungsten tip display extremely large adhesive pull-off forces upon unloading. This prompts two interesting questions regarding indentation at the atomic length scale: How does indentation progress with a fresh tip before the threshold of plasticity? And, given the large adhesive forces at play, can a hole be 'pulled' out from the substrate just by adhesion of Au to the tip without any other signs of plasticity (i.e. by performing an elastic loading curve with giant adhesion)?

6.3.1 Experimental results

We begin by examining a series of indentations on a Au(111) surface, carried out with the 8.5 nm radius W(110) tip shown inset in Figure 6.15 (a). Indentations were carried out at gradually increasing open-loop depths. The surface was inspected for signs of plasticity

by topographic STM imaging after each indentation. The first seven indentations, with depth setpoints of 1.0 to 1.8 nm showed no sign of substrate alteration (inset of Figure 6.15(b)), and produced the force-distance and conductance-distance curves shown in Figure 6.15(a) and (b) – in and out directions plotted together. The colour sequence for the curves follows the same scheme as Figure 6.8. The force curve of the very first indentation (darkest blue), shows a small hysteresis loop caused by a few pop-ins at loads between 10-20 nN. Even though this indentation is elastic as far as surface damage is concerned, energy is dissipated in irreversibly rearranging atoms on the tip apex. The subsequent force curves, in which the indentation depth is increased, show a similarly small hysteresis loop and a rather repeatable adhesive force of about −20 nN; these parameters are summarized in (f). The smooth repulsive loading of the contact above ~10 nN is perfectly reversed during unloading. The junction conductance of these indentations reaches maximum values of order 1 G_0 (sample bias -0.05 V).

The eighth indentation with a setpoint of 1.9 nm has a remarkably different behaviour which coincides with the initiation of plastic damage to the substrate and is plotted in (c) using our standard colour scheme introduced in Figure 6.5 (page 194). The inset STM image shows a small hole highlighted by a dotted circle (a pre-existing defect, not produced by indentation, is seen below and to the right of the indentation site). Multiple features set this indentation curve apart from the previous elastic curves: Firstly, two pop-ins occur during the loading curve (blue) at 43 and 45 nN indicated by (i), accompanied by a jump in the junction conductance (green) to ~ 1 G_0. As the blue force curve approaches maximum depth, it peculiarly turns upward, indicating an increase in contact stiffness – at the same time, a few rearrangements happen in the junction conductance, increasing by a multitude of small jumps up to ~ 6 G_0, indicated by (ii). When the junction is unloaded, the black unloading curve appears to be *above* the blue unloading curve which is a very strange scenario because a hysteresis loop in this direction indicates mechanical energy being released by the tip-sample junction. There appears to be 25 eV of work done to the indenter by the sample in the loop shown in yellow. The unloading force curve is also incredibly linear, reflecting the fact that the contact area remains nearly constant while unloading progresses. The conductance increases slightly when the indentation is unloaded to a maximum of 8.5 G_0 and then proceeds to shows an enormous hysteresis loop caused by atomic wire pulling – a behaviour which is distinct from the conductance traces of the elastic curves shown previously in (b).

The next indentation was carried out at a new location, shown in (d). Its elastic nature is discernible in the well-overlapping force-displacement curve, the lack of pop-ins, and the undamaged surface imaged by STM, inset. The current reaches a maximum of ~5 G_0, and shows a somewhat less pronounced hysteresis – it is interesting that the wetted tip after plastic indentation shows a considerably different behaviour than the fresh tips. The following indentation showed signs of plasticity in the form of pop-ins at ~20 nN accompanied by an increase in conductance, indicated by (i). A large conductance enhancement occurs at (ii), and a hole is produced in the surface, shown inset. The herringbone surface reconstruction has also rearranged from the parallel rows shown inset in (d) to a configuration having extra kinks and elbows. The features at points (i) and (ii), as well as the linearity of the force curve during unloading are very similar to the previous plastic curve shown in (c). We summarize the maximum junction conductance, adhesive force and indentation hysteresis energy of these indentations in (f), denoting the elastic curves by black circles and the plastic curves by red squares.

In order to highlight the intriguing features near the maximum indentation depth, the force and conductance from the first plastic curve, (c), are plotted as a function of time in Figure 6.16 using the same colour scheme to indicate force/current on loading/unloading. Dotted grey lines have been added as a guide to the eye to emphasize the departure from linearity of the loading curve and the exemplary linearity of the unloading curve. The increased stiffness at the end of loading is correlated in time with the sudden cascade of conductance jumps. During unloading at ~2780 ms, a slight pop-out is detected along with a small increase in junction conductance, however the slope of the force remains almost unchanged. The contact stiffness was fitted to the force-displacement data over the intervals indicated by brackets, showing that the loading stiffness increases from ~194 N/m to ~217 N/m just before maximum depth. The unloading contact stiffness remains at ~181 N/m throughout the unloading curve.

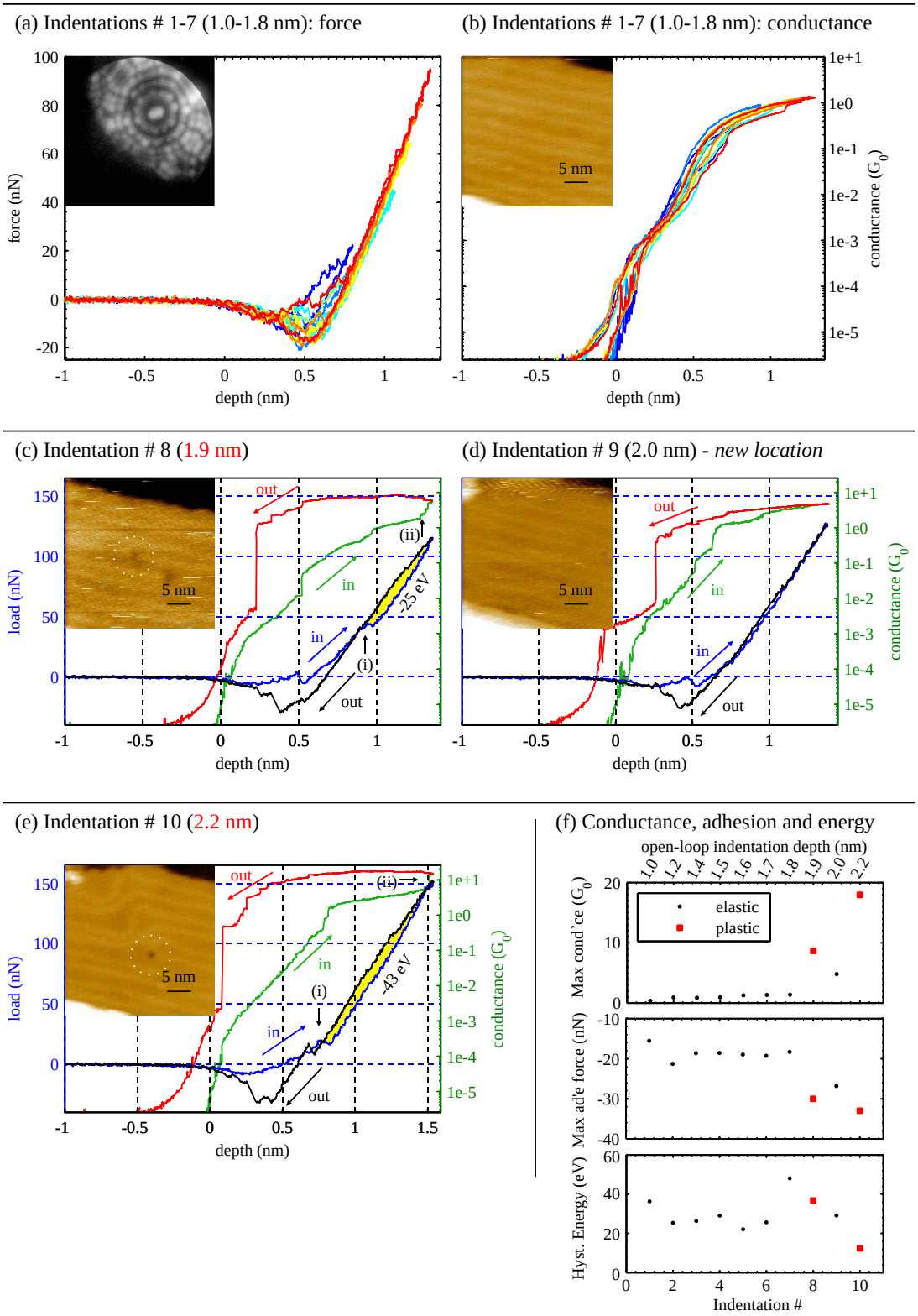

Figure 6.15: Ten first indentations with a W(110) tip. (a) and (b) The first seven elastic indentations at depth setpoints of 1.0-1.8 nm. (c) The eighth indentation showed signs of plasticity, and a hole was produced in the surface. (d) The ninth indentation in a new location was elastic. (e) The tenth indentation showed plasticity and produced a hole. (f) Maximum conductance, adhesive force, hysteresis energy for this sequence of indentations.

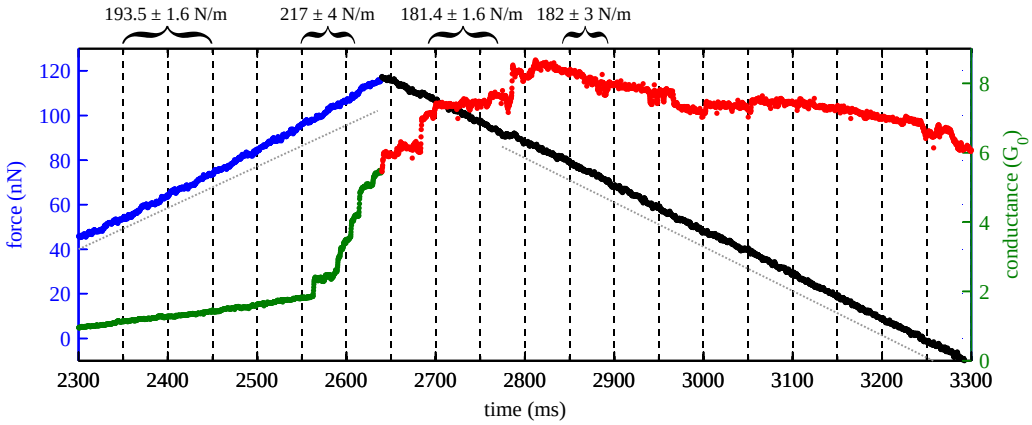

Figure 6.16: Force and conductance from the plastic indentation shown in Figure 6.15(a) as a function of time showing the behaviour near maximum load. The fitted contact stiffness in different areas of the force-displacement curve is shown along the top.

6.3.2 Discussion and summary

There appear to be several features which are linked to plasticity in these indentations which consist of:

- Pop-ins on the loading curve at (i)
- Conductance enhancement at (ii)
- Enhanced maximum conductance and adhesion forces (see (f))
- Nearly constant contact stiffness during unloading
- Transfer of some mechanical energy to the force transducer during unloading.
- Residual impression appearing in the STM image

We curiously always observe events (i) and (ii) together – a plastic indentation containing a pop-in (i) *without* a subsequent large current enhancement (ii) has not yet been measured with a fresh FIM tip. It is intriguing that the current enhancement happens near the end of the loading curve, and one must be suspicious about what could be special about the indentation just before the maximum depth. For now, we have verified that it has not been caused by some bizarre data acquisition timing artifact and believe that it is a matter of chance that is has been measured just prior to the turnaround point on several occasions.

The yield event at point (i) presumably corresponds to the nucleation of a dislocation in the sample. We anticipate that the contact area increases at this point, and question if the large adhesion that is indicative of the plastic indentations would still be present if the

contact were unloaded after point (i) but before (ii). Event (ii) might correspond to a rearrangement of the interface structure with the indenter which results in better ballistic transmission – we wonder which of (i) or (ii) is a necessary condition for plasticity, the large adhesion, and the linear unloading curve. This concern should be addressable in the future by retracting the tip after the first pop in. Such an experiment could be carried out using an analog high-pass filtered version of the force channel to signal a retraction of the indentation after the occurrence of a pop-in event (having a large derivative)[1].

The negative hysteresis loop occurring at a depth > 0.9 nm in Figure 6.15(c) indicates that ~25 eV of mechanical work has been done to the force transducer (released from the sample) during this part of the indentation process. This is a completely unique feature which is unseen in larger scale indentation experiments. We may have even attributed it to an artifact of drift or piezo creep and disregarded it had repeated elastic indentations not been measured immediately before. There is something very interesting happening in the tip-sample junction which does mechanical work on the force transducer – we can conclude that at a depth of 0.9 nm on the way out, the total energy of the atomic configuration in the indentation volume is *at least* ~25 eV lower than it was at the same depth during loading. The efficiency by which the released energy is converted to mechanical work on the transducer is not determinable, however this lower energetic bound may still prove to be a useful point of comparison for the total energy of atomic configurations in atomistic simulations of indentation.

We point out that the surface energy of tungsten is much higher than that of gold – surface energies of the low index tungsten planes are between 4.0 – 4.6 J/m^2, and those of gold are in the range 1.3 – 1.7 J/m^2 [258]. Regardless of the specific crystallographic planes involved, the difference of surface energies is of the order 18 eV/nm^2, which is enormous considering the contact area of ~50 nm^2 expected for a tip of 8.5 nm radius at a depth of 1nm (this is neglecting the interfacial energy at the Au-W interface). It is worth noting that the elastic strain energy put into loading the contact is ~230 eV by maximum load, so we are not anxiously seeking to balance an energy budget – we are pointing out that the energetics of surfaces are quite large on a relative scale. Wetting of the tungsten surface with gold may necessitate consideration as an exothermic process, but the way in which mechanical work

[1] One may want to combine the derivative detection in force with a logic AND gate which ensures that the conductance is also over some threshold to avoid false triggering from sudden force events caused by tip rearrangements near zero load (say > 10^{-3} – 10^{-2} G_0).

is transferred out of the junction is still curious. The ~25 eV released could also come from the lowering in energy of a metastable atomic configuration produced by the stressed state of the indentation volume, for which we assigned an energy budget of ~230 eV.

It is necessary to comment on the possible role of heating in the junction as an activation mechanism for substantial atomistic changes in the junction. We have performed these indentations at -0.05 V bias on the sample. At a conductance of 1 G_0, the power dissipated is 1.2×10^{12} eV/s. Though this power appears very large for a contact on the atomic length scale, we are reminded that atomic wires of single gold atoms can sustain 1 G_0 at 2 V (~0.15 mA) in the ballistic transport regime – the mean free path of electrons can be on the order of microns, so only a very small fraction of power is deposited within the contact due to inelastic scattering [241]. Current densities 10^5 higher than allowable in macroscopic conductors can be achieved because transport is ballistic through the constriction.

Heating of point contacts has been addressed in the field of point-contact spectroscopy, where the heating is often considered in the limit of Joule heating of a classical point contact where the conduction electrons serve to remove most of the heat from the junction. The effective temperature at the contact center is related to the bath temperature, T_b, by

$$T_{eff}^2 = T_b^2 + \frac{V^2}{4L} \ , \tag{66}$$

where V is the bias voltage across the contact and L is the Lorentz number. This relation is derived by assuming that the heat and electrical conductivities are related by the Wiedemann-Franz law, $\kappa/\sigma = LT$ [241, 259]. If the bath temperature were zero, the second term in the sum would raise the contact temperature by 3.2 K per 1 mV bias voltage. This relation has been shown to describe features in d^2V/dI^2 associated with the disappearance of electron-magnon scattering above the Curie temperature in ferromagnetic point contacts (deduced from the junction bias voltage corresponding to T_C). In experimental studies of two-level fluctuations in atomic-scale point contacts of Cu and Pt, the rate dependence of switching follows an Arrhenius rate behaviour with bias voltage [241]. This suggested that junction heating is of the order 1.2–5.6 K per mV bias voltage – of the same order determined by the classical approximation of Eq. (66). If this range were valid for our contact, we could expect a temperature in the range of 323–635 K for a bath temperature of 300 K. The softening of metals at approximately one third of their melting temperature is known to rearrange electrical point contacts [260]; for Au, this corresponds to a temperature of ~450 K.

We question if the dislocation created in (i) near the contact increases local inelastic scattering of electrons and contributes to locally heating the junction, permitting the avalanche of conductance increase in (ii). Although we have a very thoroughly characterized system of two single crystals of known orientation in repulsive contact made while measuring force and conductance across the junction, atomistic modeling is still needed to understand atomic rearrangements occurring inside the junction. Further experiments could be performed with a retraction of the tip after the pop-in, as well as at lower bias voltage to investigate the hypothesis of junction heating (without any modifications, a factor of ten smaller bias should be possible on the current apparatus).

Nevertheless, the data shows a spectacular departure from classical "macro"-nanoindentation. The anomalously more compliant unloading profile is in contradiction with the typical *P-h* behaviour introduced in Figure 6.2(a) (page 190) where the unloading profile is always more highly sloped – the traditional interpretation of this is that the loading curve is continuously yielding (elastic-plastic), whereas the unloading curve measures only elastic recovery properties. Deviations from this picture occur due to adhesion, anomalous changes in contact area from contact rearrangements or pileup, possible stiffness changes due to interface evolution, and the development of plasticity by sudden pop-in bursts rather than continuous deformation.

In summary, we have studied the transition from elastic to plastic indentation of a Au(111) surface using a W(110) indenter characterized in FIM. The very first plastic indentations with a fresh tip show distinct events: (i) pop-ins in the force curve, and subsequently (ii), a large conductance enhancement. So far, it is unclear which of these are necessary conditions for plasticity. The indentations show anomalous behaviour upon unloading – the contact becomes less stiff, and a small negative hysteresis loop indicates that some mechanical energy is transferred from the indented volume to the force transducer. We speculate that junction heating may have something to do with event (ii), possibly enhanced by inelastic scattering sites introduced into the junction by (i).

Returning to the questions with which we started this section, it seems that elastic behaviour is measured before the onset of plasticity. These elastic indentations do not exhibit the giant adhesion associated with plasticity; a hole cannot be created in the substrate via elastic contact loading and a giant adhesive 'pull'.

6.4 Indentation with STM imaging of residual impressions

In this section, we present new results from indentation of Au(111) consisting of individual indentation curves accompanied by STM images of the residual impressions taken after indentation. We have noticed that after indentation experiments, STM imaging quality has not always been sufficient to resolve the 6.3 nm wide discommensuration lines of the Au(111) reconstruction. This might be due to the rather large radius of curvature of the FIM tips which cannot support a small protruding asperity for stable tunneling at room temperature. We have found, however, that by sweeping the imaging bias voltage between ~ –1.5 and +1.5 V at the beginning of a STM scan, we can adjust the atomic structure of the tip apex to form a stable imaging tip which performs quite well near ~ –1 V sample bias. With these stabilized tips, along with the significant improvements in SPM stability described in Chapter 0, topographic images of the Au(111) surfaces on flexible samples can be acquired which compare favourably to images of Au(111) taken by conventional STM.

6.4.1 Experimental results

We present the initial three indentations of a 7.7 ± 0.4 nm radius W(110) tip in Figure 6.17 with open-loop depth setpoints of 1.5, 2.5, and 1.5 nm respectively. The first indentation plotted in (a) shows features associated with plasticity similar to those in Figure 6.15. That is, several pop-ins occur in the repulsive loading regime (shown by arrows) and a large conductance enhancement takes place near maximum depth. The unloading force curve is similarly linear indicating a near-constant contact area, and the adhesive force is very large as expected for a fresh W tip. A small negative hysteresis loop releases ~ –20 eV of mechanical energy into the force transducer at a depth > -0.72 nm, similar to the previously noted behaviour. The second indentation at a larger open-loop depth, (b), shows a correspondingly higher maximum force. Pop-ins are indicated in the loading curve (as well as a pop-in and a pop-out on the unloading curve). The sudden conductance enhancement happens at a much shallower depth in this curve than previously seen, and is correlated with the first pop-in event at 14 nN. The maximum conductance of the first two indentations is just over 50 G_0, and they reduce to 38 G_0 and 35 G_0 respectively before abruptly breaking contact. A third indentation to 1.5 nm (the same depth as the first) shows a correlated pop-in and current enhancement at a very low repulsive load of only ~2 nN. The loading curves are also quite linear. The unloading curve shows contact thinning events

to 4 G_0 and then to 1.5 G_0 before breaking. The unloading curves of all of these indentations have a lower stiffness (slope) than the loading curves.

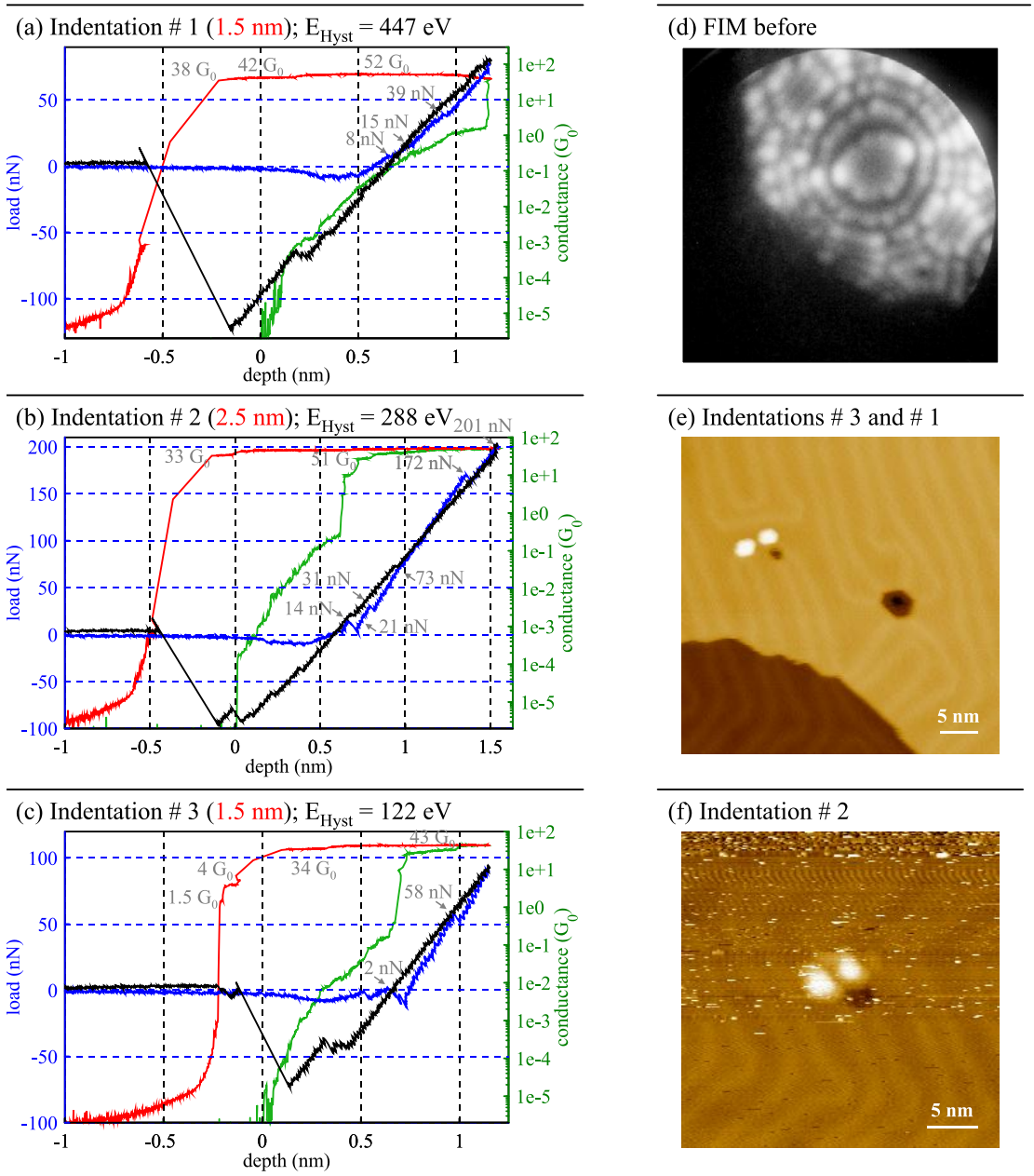

Figure 6.17: (a-c) Force-displacement and conductance-displacement curves acquired during the first three indentations of the W(110) tip shown in (d) into a Au(111) surface. (e) STM image of residual impressions from indentation #3 (left) and #1 (right). (8 pA, -0.9 V) (f) STM image of residual impression from indentation #2. (9 pA, -0.75 V)

A STM image of the residual impressions created by indentations #1 and #3 is shown in Figure 6.17(e); the hole corresponding to #1 is on the *right*, while the hole corresponding to #3 is on the *left*. The impression created by #2 can be seen in (f). The first indentation does

not show any sign of pileup, and has left a hole much larger than the third indentation which had approximately the same maximum load. The difference in surface damage might be attributed to the much lower adhesion responsible for a hysteresis energy of 120 eV (#3) rather than 450 eV (#1). Images of the surface before indentation were not taken due to the desire to perform the initial indentations with as little alteration to the tip as possible. Nevertheless, (e) suggests rather uncharacteristic arrangements of the surface reconstruction discommensuration lines, apparently due to indentation. Before indentation, the surface likely showed parallel discommensuration lines continuing through the site of indent #3 and terminating perpendicular to the step edge, and those near indent #1 were probably also parallel with a 120° bend before their termination perpendicular to the step edge. The uncharacteristic arrangements of the reconstruction after indentation include the joining of two pairs of discommensuration lines occurring above indent #3, the two U-bends terminating the pairs below indent #3, and the termination of all nearby discommensuration lines at the edges of indent #1. Though the quality of the STM image at indent #2 is rather poor and the detail around the hole is not discernible, it seems as though the herringbone pattern (regular alternation of 120° bends) continues despite the plastic damage. We will return to the subject of the reconstruction and surface stresses in the discussion that follows this results section.

Some of the first indentations with a 6.4 ± 0.7 nm radius W(111) tip are shown along with associated surface images in Figure 6.18. These force-displacement curves reflect the general tendency of adhesion to decrease after multiple indentations. In these indentations, pop-ins and conductance enhancements generally occur simultaneously, similar to the scenario shown in Figure 6.17 (b) and (c). Small negative hysteresis loops are also present in the maximum load regions of Figure 6.18(a) and (d). The first indentation, (a), shows the very linear unloading curve, presumed to be related to the large adhesion of fresh tips.

The STM image after indentation in (a) does not have sufficient resolution to resolve the surface reconstruction, but it indicates a lack of pile-up around the first indentation site. In (b), a pair of discommensuration lines has been severed, one of which terminates in a wide loop while the other terminates at the indentation site. A small island of pile-up is left next to the hole. Surface imaging after indentation in (c) is shown at two time intervals – the first image shows the hole at about 45 seconds after indentation and the second image shows the hole after a 9.3 min delay. It appears that the second layer of pileup has disappeared, and the upper section of pileup has shrunk. A small gap has also developed between the hole

and the island on the bottom-right. The residual impression and pileup reflect the symmetry of the substrate; all step edges are perpendicular to ⟨112⟩ directions (the lowest energy step configuration on a fcc (111) surface as it maintains the highest possible coordination of the edge atoms). The discommensuration lines of the surface reconstruction to the left of the indentation at first form a small closed loop terminating at the pileup. In the image taken later on, this loop has merged with the discommensuration lines to its bottom-left. It appears as if the discommensuration lines often have a tendency to avoid the pile-up islands.

The last indentation shown in (d) is interesting – the conductance enhancement and pop-in occur near 0.77 nm depth, then near 1.0 nm depth another pop-in is detected at 21 nN. The unloading adhesion is somewhat less than the indentation in (a) for about the same depth. Surprisingly, the STM image does not show a hole resulting from indentation – it shows that a small island has been deposited on the surface. We have seen this type of behaviour (pop-in at ~20 nN and protrusion left on the surface) on a few occasions. The transfer of material from the tip to the surface provides further evidence that there exists a reservoir of material on the tip after several indentations. In this case, the herringbone elbow becomes pinched near the deposited island.

Finally, we mention that another example of herringbone rearrangement due to indentation can be seen in Figure 6.15(c) (page 209) where several new elbows appear.

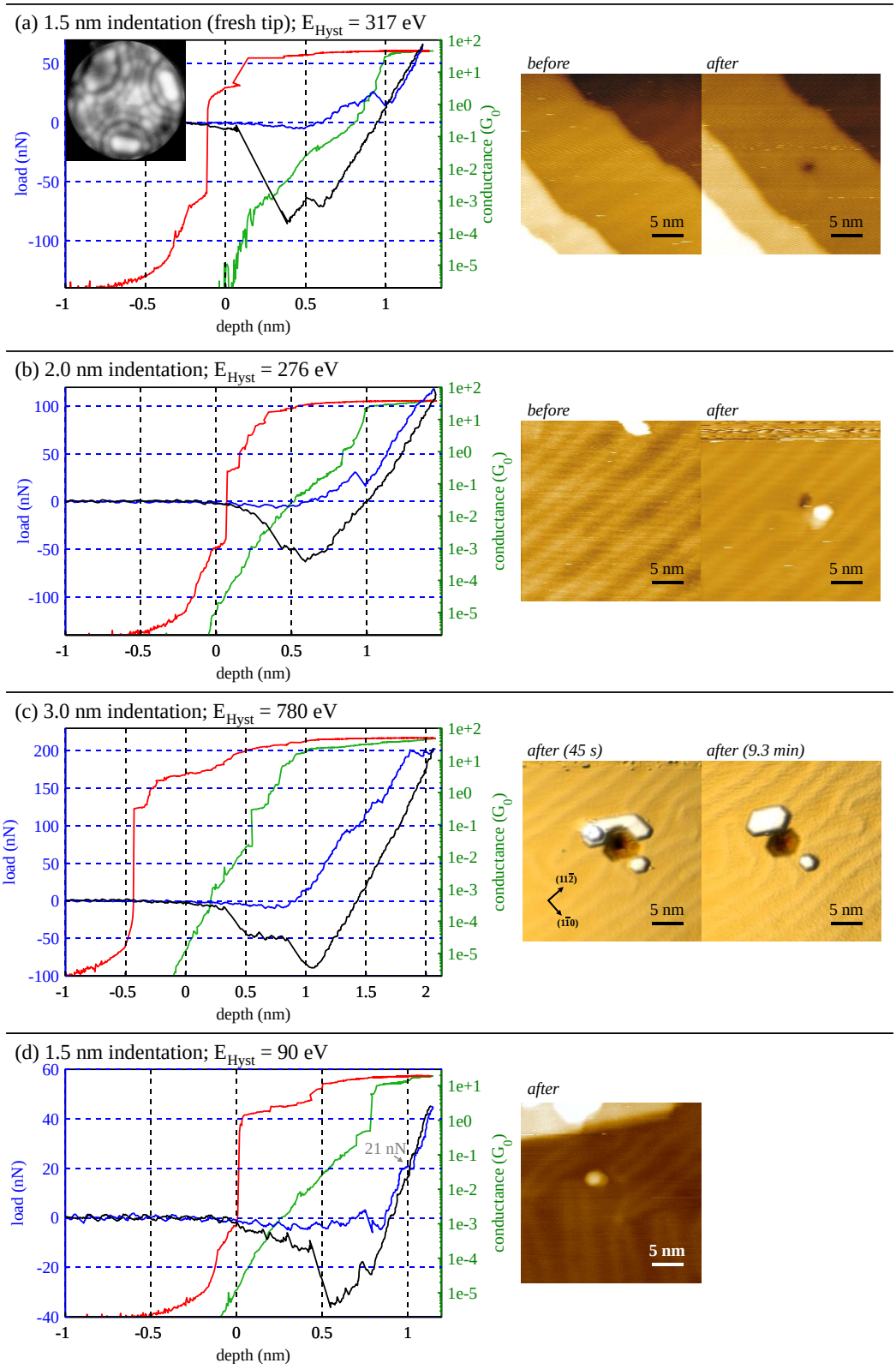

Figure 6.18: Indentations performed with the W(111) tip shown inset in (a). STM images are shown before and after where available. STM images in (c) are 3D rendered and lit from the left-hand side to emphasize the hole and pile-up structures. STM image parameters: (a) 3 pA -0.95 V, 5 pA -0.9V (b) 9 pA -0.9 V, 9 pA -0.75 V (c) 9 pA -0.9 V, 6 pA -1.0 V (d) 6 pA -1.0 V.

6.4.2 Discussion and Summary

We briefly recap the Au(111) surface reconstruction introduced in section 2.7.2, page 40. The $22 \times \sqrt{3}$ reconstruction of the Au(111) surface provides a means for the bonds of the less-coordinated surface atoms to contract. Along the $22 \times$ row, 23 surface atoms are present. To fit the extra atom in, the surface atom positions transition from the lattice-matched fcc sites to bridge sites to hcp stacking fault sites, then back to bridge sites and back to fcc sites. Atoms in the two bridge regions are slightly raised giving rise to the 'bright' stripes with a topographic height of 0.1-0.2 Å in STM imaging. To relieve the surface stress more uniformly across the surface, the discommensuration lines (bridge sites) bend regularly by 120° creating the 'herringbone' superstructure. Since the herringbone reconstruction is driven by surface stress, local perturbations to the surface stress should be expected to modify the reconstruction.

In support of our observations of discommensuration lines terminating perpendicular to step edges (Figure 6.17(e)), Avouris and Hasegawa point out that this arrangement should be expected because the surface stress component perpendicular to a free step edge must be zero [261, 262]. Therefore the $22 \times$ direction must lie parallel to the step edge. Avouris and Hasegawa studied the removal of atoms from the Au(111) substrate using a bias voltage pulsing technique to make clusters of vacancies apparently of one atomic lattice spacing deep. They studied the rearrangements of the herringbone pattern following the production of the holes and found that the discommensuration lines prefer to turn toward and terminate at the vacancy. This is because the edge of the vacancy behaves as a stress-free boundary condition in the direction perpendicular to its edge, similar to a free step edge. One feature of the rearranging herringbone that Avouris and Hasegawa point out is that the addition of an elbow to the pattern requires an extra surface atom because each elbow contains a surface edge dislocation. We certainly suspect that enough mobile adatoms exist on the surface to fulfill this requirement.

An important question in these indentation experiments concerns the type of defect remaining in the substrate after unloading the contact. The final defect may include either some dislocations pinned within the volume just under the surface or perhaps just a vacancy cluster of missing surface atoms. If a sub-surface dislocation is present, it should emerge at the surface in the vicinity of the indentation and act as a large perturbation to the herringbone reconstruction. Considering that the reconstruction rearrangements after

indentation are very similar in quality and spatial extent to those reported for vacancy clusters [261, 262] and that no sign of emerging dislocation lines are seen in STM, such as the hillocks observed in AFM indentation of KBr and Cu(100)[263, 264], we surmise that the defect most likely consists of a vacancy cluster. We will return to this subject with additional evidence from energetic considerations in section 6.5.

Another question to pose about atomistic mechanisms during the indentation is: Where does pile-up come from? Is it the remnants of atomic wire drawing and breaking? Or does it arise from material ejected from the indentation site? Molecular dynamics simulations of indentation of a W(111) indenter into a Au(111) substrate were carried out by Dr. David Oliver from our group in collaboration with Dr. Yue Qi from General Motors. The atomistic simulations correspond exactly to the size scale of our indentation experiments. From some of their preliminary results, it seems that wire-drawing occurs from the center of the indentation hole, and that the majority of pile-up is a result of material ejection during indentation. If wire-drawing were the cause of ejected material, it would be strange for more than one pile-up site to exist in experiments, which is more in agreement with the notion that material is ejected from the junction.

We note that several of the very first plastic indentations carried out with FIM tips often show no pile-up (see Figure 6.18(a), Figure 6.17(e), Figure 6.15(c)). One might wonder if the adhesion effect of the fresh tip serves to 'collect' most of the ejected material. This does not seem to be universally true as the initial indentations shown in Figure 6.9 (page 202) do show signs of pile-up. These indentations are carried out to different depth setpoints, however, and may not warrant comparison.

Additional images from the sequence acquired after the indentation of Figure 6.18(c) (page 218) are shown in Figure 6.19(a). The gradual rearrangements of the pile-up and hole geometry are notable. In Figure 6.19(b) and (c), we present highly contrasted versions of the first and last images of the sequence which highlight the shape of the hole. A double-tip artifact is recognized in both images – we believe that the hole in (c) is a perfect hexagon imaged twice by a double-tip as shown. In (b), the hexagon is more asymmetric, nearly triangular. This hole shape corresponds well with the triangular shape of the indentation in the molecular dynamics work of Dr. Oliver and Dr. Qi shown in Figure 6.19(d). In the simulation, the sides of the triangle were found to correspond with the {111} slip planes activated during indentation. It is interesting to note that the hexagonal arrangement of

atoms on the surface is six-fold symmetric, by indentation of the substrate it becomes possible to distinguish between the two possible three-fold symmetries of the bulk[1].

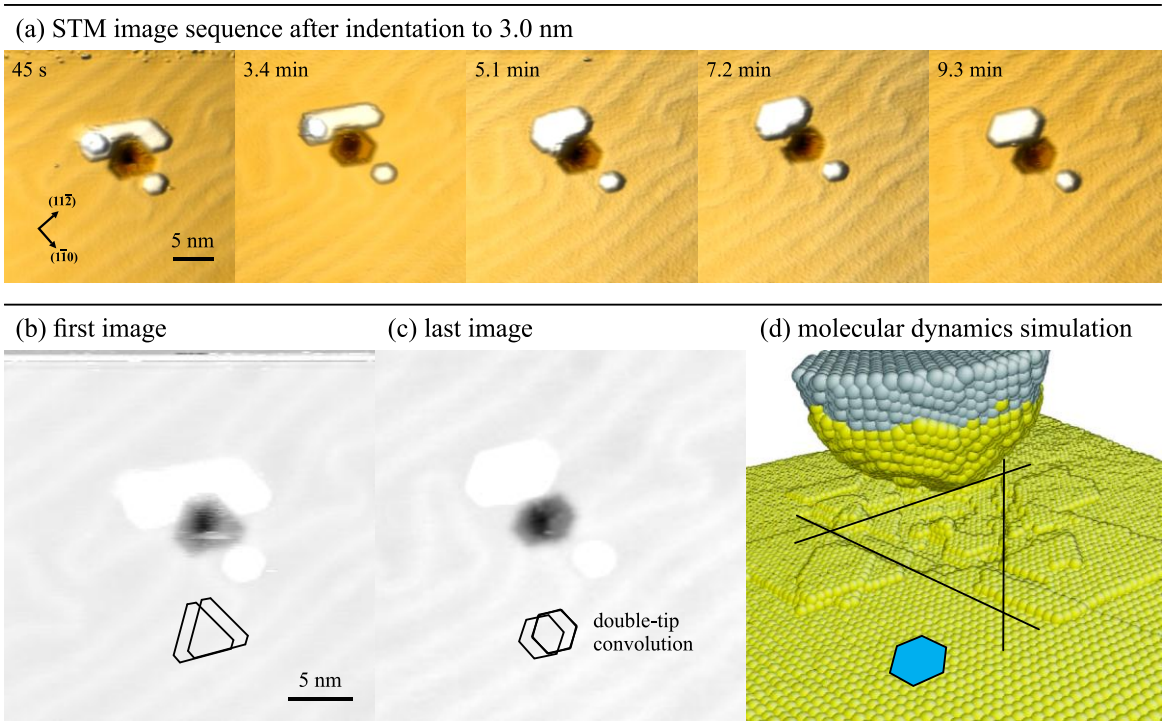

Figure 6.19: (a) STM image sequence acquired after the indentation shown in Figure 6.18(c) at the time intervals indicated. Highly contrasted versions of the first (b) and last (c) images highlight the change in hole structure. The initial triangular hole corresponds to the shape of the damage left in molecular dynamics simulations (d), which reflects the {111} slip system directions. The blue hexagon serves as a guide to the eye to the symmetry of the surface atoms (image courtesy of Dr. David Oliver, McGill University).

To summarize, the herringbone reconstruction is shown to rearrange resulting from the changes in surface stress caused by the indentation damage. The discommensuration lines tend to end at the edges of the indentation holes, as they would do at a free step edge. Surface images acquired at a very short time after indentation suggest that the threefold symmetry of the substrate is reflected in the hole before diffusing atoms produce a more regular six-fold symmetric hole.

[1] In the absence of atomic resolution in STM, this may represent one of the few ways to determine the orientation of the bulk crystal. Note also, that although we cannot routinely resolve the atomic structure of the $22 \times \sqrt{3}$ reconstruction, its structure in fact breaks the sixfold surface symmetry by alternating stacking between fcc and hcp sites: for a given orientation of $22 \times \sqrt{3}$ domain, this can be achieved in only one of two ways.

6.5 Minimum threshold for plasticity in Au(111)

In this section, we investigate incipient plasticity in Au(111) using a W(111) tip which has been wetted until saturation behaviour by previous indentations. By doing so, adhesion has been tamed to a repeatable value allowing comparisons to be drawn between individual indentations which are due mostly to phenomena in the substrate rather than at the interface of the tip. The onset of plasticity is commonly studied in nanoindentation – while the load is ramped at a constant rate, a sudden displacement burst, or 'pop-in' is often observed, which is typically interpreted as the onset of plasticity. Recent nanoindentation experiments inside a transmission electron microscope have shown that plastic deformation may in fact occur before the first obvious displacement burst is measured in the force-displacement curve [252]. In these, and many other nanoindentation experiments, the nucleation of the first dislocation is assumed to occur homogeneously within the material when the magnitude of the shear stress within the deformed volume approaches the theoretical shear strength of the material [37, 265-267].

An interesting fundamental question in the atomistic understanding of plasticity is the minimum stable defect configuration when a single crystal is indented, that is, the smallest possible 'quantum' of plasticity producible by indentation. Here, we investigate incipient plasticity in atomic-scale indentation on a single crystal and measure a clear but stochastic transition from elastic loading to plastic indentation of a contact. These indentations at the threshold of plasticity correspond to the smallest permanent damage that can be produced in the substrate and we quantify the scale of this minimum deformation. We find evidence that incipient plasticity is indeed an activated process involving heterogeneous nucleation sites. We observe that pop-ins in the force-displacement curve are correlated with incipient plasticity, but that other quantitative indicators provide a better diagnostic of plasticity at the atomic scale, which is relevant in the context of applications such as nanomachining by indentation [268].

6.5.1 *Indentation results*

The indenter consists of a W(111) tip, determined by FIM to have a spherical apex of radius 9.5 ± 1.1 nm. A FIM image of the tip apex is shown in Figure 6.20(a), where the atoms of the highly corrugated (111) plane are individually resolved. A constant-current STM topograph of the Au(111) surface is shown in Figure 6.20(c). The herringbone reconstruction is faintly resolved as rows running parallel to the $(11\bar{2})$ direction. The area of the sample in which indentations were carried out is an atomically flat Au(111) terrace: a 0.24 nm atomic step is visible at the bottom right corner of the image, and several steps occur at the top of the image. After the STM scan, the tip was moved under constant-current feedback at 20 pA and -0.05 V sample bias to the site of each indentation. At each location of the array, the tip was retracted to -2 nm from the tunneling setpoint and then approached toward the sample at a speed of 2 nm/s to +2 nm beyond the tunneling setpoint (loading). The tip was then retracted (unloading). The indentation depth was chosen to be close to the minimum threshold for observing plastic deformation of the substrate. The actual penetration depth for these indentations is less than 2 nm due to the simultaneous deflection of the cantilevered sample and varies with the elastic/plastic characteristics of each indentation.

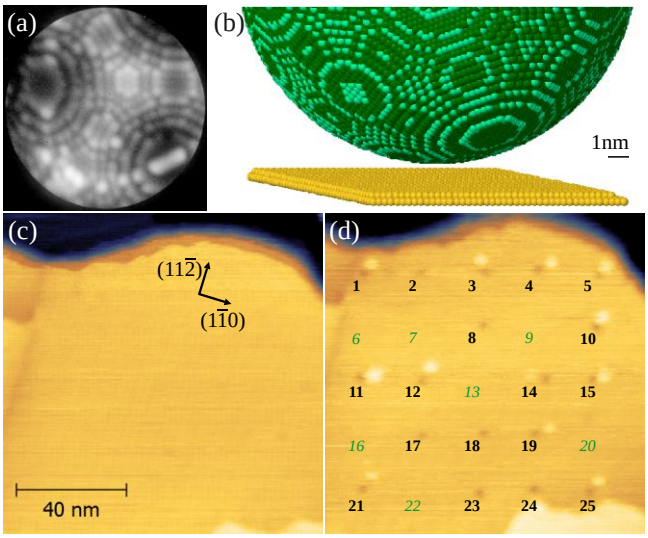

Figure 6.20: (a) FIM image of the W(111) indenter (5.5 kV tip voltage); (b) ball model of a W(111) with a 9.5 nm radius and Au(111) substrate to scale; (c) Au(111) terrace before and (d) after a 5 x 5 indentation array with 20 nm spacing between indents (20 pA, -0.05 V sample bias). Bolded numbers indicate plastic sites, italicized numbers indicate elastic sites.

The indentations were made in the numbered order indicated on the STM topograph of Figure 6.20(d). The elastic indentations (where no residual impression is imaged) are

numbered in italics. Although the maximum force at each indentation site is very similar, plasticity is not always initiated due to the fact that it is an activated process.

The plasticity visible in the indentation array corresponds to the smallest permanent damage that can be made by indentation of the Au(111) surface just beyond elastic loading. This damage is stable over many STM scans, indicating that the undamaged regions were not repaired by thermally diffusing Au adatoms or vacancies before they could be imaged. A single atomic layer of pileup next to the indentation site is observed in many cases.

A striking correspondence between the imaged surface damage in STM and the features of the force-displacement curves is observed. Figure 6.21 presents illustrative force-displacement curves from the array produced in Figure 6.20(d). The depth axis is zeroed to the crossing of the 1 GΩ tunneling gap resistance upon loading.

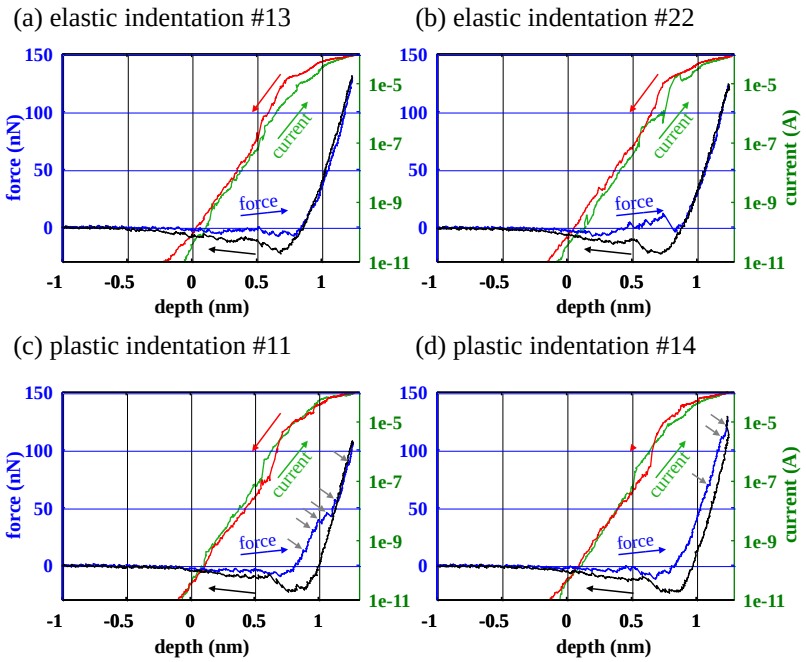

Figure 6.21: Force and current recorded during indentation at elastic sites, (a) and (b), and plastic sites, (c) and (d). Loading and unloading directions are indicated by arrows. Additional arrows in (c) and (d) point to pop-in discontinuities in the force.

Two of the elastic indentation curves are plotted in Figure 6.21(a) and (b). At zero depth, the tunneling current has reached 50 pA, and rises exponentially through the tunneling regime. At ~0.75 nm, the force becomes repulsive and smoothly increases to a maximum of ~130 nN where the conductance of the junction is ~22 G_0.

Upon retraction, the unloading force curve overlaps the loading curve closely. The elastic indentations have characteristically well-overlapping loading and unloading curves and

generally an absence of pop-ins in the repulsive force region (sometimes small pop-ins are observed as discussed later). A reduced elastic modulus of 92 ± 12 GPa is extracted from an Oliver-Pharr [238] analysis of the unloading curves using the known 9.5nm tip radius from FIM. This agrees well with the expected combined modulus (Eq. (64), page 191) of 80 GPa for a W-Au contact.

Despite the fact that no substrate damage occurs in the elastic sites, we observe a significant and variable hysteresis in the low load region of their force-displacement curves. We attribute this variability to the compression and rearrangement of Au on the tip which is picked up during indentation and scanning (discussed in section 6.2). The indentation only enters the strongly repulsive regime at about 0.75nm depth after the soft Au layers on the tip have rearranged. We refer to the initial portion of the curve as the 'tip rearrangement' region.

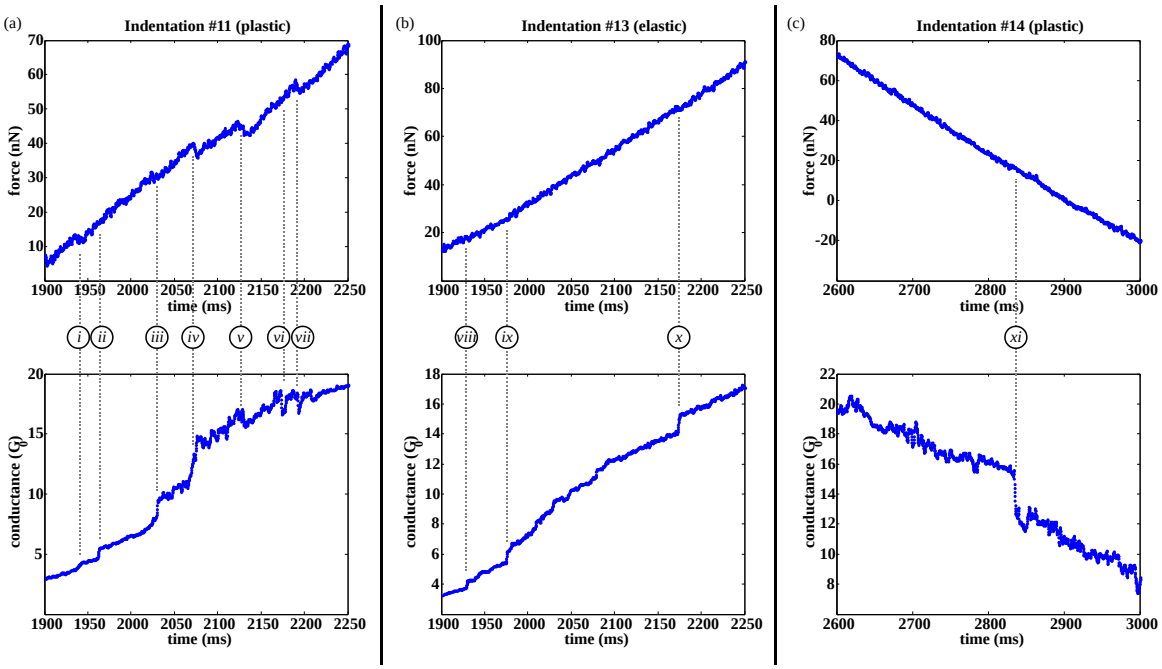

Figure 6.22: Simultaneous events recorded in the force and current channels during indentation.

The indentations corresponding to plastic sites show multiple pop-ins as a signature of plasticity. Pop-ins are characterized by an instantaneous reduction in force and a simultaneous increase in penetration depth – these quantities are linked by the ~200 N/m stiffness of the force transducer. In the plastic indentations of Figure 6.21(c) and (d), pop-ins are indicated by arrows pointing to the sudden jumps in the force curve at 14, 32, 41, 46, 58 and 89 nN and 71, 115 and 123 nN respectively. The last pop-in in Figure 6.21(d) occurs in the unloading curve. Reverse plasticity in the form of pop-outs is not observed, however

it has been observed in indentations performed to higher loads (for example Figure 6.5, page 194). Changes in junction sometimes occur simultaneously with pop-ins in the force channel. It is often observed that pop-ins in the force channel are accompanied by simultaneous increases in junction conductance, in accordance with what one would expect for a suddenly enlarging contact area. This is seen to varying extents in the examples *i, iii, iv* in Figure 6.22. There are other cases where a pop-in in force yields a decreased junction conductance, *v*, or a momentary conductance change, *vii*. There are common occurrences of suddenly increased conductance with no measurable (< 1 nN) change in force both in plastic indentations, *ii*, and in elastic indentations, *viii*, *ix*, *x*.

6.5.2 Indicators of plasticity

We now consider several indicators derived from the force-displacement data and compare them with the evidence of plasticity from STM imaging. The first is the hysteresis energy, obtained by integrating the force over the excursion of the indentation. In Figure 6.23(a), the circled points correspond to elastic sites and show a large variability due to the details of the tip rearrangement region. The elastic sites have an average hysteresis energy of 46 ± 20 eV. The quoted error is the standard deviation of the measured values, and does not take into account systematic uncertainties. At the plastic sites, the measured hysteresis energies are all substantially larger with an average of 117 ± 16 eV. Tip rearrangements also contribute to the scatter of the plastic hysteresis energies. The variability of the hysteresis energy due to tip rearrangements is well illustrated in the force-displacement curves in Figure 6.21(a) and (b): both indentations are elastic but show very different hysteresis energies of 47 and 83 eV respectively due to the tip rearrangement region.

The hysteresis energy in the elastic sites gives a measure of the energy spent to irreversibly compress and extend Au adhering to the tip. Subtracting this average 46 eV from the 117 eV measured in the plastic sites suggests that ~70 eV is available for the creation of the dislocation loops and plastic damage in the sample. This energy corresponds to that of an edge dislocation threading ~12 atomic planes [233] or the energy required to break several tens of atomic bonds [269]. It is impossible to determine directly by topographic STM imaging if the damage consists of a subsurface dislocation or a vacancy cluster, but it can be concluded that this excess energy corresponds to some minimal defect configuration associated with permanent plasticity. Further advanced atomistic modeling is

needed to understand the mechanisms and final atomic configurations of the defects involved.

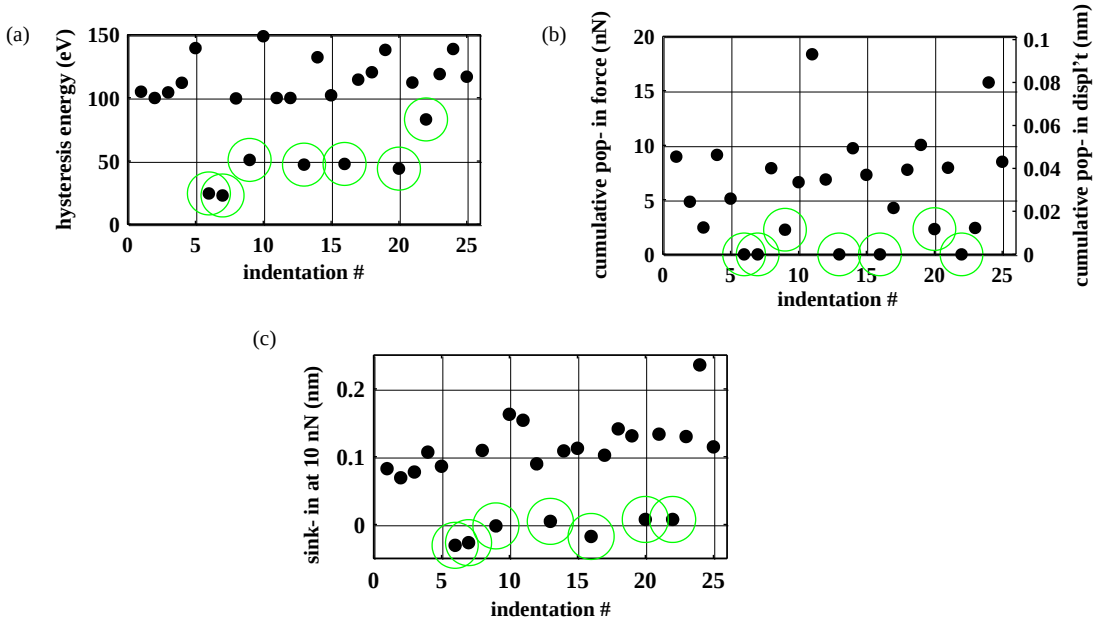

Figure 6.23: (a) Hysteresis energy obtained by integrating force-displacement curves. (b) Cumulative pop-in force and displacement obtained by summing pop-in events in each curve. (c) Sink-in depth between loading and unloading curves at 10 nN. Elastic sites are indicated by additional circles.

The sum of all pop-in discontinuities in each force-displacement curve is plotted in Figure 6.23(b). Pop-ins in the tip rearrangement region were not included in the sum. The cumulative displacement associated with these pop-ins, linked by the ~200 N/m sample stiffness, is shown on the right vertical axis. The cumulative pop-in displacement indicates the elastic or plastic nature of the indentations with an average of 0.003 ± 0.006 nm for the elastic sites and 0.04 ± 0.02 nm for the plastic sites. We note that discontinuities in displacement as small as ~0.01 nm are detected, well below the minimum pop-in distance observed in previous studies [270, 271]. These distances are far below the 0.24 nm Au(111) plane spacing, which may reflect the role of elastic recovery of the substrate after the pop-in.

Some elastic sites, indicated by additional circles, show a finite pop-in displacement. These small pop-ins may be due to the reversible nature of the first dislocation nucleation event [247], to tip rearrangements occurring at higher loads, or to reversible dislocation loops confined to the surface, as discussed later.

The indicator that was found to reflect most clearly the presence of plasticity is the sink-in depth measured at low repulsive load. This is the difference of the penetration depth where the loading and unloading curves cross a repulsive load of 10 nN (chosen to be above

the load at which tip rearrangements occur). The sink-in depth, plotted in Figure 6.23(c), is independent of the details occurring in the tip rearrangement region. The average sink-in depth is -0.01 ± 0.02 nm for the elastic sites and 0.12 ± 0.04 nm for the plastic sites. We suggest that the sink-in depth could be used as a reliable indicator of the creation of plastic damage in nanomachining applications.

An alternative sink-in depth calculated from the conductance (from any value in the range 0.01 G_0 to 10 G_0) does not serve as a reliable indicator of plastic damage due to tip rearrangements and wire formation (not shown).

In principle, one expects that the sum of all detected pop-in displacements, Figure 6.23(b), should reflect the presence of plasticity and be correlated to the measured sink-in depth, Figure 6.23(c). In order to illustrate the correlation between cumulative pop-in depth and sink-in depth, we show a correlation plot of these parameters in Figure 6.24.

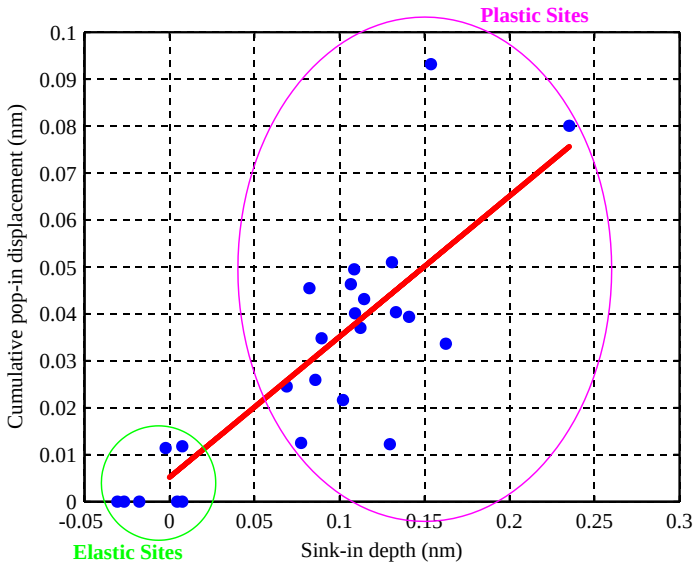

Figure 6.24: Correlation plot of the cumulative pop-in displacement versus sink-in depth from the indentations performed in Figure 6.20(d). The elastic sites and plastic sites are circled in two groups.

The red line is a linear fit with a slope of ~0.3. That is, for a given sink in depth, only ~30% of this depth is registered in the cumulative pop-in displacement. The most likely explanation for this is that our detection threshold on the order of 2 nN (0.01 nm) is insufficient to capture *all* pop-ins, and that some will occur below the detection threshold, yielding what may seem like a 'continuous' deformation within our experimental noise (even though plasticity is clear in the sink-in depth as well as STM imaging). This is presumably also why the two parameters are not perfectly correlated (R^2 = 0.69). Pop-ins also occur under large elastic stresses in the contact, whereas the sink-in depth is measured

at much lower contact stresses – at the moment it is not clear to us if we would expect a slope of unity even if all of the pop-ins had been detected.

The correlation plot shows that the pop-in displacement data from the plastic sites have a large vertical spread which blurs the distinction between elastic and plastic. A much clearer gap exists along the horizontal axis between these groups, indicating that the sink-in depth is a more robust indicator derived from the force-displacement data.

6.5.3 Defect configurations and energetic budget

In our experiment, indentations are carried out at a spacing of 20 nm. We believe that the single crystal is pristine within the relevant area of each indentation site because we know that the energy budget for plasticity in these indentations involves only ~70 eV. Although the final defect configuration is not characterizable experimentally, we can make estimations on its nature based on this energy budget.

If the final defect configuration consists of a subsurface dislocation, it can thread on the order of 12 atomic planes, therefore it would have a perimeter of ~3 nm (assuming 4 atoms/nm). Neglecting curvature energy of the dislocation line, this would constitute a loop of ~1 nm in diameter.

If there is a dislocation present in the final defect configuration, it must be of very small size, as we do not see any sign of hillocks appearing on the surface in any of our topographic STM scans. Hillocks have been observed in AFM indentation of KBr and Cu and are interpreted as the intersection of dislocation loops with the crystal surface [263, 264]. If we did observe hillocks several nm from the indentation site, we would also expect to measure a much greater hysteresis energy commensurate with the required dislocation line energy (note that the authors of the AFM studies referenced above could not determine hysteresis energies due to excessive piezo creep). Also, higher resolution images (section 6.4, page 214) do not show any more substantial arrangement of the herringbone reconstruction than expected for a vacancy clusters.

Due to the relatively unperturbed appearance of the surface in STM images outside the immediate vicinity of our indentations, we believe that if a subsurface dislocation is present, it is extremely small, or that the final configuration simply consists of a vacancy cluster which maintains perfect crystalline order with the exception of some missing surface atoms.

6.5.4 First pop-ins

Finally, we summarize the force at which the first pop-in occurs in Figure 6.25 as a cumulative distribution. In order to consider a larger statistical ensemble, we add to this plot the data from the first pop-ins in another 50 indentations performed with the same tip-sample system but to higher loads. The force at which the first pop-in occurs reflects the shear stress in the sample at the onset of plasticity. The maximum shear stress in the elastic contact at the first yield point is estimated from the Hertz model [249]

$$\tau_{max} = \left(\frac{0.56}{\pi}\right) F^{\frac{1}{3}} \left(\frac{E^*}{R}\right)^{\frac{2}{3}}, \tag{67}$$

where F corresponds to the force at the first pop-in, R is the tip radius determined by FIM, and E^* is the combined modulus for the W-Au contact of 80 GPa. The shear stress is shown on the top axis of Figure 4.

In a picture of homogeneous nucleation, one expects that the maximum shear stress within the substrate at the yield point to be on the order of the theoretical shear stress of the material. For gold, this corresponds to a shear stress of about $G/2\pi \approx 4.3$ GPa, where G is the shear modulus [272]. It is apparent from the cumulative distribution that the first detected pop-in appears at highly variable loads with corresponding stresses that are in all cases much lower than the theoretical shear strength (at the right limit of the plot).

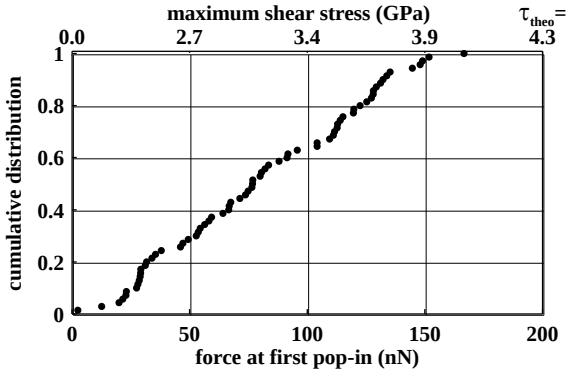

Figure 6.25: Cumulative distribution of the force measured at the first pop-in and corresponding maximum shear stress calculated from the Hertz model.

6.5.5 Discussion and summary

A transition between elastic and plastic behaviour is clearly reflected both in STM images and in properties of the force-displacement curves. Other than to show that the

homogeneous nucleation of dislocations does not occur in our system, we cannot determine the mechanisms governing the first pop-in or the initiation of plasticity.

In these experiments, the tip structure is known in exquisite detail from FIM, and a minimum energy of ~70 eV has been found necessary to produce a minimum plastic deformation in Au(111), just above the threshold of elastic loading. The length scales of our experiment – including the indenter size – match those accessible in molecular dynamics modeling, inviting an atomistic understanding of the observed plasticity threshold. Can modeling reproduce the observed energy minimum? What is the origin of the minimum plastic energy? What atomistic processes take place during the plastic deformation, and what is the atomic configuration of the defect after plastic indentations? Furthermore, modeling would be a convenient manner to explore if a threshold between elastic and plastic loading is universal in other fcc (or bcc) metals, or for other crystallographic orientations of the substrate. Results from such studies would also provide a springboard for further experiments.

The effect of the atomic-scale surface roughness of the indenter, of increasing concern in recent modeling work [36, 38], is directly accessible in our experiment as the exact crystal structure of the indenter is known. Heterogeneous nucleation of plasticity aided by surface roughness may well be plausible under the circumstance of extremely sharp tips where stress gradients are sufficiently large, and the maximal shear stress is concentrated only a few nm below the sample surface.

In summary, indentations resulting in the smallest permanent deformation of the Au(111) surface have been performed by combined AFM and STM using a well-defined W(111) indenter characterized by FIM. We find a clear correspondence between plasticity identified in STM images and characteristics of the force-displacement curves. This minimum deformation is associated with an energy budget of ~70 eV. The best indication of plasticity from the force-displacement data is found to be the sink-in depth measured at low repulsive load. We propose the utility of this parameter for determining plasticity from force-displacement curves alone, in contexts where imaging the surface is not possible or not practical.

The forces measured at the first pop-in event correspond to stresses much lower than the theoretical shear strength, suggesting that dislocations are not homogeneously nucleated within the bulk. Further modeling work would contribute to an understanding of the atomistic mechanisms involved in the threshold of plasticity and the final defect

structures, the minimum plastic energy, and the ubiquitousness of the plasticity threshold in other materials.

6.6 Summary and outlook on new materials

6.6.1 Summary of atomic-scale nanoindentation investigations of Au(111)

In summary, we have investigated atomic-scale nanoindentation phenomena with well-defined indenters. Tip wetting of fresh W tips was shown to occur over ~30 repeated indentations in Au(111), dropping the maximum adhesion by ~6× and conductance by ~12×. The reduction of adhesion is attributed to the additional Au layer(s) present on the tip apex facilitating atomic rearrangements during unloading. We speculate that the conductance drop is due to the addition of mismatched atomic interfaces between the W tip, tip Au layer, and sample which promotes backscattering and decreases overlap in electronic states. The wetting phenomenon was also demonstrated on Cu(100) by a conductance drop.

The transition from elastic to plastic loading was studied with a fresh W(110) indenter and showed several indicative features at the onset of plasticity which differed from the elastic indentations. The unique features of the plastic indentations were: pop-ins in the loading curve, a large conductance enhancement, enhanced adhesion force, nearly linear unloading contact stiffness, anomalous negative hysteresis loop indicating transfer of mechanical energy to the force transducer, and residual impressions in STM. The possible interdependence of these features, such as the requirement of a pop-in to add inelastic scattering sites to create local heating and cause a large conductance enhancement, provides motivation for further experimental work involving new experimental methodologies.

By improving the stability of the SPM and preparing stable imaging tips by carefully adjusting STM imaging parameters, we have acquired images of the surface structures remaining after indentation which are of comparable quality to STM images taken on standard rigid samples, revealing fine details of surface structure. The herringbone rearrangement reflects the change in surface stress distribution caused by the local perturbation of the indentation. We also find that images taken within a short time delay of indentation show a three-fold symmetry which may reflect the {111} slip plane symmetry of the bulk rather than the six-fold symmetry of the surface lattice.

In experiments with fully wetted FIM tips, it was possible to compare features of indentation curves performed to the same depth setpoints and correlate them with the

onset of plasticity, also imaged by STM. Plasticity was best identified quantitatively in the force-displacement curves by the sink-in depth rather than the cumulative sum of pop-ins or the hysteresis energy. We also found evidence for a minimum threshold for plastic damage in the Au(111) substrate – this minimum 'quantum' of plastic damage is associated with an energy budget of ~70 eV.

6.6.2 Outlook on new materials

The requirement of the SPM sample to act as a surface science quality substrate as well as a force transducer has so far limited our group's investigations to Au(111) substrates. The mica beam provides a well characterized mechanical force transducer which can be annealed to reasonable temperatures, and supports the growth of single-crystal Au(111) films. One may consider the future investigation of different substrate materials – Ag(111), Cu(111) and Al(111) can all be grown on mica, however with variable surface qualities [96, 109]. A major shortcoming of the mica beam technique is that the metal substrate thickness is finite – after roughly ten sputter/anneal preparations of the 100nm Au film, the surfaces begin to deteriorate in quality, and the mechanical response of the sample may become compromised as areas of the film delaminate. Also, metal films evaporated onto mica beams will only grow in the close packed (111) direction.

Given that the experiment is of direct atomic length scale comparison to atomistic simulations, and that the data we can collect is unique from the perspective of simultaneous force/current detection and excellent indenter characterization, it is worth considering what other substrates might be investigated in the future.

Glass cantilever beams can be fabricated from Schott D263T thin glass available in convenient thicknesses of 30, 50, and 70 μm. We have investigated the bending properties of the beams and have shown that a small sample can be appended to the beam without greatly affecting its mechanical properties. On a gold coated glass cantilever, we have attached a InSb(001) sample and successfully performed indentations on it. The surface, shown in Figure 6.26(a), could not be prepared with the same quality as shown in section 2.7.6 (page 55), due to the difficulties involved in the temperature control during annealing cycles. Stripes indicative of the 8×2 reconstruction are promising, nevertheless. The main drawback of the glass substrate-appended sample is a decrease in resonance frequency of the beam due to mass loading of the rather large piece of sample, leading to a large coupling of mechanical noise visible in the STM image. Two indentation curves are shown taken on

this sample in Figure 6.26(b) and (c) showing very large adhesion, and low conductance as expected for the semiconductor.

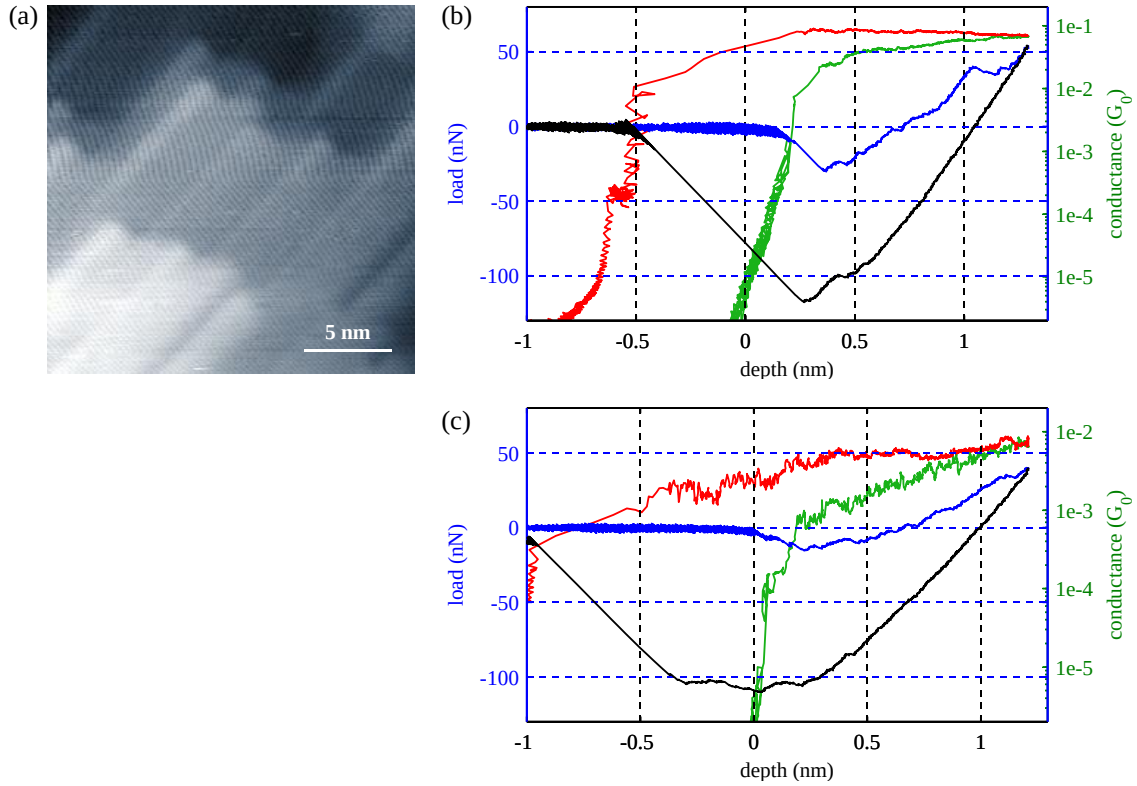

Figure 6.26: (a) STM image of InSb(001) mounted to a glass cantilever beam force transducer (18 pA, 2 V). (b) and (c) Indentation curves carried out on flat regions with bias voltages of -0.1 V and +0.1 V respectively.

Another promising alternative is to fabricate the entire cantilevered sample out of a single crystal of the desired substrate material and surface orientation. The polishing of a Cu(100) sample to a thickness of ~100 μm was the subject of an undergraduate project in fall 2012 carried out by Félix Dumont. Lacking a method to align the crystal lattice in-house, we started with a 2° miscut, single side polished Cu(100) crystal from MTI Corp and devised a method to ensure that the thinned back-side of the crystal stayed parallel to 0.1° with the supplied polished side so that we ended up with a rectangular beam and not a wedge shape. We used the supplied polished side on top as the STM surface, and at the end of thinning, polished the bottom side to enable the interferometer reflection. Though we must refine the polishing method to keep polishing grit from staying behind on the surface, there are clean, terraced areas which can be imaged and indented. The indentation of the Cu(100) single crystal with a cut PtIr STM tip is demonstrated in Figure 6.27.

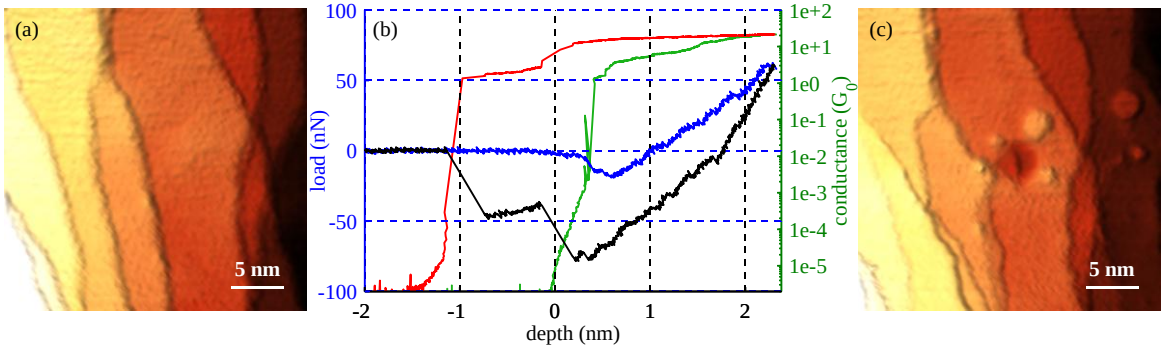

Figure 6.27: (a) STM image before indentation. 7 pA, -1.15 V (b) Indentation of a PtIr tip into the Cu(100) surface. Applied sample bias of -0.05 V. (c) Residual impression image revealing a wide double-tip convolution, and square shaped pile-up.

This type of sample provides an infinite lifetime of surface preparation and enables atomic-scale nanoindentation investigations of other materials and surface orientations.

7. Conclusions and outlook

There is something quite extraordinary about investigations of systems at the atomic scale using tools put together by one's own hands in the laboratory and without the need for sophisticated microfabrication. From the spot-welding of tip wires to cutting and cleaving mica beams – these are macroscopically large objects (Figure 2.4, page 19 is a nice reminder of this) between which we form superbly well-defined junctions and measure picometer distances, nanonewton forces and picoampere currents.

As was stated in the introduction to this thesis, a large part of our motivation for implementing FIM in SPM studies is the formation of atomically defined contacts to molecules where the FIM tip provides an electrode with known atomic geometry. Before we began investigations, many system renovations were necessary to permit reliable and low-noise SPM measurements, as well as routine use of FIM without high voltage breakdown. Owing to the relatively few combined FIM/STM experiments reported in the literature, we set out to investigate how to keep these tips atomically defined, and determine what types of crystal surfaces could be used as samples at room temperature. Because of atom transfer occurring from most types of substrates to the tips, we turned to investigate mechanical and electrical properties of nanoscale contacts between dissimilar metals.

Below, the main experimental results in this work are summarized, then broader conclusions based on the results are discussed. Following this, we offer an outlook toward future investigations.

7.1 Summary and conclusions

With regard to tip integrity, we have established a "force field" protocol for transferring FIM tips to SPM experiments. The time limitation in UHV for such an experiment to be carried out was shown to be reasonable for most gases (~60 min), except for the case of molecular H_2, to which FIM is blind. We showed the first convincing demonstration of tip-sample tunneling without modification of the atomic geometry of tip apices as determined by FIM, carried out on a cleaved Si(111) sample (without STM scanning). Au(111), graphite (HOPG), InSb(001) and GaAs(110) samples were all shown to uncontrollably transfer atoms to the FIM tip and ruin its atomic integrity at room temperature.

Atom transfer was investigated with Au(111) samples at room temperature and 150 K with W(111) and W(110) apex tips. W(111) tips are better suited to atomically defined

studies due to the larger atomic corrugation compared to W(110). This allows true atomic resolution in FIM and the larger diffusion barriers keep transferred material localized and identifiable in FIM at 150 K. The tunneling current spikes measured in experiments with Au(111) were characterized by an exponential distribution of peak heights, which likely reflects the lifetime of an adatom momentarily residing in the tunneling junction. We commented on the prospects and difficulties of obtaining intrinsic diffusion parameters from the study of current spikes – considerable challenges exist in the understanding of tip-substrate interactions as well as other effects such as the repeated measurement of individual adatoms. STM and STS were investigated with FIM tips on Si(111)-2×1, the most reactive well-defined surface available to us at this time. Although tunneling conditions are much more stable compared to other substrates, discernible tip changes occur within a few minutes of beginning STM experiments. The effect of the tip LDOS should be best observed in filled sample states spectra, but so far we cannot simultaneously obtain a well-defined sample and an atomically defined tip for STS experiments.

Mechanical contact between clean tungsten FIM tips and Au(111) surfaces is characterized by large adhesion, material transfer, and tip wetting. We have measured a ~12× drop in adhesion and a ~6× reduction in maximum junction conductance (also observed for Cu(100)) as fresh tips become saturated with sample material after about 30 indentations. We expect that these effects occur due to the added Au on the tip which helps restructure the contact upon separation, and adds additional atomically mismatched interfaces causing backscattering in ballistic transport. The transition from elastic loading to plastic indentation with fresh tips was characterized by large adhesion, large junction conductance, pop-ins, linear unloading stiffness, and an anomalous negative hysteresis loop. Further modeling should help to clarify atomistic mechanisms in these experiments. STM images of residual impressions after indentation of Au(111) show a restructuring of the herringbone reconstruction due to modification of surface stresses. Finally, using wetted tips, incipient plasticity was investigated in a Au(111) crystal, indicating a minimum quantity of plastic deformation which separates elastic from plastic indentation.

These results suggest some important conclusions with regard to the design of combined FIM/SPM experiments: Though UHV is a very clean environment, there still exists a substantial density of contaminant gas atoms, especially when dealing with FIM gas admission. The relatively short 'clean time' in UHV means that systems must be designed to rapidly transfer tips between microscopy modes. If a FIM stage is located in a separate

sample preparation chamber, the UHV pressure must be adequate for atomic cleanliness, and the transfer must be quickly performable. Such a transfer must also happen twice in order to verify tip integrity after a SPM experiment. It may also be worth considering cooling the transfer stage to mitigate rearrangements of transferred atoms by diffusion.

We conclude from our experiments with numerous types of samples that surface chemistry is a particularly important concern for experiments with atomically defined tips (especially at room temperature). A surface free of diffusing adatoms is imperative, and high surface reactivity is also desirable for chemisorbing any rest gas molecules. Our observation of well-behaved tunneling on highly-stepped areas of cleaved Si(111) where many unpaired Si dangling bonds are expected suggests that the Si(111)-7×7 surface might be a more ideal candidate at room temperature due to its partially-filled surface dangling bonds. At the moment, we do not have the facilities to prepare this surface.

The choice of crystallographic orientation of the FIM tip destined for SPM must be chosen carefully: One must be able to evaluate tip integrity in FIM after a SPM experiment. From our investigations with W(110) and W(111) apices, we conclude that the W(111) apex is preferable. Adatom diffusion and visibility should be kept in mind in any combined FIM/SPM experiment. We expect that tips created by faceting techniques or fabricated from other materials will be subject to similar concerns.

Indentation experiments can be carried out at the atomic scale with FIM tips, and we suggest that this is the most valuable experimental use of these combined techniques at room temperature. Their preparation in FIM allows for well-defined surface chemistry, accurate tip radius and atomic roughness determination – all very important parameters for comparing to atomistic simulations and understanding details of atomic scale plasticity. We also conclude that some experiments are best performed with wetted tips, if one desires to study effects occurring primarily in the sample rather than at the clean tip interface.

7.2.1 Atomically defined tip apices

SPM experiments with atomically defined tips should be much more easily achieved at liquid helium temperatures where most thermally activated processes are quenched, and vacuum quality is improved due to cryogenic pumping of the entire apparatus. We are curious as to whether distance regulation of the tip under AFM feedback may provide better tip-sample distance control with a larger gap than in tunneling (feedback on long range van der Waals or electrostatic force). This may result in improved stability against changes to the atomically defined tip. We are looking forward to the results of groups working toward FIM combined with qPlus-based AFM in the coming years.

At room temperature, it is worth pursuing the highly reactive Si(111)-7×7 surface for investigation with atomically defined tips. A good starting point would be the 5×5 reconstruction of Si(111) which is more accessible in our apparatus by the annealing of the 2×1 surface to ~350 °C [273]. The 5×5 reconstruction has a similar dimer-adatom-stacking fault structure to the 7×7, and should have comparable diffusion properties due to its similar atomic structure. If this proves reliable, a next step would be to develop a method for producing cantilevered Si samples in a similar geometry to our Au(111)/mica beams. This would constitute a rather challenging project, considering the already difficult 7×7 surface preparation by flash annealing where a current is passed through the wafer piece. Lacking two points of contact, a cantilevered sample would have to be heated by another means – likely by electron beam heating from the back side – to ~1100-1250 °C [274]. Despite these considerable challenges, this might warrant investigation if it permits the study of an atomically defined tip-molecule-surface sandwich.

At room temperature, C_{60} on Cu(100) may still be a candidate for an atomically defined system. By sufficient coverage of C_{60}, kink sites on step edges which act as adatom sources might be quenched, leading to enhanced tip stability – as long as the molecules themselves are not mobile.

Now that a better understanding of how to transfer tips from FIM to SPM has been established, the faceting and tip sharpening techniques we reviewed in section 2.8.3 (page 68) might be considered for fabricating tips of known single-atom geometry for SPM investigations. Such tips should provide a known and repeatable imaging resolution as well as spectroscopic signature from the beginning of the SPM experiment. These features would

be particularly valuable in ultra-low temperature studies of oxide electronics and superconductors where it is desirable to obtain routine and quantitative electronic spectroscopy data without tip artifacts, and where gentle crashing of the tip does not work to improve its imaging resolution.

7.2.2 FIM tips for atomic-scale nanoindentation

The match in length scales between atomistic simulations [42] and our nanoindentation experiments with FIM tips warrants serious future effort. With improved experimental reliability, and better resolution during indentation and imaging, one can now consider the study of yield mechanisms in different materials and crystallographic orientations of substrates. Due to the differing geometrical arrangements of slip systems for substrates of different orientations, one may expect the mechanisms active in incipient plasticity to be very sensitive to the choice of (111) vs (100) substrate, for example. One may even consider investigating covalently bonded materials, provided that they have a hardness less than that of the tungsten tips.

A major challenge in these indentation studies is the fabrication of samples acting simultaneously as force transducers and surface-science quality samples. The method of affixing a small crystal of InSb to a gold-on-glass cantilever was demonstrated as a solution to decouple the force transduction from the crystal sample for future studies. Although mass loading substantially lowered the sample's resonance frequency and encouraged noise coupling, the method could be refined using suitably thinned sample pieces.

In section 2.7.4 (page 50), we proposed that the graphene/Au(111) system prepared by physical vapor deposition would constitute an interesting indentation system: could a graphene sheet modify the contact pressure and act to inhibit plastic deformation of the underlying crystal? Although we cannot reach an annealing temperature required for proper graphene growth without damaging the mica substrate, such a technique could still be carried out on a solid metallic cantilever beam, the construction of which we demonstrated with Cu(100) in section 6.6.2 (page 233).

The details of heterogeneous dislocation nucleation aided by atomic-scale indenter roughness has previously only been investigable in computational simulations [38, 275] and bubble raft experiments [37] – it has simply not been controllable at the atomic scale. With the implementation of FIM tips as indentation probes, the atomic stepped structure of the tip can be controlled by choice of tip orientation and radius.

A detailed picture of incipient plasticity is being unveiled by indentation experiments and atomistic modeling [266, 276-278] – understanding the first events that lead to permanent deformation is relevant to the design of new materials and controlling friction and wear [268]. The minimum plastic threshold observed during our indentation in Au(111) opens many questions for further investigation – to start, what atomic processes govern this transition from elastic to plastic loading, and how are do these processes result in the formation of a permanent impression? Can atomistic modeling predict analogous mechanisms in other materials or orientations of substrate?

Many phenomena uncovered in our experiments warrant further investigation with new experimental protocols (modified bias voltages, retraction after pop-ins) and atomistic modeling. The pop-in followed by conductance enhancement (section 6.3, page 206), for example, must involve some very interesting atomic-scale choreography. The mechanism by which the junction relaxes to a lower energy state and transfers some mechanical energy to the force transducer is also an open question. Could FIM tip indentation be performed at low temperature and be combined with point-contact spectroscopy methods to elucidate defect structure by d^2I/dV^2 measurements of inelastic scattering? The number of interesting open questions concerning atomistic processes inspired by compelling experimental data is testament to the novelty of such experiments which will undoubtedly continue to contribute valuable results to the understanding of atomic scale plasticity.

References

1. W. Paul, Y. Miyahara, and P. H. Grütter. Simple Si(111) surface preparation by thin wafer cleavage. *Journal of Vacuum Science & Technology A: Vacuum, Surfaces, and Films*, 31 (2): 023201, 2013. doi: 10.1116/1.4790475.

2. W. Paul, Y. Miyahara, and P. H. Grütter. Implementation of atomically defined field ion microscopy tips in scanning probe microscopy. *Nanotechnology*, 23 (33): 335702, 2012. doi: 10.1088/0957-4484/23/33/335702.

3. W. Paul, D. Oliver, Y. Miyahara, and P. H. Grütter. Minimum Threshold for Incipient Plasticity in the Atomic-Scale Nanoindentation of Au(111). *Physical Review Letters*, 110 (13): 135506, 2013. doi: 10.1103/PhysRevLett.110.135506.

4. The International Technology Roadmap for Semiconductors (ITRS) 2012 Update. URL http://www.itrs.net/.

5. V. P. Georgiev, E. A. Towie, and A. Asenov. Impact of Precisely Positioned Dopants on the Performance of an Ultimate Silicon Nanowire Transistor: A Full Three-Dimensional NEGF Simulation Study. *IEEE Transactions on Electron Devices*, 60 (3): 965–971, 2013. doi: 10.1109/TED.2013.2238944.

6. S. Roy and A. Asenov. Where do the dopants go? *Science*, 309 (5733): 388–90, 2005. doi: 10.1126/science.1111104.

7. M. A. Reed and T. Lee. *Molecular Nanoelectronics*. American Scientific Publishers, Valencia CA, 2003.

8. H. Song, M. A. Reed, and T. Lee. Single molecule electronic devices. *Advanced Materials*, 23 (14): 1583–608, 2011. doi: 10.1002/adma.201004291.

9. A. Aviram and M. A. Ratner. Molecular rectifiers. *Chemical Physics Letters*, 29 (2): 277–283, 1974. doi: 10.1016/0009-2614(74)85031-1.

10. G. Binnig and H. Rohrer. Scanning tunneling microscopy - from birth to adolescence. *Reviews of Modern Physics*, 59 (3): 615–625, 1987. doi: 10.1103/RevModPhys.59.615.

11. H. Kroto. Symmetry, space, stars and C60. *Reviews of Modern Physics*, 69 (3): 703–722, 1997. doi: 10.1103/RevModPhys.69.703.

12. G. Binnig. Atomic Force Microscope and Method for Imaging Surfaces with Atomic Resolution, US Patent 4724318, 1988.

13. D. M. Eigler and E. K. Schweizer. Positioning single atoms with a scanning tunnelling microscope. *Nature*, 344 (6266): 524–526, 1990. doi: 10.1038/344524a0.

14. Y. Sugimoto, K. Ueda, M. Abe, and S. Morita. Three-dimensional scanning force/tunneling spectroscopy at room temperature. *Journal of physics. Condensed matter : an Institute of Physics journal*, 24 (8): 084008, 2012. doi: 10.1088/0953-8984/24/8/084008.

15. J. Repp, G. Meyer, S. Stojkovic, A. Gourdon, and C. Joachim. Molecules on Insulating Films: Scanning-Tunneling Microscopy Imaging of Individual Molecular Orbitals. *Physical Review Letters*, 94 (2): 026803, 2005. doi: 10.1103/PhysRevLett.94.026803.

16. L. Gross, F. Mohn, N. Moll, P. Liljeroth, and G. Meyer. The chemical structure of a molecule resolved by atomic force microscopy. *Science*, 325 (5944): 1110–4, 2009. doi: 10.1126/science.1176210.

17. L. Gross, N. Moll, F. Mohn, A. Curioni, G. Meyer, F. Hanke, and M. Persson. High-Resolution Molecular Orbital Imaging Using a p-Wave STM Tip. *Physical Review Letters*, 107 (8): 086101, 2011. doi: 10.1103/PhysRevLett.107.086101.

18. J. Stroscio and D. M. Eigler. Atomic and molecular manipulation with the scanning tunneling microscope. *Science*, 254 (5036): 1319–26, 1991. doi: 10.1126/science.254.5036.1319.

19. Y. Sugimoto, P. Pou, M. Abe, P. Jelínek, R. Pérez, S. Morita, and O. Custance. Chemical identification of individual surface atoms by atomic force microscopy. *Nature*, 446 (7131): 64–7, 2007. doi: 10.1038/nature05530.

20. H. J. W. Zandvliet and A. van Houselt. Scanning tunneling spectroscopy. *Annual review of analytical chemistry*, 2: 37–55, 2009. doi: 10.1146/annurev-anchem-060908-155213.

21. N. Lorente, R. Rurali, and H. Tang. Single-molecule manipulation and chemistry with the STM. *Journal of Physics: Condensed Matter*, 17 (13): S1049–S1074, 2005. doi: 10.1088/0953-8984/17/13/003.

22. I. R. McNab and J. C. Polanyi. Patterned atomic reaction at surfaces. *Chemical reviews*, 106 (10): 4321–54, 2006. doi: 10.1021/cr0501745.

23. J. K. Norsko. Chemisorption on metal surfaces. *Reports on Progress in Physics*, 53 (10): 1253–1295, 1990. doi: 10.1088/0034-4885/53/10/001.

24. M. Ternes, C. González, C. P. Lutz, P. Hapala, F. J. Giessibl, P. Jelínek, and A. J. Heinrich. Interplay of Conductance, Force, and Structural Change in Metallic Point Contacts. *Physical Review Letters*, 106 (1): 016802, 2011. doi: 10.1103/PhysRevLett.106.016802.

25. P. Jelínek, R. Pérez, J. Ortega, and F. Flores. Universal behaviour in the final stage of the breaking process for metal nanowires. *Nanotechnology*, 16 (8): 1023–1028, 2005. doi: 10.1088/0957-4484/16/8/004.

26. K. R. Harikumar, L. Leung, I. R. McNab, J. C. Polanyi, H. Lin, and W. A. Hofer. Cooperative molecular dynamics in surface reactions. *Nature chemistry*, 1 (9): 716–21, 2009. doi: 10.1038/nchem.440.

27. W. A. Hofer, A. J. Fisher, R. A. Wolkow, and P. H. Grütter. Surface Relaxations, Current Enhancements, and Absolute Distances in High Resolution Scanning Tunneling Microscopy. *Physical Review Letters*, 87 (23): 3–6, 2001. doi: 10.1103/PhysRevLett.87.236104.

28. Z. Majzik, B. Drevniok, W. KamiÅ„ski, M. Ondrácek, A. B. McLean, and P. Jelinek. Room Temperature Discrimination of Adsorbed Molecules and Attachment Sites on the Si(1 1 1)-7x7 Surface Using a qPlus Sensor. *ACS nano*, 7 (3): 2686, 2013. doi: 10.1021/nn400102m.

29. P. Jelínek, H. Wang, J. Lewis, O. Sankey, and J. Ortega. Multicenter approach to the exchange-correlation interactions in ab initio tight-binding methods. *Physical Review B*, 71 (23): 235101, 2005. doi: 10.1103/PhysRevB.71.235101.

30. C. Toher, R. Temirov, A. Greuling, F. Pump, M. Kaczmarski, G. Cuniberti, M. Rohlfing, and F. S. Tautz. Electrical transport through a mechanically gated molecular wire. *Physical Review B*, 83 (15): 155402, 2011. doi: 10.1103/PhysRevB.83.155402.

31. M. Fuechsle, J. A. Miwa, S. Mahapatra, H. Ryu, S. Lee, O. Warschkow, L. C. L. Hollenberg, G. Klimeck, and M. Y. Simmons. A single-atom transistor. *Nature nanotechnology*, 7 (4): 242–6, 2012. doi: 10.1038/nnano.2012.21.

32. H. Song, Y. Kim, Y. H. Jang, H. Jeong, M. A. Reed, and T. Lee. Observation of molecular orbital gating. *Nature*, 462 (7276): 1039–43, 2009. doi: 10.1038/nature08639.

33. H. Mehrez, A. Wlasenko, B. Larade, J. Taylor, P. Grütter, and H. Guo. I-V characteristics and differential conductance fluctuations of Au nanowires. *Physical Review B*, 65 (19): 195419, 2002. doi: 10.1103/PhysRevB.65.195419.

34. Y. Xue and M. Ratner. Microscopic study of electrical transport through individual molecules with metallic contacts. II. Effect of the interface structure. *Physical Review B*, 68 (11): 115407, 2003. doi: 10.1103/PhysRevB.68.115407.

35. H.-W. Fink. Mono-atomic tips for scanning tunneling microscopy. *IBM J Res Dev*, 30 (5): 460–165, 1986.

36. B. Luan and M. O. Robbins. The breakdown of continuum models for mechanical contacts. *Nature*, 435 (7044): 929–32, 2005. doi: 10.1038/nature03700.

37. A. Gouldstone, K. J. Van Vliet, and S. Suresh. Nanoindentation. Simulation of defect nucleation in a crystal. *Nature*, 411 (6838): 656, 2001. doi: 10.1038/35079687.

38. R. J. Wagner, L. Ma, F. Tavazza, and L. E. Levine. Dislocation nucleation during nanoindentation of aluminum. *Journal of Applied Physics*, 104 (11): 114311, 2008. doi: 10.1063/1.3021305.

39. Y. Mo, K. T. Turner, and I. Szlufarska. Friction laws at the nanoscale. *Nature*, 457 (7233): 1116–9, 2009. doi: 10.1038/nature07748.

40. U. Landman, W. D. Luedtke, N. A. Burnham, and R. J. Colton. Atomistic Mechanisms and Dynamics of Adhesion, Nanoindentation, and Fracture. *Science*, 248 (4954): 454–461, 1990. doi: 10.1126/science.248.4954.454.

41. J. Hagelaar, E. Bitzek, C. Flipse, and P. Gumbsch. Atomistic simulations of the formation and destruction of nanoindentation contacts in tungsten. *Physical Review B*, 73 (4): 045425, 2006. doi: 10.1103/PhysRevB.73.045425.

42. I. Szlufarska. Atomistic simulations of nanoindentation. *Materials Today*, 9 (5): 42–50, 2006.

43. D. J. Oliver, J. Maassen, M. El Ouali, W. Paul, T. Hagedorn, Y. Miyahara, Y. Qi, H. Guo, and P. H. Grütter. Conductivity of an atomically defined metallic interface. *Proceedings of the National Academy of Sciences of the United States of America*, 109 (47): 19097–102, 2012. doi: 10.1073/pnas.1208699109.

44. A. Stalder. *Mechanics and Electronics on the Atomic Scale: A Study using Scanning Probe Methods*. PhD thesis, University of Fribourg, 1995.

45. G. Cross. *Mechanics of Nanometer Scale Indentation of a Metal Surface*. PhD thesis, McGill University, 1999.

46. A. Schirmeisen. *Metallic Adhesion and Tunneling at the Atomic Scale*. PhD thesis, McGill University, 1999.

47. Y. Sun. *Study of Interactions at the Atomic Scale*. PhD thesis, McGill University, 2004.

48. A.-S. Lucier. *Preparation and Characterization of Tungsten Tips Suitable for Molecular Electronics Studies*. Master's thesis, McGill University, 2004.

49. M. El Ouali. *Nanometre scale indentation: effect of very sharp indenters on adhesion, plasticity, and electronic transport*. PhD thesis, McGill University, 2010.

50. T. Hagedorn. *Atomic Contacts characterized by Force and Current*. PhD thesis, McGill University, 2010.

51. W. Paul. Safety Interlock for Vacuum Systems, 2012. URL http://williampaulblog.blogspot.ca/2012/11/safety-interlock-circuit-for-vacuum.html.

52. E. W. Müller. Das Feldionenmikroskop. *Zeitschrift für Physik*, 131 (1): 136–142, 1951. doi: 10.1007/BF01329651.

53. T. T. Tsong. *Atom-probe field ion microscopy*. Cambridge University Press, New York, 1990.

54. G. Antczak and G. Ehrlich. *Surface Diffusion*. Cambridge University Press, New York, 2010.

55. B. Gault, M. P. Moody, J. M. Cairney, and S. P. Ringer. Atom probe crystallography. *Materials Today*, 15 (9): 378–386, 2012.

56. M. K. Miller, T. F. Kelly, K. Rajan, and S. P. Ringer. The future of atom probe tomography. *Materials Today*, 15 (4): 158–165, 2012. doi: 10.1016/S1369-7021(12)70069-X.

57. E. W. Müller, J. A. Panitz, and S. B. McLane. The Atom-Probe Field Ion Microscope. *Review of Scientific Instruments*, 39 (1): 83, 1968. doi: 10.1063/1.1683116.

58. J. A. Panitz. The 10 cm Atom Probe. *Review of Scientific Instruments*, 44 (8): 1034, 1973. doi: 10.1063/1.1686295.

59. W. Zhou and Z. L. Wang, editors. *Scanning Microscopy for Nanotechnology*. Springer New York, New York, NY, 2006. ISBN 978-0-387-33325-0. doi: 10.1007/978-0-387-39620-0. URL http://www.springerlink.com/index/10.1007/978-0-387-39620-0.

60. J.-B. Lalanne, W. Paul, D. Oliver, and P. H. Grütter. Note: electrochemical etching of sharp iridium tips. *Review of Scientific Instruments*, 82 (11): 116105, 2011. doi: 10.1063/1.3662473.

61. M. K. Miller, A. Cerezo, M. G. Hetherington, and G. D. W. Smith. *Atom Probe Field Ion Microscopy*. Oxford University Press, 1996.

62. A.-S. Lucier, H. Mortensen, Y. Sun, and P. H. Grütter. Determination of the atomic structure of scanning probe microscopy tungsten tips by field ion microscopy. *Physical Review B*, 72 (23): 235420, 2005. doi: 10.1103/PhysRevB.72.235420.

63. N. Hauptmann, F. Mohn, L. Gross, G. Meyer, T. Frederiksen, and R. Berndt. Force and conductance during contact formation to a C 60 molecule. *New Journal of Physics*, 14 (7): 073032, 2012. doi: 10.1088/1367-2630/14/7/073032.

64. G. Binnig, H. Rohrer, C. Gerber, and E. Weibel. Tunneling through a controllable vacuum gap. *Applied Physics Letters*, 40 (2): 178, 1982. doi: 10.1063/1.92999.

65. G. Binnig and H. Rohrer. Scanning tunneling microscopy. *Helvetica Physica Acta*, 55: 726, 1982.

66. D. Bonnell, editor. *Scanning Probe Microscopy and Spectroscopy*. Wiley-VCH, Toronto, 2nd edition, 2001.

67. C. J. Chen. *Introduction to Scanning Tunneling Microscopy*. Oxford University Press, Oxford, 2nd edition, 2008.

68. E. Meyer, H. J. Hug, and R. Bennewitz. *Scanning Probe Microscopy - The Lab on a Tip*. Springer-Verlag, New York, 1st edition, 2004.

69. J. A. Stroscio and W. J. Kaiser, editors. *Scanning Tunneling Microscopy*. Academic Press, San Diego, 1st edition, 1993.

70. U. Dürig, L. Novotny, B. Michel, and A. Stalder. Logarithmic current-to-voltage converter for local probe microscopy. *Review of Scientific Instruments*, 68 (10): 3814, 1997. doi: 10.1063/1.1148005.

71. B. Bhushan, editor. *Springer Handbook of Nanotechnology*. Springer Berlin Heidelberg, Berlin, Heidelberg, 2004. ISBN 978-3-540-01218-4. doi: 10.1007/3-540-29838-X. URL http://www.springerlink.com/index/10.1007/3-540-29838-X.

72. F. J. Giessibl. Advances in atomic force microscopy. *Reviews of Modern Physics*, 75 (3): 949–983, 2003. doi: 10.1103/RevModPhys.75.949.

73. D. Sarid. *Scanning Force Microscopy*. Oxford University Press, New York, 1994.

74. C. Argento and R. H. French. Parametric tip model and force-distance relation for Hamaker constant determination from atomic force microscopy. *Journal of Applied Physics*, 80 (11): 6081, 1996. doi: 10.1063/1.363680.

75. M. Guggisberg, M. Bammerlin, C. Loppacher, A. Abdurixit, O. Pfeiffer, V. Barwich, R. Bennewitz, A. Baratoff, E. Meyer, and H.-J. Güntherodt. Separation of interactions by noncontact force microscopy. *Physical Review B*, 61 (16): 11151–11155, 2000. doi: 10.1103/PhysRevB.61.11151.

76. C. J. Chen. A universal relation in NC-AFM, STM, and atom manipulation. *Nanotechnology*, 16 (3): S27–S34, 2005. doi: 10.1088/0957-4484/16/3/006.

77. W. Hofer and A. Fisher. Signature of a Chemical Bond in the Conductance between Two Metal Surfaces. *Physical Review Letters*, 91 (3): 036803, 2003. doi: 10.1103/PhysRevLett.91.036803.

78. Y. Sun, H. Mortensen, S. Schär, A.-S. Lucier, Y. Miyahara, P. H. Grütter, and W. A. Hofer. From tunneling to point contact: Correlation between forces and current. *Physical Review B*, 71 (19): 193407, 2005. doi: 10.1103/PhysRevB.71.193407.

79. P. Zahl, M. Bierkandt, S. Schröder, and A. Klust. The flexible and modern open source scanning probe microscopy software package GXSM. *Review of Scientific Instruments*, 74 (3): 1222, 2003. doi: 10.1063/1.1540718.

80. P. Zahl, T. Wagner, R. Möller, and A. Klust. Open source scanning probe microscopy control software package GXSM. *Journal of Vacuum Science & Technology B: Microelectronics and Nanometer Structures*, 28 (3): C4E39, 2010. doi: 10.1116/1.3374719.

81. W. Paul, J. R. Bates, and Y. Miyahara. GXSM user notes. URL http://spm.physics.mcgill.ca/gxsm-user-notes.

82. Q. Dai, R. Vollmer, R. W. Carpick, D. F. Ogletree, and M. Salmeron. A variable temperature ultrahigh vacuum atomic force microscope. *Review of Scientific Instruments*, 66 (11): 5266, 1995. doi: 10.1063/1.1146097.

83. L. Howald, E. Meyer, R. Lüthi, H. Haefke, R. Overney, H. Rudin, and H.-J. Güntherodt. Multifunctional probe microscope for facile operation in ultrahigh vacuum. *Applied Physics Letters*, 63 (1): 117, 1993. doi: 10.1063/1.109732.

84. H. J. Hug, B. Stiefel, P. J. A. van Schendel, A. Moser, S. Martin, and H.-J. Güntherodt. A low temperature ultrahigh vaccum scanning force microscope. *Review of Scientific Instruments*, 70 (9): 3625, 1999. doi: 10.1063/1.1149970.

85. M. Roseman and P. H. Grütter. Cryogenic magnetic force microscope. *Review of Scientific Instruments*, 71 (10): 3782–3787, 2000.

86. F. J. Giessibl. High-speed force sensor for force microscopy and profilometry utilizing a quartz tuning fork. *Applied Physics Letters*, 73 (26): 3956, 1998. doi: 10.1063/1.122948.

87. K. Bartzke, T. Antrack, K.-H. Schmidt, E. Dammann, and C. Schatterny. Needle sensor-a micromechanical detector for atomic force microscopy. *International Journal of Optoelectronics*, 8: 669, 1993.

88. A. Michels, F. Meinen, T. Murdfield, W. Göhde, U. Fischer, E. Beckmann, and H. Fuchs. 1 MHz quartz length extension resonator as a probe for scanning near-field acoustic microscopy. *Thin Solid Films*, 264 (2): 172–175, 1995. doi: 10.1016/0040-6090(95)05853-2.

89. F. J. Giessibl. A direct method to calculate tip-sample forces from frequency shifts in frequency-modulation atomic force microscopy. *Applied Physics Letters*, 78 (1): 123, 2001. doi: 10.1063/1.1335546.

90. J. E. Sader and S. P. Jarvis. Accurate formulas for interaction force and energy in frequency modulation force spectroscopy. *Applied Physics Letters*, 84 (10): 1801, 2004. doi: 10.1063/1.1667267.

91. W. S. Rasband. ImageJ. URL http://imagej.nih.gov/ij/.

92. C. A. Schneider, W. S. Rasband, and K. W. Eliceiri. NIH Image to ImageJ: 25 years of image analysis. *Nature Methods*, 9 (7): 671–675, 2012. doi: 10.1038/nmeth.2089.

93. C. Schönenberger and S. Alvarado. A differential interferometer for force microscopy. *Review of Scientific Instruments*, 60: 3131, 1989.

94. H. Hines. Epitaxial growth of gold on mica in an ultra-high vacuum. *Journal de Physique*, 25 (1-2): 134–137, 1964. doi: 10.1051/jphys:01964002501-2013400.

95. C. E. Chidsey, D. N. Loiacono, T. Sleator, and S. Nakahara. STM study of the surface morphology of gold on mica. *Surface Science*, 200 (1): 45–66, 1988. doi: 10.1016/0039-6028(88)90432-3.

96. M. Higo, K. Fujita, Y. Tanaka, M. Mitsushio, and T. Yoshidome. Surface morphology of metal films deposited on mica at various temperatures observed by atomic force microscopy. *Applied Surface Science*, 252 (14): 5083–5099, 2006. doi: 10.1016/j.apsusc.2005.07.034.

97. Z. H. Liu and N. M. Brown. Studies using AFM and STM of the correlated effects of the deposition parameters on the topography of gold on mica. *Thin Solid Films*, 300 (1-2): 84–94, 1997. doi: 10.1016/S0040-6090(96)09512-0.

98. K. Reichelt and H. Lutz. Hetero-epitaxial growth of vacuum evaporated silver and gold. *Journal of Crystal Growth*, 10 (1): 103–107, 1971. doi: 10.1016/0022-0248(71)90052-2.

99. L. E. Davis, N. C. MacDonald, P. W. Palmberg, G. E. Riach, and R. E. Weber. *Handbook of Auger Electron Spectroscopy*. Physical Electronics Industries, Inc., Eden Prairie, Minnesota, 2nd edition, 1976.

100. J. V. Barth, H. Brune, G. Ertl, and R. Behm. Scanning tunneling microscopy observations on the reconstructed Au(111) surface: Atomic structure, long-range superstructure, rotational domains, and surface defects. *Physical Review B*, 42 (15): 9307–9318, 1990. doi: 10.1103/PhysRevB.42.9307.

101. V. Hallmark, S. Chiang, J. Rabolt, J. Swalen, and R. Wilson. Observation of Atomic Corrugation on Au(111) by Scanning Tunneling Microscopy. *Physical Review Letters*, 59 (25): 2879–2882, 1987. doi: 10.1103/PhysRevLett.59.2879.

102. C. Wöll, S. Chiang, R. Wilson, and P. Lippel. Determination of atom positions at stacking-fault dislocations on Au(111) by scanning tunneling microscopy. *Physical Review B*, 39 (11): 7988–7991, 1989. doi: 10.1103/PhysRevB.39.7988.

103. F. Cardarelli. *Materials Handbook*. Springer London, London, 2008. ISBN 978-1-84628-668-1. doi: 10.1007/978-1-84628-669-8. URL http://www.springerlink.com/index/10.1007/978-1-84628-669-8.

104. J. Hwang and M. A. Dubson. Atomically flat gold films grown on hot glass. *Journal of Applied Physics*, 72 (5): 1852, 1992. doi: 10.1063/1.351657.

105. M. E. Lauer, R. Jungmann, J. H. Kindt, S. Magonov, J.-H. Fuhrhop, E. Oroudjev, and H. G. Hansma. Formation and healing of micrometer-sized channel networks on highly mobile Au(111) surfaces. *Langmuir : the ACS journal of surfaces and colloids*, 23 (10): 5459–65, 2007. doi: 10.1021/la063636y.

106. L. Tang, X. Zhang, Q. Guo, Y.-N. Wu, L.-L. Wang, and H.-P. Cheng. Two bonding configurations for individually adsorbed C_{60} molecules on Au(111). *Physical Review B*, 82 (12): 125414, 2010. doi: 10.1103/PhysRevB.82.125414.

107. E. I. Altman and R. J. Colton. Determination of the orientation of C60 adsorbed on Au(111) and Ag(111). *Physical review. B, Condensed matter*, 48 (24): 18244–18249, 1993.

108. E. I. Altman and R. J. Colton. Nucleation, growth, and structure of fullerene films on Au(111). *Surface Science*, 279 (1-2): 49–67, 1992. doi: 10.1016/0039-6028(92)90741-N.

109. E. I. Altman and R. J. Colton. The interaction of C60 with noble metal surfaces. *Surface Science*, 295 (1-2): 13–33, 1993. doi: 10.1016/0039-6028(93)90181-I.

110. J. M. Wofford, E. Starodub, A. L. Walter, S. Nie, A. Bostwick, N. C. Bartelt, K. Thürmer, E. Rotenberg, K. F. McCarty, and O. D. Dubon. Extraordinary epitaxial alignment of graphene islands on Au(111). *New Journal of Physics*, 14 (5): 053008, 2012. doi: 10.1088/1367-2630/14/5/053008.

111. S. Nie, N. C. Bartelt, J. M. Wofford, O. D. Dubon, K. F. McCarty, and K. Thürmer. Scanning tunneling microscopy study of graphene on Au(111): Growth mechanisms and substrate interactions. *Physical Review B*, 85 (20): 205406, 2012. doi: 10.1103/PhysRevB.85.205406.

112. D. R. Cooper, B. D'Anjou, N. Ghattamaneni, B. Harack, M. Hilke, A. Horth, N. Majlis, M. Massicotte, L. Vandsburger, E. Whiteway, and V. Yu. Experimental Review of Graphene. *ISRN Condensed Matter Physics*, 2012: 1–56, 2012. doi: 10.5402/2012/501686.

113. P. W. Sutter, J.-I. Flege, and E. A. Sutter. Epitaxial graphene on ruthenium. *Nature materials*, 7 (5): 406–11, 2008. doi: 10.1038/nmat2166.

114. M. Enachescu, D. Schleef, D. Ogletree, and M. Salmeron. Integration of point-contact microscopy and atomic-force microscopy: Application to characterization of graphite/Pt(111). *Physical Review B*, 60 (24): 16913–16919, 1999. doi: 10.1103/PhysRevB.60.16913.

115. T. Land, T. Michely, R. Behm, J. Hemminger, and G. Comsa. STM investigation of single layer graphite structures produced on Pt(111) by hydrocarbon decomposition. *Surface Science*, 264 (3): 261–270, 1992. doi: 10.1016/0039-6028(92)90183-7.

116. M. Breeman and D. Boerma. Migration of Cu adatoms on a Cu(100) surface, studied with low-energy ion scattering (LEIS). *Surface Science*, 269-270: 224–228, 1992. doi: 10.1016/0039-6028(92)91254-9.

117. S.-S. Wong, W. Pai, C.-H. Chen, and M.-T. Lin. Coverage-dependent adsorption superstructure transition of C_{60}/Cu(001). *Physical Review B*, 82 (12), 2010. doi: 10.1103/PhysRevB.82.125442.

118. J. Kolodziej, B. Such, M. Goryl, F. Krok, P. Piatkowski, and M. Szymonski. Surface structure investigations using noncontact atomic force microscopy. *Applied Surface Science*, 252 (21): 7614–7623, 2006. doi: 10.1016/j.apsusc.2006.03.054.

119. M. Schweitzer, F. Leibsle, T. Jones, C. McConville, and N. Richardson. An STM study of the InSb(100)-c(8x2) surface. *Surface Science*, 280 (1-2): 63–70, 1993. doi: 10.1016/0039-6028(93)90356-O.

120. G. Goryl, O. Boelling, S. Godlewski, J. Kolodziej, B. Such, and M. Szymonski. Low temperature InSb(001) surface structure studied by scanning tunneling microscopy. *Surface Science*, 601 (17): 3605–3610, 2007. doi: 10.1016/j.susc.2007.07.002.

121. G. Goryl, S. Godlewski, J. J. Kolodziej, and M. Szymonski. High resolution LT-STM imaging of PTCDA molecules assembled on an InSb(001) c(8x2) surface. *Nanotechnology*, 19 (18): 185708, 2008. doi: 10.1088/0957-4484/19/18/185708.

122. J. J. Kolodziej, B. Such, and M. Szymonski. Atomic Structure of InSb(001) and GaAs(001) Surfaces Imaged with Noncontact Atomic Force Microscopy. *Physical Review Letters*, 90 (22): 22–25, 2003. doi: 10.1103/PhysRevLett.90.226101.

123. B. Such, G. Goryl, S. Godlewski, J. J. Kolodziej, and M. Szymonski. PTCDA molecules on a KBr/InSb system: a low temperature STM study. *Nanotechnology*, 19 (47): 475705, 2008. doi: 10.1088/0957-4484/19/47/475705.

124. A. Tekiel, M. Goryl, and M. Szymonski. Copper phthalocyanine molecules on an InSb(001) c(8 x 2) surface studied by ultra-high-vacuum STM and non-contact AFM. *Nanotechnology*, 18 (47): 475707, 2007. doi: 10.1088/0957-4484/18/47/475707.

125. D. Toton, S. Godlewski, G. Goryl, J. J. Kolodziej, L. Kantorovich, and M. Szymonski. Architecture of PTCDA molecular structures on a reconstructed InSb(001) surface. *Physical Review B*, 83 (23): 235431, 2011. doi: 10.1103/PhysRevB.83.235431.

126. P. John, T. Miller, and T.-C. Chiang. InSb(100) reconstructions probed with core-level photoemission. *Physical Review B*, 39 (3): 1730–1737, 1989. doi: 10.1103/PhysRevB.39.1730.

127. N. Jones, C. Norris, C. Nicklin, P. Steadman, S. Baker, A. Johnson, and S. Bennett. Atomic structure of the InSb(001)-c(8x2) reconstruction determined by X-ray diffraction. *Surface Science*, 409 (1): 27–36, 1998. doi: 10.1016/S0039-6028(98)00192-7.

128. C. McConville, T. Jones, F. Leibsle, S. Driver, T. Noakes, M. Schweitzer, and N. Richardson. Surface reconstructions of InSb(100) observed by scanning tunneling microscopy. *Physical Review B*, 50 (20): 14965–14976, 1994. doi: 10.1103/PhysRevB.50.14965.

129. M. O. Schweitzer, F. M. Leibsle, T. S. Jones, C. F. McConville, and N. V. Richardson. Imaging ion-bombarded III-V semiconductor surfaces: a scanning tunnelling microscopy study of InSb(100). *Semiconductor Science and Technology*, 8 (1S): S342–S344, 1993. doi: 10.1088/0268-1242/8/1S/076.

130. J. T. Yates Jr. *Experimental Innovations in Surface Science*. Springer, New York, 1st edition, 1997.

131. R. M. Feenstra and M. A. Lutz. Scanning tunneling microscopy and spectroscopy of the Si(111)5x5 surface. *Journal of Vacuum Science & Technology B: Microelectronics and Nanometer Structures*, 9 (2): 716, 1991. doi: 10.1116/1.585539.

132. J. C. H. Spence, W. Lo, and M. Kuwabara. Observation of the graphite surface by reflection electron microscopy during STM operation. *Ultramicroscopy*, 33 (2): 69–82, 1990. doi: 10.1016/0304-3991(90)90009-B.

133. J. D. Todd and J. B. Pethica. A shear model for STM imaging of layered materials. *Journal of Physics: Condensed Matter*, 1 (49): 9823–9831, 1989. doi: 10.1088/0953-8984/1/49/003.

134. R. Nuffer, H.-J. Müssig, and J. Dabrowski. Cross-sectional STM/STS - a useful tool for identification of dopants in silicon. *Solid-State Electronics*, 44 (5): 875–880, 2000. doi: 10.1016/S0038-1101(99)00285-3.

135. K. C. Pandey. New π-Bonded Chain Model for Si(111)-(2x1) Surface. *Physical Review Letters*, 47 (26): 1913–1917, 1981. doi: 10.1103/PhysRevLett.47.1913.

136. J. H. Singleton. Practical guide to the use of Bayard-Alpert ionization gauges. *Journal of Vacuum Science & Technology A: Vacuum, Surfaces, and Films*, 19 (4): 1712, 2001. doi: 10.1116/1.1335679.

137. T. Hagedorn, M. El Ouali, W. Paul, D. Oliver, Y. Miyahara, and P. H. Grütter. Refined tip preparation by electrochemical etching and ultrahigh vacuum treatment to obtain atomically sharp tips for scanning tunneling microscope and atomic force microscope. *Review of Scientific Instruments*, 82 (11): 113903, 2011. doi: 10.1063/1.3660279.

138. M. Greiner and P. Kruse. Recrystallization of tungsten wire for fabrication of sharp and stable nanoprobe and field-emitter tips. *Review of Scientific Instruments*, 78 (2): 026104, 2007. doi: 10.1063/1.2670293.

139. B. Verlinden, J. Driver, I. Samajdar, and R. D. Doherty. *Thermo-Mechanical Processing of Metallic Materials*. Elsevier, Oxford, 2007.

140. R. D. Webber, J. M. Walls, and R. Smith. Ring counting in field-ion micrographs. *Journal of Microscopy*, 113 (3): 291–299, 1978. doi: 10.1111/j.1365-2818.1978.tb00107.x.

141. P. L. Bolin, B. N. Ranganathan, and R. J. Bayuzick. Determination of field ion tip shapes. *Journal of Physics E: Scientific Instruments*, 9 (5): 363–365, 1976. doi: 10.1088/0022-3735/9/5/013.

142. R. D. Webber and J. M. Walls. The shape of field-ion emitters. *Journal of Physics D: Applied Physics*, 12 (9): 1589–1595, 1979. doi: 10.1088/0022-3727/12/9/021.

143. J. L. Pitters, R. Urban, and R. Wolkow. Creation and recovery of a W(111) single atom gas field ion source. *The Journal of chemical physics*, 136 (15): 154704, 2012. doi: 10.1063/1.3702209.

144. R. Urban, R. A. Wolkow, and J. L. Pitters. Field ion microscope evaluation of tungsten nanotip shape using He and Ne imaging gases. *Ultramicroscopy*, 122: 60–4, 2012. doi: 10.1016/j.ultramic.2012.07.026.

145. O. Albrektsen, H. W. M. Salemink, K. A. Mø rch, and A. R. Thölen. Reliable tip preparation for high-resolution scanning tunneling microscopy. *Journal of Vacuum Science & Technology B: Microelectronics and Nanometer Structures*, 12 (6): 3187, 1994. doi: 10.1116/1.587497.

146. I. Ekvall, E. Wahlström, D. Claesson, H. k. Olin, and E. Olsson. Preparation and characterization of electrochemically etched W tips for STM. *Measurement Science and Technology*, 10 (1): 11–18, 1999. doi: 10.1088/0957-0233/10/1/006.

147. S. Ernst, S. Wirth, M. Rams, V. Dolocan, and F. Steglich. Tip preparation for usage in an ultra-low temperature UHV scanning tunneling microscope. *Science and Technology of Advanced Materials*, 8 (5): 347–351, 2007. doi: 10.1016/j.stam.2007.05.008.

148. Y.-C. Kim, C.-J. Yu, and D. N. Seidman. Effects of low-energy (1-1.5 kV) nitrogen-ion bombardment on sharply pointed tips: Sputtering, implantation, and metal-nitride formation. *Journal of Applied Physics*, 81 (2): 944, 1997. doi: 10.1063/1.364187.

149. M. Rezeq, J. Pitters, and R. Wolkow. Tungsten nanotip fabrication by spatially controlled field-assisted reaction with nitrogen. *The Journal of Chemical Physics*, 124 (20): 204716, 2006. doi: 10.1063/1.2198536.

150. M. Rezeq, J. Pitters, and R. Wolkow. Nano-tip Fabrication by Spatially Controlled Etching, US Patent 7431856 B2, December 2008.

151. G. Ehrlich and F. G. Hudda. Direct Observation of Individual Adatoms: Nitrogen on Tungsten. *The Journal of Chemical Physics*, 36 (12): 3233, 1962. doi: 10.1063/1.1732451.

152. J. F. Mulson and E. W. Müller. Corrosion of Tungsten and Iridium by Field Desorption of Nitrogen and Carbon Monoxide. *The Journal of Chemical Physics*, 38 (11): 2615, 1963. doi: 10.1063/1.1733560.

153. I. Ermanoski, K. Pelhos, W. Chen, J. S. Quinton, and T. E. Madey. Oxygen-induced nano-faceting of Ir(210). *Surface Science*, 549 (1): 1–23, 2004. doi: 10.1016/j.susc.2003.10.052.

154. K.-J. Song, C.-Z. Dong, and T. E. Madey. Faceting of W (111) Induced by Ultrathin Pd Films. *Langmuir*, (6): 3019–3026, 1991. doi: 10.1021/la00060a019.

155. A. Szczepkowicz, A. Ciszewski, R. Bryl, C. Oleksy, C.-H. Nien, Q. Wu, and T. E. Madey. A comparison of adsorbate-induced faceting on flat and curved crystal surfaces. *Surface Science*, 599 (1-3): 55–68, 2005. doi: 10.1016/j.susc.2005.09.036.

156. C.-C. Chang, H.-S. Kuo, T. T. Tsong, and I.-S. Hwang. A fully coherent electron beam from a noble-metal covered W(111) single-atom emitter. *Nanotechnology*, 20 (11): 115401, 2009. doi: 10.1088/0957-4484/20/11/115401.

157. T.-Y. Fu, Y.-C. Lin, H.-S. Kuo, I.-S. Hwang, and T. T. Tsong. Study of two types of Ir or Rh covered single atom pyramidal W tips. *Surface Science*, 601 (18): 3992–3995, 2007. doi: 10.1016/j.susc.2007.04.043.

158. I.-S. Hwang, H.-S. Kuo, C.-C. Chang, and T. T. Tsong. Noble-Metal Covered W(111) Single-Atom Electron Sources. *Journal of The Electrochemical Society*, 157 (2): P7, 2010. doi: 10.1149/1.3269925.

159. H.-S. Kuo, I.-S. Hwang, T.-Y. Fu, Y.-C. Lin, C.-C. Chang, and T. T. Tsong. Noble Metal/W(111) Single-Atom Tips and Their Field Electron and Ion Emission Characteristics. *Japanese Journal of Applied Physics*, 45 (No. 11): 8972–8983, 2006. doi: 10.1143/JJAP.45.8972.

160. H.-S. Kuo, I.-S. Hwang, T.-Y. Fu, Y.-C. Lin, C.-C. Chang, and T. T. Tsong. Preparation of Single-Atom Tips and Their Field Emission Behaviors. *e-Journal of Surface Science and Nanotechnology*, 4 (February): 233–238, 2006. doi: 10.1380/ejssnt.2006.233.

161. H.-S. Kuo, I.-S. Hwang, T.-Y. Fu, Y.-H. Lu, C.-Y. Lin, and T. T. Tsong. Gas field ion source from an Ir/W(111) single-atom tip. *Applied Physics Letters*, 92 (6): 063106, 2008. doi: 10.1063/1.2844851.

162. H.-S. Kuo, I.-S. Hwang, T.-Y. Fu, Y.-S. Hwang, Y.-H. Lu, C.-Y. Lin, T. T. Tsong, and J.-L. Hou. A single-atom sharp iridium tip as an emitter of gas field ion sources. *Nanotechnology*, 20 (33): 335701, 2009. doi: 10.1088/0957-4484/20/33/335701.

163. K. Nomura, E. Rokuta, T. Itagaki, C. Oshima, H.-S. Kuo, and T. T. Tsong. Electron Emission Characteristics of Au-covered Tungsten<111> Nanotips. *e-Journal of Surface Science and Nanotechnology*, 6 (January): 25–28, 2008. doi: 10.1380/ejssnt.2008.25.

164. A. Golubok, S. Masalov, and N. Tarasov. Thermofield tip formation in UHV/STM combined with field-emission microscope. *Ultramicroscopy*, 42-44: 1574–1579, 1992. doi: 10.1016/0304-3991(92)90486-4.

165. V. G. Pavlov. Field-Desorption Microscopy Study of the Deformation of a Tungsten Tip Subjected to Thermal Treatment in an Electric Field. *Physics of the Solid State*, 47 (11): 2180, 2005. doi: 10.1134/1.2131165.

166. V. G. Pavlov. Variations in shapes of outgrowths on a tungsten tip during growth in an electric field. *Physics of the Solid State*, 48 (5): 969–972, 2006. doi: 10.1134/S1063783406050258.

167. V. G. Pavlov. Atomically sharp <111> trihedral angle of a tungsten tip. *Physics of the Solid State*, 49 (8): 1579–1582, 2007. doi: 10.1134/S1063783407080306.

168. H.-T. Jeng, H.-S. Kuo, I.-S. Hwang, and T. T. Tsong. High stability and electronic structures of noble-metal covered W(111) atom perfect pyramidal tips. *Physical Review B*, 81 (15): 155424, 2010. doi: 10.1103/PhysRevB.81.155424.

169. S. Wolfram. The Personal Analytics of My Life, 2012. URL http://blog.stephenwolfram.com/2012/03/the-personal-analytics-of-my-life/.

170. A. Labuda, W. Paul, B. Pietrobon, R. B. Lennox, P. H. Grütter, and R. Bennewitz. High-resolution friction force microscopy under electrochemical control. *Review of Scientific Instruments*, 81 (8): 083701, 2010. doi: 10.1063/1.3470107.

171. M. Carlà, L. Lanzi, E. Pallecchi, and G. Aloisi. Development of an ultralow current amplifier for scanning tunneling microscopy. *Review of Scientific Instruments*, 75 (2): 497, 2004. doi: 10.1063/1.1641159.

172. D. J. Kim and J. Y. Koo. A low-noise and wide-band ac boosting current-to-voltage amplifier for scanning tunneling microscopy. *Review of Scientific Instruments*, 76 (2), 2005.

173. L. Libioulle, A. Radenovic, E. Bystrenova, and G. Dietler. Low noise current-to-voltage converter and vibration damping system for a low-temperature ultrahigh vacuum scanning tunneling microscope. *Review of Scientific Instruments*, 74 (2): 1016, 2003. doi: 10.1063/1.1533100.

174. B. Michel, L. Novotny, and U. Dürig. Low-temperature compatible I-V converter. *Ultramicroscopy*, 42-44: 1647–1652, 1992. doi: 10.1016/0304-3991(92)90499-A.

175. Wikipedia. Ground loop (electricity) — Wikipedia: The Free Encyclopedia, . URL http://en.wikipedia.org/wiki/-Ground_loop_(electricity).

176. P. Horowitz and W. Hill. *The Art of Electronics*. Cambridge University Press, New York, 2nd edition, 1989.

177. W. Jung, editor. *Op Amp Applications Handbook*. Newnes, Burlington, 2005. ISBN 9780750678445. doi: 10.1016/B978-075067844-5/50109-0.

178. Macor dielectric constant. URL http://www.wolframalpha.com/input/?i=Macor+dielectric+constant.

179. Y. Kuk and P. J. Silverman. Scanning tunneling microscope instrumentation. *Review of Scientific Instruments*, 60 (2): 165, 1989. doi: 10.1063/1.1140457.

180. Wikipedia. Induction motor — Wikipedia: The Free Encyclopedia, . URL http://en.wikipedia.org/wiki/Induction_motor.

181. A. Labuda, J. R. Bates, and P. H. Grütter. The noise of coated cantilevers. *Nanotechnology*, 23 (2): 025503, 2012. doi: 10.1088/0957-4484/23/2/025503.

182. A. Labuda, M. Lysy, W. Paul, Y. Miyahara, P. H. Grütter, R. Bennewitz, and M. Sutton. Stochastic noise in atomic force microscopy. *Physical Review E*, 86 (3): 033104, 2012. doi: 10.1103/PhysRevE.86.031104.

183. J. F. O'Hanlon. *A User's Guide to Vacuum Technology*. John Wiley & Sons, Hoboken, 3rd edition, 2003.

184. N. Yoshimura. *Vacuum Technology*. Springer, Berlin, 2008.

185. W. H. Kohl. Vacuum Breakdown. In *Handbook of Materials and Techniques for Vacuum Devices*, chapter 20. AIP Press, New York, September 1995.

186. V. N. Maller and M. S. Naidu. High Voltage Breakdown in Vacuum. In *Advances in High Voltage Insulation and Arc Interruption in SF6 and Vacuum*, chapter 6. Pergamon Press, Toronto, 1981.

187. J.-M. Torres and R. S. Dhariwal. Electric field breakdown at micrometre separations in air and vacuum. *Microsystem Technologies*, 6 (1): 6–10, 1999. doi: 10.1007/s005420050166.

188. R. P. Little and S. T. Smith. Field Enhancing Projections Produced by the Application of an Electric Field. *Journal of Applied Physics*, 36 (4): 1502, 1965. doi: 10.1063/1.1714350.

189. R. P. Little and W. T. Whitney. Electron Emission Preceding Electrical Breakdown in Vacuum. *Journal of Applied Physics*, 34 (8): 2430, 1963. doi: 10.1063/1.1702760.

190. M. J. Kofoid. Effect of Metal-Dielectric Junction Phenomena on High-Voltage Breakdown over Insulators in Vacuum. *Transactions of the American Institute of Electrical Engineers. Part III: Power Apparatus and Systems*, 79 (3): 999–1004, 1960. doi: 10.1109/AIEEPAS.1960.4500899.

191. Y. Kuk and P. J. Silverman. Role of tip structure in scanning tunneling microscopy. *Applied Physics Letters*, 48 (23): 1597, 1986. doi: 10.1063/1.96828.

192. T. Sakurai, T. Hashizume, Y. Hasegawa, I. Kamiya, N. Sano, H. Yokoyama, H. Tanaka, I. Sumita, and S. Hyodo. New versatile room-temperature field ion scanning tunneling microscopy. *Journal of Vacuum Science & Technology A: Vacuum, Surfaces, and Films*, 8 (1): 324, 1990. doi: 10.1116/1.577098.

193. T. Sakurai, T. Hashizume, I. Kamiya, Y. Hasegawa, N. Sano, H. Pickering, and A. Sakai. Field ion-scanning tunneling microscopy. *Progress in Surface Science*, 33 (1): 3–89, 1990. doi: 10.1016/0079-6816(90)90012-9.

194. T. Hashizume and T. Sakurai. FI-STM Investigation of Fullerenes Adsorbed on the Semiconductor and Metal Surfaces (STM-C60). *Science reports of the Research Institutes, Tohoku University. Ser. A, Physics, chemistry and metallurgy1*, A44: 17, 1997.

195. T. Hashizume, X.-D. Wang, Y. Nishina, H. Shinohara, Y. Saito, Y. Kuk, and T. Sakurai. Field Ion-Scanning Tunneling Microscopy Study of C 60 on the Si(100) Surface. *Japanese Journal of Applied Physics*, 31 (Part 2, No. 7A): L880–L883, 1992. doi: 10.1143/JJAP.31.L880.

196. X.-D. Wang, T. Hashizume, H. Shinohara, Y. Saito, Y. Nishina, and T. Sakurai. Scanning Tunneling Microscopy of C 60 on the Si(111)7x7 Surface. *Japanese Journal of Applied Physics*, 31 (Part 2, No. 7B): L983–L986, 1992. doi: 10.1143/JJAP.31.L983.

197. T. Hashizume, I. Sumita, Y. Murata, S. Hyodo, and T. Sakurai. Cs adsorption on the Si(100)2x1 surfaces. *Journal of Vacuum Science & Technology B: Microelectronics and Nanometer Structures*, 9 (2): 742, 1991. doi: 10.1116/1.585545.

198. M. Tomitori, N. Hirano, F. Iwawaki, Y. Watanabe, T. Takayanagi, and O. Nishikawa. Elaboration and evaluation of tip manipulation of scanning tunneling microscopy. *Journal of Vacuum Science & Technology A: Vacuum, Surfaces, and Films*, 8 (1): 425, 1990. doi: 10.1116/1.576412.

199. J. C. H. Spence, U. Weierstall, and W. Lo. Atomic species identification in scanning tunneling microscopy by time-of-flight spectroscopy. *Journal of Vacuum Science & Technology B: Microelectronics and Nanometer Structures*, 14 (3): 1587, 1996. doi: 10.1116/1.589195.

200. U. Weierstall and J. C. H. Spence. Atomic species identification in STM using an imaging atom-probe technique. *Surface Science*, 398 (1-2): 267–279, 1998. doi: 10.1016/S0039-6028(98)80030-7.

201. A. Fian, C. Ernst, and M. Leisch. Combined atom probe and STM study of tip-substrate interactions. *Fresenius' Journal of Analytical Chemistry*, 365 (1-3): 38–42, 1999. doi: 10.1007/s002160051441.

202. A. Fian and M. Leisch. Study on tip-substrate interactions by STM and APFIM. *Ultramicroscopy*, 95 (1-4): 189–197, 2003. doi: 10.1016/S0304-3991(02)00316-9.

203. J. Welker and F. J. Giessibl. Revealing the Angular Symmetry of Chemical Bonds by Atomic Force Microscopy. *Science*, 336 (6080): 444–449, 2012. doi: 10.1126/science.1219850.

204. G. Ehrlich and F. G. Hudda. Observation of Adsorption on an Atomic Scale. *The Journal of Chemical Physics*, 33 (4): 1253, 1960. doi: 10.1063/1.1731366.

205. A. A. Holscher and W. M. H. Sachtler. Chemisorption and surface corrosion in the tungsten + carbon monoxide system, as studied by field emission and field ion microscopy. *Discussions of the Faraday Society*, 41: 29, 1966. doi: 10.1039/df9664100029.

206. R. Lewis and R. Gomer. Adsorption studies in the field ion microscope with argon imaging. *Surface Science*, 26 (1): 197–229, 1971. doi: 10.1016/0039-6028(71)90123-3.

207. G. Cranstoun and J. Anderson. Field ion microscope studies of very low coverage low temperature oxygen adsorption on tungsten. *Surface Science*, 32 (2): 397–421, 1972. doi: 10.1016/0039-6028(72)90169-0.

208. G. Ehrlich and F. G. Hudda. Promoted field desorption and the visibility of adsorbed atoms in the ion microscope. *Philosophical Magazine*, 8 (93): 1587–1591, 1963. doi: 10.1080/14786436308207321.

209. E. Müller and T. Tsong. Field ion microscopy, field ionization and field evaporation. *Progress in Surface Science*, 4 (i): 1–139, 1974. doi: 10.1016/S0079-6816(74)80005-5.

210. E. W. Müller. Study of Atomic Structure of Metal Surfaces in the Field Ion Microscope. *Journal of Applied Physics*, 28 (1): 1, 1957. doi: 10.1063/1.1722557.

211. S. G. Lias. Ionization Energies of Gas-Phase Molecules. In *CRC Handbook of Chemistry and Physics*. 92nd edition, 2011.

212. G. F. Weston. *Ultrahigh Vacuum Practice*. Butterworth & Co., Toronto, 1985.

213. D. Zelterman. *Models for Discrete Data*. Oxford University Press, New York, 2006.

214. U. Kürpick and T. Rahman. Tip Induced Motion of Adatoms on Metal Surfaces. *Physical Review Letters*, 83 (14): 2765–2768, 1999. doi: 10.1103/PhysRevLett.83.2765.

215. J. Li, R. Berndt, and W.-D. Schneider. Tip-Assisted Diffusion on Ag(110) in Scanning Tunneling Microscopy. *Physical Review Letters*, 76 (11): 1888–1891, 1996. doi: 10.1103/PhysRevLett.76.1888.

216. M. Sø rensen, K. Jacobsen, and H. Jónsson. Thermal Diffusion Processes in Metal-Tip-Surface Interactions: Contact Formation and Adatom Mobility. *Physical Review Letters*, 77 (25): 5067–5070, 1996. doi: 10.1103/PhysRevLett.77.5067.

217. L. J. Whitman, J. A. Stroscio, R. A. Dragoset, and R. J. Celotta. Manipulation of adsorbed atoms and creation of new structures on room-temperature surfaces with a scanning tunneling microscope. *Science*, 251 (4998): 1206–10, 1991. doi: 10.1126/science.251.4998.1206.

218. R. J. Hamers and D. F. Padowitz. Methods of Tunneling Spectroscopy with the STM. In *Scanning Probe Microscopy and Spectroscopy: Theory, Techniques, and Applications*, chapter 4. Wiley-VCH, New York, 2001.

219. J. A. Stroscio and R. M. Feenstra. Methods of Tunneling Spectroscopy. In *Scanning tunneling microscopy*, number 1, chapter 4. Academic Press, San Diego, 1993.

220. J. Stroscio, R. M. Feenstra, and A. P. Fein. Electronic Structure of the Si(111)2x1 Surface by Scanning-Tunneling Microscopy. *Physical Review Letters*, 57 (20): 2579–2582, 1986. doi: 10.1103/PhysRevLett.57.2579.

221. R. M. Feenstra, J. A. Stroscio, and A. Fein. Tunneling spectroscopy of the Si(111)2x1 surface. *Surface Science*, 181 (1-2): 295–306, 1987. doi: 10.1016/0039-6028(87)90170-1.

222. B. Koslowski, C. Dietrich, A. Tschetschetkin, and P. Ziemann. Evaluation of scanning tunneling spectroscopy data: Approaching a quantitative determination of the electronic density of states. *Physical Review B*, 75 (3): 035421, 2007. doi: 10.1103/PhysRevB.75.035421.

223. B. Koslowski, H. Pfeifer, and P. Ziemann. Deconvolution of the electronic density of states of tip and sample from scanning tunneling spectroscopy data: Proof of principle. *Physical Review B*, 80: 165419, 2009. doi: 10.1103/PhysRevB.80.165419.

224. M. Ziegler, N. Néel, A. Sperl, J. Kröger, and R. Berndt. Local density of states from constant-current tunneling spectra. *Physical Review B*, 80 (12): 125402, 2009. doi: 10.1103/PhysRevB.80.125402.

225. J. Stroscio, R. M. Feenstra, and A. P. Fein. Imaging electronic surface states in real space on the Si(111) 2x1 surface. *Journal of Vacuum Science & Technology A: Vacuum, Surfaces, and Films*, 5 (4): 838, 1987. doi: 10.1116/1.574321.

226. G. Bussetti, B. Bonanni, S. Cirilli, A. Violante, M. Russo, C. Goletti, P. Chiaradia, O. Pulci, M. Palummo, R. Del Sole, P. Gargiani, M. G. Betti, C. Mariani, R. M. Feenstra, G. Meyer, and K. H. Rieder. Coexistence of Negatively and Positively Buckled Isomers on n{+}-Doped Si(111)-2x1. *Physical Review Letters*, 106 (6): 067601, 2011. doi: 10.1103/PhysRevLett.106.067601.

227. R. M. Feenstra, G. Bussetti, B. Bonanni, A. Violante, C. Goletti, P. Chiaradia, M. G. Betti, and C. Mariani. Charge transfer between isomer domains on n+-doped Si(111)-2x1: energetic stabilization. *Journal of physics. Condensed matter : an Institute of Physics journal*, 24 (35): 354009, 2012. doi: 10.1088/0953-8984/24/35/354009.

228. K. Löser, M. Wenderoth, T. K. a. Spaeth, J. K. Garleff, R. G. Ulbrich, M. Pötter, and M. Rohlfing. Spectroscopy of positively and negatively buckled domains on Si(111)-2x1. *Physical Review B*, 86 (8): 085303, 2012. doi: 10.1103/PhysRevB.86.085303.

229. K. Wang, C. Zhang, M. Loy, and X. Xiao. Time-Dependent Tunneling Spectroscopy for Studying Surface Diffusion Confined in Nanostructures. *Physical Review Letters*, 94 (3): 036103, 2005. doi: 10.1103/PhysRevLett.94.036103.

230. R. Valiev. Materials science: nanomaterial advantage. *Nature*, 419 (6910): 887, 889, 2002. doi: 10.1038/419887a.

231. B. Bhushan, J. N. Israelachvili, and U. Landman. Nanotribology: friction, wear and lubrication at the atomic scale. *Nature*, 374 (6523): 607–616, 1995. doi: 10.1038/374607a0.

232. M. Urbakh, J. Klafter, D. Gourdon, and J. Israelachvili. The nonlinear nature of friction. *Nature*, 430 (6999): 525–8, 2004. doi: 10.1038/nature02750.

233. D. Hull and D. J. Bacon. *Introduction to Dislocations*. Elsevier, New York, 5th edition, 2011. ISBN 9780080966724.

234. M. Doerner and W. Nix. A method for interpreting the data from depth-sensing indentation instruments. *Journal of Materials Research*, 1 (04): 601–609, 1986. doi: 10.1557/JMR.1986.0601.

235. A. Gouldstone, N. Chollacoop, M. Dao, J. Li, A. M. Minor, and Y.-L. Shen. Indentation across size scales and disciplines: Recent developments in experimentation and modeling. *Acta Materialia*, 55 (12): 4015–4039, 2007. doi: 10.1016/j.actamat.2006.08.044.

236. J. F. Waters, P. R. Guduru, M. Jouzi, J. M. Xu, T. Hanlon, and S. Suresh. Shell buckling of individual multiwalled carbon nanotubes using nanoindentation. *Applied Physics Letters*, 87 (10): 103109, 2005. doi: 10.1063/1.2012530.

237. W. Oliver and G. Pharr. An improved technique for determining hardness and elastic modulus using load and displacement sensing indentation experiments. *Journal of Materials Research*, 7 (06): 1564–1583, 1992. doi: 10.1557/JMR.1992.1564.

238. W. Oliver and G. Pharr. Measurement of hardness and elastic modulus by instrumented indentation: Advances in understanding and refinements to methodology. *Journal of Materials Research*, 19 (1): 3–20, 2004. doi: 10.1557/jmr.2004.19.1.3.

239. A. C. Fischer-Cripps. *Nanoindentation*, volume 1 of *Mechanical Engineering Series*. Springer, New York, 2011. ISBN 978-1-4419-9871-2. doi: 10.1007/978-1-4419-9872-9. URL http://www.springerlink.com/index/10.1007/978-1-4419-9872-9.

240. O. Warren, S. Downs, and T. Wyrobek. Challenges and interesting observations associated with feedback-controlled nanoindentation. *Zeitschrift fur Metallkunde*, 95, 2004.

241. N. Agrat, A. Levy Yeyati, and J. M. van Ruitenbeek. Quantum properties of atomic-sized conductors. *Physics Reports*, 377 (2-3): 81–279, 2003. doi: 10.1016/S0370-1573(02)00633-6.

242. T. Kizuka. Atomic configuration and mechanical and electrical properties of stable gold wires of single-atom width. *Physical Review B*, 77 (15): 155401, 2008. doi: 10.1103/PhysRevB.77.155401.

243. J. Kröger, N. Néel, A. Sperl, Y. F. Wang, and R. Berndt. Single-atom contacts with a scanning tunnelling microscope. *New Journal of Physics*, 11 (12): 125006, 2009. doi: 10.1088/1367-2630/11/12/125006.

244. Y. Kurui, Y. Oshima, M. Okamoto, and K. Takayanagi. Conductance quantization and dequantization in gold nanowires due to multiple reflection at the interface. *Physical Review B*, 79 (16): 165414, 2009. doi: 10.1103/PhysRevB.79.165414.

245. Y. Oshima. Study of ballistic gold conductor using ultra-high-vacuum transmission electron microscopy. *Journal of electron microscopy*, 61 (3): 133–44, 2012. doi: 10.1093/jmicro/dfs040.

246. J. I. Pascual, J. Mendez, J. Gomez-Herrero, A. M. Baro, U. Landman, N. Garcia, W. D. Luedtke, E. N. Bogachek, and H. P. Cheng. Properties of metallic nanowires: from conductance quantization to localization. *Science*, 267 (5205): 1793, 1995.

247. C. Kelchner, S. Plimpton, and J. Hamilton. Dislocation nucleation and defect structure during surface indentation. *Physical Review B*, 58 (17): 11085–11088, 1998. doi: 10.1103/PhysRevB.58.11085.

248. A. C. Fischer-Cripps. *Introduction to Contact Mechanics*. Mechanical Engineering Series. Springer, Boston, 2007. ISBN 978-0-387-68187-0. doi: 10.1007/978-0-387-68188-7. URL http://www.springerlink.com/index/10.1007/978-0-387-68188-7.

249. K. L. Johnson. *Contact Mechanics*. Cambridge University Press, New York, 1996.

250. T. Zhu, J. Li, K. J. Van Vliet, S. Ogata, S. Yip, and S. Suresh. Predictive modeling of nanoindentation-induced homogeneous dislocation nucleation in copper. *Journal of the Mechanics and Physics of Solids*, 52 (3): 691–724, 2004. doi: 10.1016/j.jmps.2003.07.006.

251. C. A. Schuh, J. K. Mason, and A. C. Lund. Quantitative insight into dislocation nucleation from high-temperature nanoindentation experiments. *Nat Mater*, 4 (8): 617–621, 2005. doi: 10.1038/nmat1429.

252. A. M. Minor, S. A. S. Asif, Z. Shan, E. A. Stach, E. Cyrankowski, T. J. Wyrobek, and O. L. Warren. A new view of the onset of plasticity during the nanoindentation of aluminium. *Nature materials*, 5 (9): 697–702, 2006. doi: 10.1038/nmat1714.

253. W. Gerberich, S. Venkataraman, H. Huang, S. Harvey, and D. Kohlstedt. The injection of plasticity by millinewton contacts. *Acta Metallurgica et Materialia*, 43 (4): 1569–1576, 1995. doi: 10.1016/0956-7151(94)00351-H.

254. D. E. Kramer, K. B. Yoder, and W. W. Gerberich. Surface constrained plasticity: Oxide rupture and the yield point process. *Philosophical Magazine A*, 81 (8): 2033–2058, 2001. doi: 10.1080/01418610108216651.

255. J. A. Zimmerman, C. L. Kelchner, P. A. Klein, J. C. Hamilton, and S. M. Foiles. Surface Step Effects on Nanoindentation. *Physical Review Letters*, 87 (16): 14–17, 2001. doi: 10.1103/PhysRevLett.87.165507.

256. J. R. Morris, H. Bei, G. M. Pharr, and E. P. George. Size Effects and Stochastic Behavior of Nanoindentation Pop In. *Physical Review Letters*, 106 (16): 165502, 2011. doi: 10.1103/PhysRevLett.106.165502.

257. H. Knoppe and E. Bauer. Ultrathin Au films on W(110): Epitaxial growth and electronic structure. *Physical Review B*, 48 (8): 5621–5629, 1993. doi: 10.1103/PhysRevB.48.5621.

258. L. Vitos, A. Ruban, H. Skriver, and J. Kollár. The surface energy of metals. *Surface Science*, 411 (1-2): 186–202, 1998. doi: 10.1016/S0039-6028(98)00363-X.

259. Y. G. Naidyuk and I. K. Yanson. *Point-Contact Spectroscopy*. Springer, New York, 2005.

260. R. Holm. *Electric contacts : theory and application*. Springer-Verlag, New York, 4th edition, 1967.

261. Y. Hasegawa and P. Avouris. Manipulation of the Reconstruction of the Au(111) Surface with the STM. *Science*, 258 (5089): 1763–5, 1992. doi: 10.1126/science.258.5089.1763.

262. Y. Hasegawa and P. Avouris. Observation of the relaxation processes that follow atom removal from the Au(111) surface with the scanning tunneling microscope. *Journal of Vacuum Science & Technology B: Microelectronics and Nanometer Structures*, 12 (3): 1797, 1994. doi: 10.1116/1.587602.

263. P. Egberts, T. Filleter, and R. Bennewitz. A kelvin probe force microscopy of charged indentation-induced dislocation structures in KBr. *Nanotechnology*, 20 (26): 264005, 2009. doi: 10.1088/0957-4484/20/26/264005.

264. T. Filleter and R. Bennewitz. Nanometre-scale plasticity of Cu(100). *Nanotechnology*, 18 (4): 044004, 2007. doi: 10.1088/0957-4484/18/4/044004.

265. S. N. Dub, Y. Y. Lim, and M. M. Chaudhri. Nanohardness of high purity Cu (111) single crystals: The effect of indenter load and prior plastic sample strain. *Journal of Applied Physics*, 107 (4): 043510, 2010. doi: 10.1063/1.3290970.

266. J. Li, K. J. Van Vliet, T. Zhu, S. Yip, and S. Suresh. Atomistic mechanisms governing elastic limit and incipient plasticity in crystals. *Nature*, 418 (6895): 307–10, 2002. doi: 10.1038/nature00865.

267. P. Tangyunyong, R. Thomas, J. Houston, T. Michalske, R. Crooks, and A. Howard. Nanometer-scale mechanics of gold films. *Physical Review Letters*, 71 (20): 3319–3322, 1993. doi: 10.1103/PhysRevLett.71.3319.

268. B. Bhushan, editor. *Nanotribology and Nanomechanics II*. Springer, New York, 2011. ISBN 978-3-642-15262-7. doi: 10.1007/978-3-642-15263-4. URL http://www.springerlink.com/index/10.1007/3-540-28248-3 http://-www.springerlink.com/index/10.1007/978-3-642-15263-4.

269. G. S. Rohrer. *Structure and Bonding in Crystalline Materials*. Cambridge University Press, New York, 2001.

270. P. Egberts and R. Bennewitz. Atomic-scale nanoindentation: detection and identification of single glide events in three dimensions by force microscopy. *Nanotechnology*, 22 (42): 425703, 2011. doi: 10.1088/0957-4484/22/42/425703.

271. T. Filleter, S. Maier, and R. Bennewitz. Atomic-scale yield and dislocation nucleation in KBr. *Physical Review B*, 73 (15): 155433, 2006. doi: 10.1103/PhysRevB.73.155433.

272. W. Soboyejo. *Mechanical Properties of Engineered Materials*. Marcel Dekker, New York, 2003. ISBN 0824789008.

273. R. Feenstra and M. Lutz. Kinetics of the Si(111)2x1 -> 5x5 and 7x7 transformation studied by scanning tunneling microscopy. *Surface Science*, 243 (1-3): 151–165, 1991. doi: 10.1016/0039-6028(91)90354-U.

274. A. G. Mark. *Domain Boundaries of the 5x5 DAS Reconstruction*. PhD thesis, Queen's University, 2009.

275. C. Shin, Y. N. Osetsky, and R. E. Stoller. Dislocation nucleation and defect formation in copper by stepped spherical indenter. *Philosophical Magazine*, 92 (25-27): 3158–3171, 2012. doi: 10.1080/14786435.2012.682177.

276. W. A. Soer, J. T. M. D. Hosson, A. M. Minor, Z. Shan, S. A. S. Asif, and O. L. Warren. Incipient plasticity in metallic thin films. *Applied Physics Letters*, 90 (18), 2007.

277. V. Navarro, O. R. de la Fuente, A. Mascaraque, and J. M. Rojo. Uncommon Dislocation Processes at the Incipient Plasticity of Stepped Gold Surfaces. *Physical Review Letters*, 100 (10), 2008. doi: 10.1103/PhysRevLett.100.105504.

278. T. Tsuru, Y. Kaji, D. Matsunaka, and Y. Shibutani. Incipient plasticity of twin and stable/unstable grain boundaries during nanoindentation in copper. *Physical Review B*, 82 (2): 1–6, 2010. doi: 10.1103/PhysRevB.82.024101.

279. T. Ala-Nissila, R. Ferrando, and S. C. Ying. Collective and single particle diffusion on surfaces. *Advances in Physics*, 51 (3): 949–1078, 2002. doi: 10.1080/00018730110107902.

280. J. Barth. Transport of adsorbates at metal surfaces: from thermal migration to hot precursors. *Surface Science Reports*, 40 (3-5): 75–149, 2000. doi: 10.1016/S0167-5729(00)00002-9.

281. H. Brune. Thermal dynamics at surfaces. *Annalen der Physik*, 18 (10-11): 675–698, 2009. doi: 10.1002/andp.200910367.

282. G. Kellogg. Field ion microscope studies of single-atom surface diffusion and cluster nucleation on metal surfaces. *Surface Science Reports*, 21 (1-2): 1–88, 1994. doi: 10.1016/0167-5729(94)90007-8.

283. K. Morgenstern. Fast scanning tunnelling microscopy as a tool to understand changes on metal surfaces: from nanostructures to single atoms. *Physica Status Solidi (B)*, 242 (4): 773–796, 2005. doi: 10.1002/pssb.200440002.

284. B. Swartzentruber. Direct Measurement of Surface Diffusion Using Atom-Tracking Scanning Tunneling Microscopy. *Physical Review Letters*, 76 (3): 459–462, 1996. doi: 10.1103/PhysRevLett.76.459.

285. D. W. Pohl and R. Möller. "Tracking" tunneling microscopy. *Review of Scientific Instruments*, 59 (6): 840, 1988. doi: 10.1063/1.1139790.

286. M. Bott, M. Hohage, M. Morgenstern, T. Michely, and G. Comsa. New Approach for Determination of Diffusion Parameters of Adatoms. *Physical Review Letters*, 76 (8): 1304–1307, 1996. doi: 10.1103/PhysRevLett.76.1304.

287. J. Repp, G. Meyer, K.-H. Rieder, and P. Hyldgaard. Site Determination and Thermally Assisted Tunneling in Homogenous Nucleation. *Physical Review Letters*, 91 (20): 206102, 2003. doi: 10.1103/PhysRevLett.91.206102.

288. Q. Liu, K.-D. Wang, and X.-D. Xiao. Surface dynamics studied by time-dependent tunneling current. *Frontiers of Physics in China*, 5 (4): 357–368, 2010. doi: 10.1007/s11467-010-0108-5.

289. G. Binnig, H. Fuchs, and E. Stoll. Surface diffusion of oxygen atoms individually observed by STM. *Surface Science Letters*, 169 (2-3): L295–L300, 1986. doi: 10.1016/0167-2584(86)91230-2.

290. K. Wang, F. Ming, Q. Huang, X. Zhang, and X. Xiao. Study of CO diffusion on stepped Pt(111) surface by scanning tunneling microscopy. *Surface Science*, 604 (3-4): 322–326, 2010. doi: 10.1016/j.susc.2009.11.024.

291. H. J. Lee and W. Ho. Single-Bond Formation and Characterization with a Scanning Tunneling Microscope. *Science*, 286 (5445): 1719–1722, 1999. doi: 10.1126/science.286.5445.1719.

292. B. C. Stipe, M. A. Rezaei, and W. Ho. Single-Molecule Vibrational Spectroscopy and Microscopy. *Science*, 280 (5370): 1732–1735, 1998. doi: 10.1126/science.280.5370.1732.

293. F. Mohn, L. Gross, N. Moll, and G. Meyer. Imaging the charge distribution within a single molecule. *Nature nanotechnology*, 7 (4): 227–31, 2012. doi: 10.1038/nnano.2012.20.

294. S. Sadewasser and T. Glatzel, editors. *Kelvin Probe Force Microscopy*. Springer, New York, 2012.

295. D. Ziegler and A. Stemmer. Force gradient sensitive detection in lift-mode Kelvin probe force microscopy. *Nanotechnology*, 22 (7): 075501, 2011. doi: 10.1088/0957-4484/22/7/075501.

296. H. Lüth. *Solid Surfaces, Interfaces and Thin Films*. Graduate Texts in Physics. Springer Berlin Heidelberg, Berlin, Heidelberg, 2010. ISBN 978-3-642-13591-0. doi: 10.1007/978-3-642-13592-7. URL http://www.springerlink.com/index/-10.1007/978-3-642-13592-7.

297. J. Villain, J. L. Rouviere, and I. Vilfan. Phenomenology of Surface Reconstruction. In *Phase Transitions in Surface Films 2*, chapter 12. Springer US, New York, 1991. doi: 10.1007/978-1-4684-5970-8_12.

Appendix A: Surface diffusion

Surface diffusion

Several reviews on the diffusion of single atoms and clusters on crystal surfaces contain good introductions to the thermally activated transport of adatoms [54, 279-282]. We begin by briefly reviewing the relationship between activation energies, diffusion rates, and mean-square displacements of diffusing material.

The 'intrinsic' or 'tracer' diffusion coefficient, D, describes the rate of diffusion of an individual atom on a semi-infinite crystal surface. The unit of D is area per time, and its relation to the mean-square displacement of the adatom is given by

$$2m\tau D = \langle |\vec{r}(\tau) - \vec{r}(0)|^2 \rangle \,, \tag{68}$$

where $\vec{r}$ is the vector position of the atom, τ is the elapsed time, and m is the dimensionality of the diffusion. For a particle diffusing in two dimensions over a crystal surface, $m = 2$. If a diffusing particle is confined to displace along a one-dimensional lattice, such as along the rows of a W(211) plane, $m = 1$. $\vec{r}(0)$ can be defined as the origin, so the mean-square displacement from the origin during the time interval τ is expressed as

$$\langle r^2 \rangle = 2m\tau D \,. \tag{69}$$

A particle executing a random walk of N jumps of distance l has a mean-square displacement given by

$$\langle r^2 \rangle = Nl^2 \,. \tag{70}$$

If thermal activation is the mechanism by which the jumps are instigated, the frequency of the jumps can be expressed as

$$\nu = \frac{N}{\tau} = \nu_0 \exp\left(-\frac{\Delta G}{k_B T}\right), \tag{71}$$

where ΔG is the difference in Gibbs free energy between the equilibrium site and the saddle point in the diffusing atom's energy landscape. The Gibbs free energy is the sum of the activation energy for surface diffusion E_d and the entropy term $-T\Delta S$. In most cases, the entropy difference between the saddle point and the minimum energy configuration is negligible. Combining Eqs. (71), (70), and (69) and defining $D = D_0 \exp(-E_d/k_B T)$, we obtain:

$$\langle r^2 \rangle = \nu_0 \tau l^2 \exp\left(-\frac{E_d}{k_B T}\right) = 2m\tau D_0 \exp\left(-\frac{E_d}{k_B T}\right). \tag{72}$$

The diffusion prefactor, D_0, is thus determined by the attempt frequency, ν_0, jump length, l, and dimensionality, m:

$$D_0 = \frac{\nu_0 l^2}{2m}. \tag{73}$$

The attempt frequency should be of the same order as the frequency of atomic vibrations $\sim 10^{12}$ Hz. The jump length, determined by the spacing of binding sites, is about ~3 Å on crystal surfaces. This yields a value of D_0 of $\sim 10^{-3}$ cm^{2}s^{-1}, which is always measured within an order of magnitude in single atom diffusion experiments [282]. This additionally indicates that the ΔS term in the Gibbs free energy can be neglected.

Real-space observations of adatoms diffusing on crystal surfaces can be made by FIM or STM [54], and from these observations, one can obtain the mean-square displacement per unit time:

$$\frac{\langle r^2 \rangle}{2m\tau} = D_0 \exp\left(-\frac{E_d}{k_B T}\right). \tag{74}$$

If the temperature can be varied, an Arrhenius analysis of the data can be performed to determine both D_0 and E_d.

Due to the relatively constant value of $D_0 \approx 10^{-3}$ cm^{2}s^{-1}, it is even reasonable to estimate the activation energy using data obtained at one temperature and assume this value for D_0. Re-writing the activation energy for diffusion as

$$E_d = -k_B T \ln\left(\frac{\langle r^2 \rangle}{4D_0\tau}\right) = -k_B T(\ln\langle r^2 \rangle - \ln(4D_0\tau)), \tag{75}$$

and noting that for most experiments $\langle r^2 \rangle \approx 10^{-16}$ cm^{2}s^{-1}, and $4D_0\tau \approx 10^{-3}$ cm^{2}s^{-1}, an error of one order of magnitude in D_0 or τ will only affect the determination of E_d by ~10% or less. This relative insensitivity has prompted many researchers to determine E_d to ~10% based solely on the onset temperature of adatom motion [282].

Measuring surface diffusion with FIM and STM

Diffusion of atoms on crystal surfaces is one of the most fundamental processes relevant to thin film growth in molecular beam epitaxy, crystal growth, oxidation, and heterogeneous catalysis [283]. The development of the FIM permitted individually adsorbed and diffusing atoms to be studied by direct real-space imaging, and from this technique comes much of our understanding of these dynamic surface processes [54, 282].

In FIM, the diffusion of adatoms is allowed to occur during a time interval during which the imaging field is turned off and the tip is momentarily heated to promote the thermal activation of diffusion. The tip is then returned to its base temperature of ~20 K so that the

structural state of the surface is frozen during imaging. This thermal cycling technique is a convenient way to avoiding artifacts caused by the strong imaging field and to access a wide variety of temperatures (the tip is mounted to a heating filament for direct heating).

The STM can be used to monitor the position of individual atoms on surfaces in a similar manner by repeatedly imaging the surface, however the rate of diffusion of the adatom must be appropriate to the scanning speed (on the order of tens of seconds to several minutes per frame). A notable advantage of the STM is that adatoms can be observed on softer metals for which FIM would not be possible.

Several groups have used the STM in ways other than repeated surface imaging to gain insight into diffusion processes: Swartzentruber implemented an atom tracking method to follow the path of diffusing Si adatoms on a Si(100) surface [284] in which the tip carries out a 5 Å circular motion at 10 kHz and feedback is used to track local changes in the adatom location, similar to a technique first introduced by Pohl and Möller [285].

Observation of adatom islands can also be used to determine activation energies and prefactors. Bott *et al*. could not obtain reasonable values for E_d for Pt on Pt(111) by scanning due to the influence of tip, so the authors developed a method to obtain diffusion parameters from the object density of sub-monolayer Pt depositions at various temperatures [286]. At T < 110 K, the object density was constant due to the lack of adatom diffusion; for T > 110K, the object density decreased due to adatom mobility. A simple Monte Carlo model with only two free parameters (E_d and D_0) was used to fit the object density vs. temperature data.

The study of metastable adsorption sites, like hcp stacking fault sites on an fcc crystal, is quite difficult because of the dissimilar energetic barriers for transition to and from these sites. At a temperature appropriate to promote thermally activated access to the sites, the rate of decay out of the metastable state will be too fast to study. Repp *et al*. circumvented this problem by using atomic manipulation to artificially occupy non-equilibrium surface sites to estimate energetic barriers between hcp and fcc sites on Cu(111) at low temperature [287]. The authors also studied the transition between thermally activated dimer motion to thermally assisted tunneling on the Cu(111) surface, noted by the departure from Arrhenius behaviour as the sample temperature was decreased.

Information about dynamic processes occurring on surfaces can also be extracted from time variations of the tunneling current between the STM tip and sample. A good review of experiments related to this technique was recently written by Liu *et al* [288]. Binnig *et al*.

first reported the possibility of measuring diffusion in such a fashion by measuring the width of tunneling current peaks during the diffusion of O on Ni beneath the STM tip [289]. By monitoring time variations of the tunneling current rather than performing sequential imaging, much faster diffusion rates can be captured than with imaging – it is possible to measure fluctuations in the tunneling current up to ~100 kHz (if the currents are reasonably large). Wang *et al*. extracted the residency time of Cu and Ag adatoms under a STM tip at several temperatures; the adatoms were trapped to diffuse within the half-unit-cells of the Si(111)-7×7 surface [229]. In this study, the 7×7 surface reconstruction provided a large confinement potential which was necessary to keep the adatom returning to the sites of interest in order to gather reasonable statistics. In the case of a large adatom density, when the waiting time between hopping events is not an issue, one can remove the confinement and study diffusion on open atomic terraces or step edges, as done in a study of CO molecules dosed on a Pt(111) surface [290].

In STM studies, it is important to verify that the tip-surface interaction is sufficiently weak so that the measured data reflects the intrinsic phenomena being studied, unmodified by the presence of the tip. This can be accomplished by varying tip-substrate distance and imaging bias voltage and checking for the independence of the obtained results.

Appendix B: 'High-bias' indentation effects

The effect of sample bias during indentation was first noticed when a slightly higher bias was mistakenly left applied to the sample after imaging and maintained throughout a subsequent indentation array. 5×5 indentation arrays to open-loop depths of 3.0 nm and 3.5 nm were carried out at sample biases of −0.05 V and −0.11 V, and the residual impressions of the two indentation sets are shown in Figure B1. The impressions in Figure B1(b) are remarkably larger than those in (a) considering the rather small increase in indentation depth setpoint.

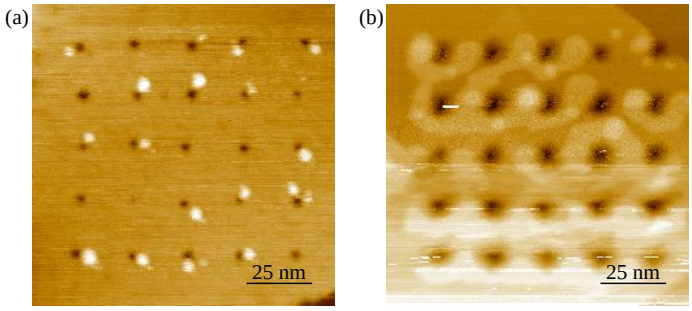

Figure B1: (a) Indentations to 3.0 nm setpoint at −0.05 V sample bias. (b) Indentations to 3.5 nm setpoint at −0.11 V sample bias. (Feb 17, 2012)

A representative indentation curve is shown in Figure B2 from each of these cases. The curve shown in Figure B2(a) is indicative of the plastic behaviour we normally measure at low bias – several pop-ins indicative of plasticity, and a section of overlapping elastic loading/unloading. In (b), an entirely different type of loading happens, where several giant pop-ins are seen at loads above 150 nN, the cantilever beam gets excited (light blue shows an unfiltered data curve), and deformation seems to continue in bursts until the contact is unloaded.

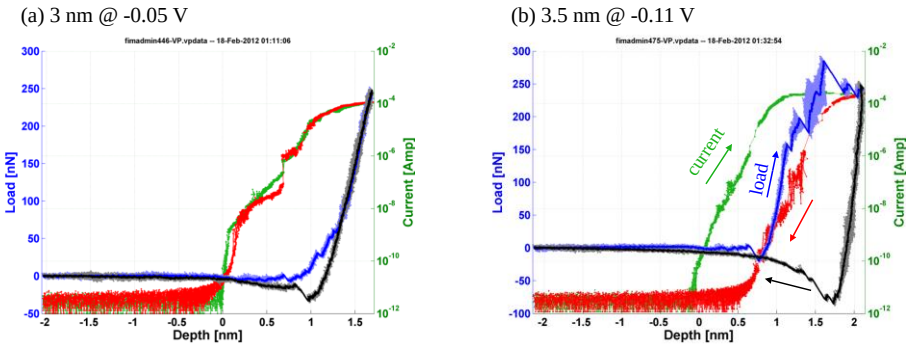

Figure B2: Examples of indentation curves from the arrays shown in Figure B1.

Also remarkable is the current-displacement curve which shows the first evidence we have seen of contact separation within the hole: The red curve is the current in the 'out' direction which returns to the baseline at a greater depth than the loading curve. A substantial attractive force (van der Waals and/or electrostatic) is still measured after electrical separation of the contact.

We must consider spurious mechanical excitation of the beam as a cause of the indentation – perhaps due to the increased penetration depth, the cantilever beam resonance frequency increased to a much higher value and ended up coupling to some mechanical noise[1]. In order to investigate this possibility, we plot a power spectral density evolution for two indentation curves in Figure B3; (a) shows the low-bias case, and (b) shows the high-bias case. The power spectra are shown as a mirror image about the Nyquist frequency – they were unfolded because the sample rate was insufficient to track the resonance of the cantilever beam throughout the indentation (see figure caption for details).

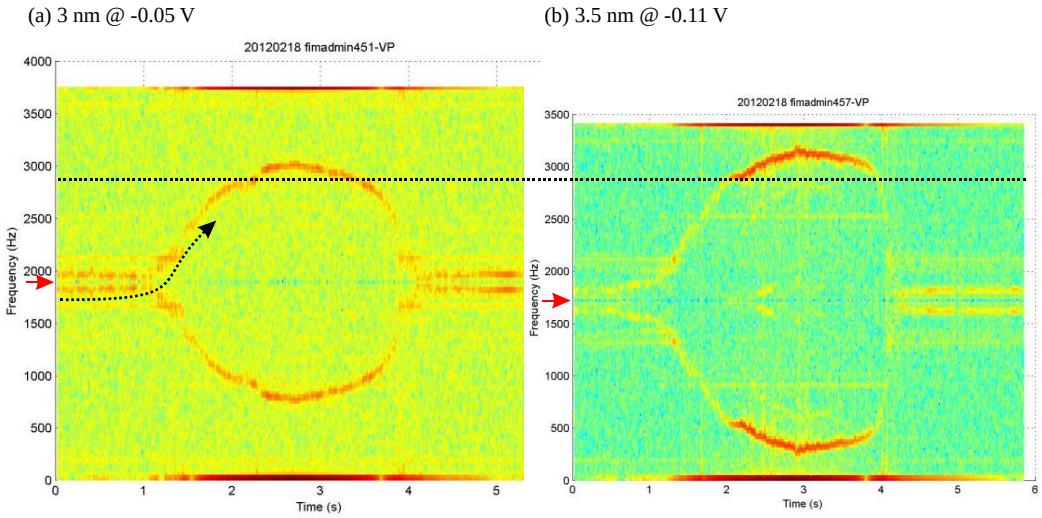

Figure B3: Cantilever frequency shift under (a) low-bias indentation and (b) 'high-bias' indentation. The sample rates for these data sets were 3570 Hz and 3409 Hz respectively, so the frequency shift of the beam goes above the Nyquist frequency, $f_s/2$, and is actually aliased. We have unfolded the power spectra at the Nyquist frequency (red arrow on the frequency axis) to be able to more easily see the resonance frequency change with proper units on the axis. The dotted black arrow shows that in (a), the resonance starts out below $f_s/2$ and crosses it. In (b), the resonance is always above $f_s/2$. The frequency at which the giant plasticity is initiated in the high bias indentation (b) is indicated across both graphs by a dotted line.

[1] This data was taken previous to substantial efforts to reduce these spurious excitations (section 3.4.1, page 102).

The frequency at which the high bias indentation becomes excited is indicated by the dotted line extending through both plots. It is apparent that there is no correlation with spurious excitations at this frequency in the low-bias indentation – we therefore expect that the effect of giant plasticity is due to the bias voltage rather than cantilever excitation.

To further test this hypothesis, we performed a 5×5 array of indentations in which the bias voltage was changed for each row. The indentation array shown in Figure B4 was carried out with the bias voltages indicated in the figure. The largest bias of -0.15V contributed to much larger plastic damage than the lower biases.

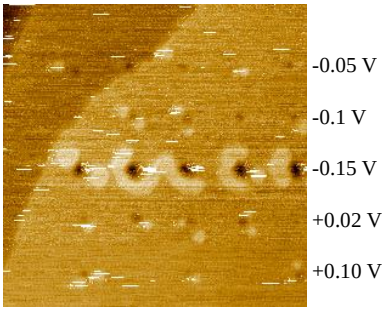

Figure B4: Indentations to 3 nm open-loop setpoint. (Feb 25, 2012)

From the results of this study we decided to carry out indentation at a sample bias of -0.05 V to be reasonably far from the regime at which substantial junction heating is likely to play a role.

At these bias voltages, -0.15 V being the largest investigated, the tungsten tip returns undamaged to FIM (with the exception of adsorbed adatoms) after the indentation experiments. Upon accidental indentation at larger bias voltages close to 1 V magnitude (which we were using to stabilize the tunneling junction in section 6.4, page 214), the tip is completely obliterated and no longer possible to image in FIM. It is important to realize when reading literature about bias voltage pulsing or indentation in STM that the impedance of the current preamplifier plays a significant role in the damage that ensues at the tip-sample junction. In the case of our logarithmic preamplifier, the virtual ground is of low impedance for nearly all relative currents, so the voltage drop really does occur at the tip-sample junction. In the case of a linear preamplifier, the opamp's output saturation at a power supply rail will effectively limit the voltage drop at the tip-sample junction as we discussed in a footnote in section 4.1.5, page 127.

A full elucidation of bias voltage effects on indentation is left to future investigations.

Appendix C: Piezo motor relay

The piezo motor relay was implemented to connect on the piezo motor high voltage amplifiers only when needed. It was found that leaving the amplifers connected added a 1-1.5 Å RMS vibration to the Z motor piezos in the 2-5kHz bandwidth. Subsequent measurements described in section 3.4 (page 102) showed that in fact *all* of the piezo motors should be grounded at the STM chamber.

The solution that is implemented involves a bank of relays (Figure 3.23, page 106) which can be enabled (closed circuit) by an enable pushbutton switch (ENABLE) for coarse movement of the tip/sample by remote control. The ENABLE switch should be turned off for coarse approach. The SPM control software (previously Scanita, and as of August 2011 GXSM) provides a single pulse to trigger a step. This pulse must also momentarily enable the relay connections, even if the ENABLE switch is off.

Implementation

There are two main sections of implementation: The first section involves the logic governing the pushbutton switch and the single trigger. The second section involves the control over the relay when a single trigger pulse is sent.

Pushbutton enable and single trigger override

The logic truth table that describes the ENABLE pushbutton and SINGLE logic pulse is shown below

ENABLE	SINGLE	OUTPUT
1	1	1
1	0	1
0	1	1
0	0	0

Note that sometimes the terminology appears as BYPASS rather than ENABLE ($BYPASS = \overline{ENABLE}$). In that case the truth table is

BYPASS	SINGLE	OUTPUT
0	1	1
0	0	1
1	1	1
1	0	0

This truth table corresponds to *logical implication*: $BYPASS \rightarrow SINGLE$

The logic gate implementation of $BYPASS \rightarrow SINGLE$ is:

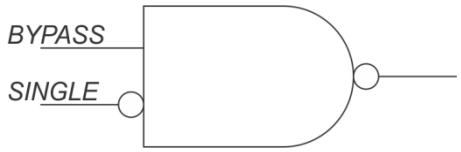

Timing circuit: pulse in, relay out, pulse out

Upon receiving a pulse, the relay must be engaged so that the Z piezo is connected to the high voltage transformer. We must ensure that the relay is fully engaged before sending the high voltage step - this takes typically 7 ms (12 ms max) for the Tyco RT314012F relay. The timing circuit should therefore do the following things:

i. Receive the CONTROL signal (PULSE IN) - this was measured to be about 1.5 ms width (can be longer as step generator sends only one step when triggered)
ii. Engage the relay with the RELAY signal and keep it engaged for sufficient time to send the high voltage step
iii. Wait for 15 ms, then send the PULSE OUT signal to the step generator.
iv. Disengage the relay.

The desired signal sequence is shown below:

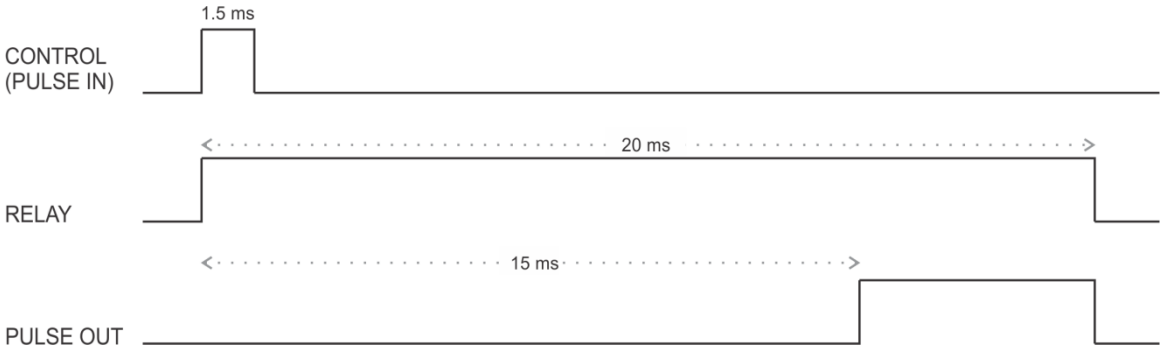

The pulse delays can be implemented with some one-shot timers and a few logic components to generate some intermediate signals.

The one-shot timer based on the LM555 (detailed later) generates an output high on the downward slope of a pulse, and keeps the output high for a pre-determined amount of time. The only catch is that the input signal must be kept high for the duration of the one shot. This brings us to the first intermediate signal, which is $\overline{CONTROL}$.

The $\overline{CONTROL}$ signal is used to trigger the two one-shot timers, one generates the RELAY signal, the other generates the DELAY signal. The DELAY signal is another intermediate signal. Combining RELAY and DELAY with some logic, we can generate the desired PULSE OUT. The complete signal timing diagram is shown below:

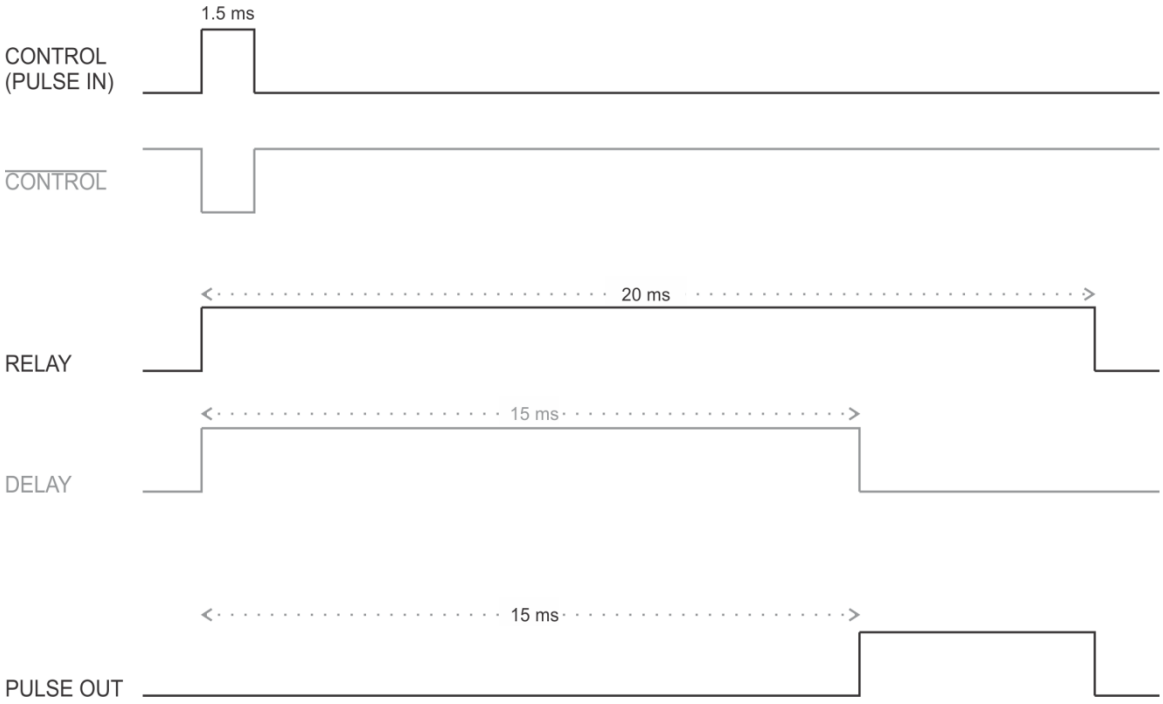

The logic truth table that combines RELAY and DELAY into PULSE OUT is:

REL	DEL	OUT
0	0	0
1	0	1
0	1	n/a
1	1	0

The combination of the BYPASS logic and the PULSE timing logic is shown below. Note that the double inverter before the PULSE OUT exists as a current buffer since the AND chip cannot source much current.

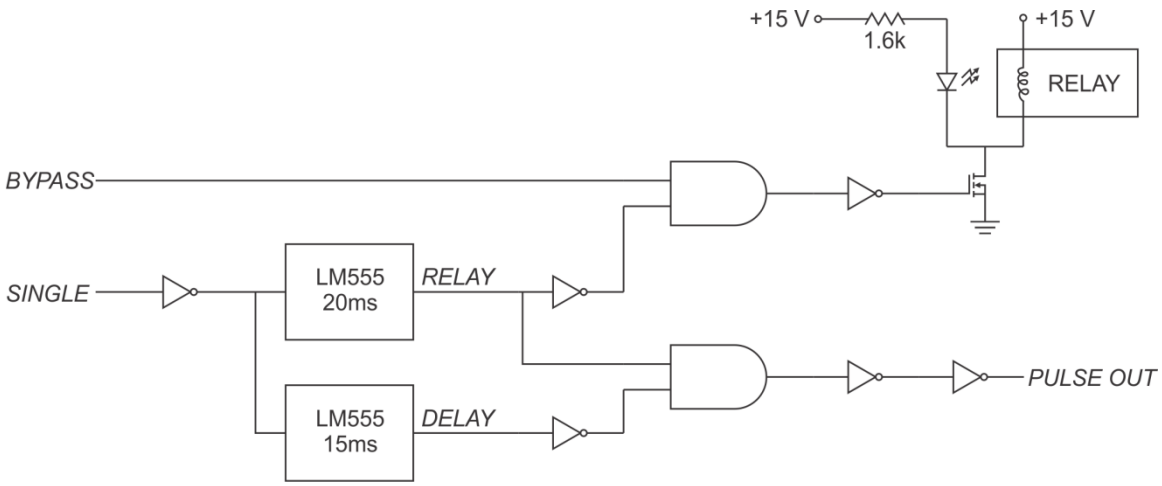

The circuit was added to the existing Z motor amplifier proto-board as shown below:

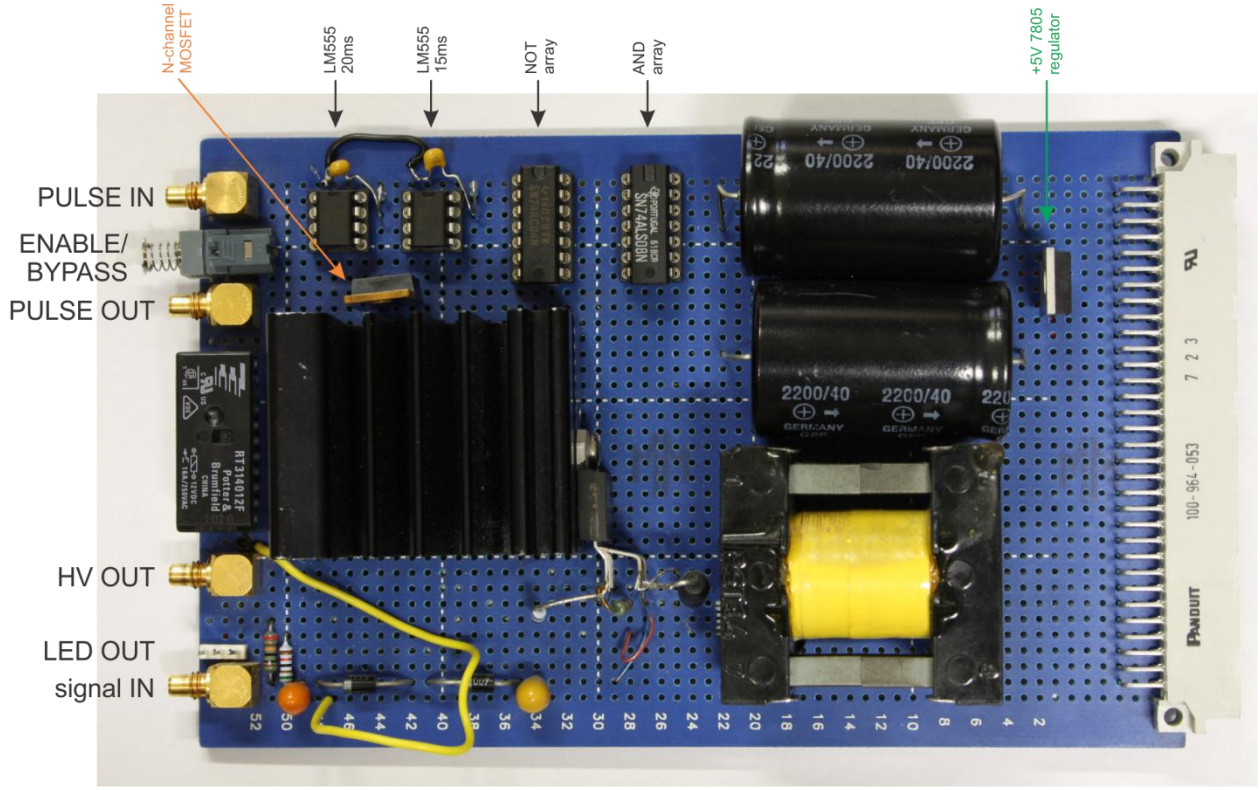

The back of this board looks like:

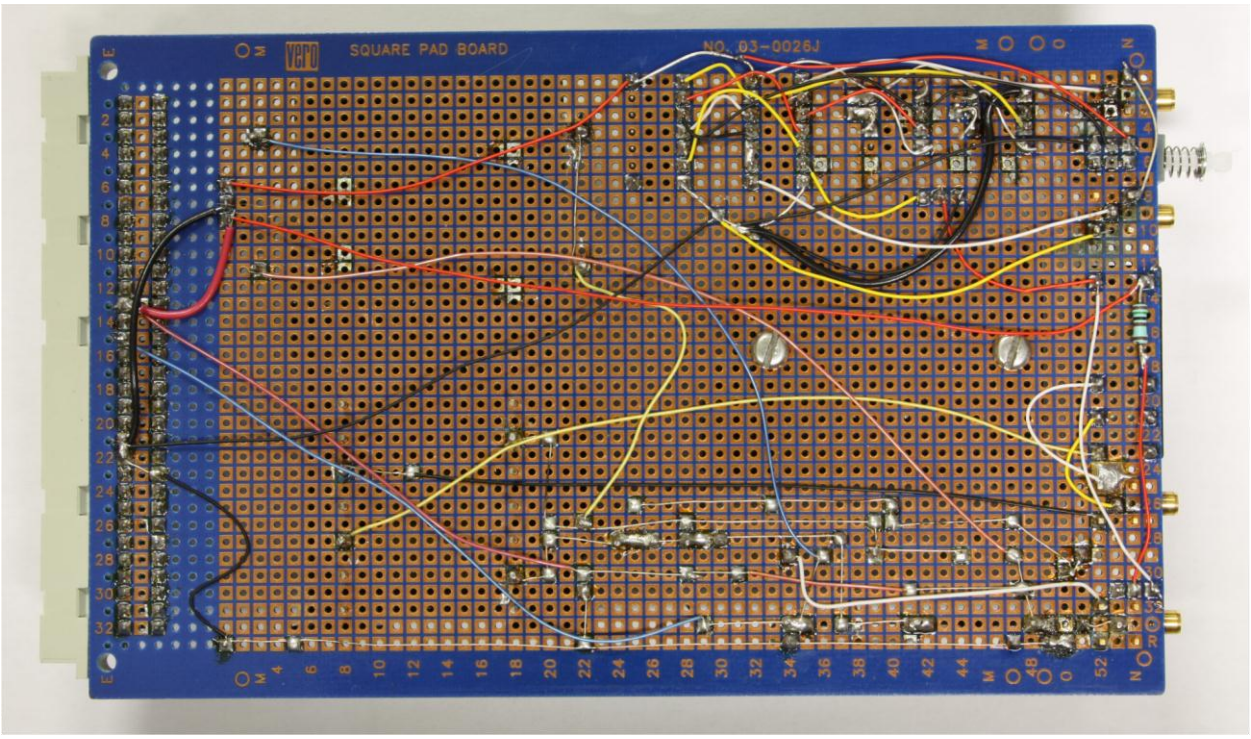

The inputs/outputs look like this on the rack:

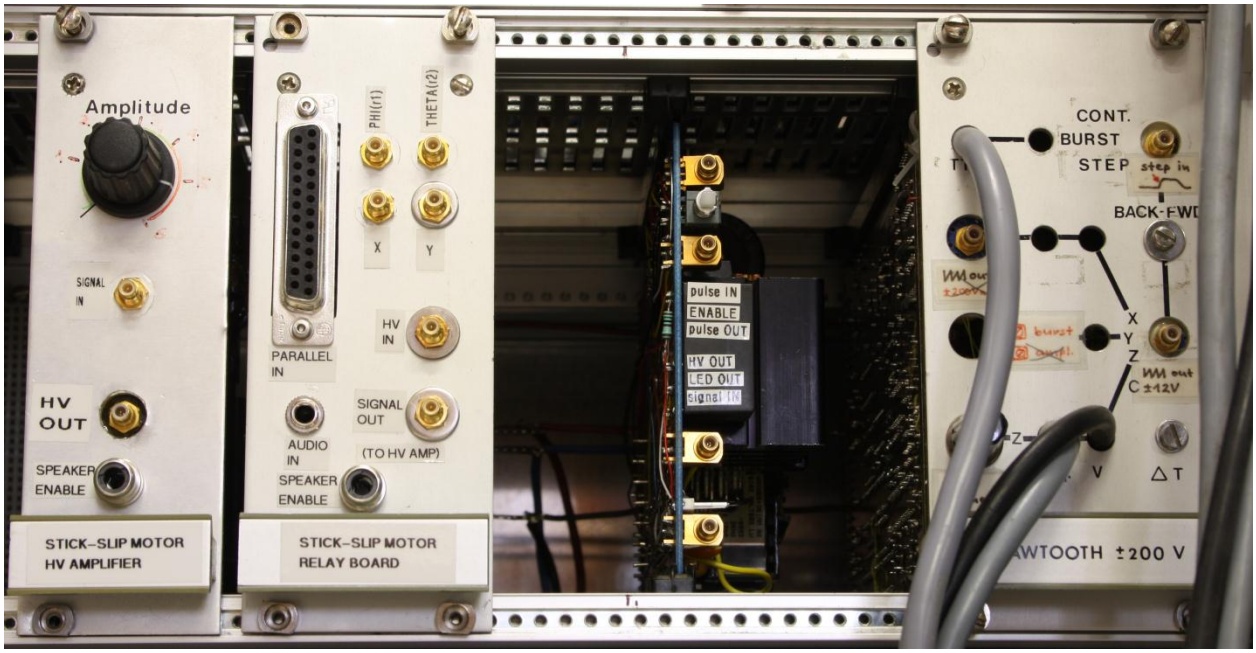

Instructions

Make sure the following connections are made:

1. "pulse IN" comes from controller digital output
2. "pulse OUT" goes to sawtooth generator "step in" (the card shown to the right of this board in the figure above)
3. "HV OUT" to Zg piezo connection
4. "LED OUT" to remote LED
5. "signal IN" from sawtooth generator output "$\pm$12V"

While coarse positioning the tip/sample with the remote, press the "ENABLE" button - the LED lights will warn the user that the HV is connected to the piezo motor.

When using automated coarse approach from the SPM control software, switch off the "ENABLE" button - the LED light should be off. Upon receiving the controller's pulse, the LED will flash for the duration of the relay closure (about 20ms), and the pulse will be sent to the piezo motor while the circuit is closed by the relay.

LM555 one shot timers

The LM555 based one-shot, also known as the monostable configuration, is based on the following circuit (taken from the data sheet):

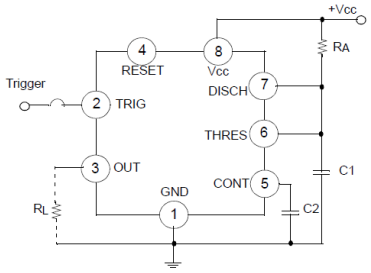

Resistor R_A and capacitor C_1 determine the time of the one shot given by $T = 1.1R_AC_1$. With $C_1 = 0.1\mu F$, this makes R_A = 180 kΩ (20ms) and 130 kΩ (15ms). C_2 can be left out, letting pin 5 float. Note that pin 4 should be tied to V_{CC} for operation (it seems to be a $\overline{RESET}$).

Although this circuit would be easier to implement with OR gates, a NOT array chip and an AND array chip were found in the lab supplies. The chips that were used are the SN74AC04N (NOT) and SN74ALS08N (AND):

SN54AC04 . . . J OR W PACKAGE
SN74AC04 . . . D, DB, N, NS, OR PW PACKAGE
(TOP VIEW)

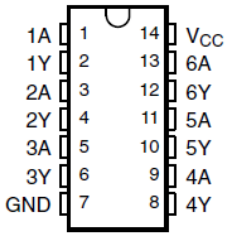

SN54ALS08, SN54AS08 . . . J PACKAGE
SN74ALS08, SN74AS08 . . . D OR N PACKAGE
(TOP VIEW)

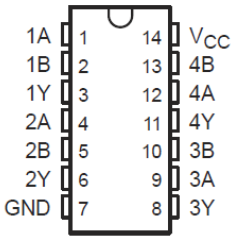

Appendix D: Antialiasing filter design

Data acquisition hardware is a common and valuable part of most physics laboratories. Programming these devices to perform measurement control and acquisition tasks is easy with common software packages like LabView or MATLAB. For many measurements, the maximum bandwidth of the acquisition device far exceeds the necessary measurement bandwidth. Unfortunately, when the user requests a lower sampling rate from the card, frequency components above the Nyquist frequency are aliased into the measured bandwidth. This is because built-in antialiasing filters have a fixed cutoff frequency of half of the maximum sample rate, so lower sample rates are not properly antialiased. This motivates the need for an analog antialiasing filter with a variable cutoff frequency which can be changed as appropriate to the measurement being performed.

We propose a very flexible circuit design which can be easily be configured for various needs (AC/DC coupling, single ended or differential input, large input gain, to name a few). Care has been taken to ensure that the circuit is robust with features such as input over-voltage protection. Because of its built-in voltage regulators and adequate capacitive bypassing of power supply ripple, it can be operated without excess noise from inexpensive switching power supplies.

Circuit description

The core sections of the circuit are the power supply, instrumentation amplifier input, pre-gain stage, filter stage, and output buffer amplifiers. These are described in order below:

I. Power supply: The power supply outputs ±12 V and ±5 V regulated power rails provided by small SMD regulators (7812, 7912, 7805, and 7905). The ± 5 V rails are particularly useful for implementing some of the modern filter chips available which only work on lower voltages. The ±12 V rails can be used to power input/output instrumentation/buffer amplifiers. The bypass capacitor values are shown in the schematic in Figure D1.

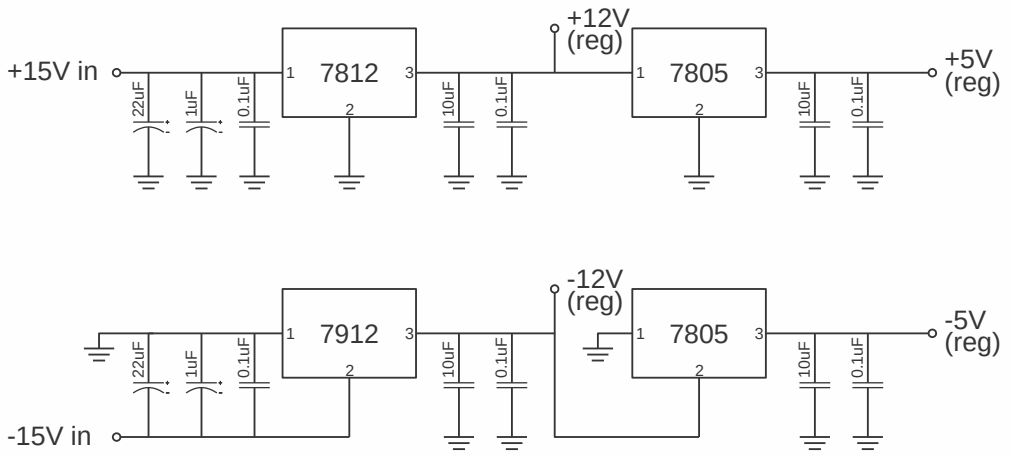

Figure D1: Regulated power supplies and capacitive bypass for antialiasing filter circuits.

II. Instrumentation amplifier input: The INA128 is used as an input instrumentation amplifier, shown in Figure D2. Several resistor pads are available to modify the input impedance of the circuit, to configure single-ended or differential inputs, or to adjust the overvoltage protection (see INA128 data sheet). AC coupling could be achieved by replacing a capacitor in series before the +in input, and adjusting R_{i+} to the desired rolloff frequency. The gain resistor between pins 1 and 8, R_G, sets the input gain as per the equation $G = 1 + 50\text{k}\Omega/R_G$. A gain of 1 is achieved by leaving this resistor out.

III. Pre-gain stage: This stage consists of ¼ of a TL074 which can be configured to voltage divide the input signal to a level appropriate for the filter chip implemented. This is necessary for the ±5 V chips, and we typically choose to divide by 2.5 to maintain a linear range throughout ±10 V (if we were to divide by 2, we would be sensitive to the near-rail nonlinearities of the LTC1564, for example).

IV. Filter stage: This stage contains the low-pass filter. We have made circuit boards for the Linear Technology LTC1564 for which the cutoff frequency can be set between 10 kHz and 150 kHz using logic control signals, or jumper pins which we have put on the circuit board. The Linear Technology LTC1563 is another convenient choice – it is a 4th order filter chip, available in Bessel or Butterworth configurations. Its cutoff frequency can be set between 256 Hz and 256 kHz by setting the value of external resistors at the time of assembly. We illustrate only the LTC1564 here; the LTC1563 has an identical design except for the filter chips.

V. Buffer amplifiers: This stage consists of the other three quarters of the TL074 amplifier. One amplifier is used to provide an unfiltered copy the input signal, useful to

avoid noise coupling between devices if one desires to monitor the input signal. The other two amplifiers provide independently buffered outputs of the filtered signal (to avoid noise/crosstalk from connected devices) – only one is shown on the schematic in Figure D2 (see note).

We note that the TL074's voltage noise is low enough for most of our purposes, but in cases where the desired sampling filter frequency is very low, be sure to roll off the RC bandwidth of the buffer amplifiers appropriately to avoid aliasing an excess bandwidth of opamp voltage noise.

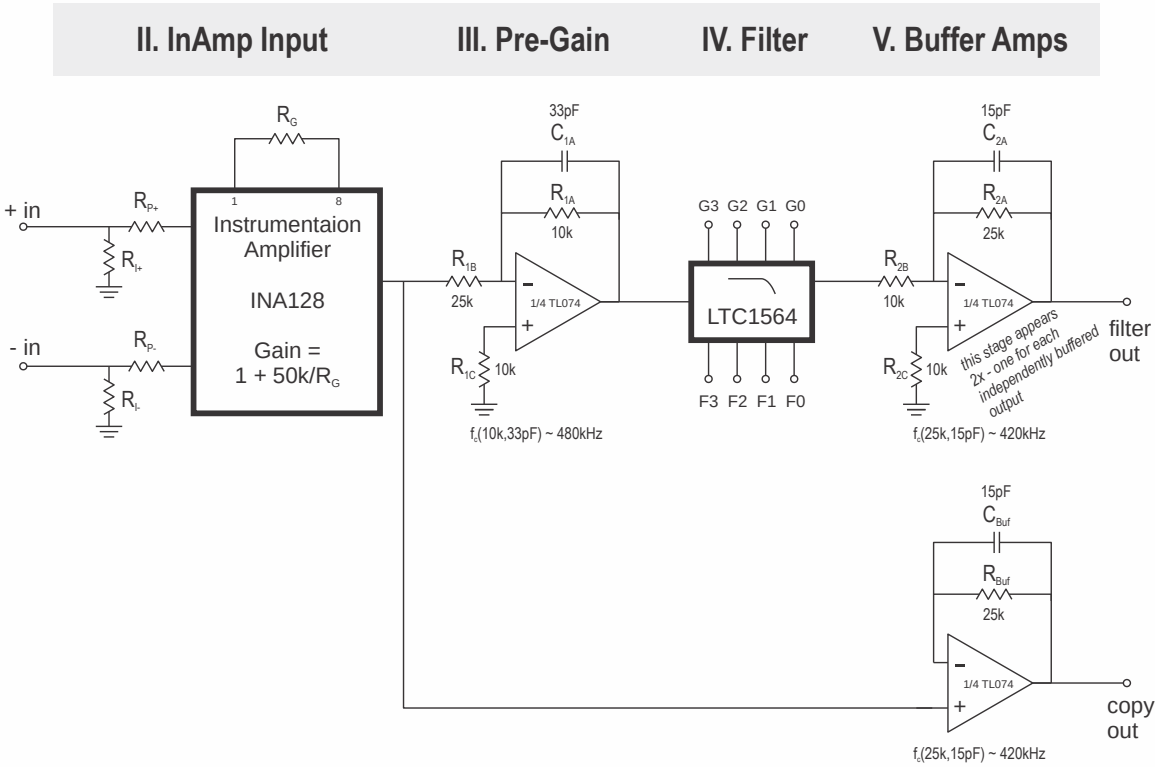

Figure D2: Circuit diagram of the signal paths for antialiasing filters.

Board assembly

Referring to Figure D3, we offer the following notes about board assembly:

Power supply

The power supply terminal blocks are connected to each other for easy daisy chaining of boards within one enclosure. Terminal blocks: 1x 277-1727-ND (10 pos) can be separated into 2x 3 pos and 2x 2 pos sections for the power and signal connections.

Digikey part numbers for regulators: MC7805BDTGOS-ND, MC7812BDTRKGOSCT-ND, MC79M12CDTRKGOSCT-ND, MC79M05CDTRKGOSCT-ND.

Install through-hole power supply bypass caps (22, 1, 0.1 µF) near the top of the board in the polarities indicated (where applicable).

Install 10uF SMD caps in the positions around the regulators. Use 0.1uF caps around all ICs. All SMD components are 0805 size.

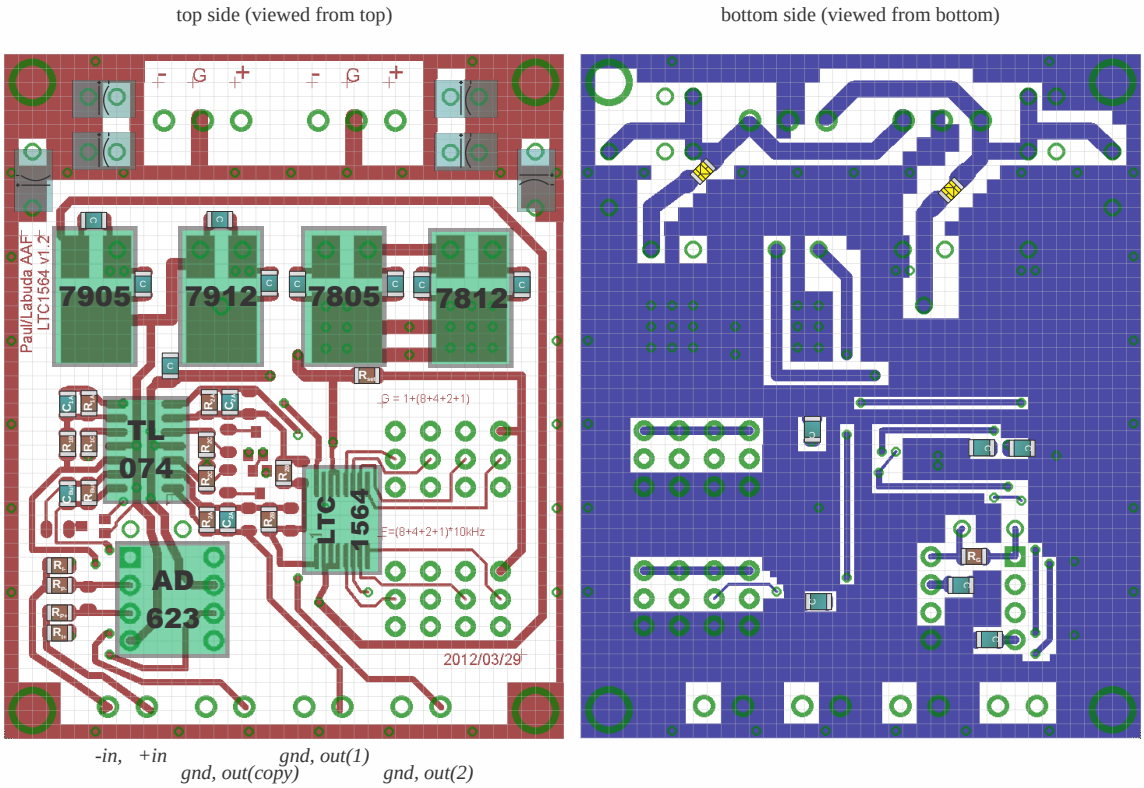

Figure D3: Component placement on printed circuit board. See text for full description of assembly.

Instrumentation amplifier input

Use an IC socket for the 8 pin DIP InAmp (INA128 or equivalent)

The gain resistor R is located on the BOTTOM side of the board (not shown). If none is installed (default configuration), the gain will be 1.

Input impedance of AA filter is set by R_i resistors (impedance of inamp inputs is 2 GΩ). The R_{i-} could be replaced by a jumper to ground for single ended input.

Buffer amplifiers (and pre-gain)

Use TL074 or similar (might want lower voltage noise in some applications)

See Figure D2 for suggested values.

Filter block (LTC1564)

Install columns of jumper pins: A31113-ND.

2 pos jumper A31697-ND can be used to set frequency or gain (logic 1 = connect upper 2 jumper pins, logic 0 = connect lower 2 pins). A 3 pos connector S7001-ND can be used to bring these pins to a front panel switch.

The upper 4 pin columns correspond to G3, G2, G1, G0; the lower 4 columns correspond to F3, F2, F1, F0. Upper jumper position = TRUE. Lower jumper position = FALSE.

Enclosures and power connectors

An appropriate enclosure in which to mount 2 filter boards side-by-side is HM366-N, available from Digikey.

We had previously used Fisher 3-pin connectors for power supplies, but these are hard to find and very expensive, so a new lab convention was developed based on S-Video style connectors – the miniDIN 6-pin connector. When **looking at the exterior** of a connector mounted on a box, pins 1&2 are GND, pins 3&5 are V+, pins 4&6 are V-.

Useful part #s: CP-2860 (female connector), AE9876 (cable)

We suggest mounting such connectors on any piece of equipment so that multiple units can be daisy-chained together easy power distribution.

Appendix E: X-Y/Φ-Θ piezo motor signal generator

Introduction

A new stick-slip motor driver was built using Matlab and a PC sound card as a signal generator. The motor driver was designed to control 4 axes of motion: X, Y, Φ, Θ. This was accomplished by using relays to connect the amplified high voltage sawtooth wave to the appropriate piezo stacks in the system. The relays are controlled by the logic state of parallel port pins.

Why was the old controller replaced? The signal generation boards would latch up: status lights on the remote would stay on, and signals would be generated and sent to the system. This could be resolved on occasion by turning off the signal generation power supply and restarting it several minutes later. Eventually, it could not be restarted in such a manner, and latched up so badly that the signals drove the sphere and X glider plate off their tracks. It also made sample preparation attempts useless because the sample could not be moved under the tip. It was decided on the afternoon of Friday Sept 17 2010 (Shawn Fostner's defence day) that this system had to be replaced, and preliminary tests started on using a PC sound card for signal generation were shown to be successful.

Design requirements (aka what the old controller did when it worked)

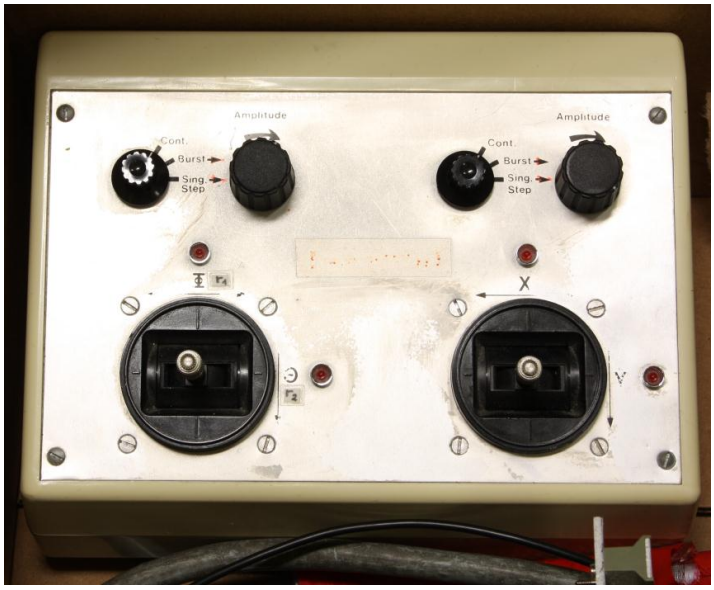

Modes of operation

The old controller worked in three modes:

1. Single Step
2. Burst
3. Continuous

In Single Step, one sawtooth pulse is sent to the piezo motor. In Burst mode, a burst of steps is sent to the piezo motor. Burst mode is used to make sub-mm motions of the piezo when the actuation button is pressed. These are useful for making fine adjustments to the laser or sample alignment. Finally, Continuous mode is used to drive the sample from its parked position, and to accomplish larger motions of the sample stage. In Continuous mode, it is advantageous to be able to control the amplitude of the sawtooth wave while performing the motion in order to speed up/slow down. This was controlled previously by the voltage output signal from an analog potentiometer joystick.

Signal characteristics

The signal generated by the old controller had an adjustable frequency in the 10^2 to several 10^3 Hz range. Its amplitude was about 10V at maximum output amplitude. A typical waveform for Burst mode is shown below:

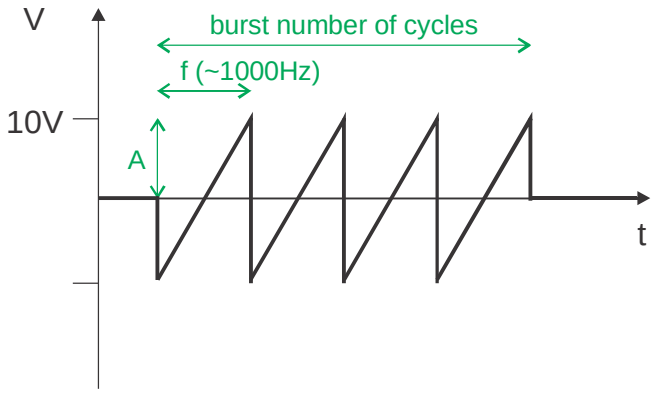

MATLAB - Wiimote implementation

Signal generation

The signal is generated as a wavetable for single step operation (`wavetableSingle`), and a wavetable for burst operation (`wavetableBurst`). When a single step is called, the single wavetable is played back through the sound card. When a burst is called, the burst

wavetable is played back, modulated by the desired amplitude read from the Wiimote. For continuous operation, the burst mode is called repeatedly until the actuation key is released. The `sound(y,FS)` function is used to output the signal through the sound card. Originally the Analog Output object was used to control the sound card, but it added significant and unnecessary startup delays to the program.

Wiimote communication

Wiimotes use Bluetooth communication. A Bluetooth USB receiver is used to establish communication with the Wiimote.

WiiLAB[1] code was used to interface with the Wiimote. This code is simple to use and seems to be robust. Unfortunately there are no callback functions, so `SawtoothDriver` is forced to check for key presses every 0.1s (implemented as `pause(obj.pauseTime);` in the while loop which calls `loopFunction)`.

Relay board electronics

The parallel port pins provide a voltage of about 3.3 V. This is not high enough to reliably gate a MOSFET switch to enable the actuation of the relay coil (Digikey PB958-ND). Instead a transistor circuit is used to draw a current through the coil. The relay coil is specified to work at 33 mA. We will aim to draw at this current through the transistor in the following circuit:

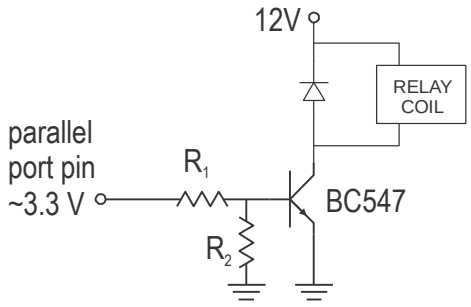

If the h_{FE} of the transistor (BC547) is about 100, and the current we require is $I_{coil} = 33.3\ mA$, then the current through the base of the transistor is

$$I_{Base} = \frac{I_{coil}}{h_{FE}} \simeq 0.33\ mA\,.$$

[1] http://netscale.cse.nd.edu/twiki/bin/view/Edu/WiiMote

If we fix resistor R_2 to be 10kΩ, the current though it is

$$I_{R_2} = \frac{0.6V}{10k\Omega} = 0.06\ mA$$

because we know that the base voltage is about one diode drop (0.6V) higher than the ground.

Because the currents through the Base and R_2 must sum to the current through R_1 (i.e. about 0.4 mA from above), the parallel port is shown to provide 3.3V, and the voltage at the transistor's base is 0.6V, then R1 should have the value:

$$R_1 = \frac{(3.3 - 0.6)V}{0.4mA} \simeq 6.75\ k\Omega$$

High voltage amplifier

Before modification

The OPA541 opamp will operate on rails up to ±40 V. In our rack the rails are around 15V. The high power opamp runs as an inverting amplifier, which drives the step-up transformer.

The output is switched by a relay. When the output relay is not powered, the coax center and shield conductors are shorted together. When the relay is powered, the coax center and shield are connected (floating) to the high voltage side of the transformer with the 5W resistor in series.

In our setup, the SMC coax cable carries the signal to the chamber where the shield is referenced to ground on the chamber star ground point. Internally, our piezos are referenced to the STM cage, so there is only one (HV) electrical connection per piezo stack.

The input signal is connected to the pads labeled >IN and >SIG. >IN is the input signal and >SIG is a ground. The 10kΩ potentiometer on the front panel connects between the >IN and >SIG terminals. Its wiper selects the level of the signal which will be sent to the input of the inverting amplifier opamp.

Modification for Matlab-Wiimote system

In the new implementation of the 4-axis piezo controller, the relay is bypassed, and the signal input is connected to the front panel by a SMC connector. This modification (with a BNC installed for testing) is shown.

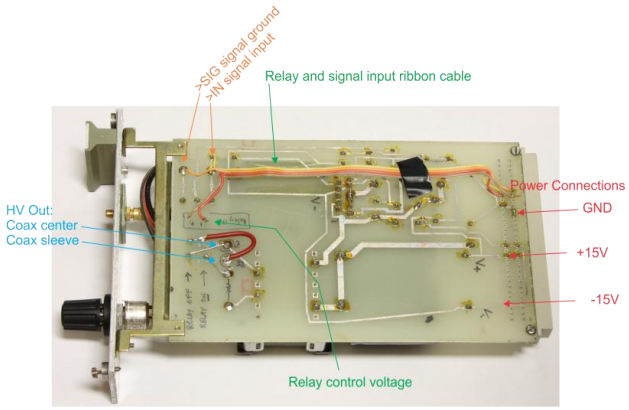

Modification to permanently connect output coax to transformer HV side, and add input connection:

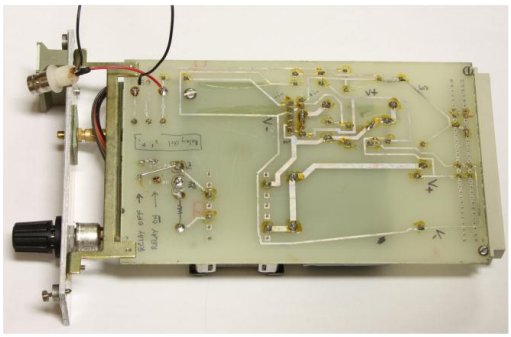

Usage Instructions

1. Ensure connections are established:

   i. Parallel port cable and audio cable from PC to Stick-Slip Motor Relay Board.
   ii. "Signal out" from Relay Board to "Input" on HV Amplifier.
   iii. "HV Out" from HV Amplifier to "HV In" on Relay Board.
   iv. X, Y, Φ(R1), Θ(R2), connections to UHV system.

Note: "Speaker Enable" connection has been abandoned; this was a cute feature but turned out to be quite difficult to implement reliably.

2. Establish Bluetooth connection with Wiimote. To connect Wiimote, press + and - keys simultaneously. The blue lights will flash, indicating that it is ready to establish connection. In the list of Bluetooth devices, right click on the Nintendo controller device, and choose "Connect".
3. Open Matlab and run SawtoothDriver
4. To operate the motors, use the direction buttons. By default, SawtoothDriver operates in **Single Step** mode.

   Burst Mode: Press "Toggle Burst" (1). The controller will rumble to indicate to the user that the next actuation (performed with the direction buttons) will be a burst. After the Burst actuation, the controller reverts to Single Step mode for safety reasons. Burst must therefore be toggled before each desired Burst step. The "Toggle Burst" button can also be pressed to cancel the Burst mode.

   Continuous Mode: The "Continuous" button (2) must be held down to enable Continuous operation while using the direction buttons to specify the axis of motion.

   Speed Control: In Burst and Continuous modes, the amplitude of the sawtooth is modulated by the *absolute value* of the tilt angle (accelerometer reading) *in the direction* of the motion axis. This means for X amplitude control, the X direction button must be pressed (Left or Right), and the controller must be tilted in the X direction. It does not matter if the controller is tilted left or right because of the absolute value operation. The direction is solely determined by the direction button which is pressed.

   X-Y / Φ-Θ control: The direction buttons of the controller only control one set of axes at a time -either X-Y or Φ-Θ control is enabled. To toggle between these modes, use the "TOGGLE X-Y / Phi-Theta" button (A). The blue status lights will change to indicate the active control mode.

   Frequency control: If necessary, the frequency of operation can be changed using the (+) and (-) buttons of the controller.